

Department of Exploration Geophysics

**Feasibility of Seismic Monitoring Methods for Australian CO₂ Storage
Projects**

Mamdoh Saad Alajmi

**This thesis is presented for the Degree of
Doctor of Philosophy
of
Curtin University**

January 2015

Declaration

To the best my knowledge and brief this thesis contains no material previously published by any other person expect where due acknowledgement has been made. This thesis contains no material has been accepted for the award of any degree or diploma in any university.

Signature:

A handwritten signature in blue ink, consisting of a large, sweeping curve followed by a smaller, more complex mark.

Date: 28/09/2015

To my parents, my wife and my respected brothers and sisters.

Abstract

Global warming is the natural consequence of increasing greenhouse gas (GHG) levels in the atmosphere, which contributes to global climate change. The technique of Carbon Capture and Storage (CCS) is one of the solutions used to capture CO₂ emissions and inject them into deep geological storage. Several projects have been established or proposed for different parts of Australia to evaluate and implement this technique in order to eliminate CO₂ from the atmosphere. CO₂ storage verification and monitoring is crucial both during and after CCS and geophysics plays important role in this process; first it is required to find the appropriate geological storage for injection and then it is involved in tracking and imaging CO₂ storage and movement. Also, the need for both conformance monitoring of the plume within the intended reservoir and detection of leakage should CO₂ migrate vertically and accumulate to a shallower zone, requires sufficiently sensitive monitoring methods. Among the geophysical methods, seismic methods play a crucial role in these tasks in most projects around the world.

Many factors influence the accuracy and sensitivity of CO₂ seismic monitoring; some of them relate to the survey design and quality, while others relate to processing and imaging issues. I studied both of these factors by modelling synthetic seismic data based on different seismic survey types, including surface, marine and VSP. To study these, I designed the surveys based on the expected needs for different proposed or existing storage projects across Australia. I modelled a variety of volumes of carbon dioxide plumes and inject them into realistic finite difference models in order to acquire several synthetic time-lapse data sets. The main purpose of this work is to establish the CO₂ detectability limits for Australian CCS projects. One of the main factors in detecting changes in time-lapse surveys is the level of noise in the data. I generated diverse realistic time-lapse noise models for all project areas in order to evaluate the use of seismic applications for accurate CO₂ monitoring. In this thesis, I studied the feasibility of using the seismic exploration methods (surface, marine streamers, ocean-bottom cables and VSP) in order to assess CO₂ storage verification and monitoring for three Australian projects: Southwest Hub, CarbonNet and Otway.

In detection feasibility studies for the Southwest Hub and CarbonNet projects, I identified the noise levels from real data, and model several injection scenarios in finite difference models in order to assess the detectability of different CO₂ plumes. I simulated the rock physics properties of the CO₂-saturated reservoir from log data, expected brine salinity and CO₂ temperature and pressure using Gassmann's fluid substitution equations to create a realistic finite difference model for several volumes of CO₂ plumes. For these two storage projects, I constructed numerical models using all these proprieties to evaluate effectiveness of surface, VSP, marine streamers and ocean-bottom cables time-lapse seismic monitoring methods.

For the Otway project, I presented two feasibility analyses to investigate CO₂ detectability and model a realistic time-lapse noise. First, I verified the seismic monitoring imaging ability of CO₂ detectability using two seismic migration application techniques. I compared the detectability of the CO₂ plume using pre- and post-stack Kirchhoff migration algorithms on synthetic time-lapse data sets. For this feasibility study I used real seismic noise from the baseline Sodas Road field data to model realistic band-limited random noise.

Second, I performed a seismic monitoring feasibility analysis for the Otway region by predicting the time-lapse seismic signal and noise and then model realistic 3D time-lapse noise using Otway 4D seismic field data. In general, the observed time-lapse noise is spatially-correlated, band-limited and exhibits lateral and temporal variations in its characteristics. If one wants to perform a statistical analysis of the detectability of the time-lapse signal, one would need to have multiple realisations of such noise. To obtain such realisations, I proposed a method for the modification of a single measured time-lapse noise volume.

The research presents techniques and modelling concepts to evaluate the use of seismic methods in CO₂ storage verification and monitoring. The main new developments and workflows in this thesis are the modelling of the time-lapse noise and its use for evaluating time-lapse monitoring methods. I trust that the presented results can improve feasibility studies of seismic CO₂ detectability and contribute to future applications in Australian CCS projects.

Acknowledgements

First of all I would like to thank my mother, Sarraa Asiri, who have supported me through whole my life and my study.

I am grateful to acknowledge King Abdullaziz City for Science and Technology (KACST) for granting my PhD and providing the financial support for my family and me during my study.

I would like to thank sincerely my supervisor Dr Andrej Bona for his help, guidance, valuable advice and outstanding supervision. I am also grateful to my co-supervisor Dr Roman Pevzner, for his good advice and support during my PhD. Also, I am thankful to the head of Department of Exploration Geophysics, Professor Boris Gurevich, for his valuable comments. I want to thank the faculty and all staff and my colleagues in the Department of Exploration Geophysics. Also my thanks goes to Dr Valeriya Shulakova for her help in data processing and to Dr Milovan Urosevic.

I am also grateful to acknowledge the Australian Commonwealth Government through the Cooperative Research Centre for Greenhouse Gas Technologies (CO2CRC) for their support and allowing me to work on their Otway project data.

Special thank goes to my wife, Areej, for her love and support throughout my study and for my kids, Omar, Sarraa and Abdulrahman, for their patience and understanding. Also I am very thankful to my brothers, Sultan, Bandar and Rakan, and my sisters, Maha, Hala and Ashwag, for their supports and encouragements.

I wish to express my gratitude to Mr Robert Verstandig for proofreading my thesis and to the secretarial, Deirdre Hollingsworth, Jennifer McPherson, Rhiannon Howe and Zuzanna Kuklinski.

Table of Contents

Declaration	i
Abstract.....	iii
Acknowledgements	v
CHAPTER 1: INTRODUCTION.....	24
1.1 CO ₂ Emission and Climate Change.....	24
1.2 Geologic Sequestration of CO ₂	26
1.2.1 Overview.....	26
1.2.2 CO ₂ Properties.....	28
1.2.3 CO ₂ Trapping Mechanisms.....	30
1.3 CCS in Australia	33
1.3.1 Overview.....	33
1.3.2 CO ₂ CRC Otway Project.....	33
1.3.3 South West Hub Project.....	34
1.3.4 CarbonNet South.....	34
1.3.5 Surat Basin Project.....	35
1.3.6 Gorgon Project.....	35
1.4 Motivation.....	35
1.5 Objectives.....	37
1.6 Dissertation Methodology.....	38
1.7 References.....	40
CHAPTER 2: METHODOLOGY	43
2.1 Introduction.....	43
2.2 Seismic Methods	47
2.2.1 Reflection surface seismic	47
2.2.2 Vertical Seismic Profile	48
2.2.3 Time-lapse seismic.....	49
2.3 Modelling Methods	52
2.3.1 Introduction.....	52
2.3.2 Finite-difference methods	53
2.3.3 Rock physics methods	56
2.3.4 Fourier transform	58
2.4 Seismic Noise.....	66

2.4.1	Seismic repeatability	66
2.4.2	Signal-to-noise ratio estimation	67
2.5	References	68
CHAPTER 3: QUANTIFYING TIME-LAPSE SEISMIC SIGNAL DETECTION FOR CO ₂ MONITORING AND VERIFICATION AT THE SOUTH WEST HUB		72
3.1	Introduction	72
3.2	Study Area and Geology	74
3.3	Data and Site Characterisation	80
3.4	Time-Lapse Seismic Monitoring Feasibility Analysis.....	88
3.4.1	Overview.....	88
3.4.2	Rock Physics and Fluid Substitution Modelling.....	90
3.4.3	Numerical Forward Seismic Modelling.....	97
3.5	Conclusion.....	121
3.6	References	123
CHAPTER 4: QUANTIFYING TIME-LAPSE SEISMIC SIGNAL DETECTION FOR CO ₂ MONITORING AND VERIFICATION AT THE CARBONNET PROJECT (GIPPSLAND BASIN).....		125
4.1	Introduction	125
4.2	Study Area and Geology	126
4.3	Data and Site Characterisation Approach	128
4.4	Time-Lapse Seismic Monitoring Feasibility Analysis.....	133
4.4.1	Overview.....	133
4.4.2	Rock Physics and Fluid Substitution Modelling.....	134
4.4.3	Numerical Forward Seismic Modelling.....	137
4.5	Conclusion.....	152
4.6	Reference.....	154
CHAPTER 5: QUANTIFYING TIME-LAPSE SEISMIC SIGNAL DETECTION FOR THE OTWAY PROJECT USING PRESTACK MIGRATION.....		157
5.1	Introduction	157
5.2	Study Area and Geology	157
5.3	Data and Site Characterisation Approach	160
5.4	2D Synthetic Modelling Data.....	163
5.5	Seismic Migration	165
5.6	Modelling of 2D Time-Lapse Noise	167

5.6.1	Overview.....	167
5.6.2	Estimating the SNR of real data	168
5.6.3	Migration Comparison and CO ₂ Detectability.....	174
5.7	Conclusion.....	181
5.8	References	183
CHAPTER 6: 3D TIME-LAPSE NOISE MODELLING USING DATA FROM THE CO2CRC OTWAY PROJECT		186
6.1	Introduction.....	186
6.2	Time-lapse Repeatability	188
6.2.1	Sources and Receivers Repeatability	188
6.2.2	Cross-equalisation Processing	196
6.3	Modelling of 3D Time-Lapse Noise	199
6.3.1	Theory	199
6.3.2	Modelling of time-lapse noise for the Otway Project.....	207
6.4	Discussion	210
6.5	Conclusion.....	215
6.6	References	216
CHAPTER7: SUMMARY, CONCLUSIONS AND FUTURE RESEARCH		219
7.1	Summary	219
7.2	Conclusions and recommendations.....	221
7.3	Future Research.....	222
Appendix.....		225

LIST OF FIGURES

Figure 1.1: The world demand for hydrocarbon and renewable energy sources. The expectation is that global energy demand will rely primarily on hydrocarbon resources for the next 20–40 years (EIA, 2013).	24
Figure 1.2: The main processing steps of carbon capture and storage (after CO2CRC, 2013).	26
Figure 1.3: Sedimentary basins for use as CO ₂ sequestration sites and their storage prospectivity distribution around the world (IPCC, 2005).	27
Figure 1.4: The suitable options of geological storage formations and reservoirs for CO ₂ sequestration (after CO2CRC, 2013).	28
Figure 1.5: The pressure-temperature phase diagram for CO ₂ (after Benson and Cole, 2008). The supercritical phase zone is shown in the yellow box, where the properties of the CO ₂ are similar to those of both a liquid and gas. The pressure unit is 1 bar = 0.1 Mpa.	29
Figure 1.6: Schematic representation of the security of the major CO ₂ physical and chemical trapping mechanisms over time (after CO2CRC, 2013). It can be seen how many of the trapping systems contribute to increased storage security over time (red line). The figure also shows that physical trapping dominates, while chemical trapping increases gradually over years.	31
Figure 1.7: Residual mechanism gas-trapping process (CO2CRC, 2013).	33
Figure 1.8: Australian CCS projects. The storage sites, such as the Otway project, South West Hub project, the CarbonNet project and the Surat Basin project, will be discussed here. The Gorgon project is also discussed in this report.	34
Figure 1.9: Flow chart of the research methodology steps. The research has three main stages that indicate the structure and work methodology of the thesis based on the research objectives.	39
Figure 2.1: An example of the reflection surface seismic end-on spread geometry and the seismic signal record of a P-wave field. In this survey, the depiction of the source (red star) is placed on the left side of the spreading geophones (blue triangles), with a group interval Δx between the geophones, or channels. This experiment's model has two media, 1 and 2, with a different P-wave velocity, S-wave velocity and density for each medium. A seismic section of two-way travelttime $t(s)$ and the distance $x(m)$ shows the seismic signal response for each geophone. The delay response of	

traveltime is clarified by the hyperbolic relation shown at the bottom of the graphic.

..... 46

Figure 2.2: An illustration of the vertical seismic profile method, for an Earth subsurface model of two mediums, 1 and 2, with a different P-wave velocity, S-wave velocity and density for each medium. The source (red star) is placed on the surface and geophones (green triangles) are placed inside the borehole at different depths. The one way traveltime $t(s)$ and the depth $x(m)$ are presented with the depth level for each signal of geophones in the cross-seismic section at the bottom of the figure. A VSP section is made up of the two seismic waves, the upgoing (referred to by blue arrows) and the downgoing (referred to by orange arrows). 48

Figure 2.3: The time-lapse seismic signal and its response to the changes in rock and fluid properties VP, VS, density and pressure. The graphic shows how the changes in the injection properties of the CO₂ reform the original signal in Survey 1 by decreasing the acoustic and shear impedance and causing shifts in the time and amplitude in Survey 2. These shifts can be monitored using a 4D seismic survey (modified after Calvert, 2005). 51

Figure 2.4: A time-lapse seismic image of the Sleipner CO₂ injection project from (a) the baseline pre-injection 1994; (b) the monitoring image 2001; (c) the monitoring image 2004; and (d) the monitoring image 2006. The lower figure shows the integrated reflection amplitude response of the CO₂ plume and its development from 1994, before injection, to 2006, after injection (modified after Chadwick et al., 2009). 52

Figure 2.5: The model of the 2D finite-difference method. This mathematical model is represented by a grid of different time Δt and space Δx steps. The node's backward, centred and forward difference steps, respectively (three dots) explain how the wavefield is calculated by FD in space. Simply, the first derivative approximation of a spatial value step is used and is represented by three steps (red dots). 56

Figure 2.6: A depicted cube of rock characterising four major geological components, according to the Gassmann theory: the saturated frame, dry frame, rock matrix and fluid system (Russell et al., 2003). 58

Figure 2.7: The conventional model of the Fourier transform with a long window. In this conventional transform (symmetrical variable window), the Fourier analysis is done by encompassing all frequencies of the seismic signal in a long window in a

time domain. As a result, a band-limited white amplitude spectrum is observed in the frequency domain, which makes seismic data interpretation very complicated (Partyka et al., 1999).....	61
Figure 2.8: The short window spectral decomposition, or the fixed window analysis of Fourier transform. It can be seen how the short window technique addresses the seismic signal in the details to help in the interpretation of the small and thin events shown in the data. The fixed time of the short time of the Fourier analysis is done by decomposing a short temporal window of the seismic signal for a small group of frequencies. This short window in the frequency domain shows a series of chirp frequencies in the coloured spectrum and gives a band-limited coloured spectrum of the seismic signal. This technique of the Fourier transform is a good way to reduce the randomness of geological interpretation in seismic signal processing (Partyka et al., 1999).	62
Figure 2.9: A simple example of the STFT windows' moving and overlapping technique. STFT analysis transforms the window individually by making the rest have a value (out of the window) of zero and then moves to the next window. The time to frequency transform technique continues to cover the entire seismic signal.	63
Figure 2.10: The Hann window in (a) time and (b) frequency domains. The smoothness shown in the Hann window is reflected in the transform frequency window by reducing the level of the side lobe and in contrast, increasing the width of the main lobe. This effect causes a decrease in the leakage of spectral amplitude in a time-frequency transform decomposition.	65
Figure 3.1: Map showing the location of the South West Hub project for CO ₂ capture and storage. The blue rectangle shows the area within which the project expects to inject the gas (Modified after Dance and Tyson, 2006).	72
Figure 3.2: Simplified geological maps of the Southern Perth Basin. On the left is a general map of the study area, showing the major fault in the Darling Fault in the east of the Perth Basin. The geological structure, faults, anticline and syncline are presented in the map on the right. The boundaries of the Southern Perth Basin are clarified in this map, with the subdivisions and tectonic lineament of the basin. The target area for the South West Hub CCS project falls to the east of the apex of the Harvey Ridge (after Crostella and Backhouse, 2000).	75
Figure 3.3. Stratigraphy of the Southern Perth Basin (Crostella and Backhouse, 2000).	76

Figure 3.4: South-to-north strata correlation and a map of the wells over the Southern Perth Basin. The geological formations of the Southern Perth Basin within many wells in the area are shown with their depth in meters. The CO ₂ trapping sequence of interleaved sands and shale, which extends to at least 2600 m below the surface, is shown. The closest wells to the SW Hub project are Lake Preston 1 and Pinjarra 1, which are marked with the red rectangle. The Lesueur sandstone, the suggested formation for CO ₂ injection, is located at a depth of 1520 m in Preston 1 and at a depth of 2400 m in Pinjarra (after Crostella and Backhouse, 2000).....	79
Figure 3.5: The location of the six 2D surface seismic data lines. These lines were utilised to evaluate the CO ₂ seismic monitoring for the SW Hub project for CO ₂ capture and storage. The available well logs in the area are from wells Pinjarra 1 and Lake Preston 1, which are also shown. No wells intersect any of the lines.	82
Figure 3.6: The various log types of Lake Preston 1 (a) and some core samples of the Pinjarra 1 well (b). The photographs of core samples 1, 2 and 3 present the cores at depths of 625 m, 2587 m and 1385 m, respectively. The lithology of these cores shows fine-grained sandstone (2) and shale (1), fine-grained sandstone overlying shale and shale overlying very fine-grained sandstone (3).....	83
Figure 3.7: The 3D interpretation view of 11GA_LL2. The interpreted section shows the geological structure of the southern Perth Basin, with collared horizons of the subsurface formation from lower to upper: Wonnerup Member (Lower Lesueur formation), Myalup Member (Upper Lesueur formation), Eneabba Member, Cattamarra Member, Cadda Formation, Warnbro Group and the near-surface superficial sediments. It also shows the fault system in the area (marked in black) and how the seismic line is crooked in the faulting area.	86
Figure 3.8: Gravity anomaly map of the basement depth of the Southern Perth Basin. The South West Hub project area (red square) is located near the Harvey Ridge, south of the study area (after Iasky and Lockwood, 2004).....	87
Figure 3.9: A flowchart of the main experimental steps of a feasibility analysis for the CO ₂ capture and storage South West Hub project. Some hints into insights that were applied through the investigation in time-lapse seismic signal response for CO ₂ injection are also shown.....	89
Figure 3.10: The interpretation of 11GA_LL2. The interpreted section shows the geological structure of the Southern Perth Basin, with collared horizons of the subsurface formation from lower to upper: Wonnerup Member (Lower Lesueur	

formation), Myalup Member (Upper Lesueur formation), Eneabba Member, Cattamarra Member, Cadda Formation, Warnbro Group and the near-surface superficial sediments. It shows also the fault system in the area, which is marked in black.....	91
Figure 3.11: The percentage and gradient changes in impedance crossplot with the CO ₂ saturation percentage in the South West Hub project for CO ₂ capture and storage. Impedance will decrease with high changes of CO ₂ saturation, which means that injection procedures have less of an effect on seismic response (Annetts et al., 2012).	94
Figure 3.12: The acoustic and shear impedance changes of CO ₂ saturation before and after injection into the Lesueur formation.	96
Figure 3.13: A cross-section of shape dimensions, diameters and thicknesses for the volumes of the six different plumes. The black dots show the selection of diameter/thickness pairs. The d_F indicates the diameter of the first Fresnel zone in the injection area in the Lesueur formation. h_0 refers to the tuning thickness for a wavelength of 60 m.....	99
Figure 3.14: The horizontal axis is oriented east-west along 11GA-LL2 (top) and the values of signal-to-noise ratio (SNR) are shown in log10 scale (bottom). The amount of noise, as shown in the SNR result, is low in the deep and that may have been caused by the source energy or the attenuation of the seismic wave. However, the unusual values that are shown in the area are in the western region—the ‘mute zone’.	102
Figure 3.15: Depiction of the noise attributes analysis windows of common source and receivers gathers. The analysis windows are divided into three main windows; signal, ground roll and noise, and direct arrival. They display shot and receiver offset in the horizontal axis and two-way travelttime in the vertical axis. The red line indicates the direct arrival waves, the green curves indicate the range of reflected signals and the orange line indicates the ground roll.....	103
Figure 3.16: The results of the quality control (QC) attributes: the mean absolute amplitudes in ‘signal’ and ‘noise’ windows (SNR _{QC}), in the ‘ground roll’ window, and centroid frequency in the ‘signal’ window. These analysis windows are computed by using common source and receivers gathers. In the SNR _{QC} attribute, it	

is clear that there is a large increase in the receiver's gathers, while the source's gathers remain relatively unchanged. 104

Figure 3.17: Quality control signal-to-noise (SNR_{QC}) attribute (top) and 11GA-LL2 (bottom). The horizontal axis is oriented east-west along 11GA-LL2 (top), with increasing station numbers that are related to the geometry of the seismic acquisition. The marked area on the seismic section represents the 'mute zone', which hides the most reflected waves and layer interfaces inside this area (the location of the Lesueur formation). In the 'mute zone', the SNR_{QC} attribute shows a great increase in receivers gathers, while the sources are stable without observed changes. The suggested reason behind these variations is changes in the near-surface conditions. 105

Figure 3.18: The model of the South West Hub area with six difference volumes of CO_2 plumes; 2, 5, 10, 20, 40 and 80 Kt. The model is driven on the basis of seismic line 11GA-LL2. The enlarged figure shows the locations of the suggested plumes, which are placed on the interface at the top of Myalup (the top of the Lesueur formation) and inside the formation to assess the CO_2 detectability in the plumes area and after CO_2 migration. The red dashed rectangle indicates the subset of the model, which was used to present the remainder of the work and results..... 108

Figure 3.19: Noise-free seismic response sections of baseline, monitor line, and difference of the synthetic data. The six CO_2 plumes are clearly detectable in the difference section. Realistic noise should be modelled and added to evaluate the detectability of CO_2 111

Figure 3.20: The signal-to-noise ratio (SNR) histograms for (a) real and (b) synthetic sections, according to the modelled injection location. A high SNR count is shown on the interface layers of synthetic data at the given time. (c) The synthetic section of the SNR result is shown with a log10 scale. The amount of noise that was added approximately a SNR of 5 to match the measured SNR at the reflector corresponding to the interface between the formations of the finite difference model of the Eneabba Me and Myalup formations..... 112

Figure 3.21: The results of the migrated baseline, monitor line and difference synthetic section, with added filtered realistic noise. The CO_2 detectability is low in the difference section. The detectability of the plumes is higher in the monitor section than in the difference section. That is because the difference section contains noise from both the monitor and baseline surveys, while the monitor only contains

one realistic noise. However, plumes located at an interface would not be visible in the monitor section.....	113
Figure 3.22: The distribution of the CO ₂ plumes within the model. The location of the six plumes is distributed in the Myalup formation as show in figure 3.18. The black vertical lines indicate the location of the modelled monitoring and/or injection wells. The grid size is 0.5 km×0.5 km.	115
Figure 3.23: The well six VSP zero-offset (100 m offset) noise-free sections for baseline, monitor line and difference. In VSP modelling, the plumes are detectable because they are not placed on the interface. Therefore, any modelled plumes placed on the interface will be covered by the strength of the interface reflected wave. Here, the plume seismic response is apparent in the difference section, which is indicated by the arrow.	118
Figure 3.24: The well five VSP zero-offset (100 m offset) noise-free sections for baseline, monitor and difference. Again, the CO ₂ detectability is high in the difference section and low in the monitor section, due to the reflected wave strength. The arrows indicate the locations of the injected CO ₂ on the interface and inside the layer in the difference section.	119
Figure 3.25: The zoom plume location of the migrated VSP zero-offset (100 m offset) noise-free migrated monitor and difference sections of well five. The amplitude of the difference signal is only approximately 10% of the amplitude of the reflector in the monitor section.	120
Figure 3.26: The enlarged plumes zone of the walkaway VSP migrated difference sections for receiver depth ranges of 50–2950 m, 50–1000 m and 50–500 m. The source-offset range is ±1500 m. These results show a very slight change in the degradation quality between the depths. This change is considered irrelevant if we compare the advantage of the well-drilling cost between shallow and deep wells.	120
Figure 4.1: Map showing the location of the CarbonNet project for CO ₂ capture and storage. The location of the project in the south-east of Australia in the Gippsland basin, which represents the major tectonic elements in the area and the oldest produced hydrocarbon fields in Australia (after Power, Hill, Hoffman, Bernecker and Norvick, 2001).	125
Figure 4.2: The map of the Gippsland basin, which extends onshore and offshore of the south-east of Australia. The oil and gas field spreads throughout the basin. The	

offshore depleted fields are suggested for use in investigating CO ₂ geosequestration for the CarbonNet project (Geoscience Australia, 2013).	126
Figure 4.3: Stratigraphy column of Gippsland onshore and offshore (after Power, Hill, Hoffman, Bernecker and Norvick, 2001).	128
Figure 4.4: Seismic section G92A-3000, the basis of a 2D geological model to assess the CO ₂ detectability for the CarbonNet project.....	129
Figure 4.5: The location of seismic line G92A-3000 shown in red, the line GGS185B-17a shown in yellow and the intersection well, Kyarra-1. The line GGS185B-17a is used as guide in constructing the geological model of G92A-3000 for the CarbonNet project.	130
Figure 4.6: The Nearshore Gippsland concept for CCS of CarbonNet project. This simulation is a one of several opportunities that are suggested by (Gibson-Poole et al., 2006).	131
Figure 4.7: Two examples of seismic lines interpreting the geological structure in the onshore Gippsland Basin (after Moore and Wong, 2002) and (after Power et al., 2001). The location of the line G92A-3000 is roughly located near the area in red box.	132
Figure 4.8: A flowchart of the main experimental steps of a feasibility analysis for the CO ₂ capture and storage CarbonNet project. Some hints into insights that were applied through the investigation in time-lapse seismic signal response for CO ₂ injection are also shown.....	133
Figure 4.9: The interpretation of seismic line a G92A-3000 shows the subsurface geological structure of Gippsland Basin offshore. The geological structures are shown with collared horizons of the subsurface formation from lower to upper: The Strzelecki Group, The Latrobe Group, Lakes Entrance Formation, Lower and Upper Gippsland Limestone and the nearshore of the ocean. It shows also the fault system in the area, which is marked in black.....	134
Figure 4.10: The acoustic and shear impedance changes of CO ₂ saturation into the Latrobe Group of the Gippsland Basin. The blue arrows show the acoustic and shear impedance for the pre-injection case of 100% brine saturation of 7.203 and 4.017, respectively. The post-injection results of acoustic and shear impedance on a 50% CO ₂ saturation are 6.639 and 3.933 kg/(km ² .s), respectively. These differences between pre- and post-injection indicates that approximately 0.19% of the seismic energy is reflected from the CO ₂ plume.	138

Figure 4.11: The finite difference model on the basis of interpreted seismic line G92A-3000 with five difference volumes of CO₂ plumes; 0.64, 1.95, 3.18, 6.37 and 12.73 Kt. The size of the plumes gradually increases from left to right and all sizes are listed in Table 4.4. The model is used to investigate the CO₂ detectability in CarbonNet project area. The enlarged figures in red rectangle shows the locations of the suggested plumes, which are placed on the interface at the top of Latrobe Group sealed by Lakes Entrance formation. The yellow dashed rectangle indicates the subset of the model, which was used to present the remainder of the work and results.

..... 139

Figure 4.12: A cross-section of shape dimensions, diameters and thickness for the volumes of five different plumes. The black dots show the selection of diameter/thickness pairs. The d_f indicates the diameter of the first Fresnel zone in the injection level on the top of Latrobe Group. h_0 refers to the tuning thickness for a wavelength of 60 m..... 141

Figure 4.13: Noise-free seismic response sections of baseline, monitor line, and difference of the synthetic data. The five CO₂ plumes are clearly detectable in the difference section. Realistic noise should be modelled and added to evaluate the real detectability of CO₂. 144

Figure 4.14: The SNR for real data computed with 100 ms window in a log10 scale (right) and in histograms for each time slice (left) where the hot colours correspond to high count of SNR values. In the white circles show the suggested location for CO₂ plumes. The amount of noise in plume zones approximately matches a SNR of 10, which is located at the top of Latrobe Group subsurface formation..... 144

Figure 4.15: The result of matching 10 SNR for synthetic data computing with 100 ms window in a log10 scale (right) and in histograms for each time slice (left) where the hot colours correspond to high count of SNR values. The white circles show the level of noise, which was added to synthetic data to match the level noise in the injection zone to investigate the detectability of CO₂ plumes at the top of Latrobe Group subsurface formation. 145

Figure 4.16 The results of the synthetic migrated baseline, monitor line and difference synthetic section, with added filtered realistic noise from SNR estimation. In the enlarged figure (below) the CO₂ plumes are detectable for the largest volumes 6.37 and 12.73 kt, as marked with a white circle..... 147

Figure 4.17: The result of the NRMS attribute for the synthetic data in the histogram (on the left) and the synthetic section (on the right). Hot colours refer to the high count values of NRMS. The produced NRMS is 50%, which was chosen to match the noise in the injection zone (the top of Latrobe Group subsurface formation)...	148
Figure 4.18: The results of the synthetic migrated baseline, monitor line and difference synthetic section with added noise matching roughly 50% NRMS. The observed amount of noise is very similar to what I had observed in the SNR estimation. The CO ₂ plumes are detectable for approximately 3 kt and more.	148
Figure 4.19: The result of the NRMS attribute for the synthetic data in the histogram (on the left) and the synthetic section (on the right). Hot colours refer to the high count values of NRMS. The produced NRMS is 17%, which I chose to match the noise in the injection zone.	150
Figure 4.20: The results of the synthetic migrated baseline, monitor line and difference synthetic section with added noise matching roughly 50% NRMS.	151
Figure 5.1: Otway project location map. The map shows the injection wells for Stage 1 (CRC1) and Stage 2 (CRC2) and the production well (Naylor-1) opposite the Sodas road (red line) (after CO2CRC, 2013).	158
Figure 5.2: The Otway Project: Stages 1 and 2 of CO ₂ sequestration. The injection zone of Stage 1, which is below that of Stage 2, provides the opportunity to model time-lapse seismic noise without a CO ₂ plume cloud effect (CO2CRC, 2013).	159
Figure 5.3: Seismic section of Sodas Road, the basis of a 2D synthetic dataset generating data to assess CO ₂ detectability for the Otway Project.	160
Figure 5.4: Pre-stack time migration of Sodas Road data from the Otway region with a CDP range of 2001–2314.	161
Figure 5.5: A flowchart of the main steps of feasibility analysis for CO ₂ capture and storage for the Otway Project.	162
Figure 5.6: The 3D geometry layout of synthetic data with the sources line (white) and the receivers lines (black). The selected 2D line for the entire test is in the yellow box.	164
Figure 5.7: Noise-free shot gathers of synthetic baseline (left) and monitor (right) data acquired using MPI code SOFI 3D software.	165
Figure 5.8: The depiction of seismic wave scattering on both reflection surfaces (blue) and diffraction hypersurfaces (yellow) (Tertyshnikov, 2014).	167

Figure 5.9: The migration section of Sodas Road data and its SNR results. The red ellipses show the level of noise around the suggested injection plume depth, which was added to the synthetic data to match the level noise.....	169
Figure 5.10 Noise-free seismic sections of the synthetic baseline, monitor, and difference data. The CO ₂ plume is clearly detectable in the difference section and can be detected in the monitor section in the enlarged figure below. Realistic noise should be modelled and added to evaluate the actual detectability of CO ₂	171
Figure 5.11: The comparison of the SNR computed with a 100 ms window in histograms for each time slice for real data (left) and matching realistic modelling noise (right). The red ellipses indicate the amount of noise that was added to the synthetic data to match the real level of noise in the injection zone. This amount of noise has a range of SNR between approximately 3 and 20 and the maxima of the distribution of SNR matches well for the deeper parts of the data.	172
Figure 5.12: The results of the migrated synthetic baseline, monitor and difference section, with added filtered realistic noise from the SNR estimation. In the enlarged figure (below), the CO ₂ plume is detectable, but the noise around the plume did not model realistically as it is affected by the migration algorithm and moveout correction.	173
Figure 5.13: The synthetic shot gather baseline and monitor line with added filtered realistic noise from the SNR estimation.	174
Figure 5.14: Smoothed root mean squared (RMS) velocity model of Sodas Road synthetic data.	175
Figure 5.15: The imaging results of the post-stack migration baseline, monitor and difference synthetic section. It is clear that the modelled time-lapse noise is affected by the migration operation. In the zoomed figure (below), the low detectability of CO ₂ in the monitor and difference sections is greatly affected by the post-stack migration technique, as shown in the white circle.....	176
Figure 5.16: The imaging results of the pre-stack migration baseline, monitor and difference synthetic sections. In the zoomed figure below, the improvement in the detection of the CO ₂ plume in the monitor and difference sections (in the white circle) can be seen, corresponding to the post-stack result. This makes this migration technique more powerful in time-lapse seismic evaluation of CO ₂ detectability. ...	178
Figure 5.17: The comparison of the difference sections of pre-stack migration results (left) and post-stack (right) migration results. In the white circles in the zoomed	

figure below, it is clear that the pre-stack migration in the difference section can detect the time-lapse signal of the CO₂ plume using the same parameters and velocity that were used in the post-stack test. This proves the ability of the pre-stack migration algorithm in the time-lapse seismic evaluation of CO₂ detectability. 179

Figure 18: The NRMS result computing with a time window of 30 ms in log₁₀ scale for pre-stack migration (left) and post-stack migration (right). The NRMS values show increasing non-repeatability in the pre-stack image comparing to post-stack image at the injection zone (the white circle). 180

Figure 5.19: The comparison of the results of adding modelled noise before migration pre-stack (left) and post-stack (middle) and after migration (right). The evaluation of CO₂ seismic monitoring is more realistic when adding noise before migration compared to adding noise after migration. 180

Figure 6.1: Basemap of the 3D Otway acquisition survey layout. The 10 lines in the yellow box are the receiver lines at 10 m intervals. The other lines are the source lines at 20 m intervals. 190

Figure 6.2: Basemap of the 3D Otway acquisition survey layout for (a) 2008 and (b) 2009 and 2010. (a) The right hand side figure shows the odd source lines 1–27 and 28 (marked as blue dots) recorded by receiver lines 1–5 (highlighted by the red rectangle). The left hand figure (a) shows even source lines 2–24 and 29 recorded by receiver lines 6–10. (b) For the 2009 and 2010 surveys all the source lines were recorded by all the receiver lines (highlighted by the red rectangle). 191

Figure 6.3: Seismic signal sources used in the Otway Project. (a) The weight drop source (a 1350 kg concrete breaker that free fell from 1.2 m) used in the 2008 baseline survey. (b) The mini-buggy source (IVI 15,000 lbs vibroseis) with a sweep frequency range of 10–140 Hz used in the 2009 and 2010 surveys. 192

Figure 6.4: The CDP geometry fold map for (a) the 2008 survey and for (b) the 2009 and 2010 surveys. In 2008, the nominal fold was approximately 100, but with survey parameter changes, the nominal fold doubled in the 2009 and 2010 surveys to approximately 200. 194

Figure 6.5: An example of the raw shot gather sections of the three volumes for 2008, 2009 and 2010. This example shows the differences in resolution between 2008, 2009 and 2010 that were mainly caused by the changes in the seismic energy, which was much weaker in 2008 using the weight drop source. That weakness in

energy occurred because the spectral content varied significantly in the 2008 survey.	195
Figure 6.6: A comparison example of the inline 87 migrated section of the three surveys with conventional seismic data processing (top) and after applying the cross-equalisation processing steps (bottom). Note the weakness in the 2008 volume throughout the whole section, particularly in the near surface horizons. The 2009 and 2010 sections show high resolution and repeatability, making the 3D noise modelling results more reliable.....	198
Figure 6.7: Examples of two cross-equalised, processed volumes (a) 2009 and (b) 2010 and (c), their difference in both temporal (Inline 112) and (d) spatial domains (Time slice 1400 ms). The difference section shows the real noise, which is used to model time-lapse noise for the Otway data. This result contains not only the differences of the two acquisitions but also the result of imperfect cross-equalisation processing.	201
Figure 6.8: (top) Example of a signal with a window and (bottom) the windowed signal and the result of the changed phase spectrum.	202
Figure 6.9: (top) Example of the original signal, (middle) the weighted average of the windowed signal with modified phase spectra and (bottom), the same average scaled using sliding windows to match the amplitudes or the original signal.	203
Figure 6.10: Workflow schematic for generation of the "randomised" signal.	204
Figure 6.11: The Hann window in (a) time and (b) frequency domains. The smoothness shown in the Hann window is reflected on the transform frequency window by reducing the level of the side lobe and, in contrast, increasing the width of main lobe. This effect causes a decrease in the leakage of spectral amplitude in time-frequency transform decomposition.	206
Figure 6.12: Window function used for the generation of the modified time-lapse noise in (a) 3d and (b) 2d displays. The sliding windows have an overlap of 83% in all the three directions—two spatial and one temporal.....	209
Figure 6.13: Inline section of the noise generated from (left) real time-lapse data and (right) our synthetic modelling noise. The simulation result of the modelled noise is seen to be similar to the actual noise of the difference section.....	211
Figure 6.14: Amplitude spectrum comparison for a one trace of (a) the measured noise and (b) modelled noise. The spectrum shows high similarity between the	

modelled noise and the actual noise which denotes how the method preserves such frequencies of the real data.	212
Figure 6.15: Amplitude spectrum comparison of (above) the measured noise and (below) modelled noise. The spectrum shows high similarity between the modelled noise and the actual noise, which denotes how the method preserves such frequencies of the real data.....	213
Figure 6.16: Time-slice comparison of (left) the real noise and (right) modelled noise at t=1400 ms.	214

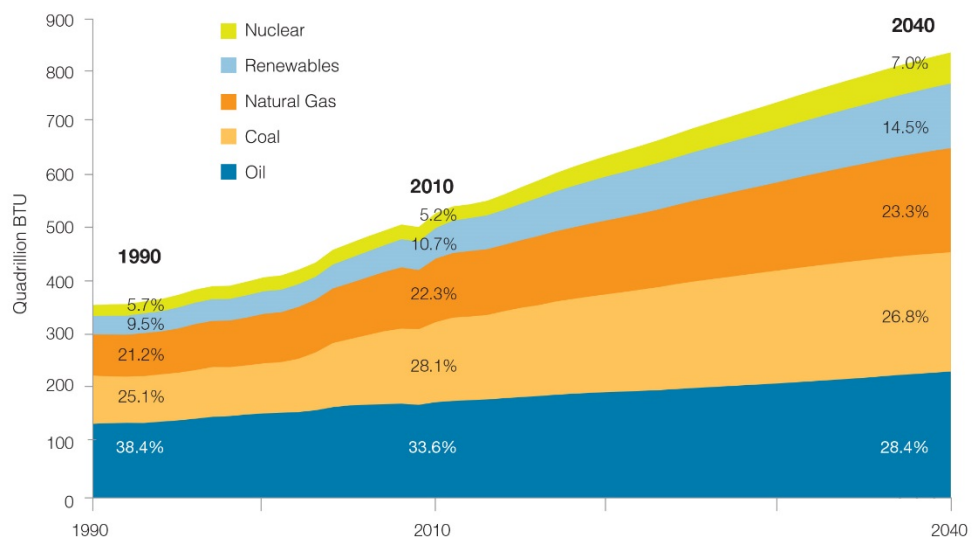
CHAPTER 1: INTRODUCTION

1.1 CO₂ Emission and Climate Change

Greenhouse gas (GHG) emissions are one of the main factors that contribute to climate change. Normally, GHG concentrations and the amount of energy (global temperature) in the atmosphere are balanced between the energy transmitted (heat) from the atmosphere to Earth and its reflection back into the atmosphere (IPCC, 2005). Climate change is the consequence of increasing and trapping the GHG concentration in Earth's atmosphere, where it causes global warming. Globally, the demand for energy and therefore the consumption of coal, oil and gas resources, is increasing and their use is a major cause of rising carbon dioxide (CO₂) emissions. It is predicted that the demand for global energy will double in the next 20 to 30 years (Lumley, 2010). Renewable energy sources, such as wind, solar and so on, are one of the solutions to help decrease global warming; however, they currently provide an insufficient amount of energy to meet global demand, as shown in in Figure 1.1.

Future Global Energy Demand

The world will require 56 percent more energy in 2040 than in 2010.



Source: EIA, *International Energy Outlook 2013*.

Figure 1.1: The world demand for hydrocarbon and renewable energy sources. The expectation is that global energy demand will rely primarily on hydrocarbon resources for the next 20–40 years (EIA, 2013).

Naturally, the variety of geological and biological processing cause CO₂ and other GHGs to be released into the atmosphere (IPCC, 2007). In addition, the same study found that the major atmospheric concentration of CO₂ is caused by humans. To illustrate this, the IPCC report shows that the CO₂ concentration in the atmosphere before 1750 was between ~255 and 280 parts per million (ppm). By 2005, this value had increased by 35% to become 379 ppm. Del Pino et al. (2006) established in 2000 that 77% of the total GHGs are made up of anthropogenic CO₂. That sharp increase of CO₂ and other important GHG emissions into the atmosphere corresponded with industrial waste products, the burning of fossil fuels and the growth in land use (IPCC, 2007). Currently, CO₂ emissions are more than 21.3 billion tonnes per year, which are mainly caused by the industrial combustion of fossil fuels and other human activities (DCCEE, 2012). However, of particular interest to Australian CO₂ emissions, the per-person production of CO₂ is more in developed countries, making Australia one of the top 20 countries in CO₂ emissions. The predictions are that Australia's CO₂ emissions will be approximate by 20% of global CO₂ emissions by the end of 2020 if no action is taken to decrease them (DCCEE, 2012).

Energy-intensive industry and electricity usage are the major causes of Australia's CO₂ emissions. The locations of CO₂ emissions in Australia are concentrated in seven or eight regions. These regions produce approximately 95% of Australia's total CO₂ emissions (DCCEE, 2012). In fact, the CO₂ emission sources are mostly stationary, which means that this CO₂ can potentially be captured and stored by using the developing technologies in this field. Australia is a coal exporter and liability for this mined carbon might in some way be Australia's responsibility, for example, in terms of maintaining a viable future for coal as a resource. Australia has moved seriously towards decreasing the emission of CO₂ in the atmosphere by establishing a number of CO₂ capture-and-storage projects and supporting their evolving technologies.

1.2 Geologic Sequestration of CO₂

1.2.1 Overview

CO₂ geosequestration, known as carbon capture and storage (CCS), is the process of capturing CO₂ at its source and storing it in deep geological formations, thus preventing its emission into the atmosphere. CCS consists of three major processing steps: CO₂ capture, compression and transport, and finally, storage (Figure 1.2). In the first step, CO₂ is captured from industrial and energy-related waste gases by using capturing techniques. The next step is the separation and compression of CO₂ into a supercritical fluid form. Currently, different technologies are used to capture CO₂ after combustion, particularly in fuel-burning processes, and then to prepare the gas for transport to a storage site (IPCC, 2005). Finally, the transported CO₂ is injected, typically as a supercritical fluid, into a suitable subsurface geological site, such as a depleted reservoir or an aquifer. The supercritical fluid is transported by pipeline or road for long-term storage and/or for enhancing hydrocarbon recovery processing.

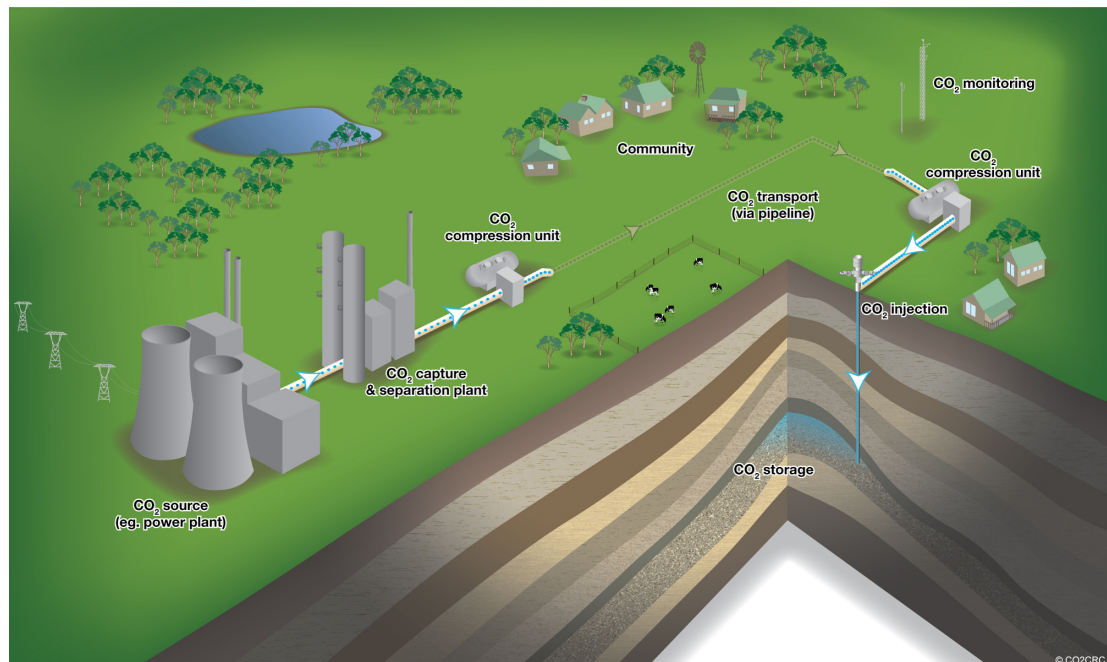


Figure 1.2 The main processing steps of carbon capture and storage (after CO₂CRC, 2013).

Many studies and much research have established the feasibility of using CCS technology in mitigating climate change. Cook (2014) presents the results of many reports published by the Intergovernmental Panel on Climate Change over the last decade and shows that reducing the concentration of CO₂ in the atmosphere by using CO₂ geological sequestration is probably one of the most appropriate ways to eliminate CO₂ emissions. But this approach is based on many criteria that determine whether the use of CCS is feasible. These criteria include storage capacity, injectivity, confinement, safety and cost.

Worldwide distribution of sedimentary basins and their prospectively for CO₂ sequestration are usually located nearby many of the world's gases sources and therefore a reasonable percentage of these emissions could be sequestered in the future (IPCC, 2005), as shown in Figure 1.3. These CO₂ geosequestration processes secure the gas under the surface into geological formations. The oil and gas industry has developed many technological techniques for CCS, for example, well drilling, data processing, simulation imaging of storage reservoir dynamics and monitoring methods. These techniques have been adapted to achieve the needs of geological storage.

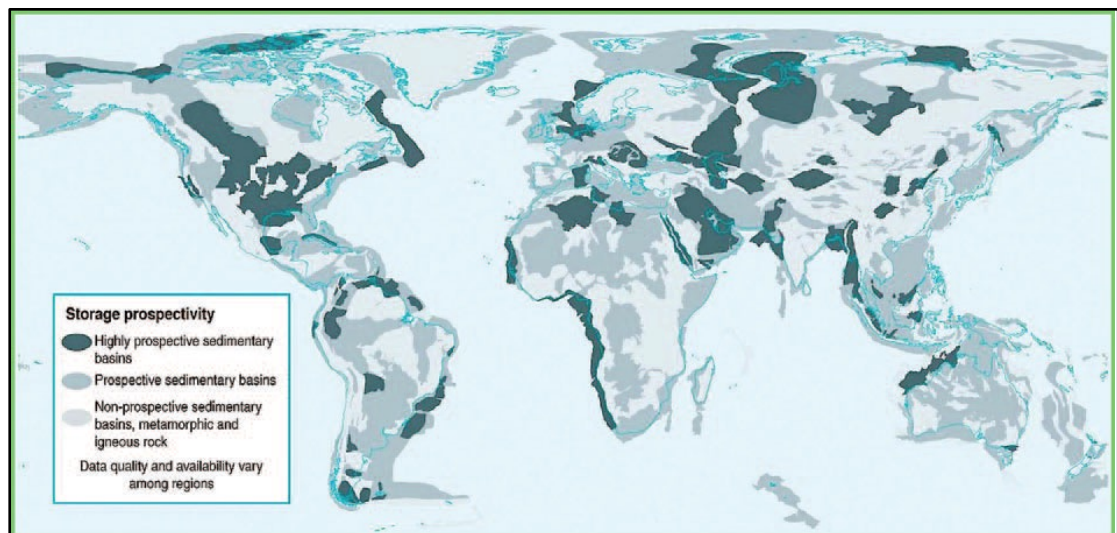


Figure 1.3 Sedimentary basins for use as CO₂ sequestration sites and their storage prospectivity distribution around the world (IPCC, 2005).

Currently, many CO₂ injection options exist for geological storage and have been applied in different projects around the world. These projects were implanted in onshore or offshore fields in depleted oil and gas fields, deep saline aquifers or coal beds (Figure 1.4). The estimate of the global capacity to sequester CO₂ deep underground is large (Benson and Cole, 2008). Some estimates of the capacity for CO₂ sequestration are in the range of approximately 675 to 900 billion tonnes of CO₂ (GT C) in depleted oil and gas fields, 1000 to 10,000 GT C in deep saline aquifers and three to 200 GT C in unmineable coal beds (IPCC, 2005).

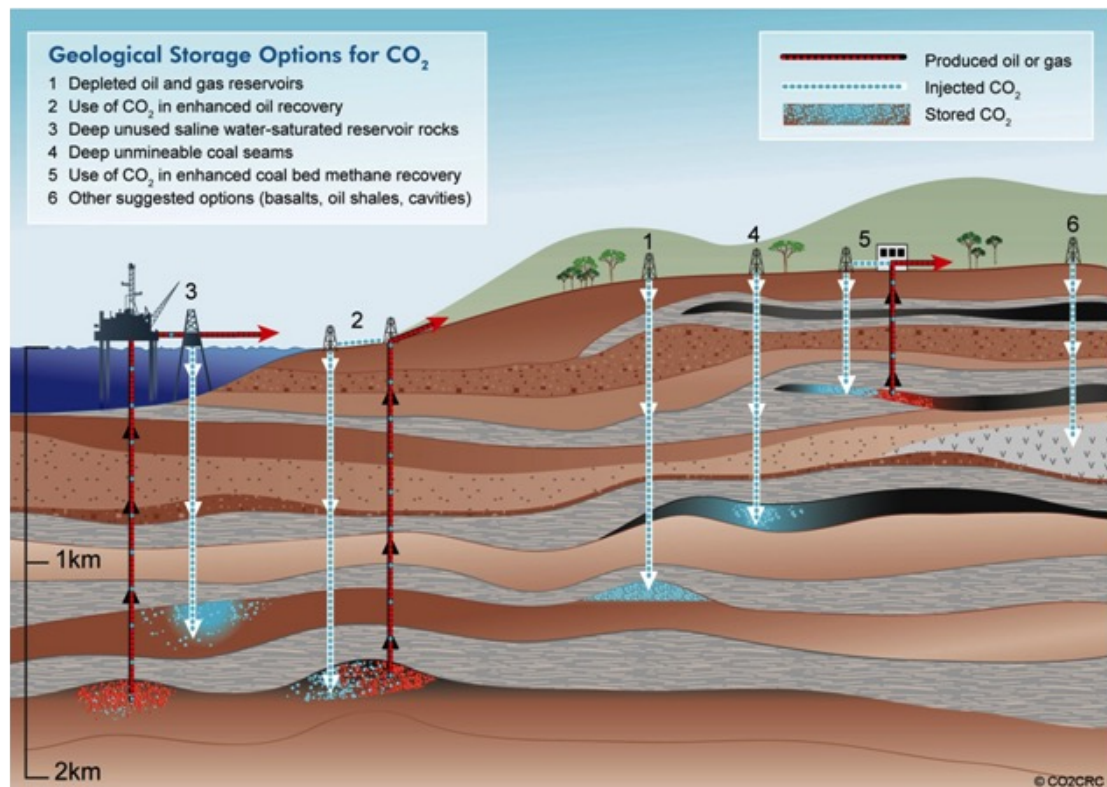


Figure 1.4: The suitable options of geological storage formations and reservoirs for CO₂ sequestration (after CO2CRC, 2013).

1.2.2 CO₂ Properties

CO₂ chemically consists of two elements, carbon and oxygen and it is one of the many GHGs. In the last decade, CO₂ has gradually increased by 2.0 ppm per year and the recent estimation of CO₂ concentration in the Earth's atmosphere is 393.11 ppm (NOAA, 2013). The state of CO₂ under normal atmospheric pressure and temperature is colourless, relatively odourless and denser than air. Typically,

before the subsurface injection process, gaseous CO₂ is compressed until it is transformed into a supercritical fluid (Figure 1.2). To illustrate this process, the phase diagram (Figure 1.5) explains the relationship between different CO₂ phases with pressure and temperature changes. The interesting CO₂ properties in the supercritical phase are that it has a density similar to liquids and a viscosity similar to its gaseous phase (Benson and Cole, 2008). In the diagram, for example, for CO₂ sequestration at a temperature of 300 K, note that equilibrium is reached at the critical point between the gas and liquid (Figure 1.5).

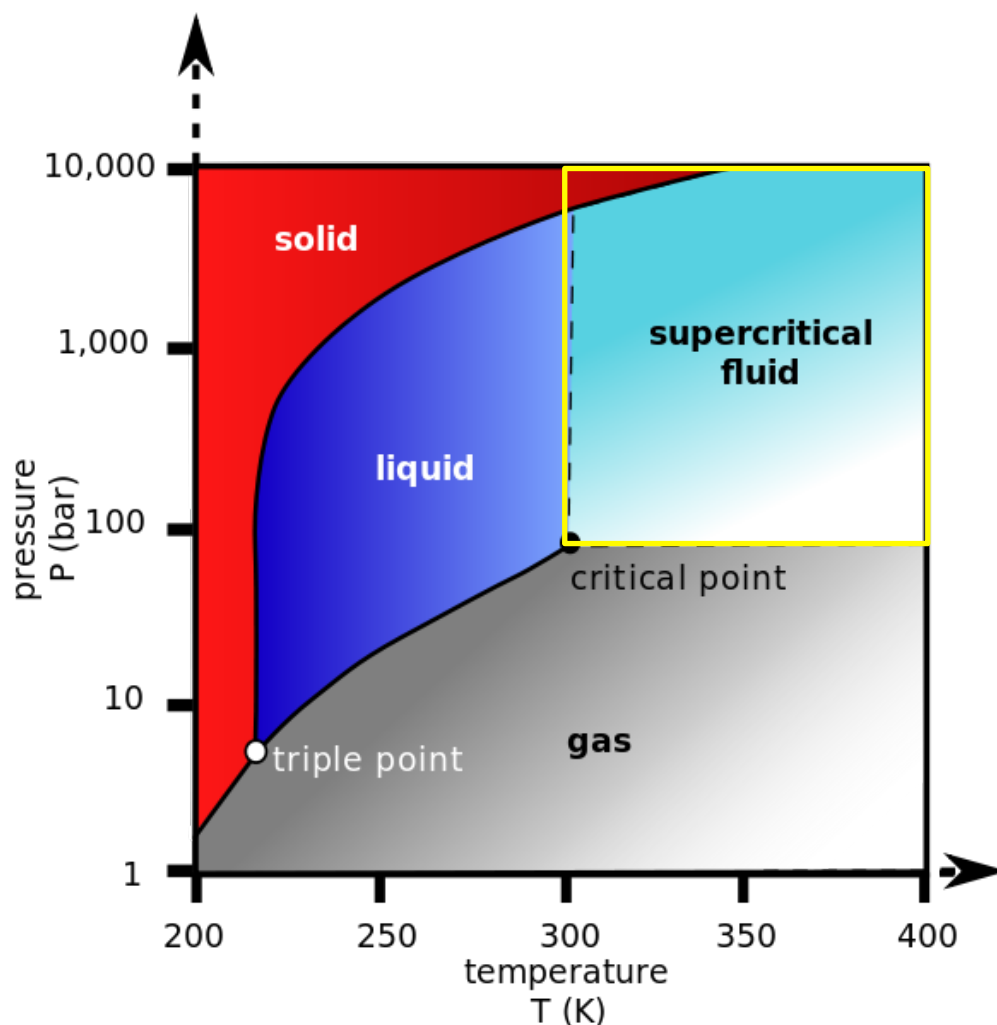


Figure 1.5: The pressure-temperature phase diagram for CO₂ (after Benson and Cole, 2008). The supercritical phase zone is shown in the yellow box, where the properties of the CO₂ are similar to those of both a liquid and gas. The pressure unit is 1 bar = 0.1 Mpa.

The environment of the subsurface geological storage plays a major role and therefore the potential miscibility of CO₂ differs with sequestration from storage unit to storage unit. Typically, CO₂ sequestration can inject and displace most of the brine from pore spaces in rocks, something that a fluid cannot do in the same situation (Benson and Cole, 2008). In CO₂ injection, the filling of pore spaces in aquifers and fractures is based on multiphase flow relationships (Bear, 1972). However, as the pressure and/or temperature varies, there are two main consequences that affect these relationships. First, there are some limitations when injecting CO₂ into pore spaces. These include limitations to flow dynamics, capillary pressure and the interaction between the two material phases. Moreover, the porosity and permeability represent one-third of the pore space in the rock, which may be filled in the initial injection of CO₂, (Annetts et al., 2012). The second consequence of multiphase flow relationships is the post-injection movement of CO₂. Here, some of the CO₂ trapped as pore fluids is returned by capillary forces in certain fractions based on formation water dissolution (Hesse et al., 2009). More details and discussions on trapping mechanisms are presented in the next section.

1.2.3 CO₂ Trapping Mechanisms

CO₂ sequestration sites must have a well-characterised geology, with a consideration of the CO₂ interactivity and reactivity in the supercritical phase. The efficiency of supercritical CO₂ storage is based on the combination of trapping mechanisms in physical (structural, stratigraphic and residual) and chemical (solubility and mineral) trapping mechanisms (Figure 1.6).

Geological structures are the most common physical trapping mechanisms. In this trap, CO₂ is injected, for example, into a depleted hydrocarbon reservoir where it behaves similar to the way a hydrocarbon behaves inside a reservoir. Therefore, after the supercritical CO₂ is injected into the reservoir, the CO₂ plume moves upward, based on its density and gaseous phase and is then trapped by an impermeable cap rock (IPCC, 2005). In fact, this system of trapping is very effective; it has been proven to be able to trap hydrocarbons for a billion years. Another physical trapping mechanism is the residual CO₂ trapping system. This trap appears when an injection

into a reservoir stops; brine imbibes the CO₂ plume, slowing the progress of the plume's trailing edge. In other words, when the supercritical CO₂ is injected into the formation, it displaces the existing fluid (e.g., formation water) and moves through the porous rock. Therefore, the CO₂ plume passes out of the pore's throat and the previous fluid again replaces the plume; some of the plume's tail is left behind as residual CO₂ droplets in the pore spaces, as shown in Figure 1.7. This trapping mechanism is important because with enough time, all injected CO₂ can be trapped using it (Hesse, Orr Jr and Tchelepi, 2009). In coal seams, the CO₂ plume is trapped by an absorption trapping mechanism, which is common in these areas.

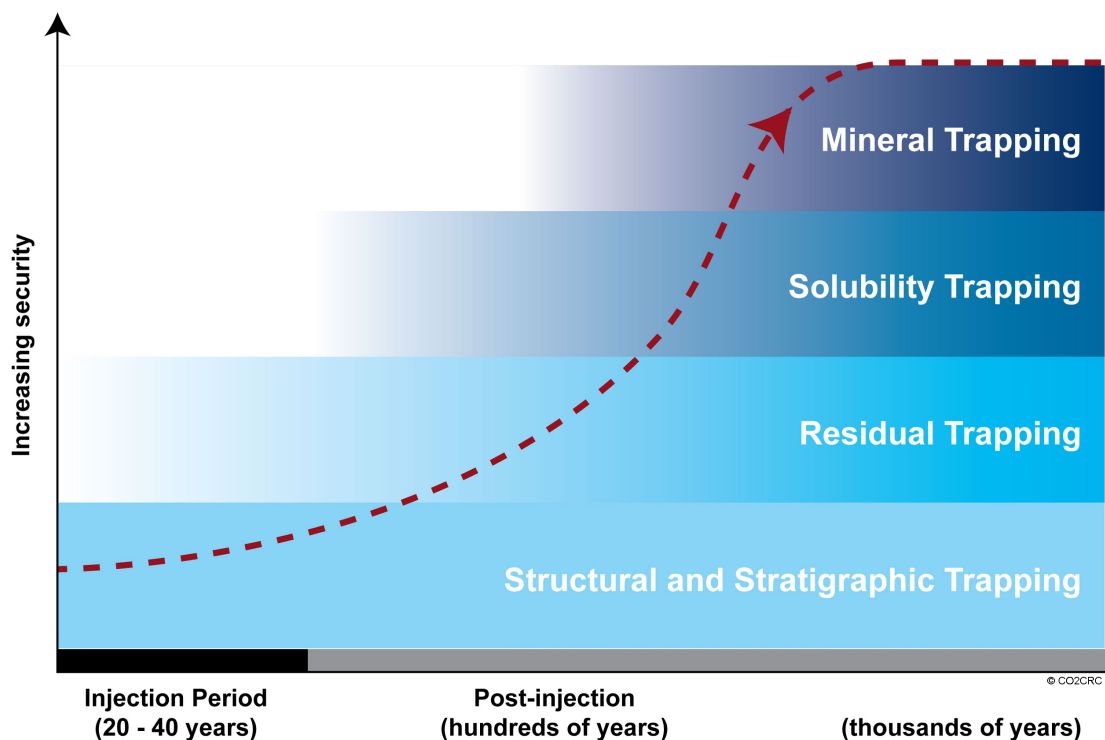
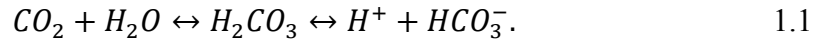


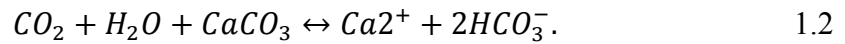
Figure 1.6: Schematic representation of the security of the major CO₂ physical and chemical trapping mechanisms over time (after CO2CRC, 2013). It can be seen how many of the trapping systems contribute to increased storage security over time (red line). The figure also shows that physical trapping dominates, while chemical trapping increases gradually over years.

Other kinds of trapping mechanisms are classified as chemical mechanisms and consist of solubility and mineral trapping. Solubility trapping occurs when CO₂ is dissolved in pore fluids in a water-bearing reservoir; this method is based on a

chemical reaction. To illustrate this method, a CO₂ reaction occurs by mixing injected CO₂ and formation water then dissolving them into the formation to produce carbonic acid (H₂CO₃) and a carbonate (H⁺, HCO₃⁻) aqueous species. This dissolution removes a portion of the immiscible CO₂ phase, thus reducing the buoyancy effect and the reliance on a physical trapping mechanism (Shevalier et al., 2011).



In this trapping system, the balance between the pressures, temperature and salinity determines the potential effectiveness of the CO₂ trapping mechanism. Thus, increasing the pressure causes an increase in CO₂ solubility; in contrast, increasing temperature and salinity reduces CO₂ solubility. Ionic trapping follows solubility when the CO₂ plume enters into the aqueous phase (Shevalier et al., 2011).



Eventually, the mineral trapping mechanism of the CO₂ plume, which occurs when the trapped CO₂ reacts with the formation minerals, precipitates carbonate minerals. For instance, injected CO₂ present in the reservoir precipitates into calcite or other minerals, based on the reaction of the CO₂ with siliclastic minerals (Shevalier et al., 2011).



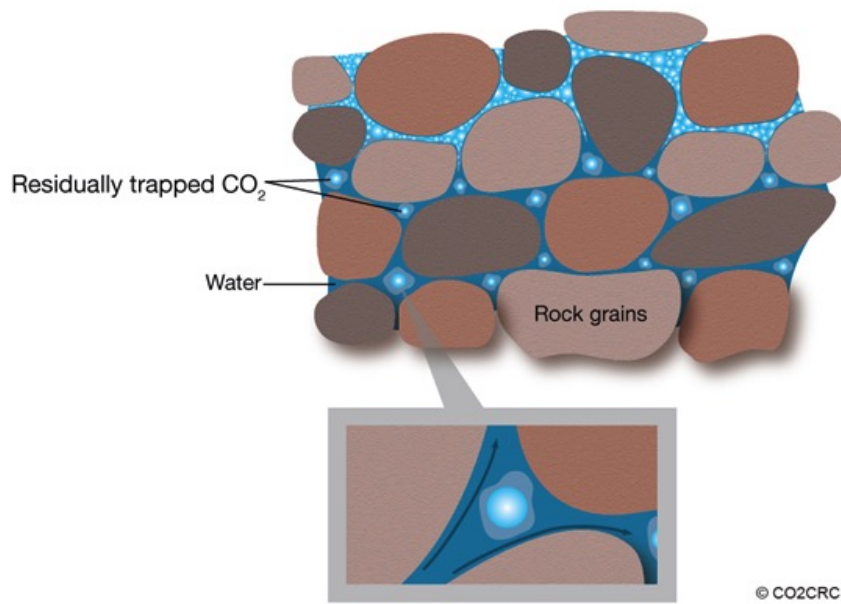


Figure 1.7: Residual mechanism gas-trapping process (CO2CRC, 2013).

1.3 CCS in Australia

1.3.1 Overview

Australia is one of the world leaders in CCS for its planning and establishment of many projects designed to help decrease GHG emissions by 60% by 2050 (Cook, 2009). Many studies are required for these storage-and-capture projects to determine their feasibility. Currently, several CO₂ geosequestration projects are underway or planned and will be fully operational by 2015 or later, such as the CO2CRC Otway, the West Hub CCS, the CarbonNet, the Surat Basin and the Gorgon projects (Figure 1.8).

1.3.2 CO2CRC Otway Project

The Otway project of the Cooperative Research Centre for Greenhouse Gas Technologies (CO2CRC) is located onshore in Victoria, Australia and is Australia's first and only demonstration of deep geological storage of CO₂ (geosequestration). The project is divided into two stages and sequestered CO₂ into a depleted gas field. It has been running since 2003 and injecting since 2008 (CO2CRC, 2013). I provided more details about the Otway site and its stages later in section 5. I also discussed the use of seismic methods to detect CO₂ in this project.

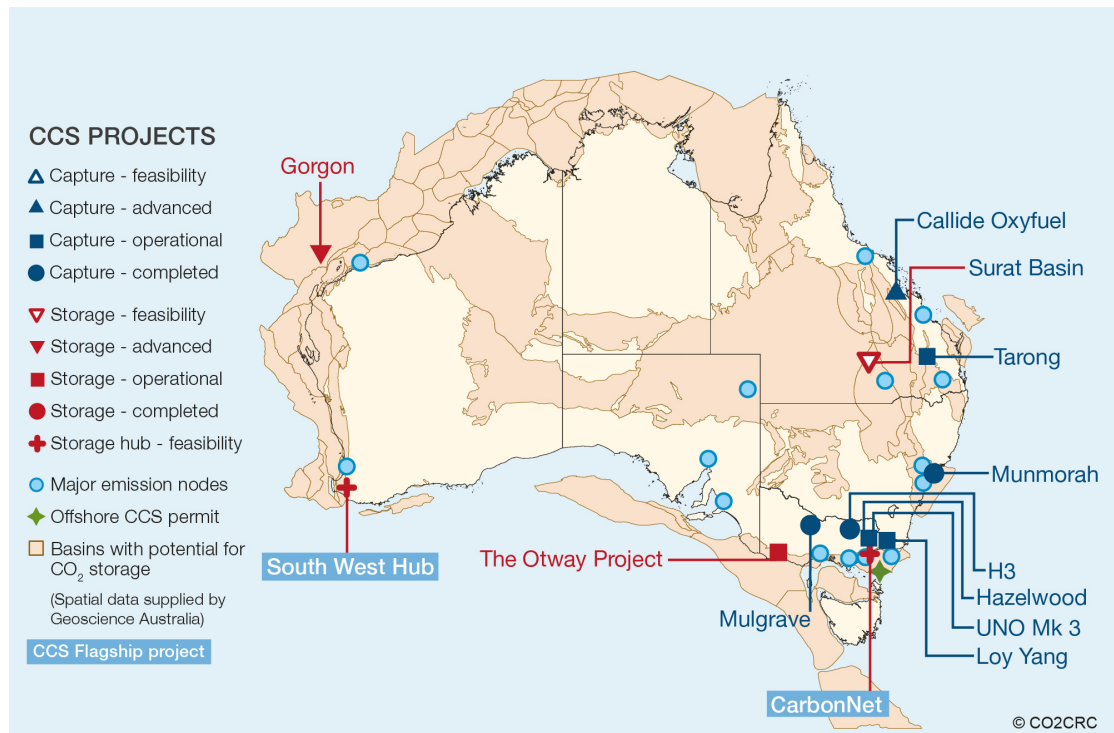


Figure 1.8: Australian CCS projects (CO2CRC, 2013). The storage sites, such as the Otway project, South West Hub project, the CarbonNet project and the Surat Basin project, will be discussed here. The Gorgon project is also discussed in this report.

1.3.3 South West Hub Project

This project is located near Collie in the south-west of Western Australia. The project began with the drilling and the collection of cored stratigraphic well samples for easements and feasibility studies (CO2CRC, 2013). In this project it was planned to inject between 2.5 and 7.5 million tonnes of CO₂ per year (Mtpa) in deep onshore saline formations. The feasibility studies and further information about the project will be discussed in section 3 of this dissertation.

1.3.4 CarbonNet South

The CarbonNet CCS Network project is one of Australia's CCS Flagship Program projects and is selected for funding through the feasibility stage. It will aid in Australia's commitment to significantly reduce GHGs. The project site is located

in the saline formations of the Gippsland Basin in south-eastern Australia where it was initially planned to store 1.2–20 Mtpa of CO₂ emissions (CO₂CRC, 2013). Details of the geological storage and seismic monitoring of CO₂ will be provided in section 4.

1.3.5 Surat Basin Project

The Surat Basin Project is Australia's third CCS Flagship Program project. In this project, approximately 3.3 Mtpa of CO₂ is planned to be injected into the Surat Basin at a depth of about 2.4 km. A regional storage capacity assessment has indicated that the Surat Basin is a prospective region for saline formation CO₂ storage (CO₂CRC, 2013).

1.3.6 Gorgon Project

The Gorgon Project is located on the north-west coast of Western Australia at Barrow Island. It was planned to be the first commercial project in Australia to inject and store around 120 Mtpa of CO₂ into a deep saline formation under Barrow Island. It will be run by Chevron (the operator), Shell and ExxonMobil. They also plan to enhance gas recovery for the Greater Gorgon gas reservoir liquefied natural gas (LNG) plant on Barrow Island, by removing up to 14% of the CO₂ during LNG processing (CO₂CRC, 2013).

1.4 Motivation

Capturing CO₂ before it is released into the atmosphere and then injecting it into geological subsurface formations is a relatively new approach that demands new technology for the method to be fully successful. Therefore, to monitor and verify CO₂ sequestration correctly and to detect possible leakage into the atmosphere from the desired storage area, an effective method is needed that will perform all of these functions. The possible estimation of the seepage size is required by detection the CO₂ plume with the proposed methods. The time-lapse seismic method is one approach that can be deployed to monitor CO₂ plumes.

The feasibility of using repeated 3D time-lapse seismic data to monitor and verify CO₂ sequestration has been studied in several works (IPCC, 2005; IPCC, 2007; Lumley, 2010; Cook, 2014). They concluded that time-lapse data, with a high signal-to-noise ratio (SNR) and decreased non-repeated noise, should be acquired from multiple 3D seismic surveys and used to detect changes in the geologic formations that are caused by the CO₂ injection process.

All seismic data sets, whether land, marine, or vertical seismic profiles, can be contaminated by various types of unwanted noise signals. The designs of many seismic analysis algorithms used in processing steps and seismic-imaging techniques are based on the assumption of noise-free data. Thus, the main task of pre-processing data is to separate the signal and the noise, where the noise is partially defined by the imaging techniques (Linville and Meek, 1995); for example, multiples can be viewed as noise or as part of the signal, depending on the imaging algorithm. In multiple 4D surveys, the suppression of coherent noise will be influenced by the level of repeatability of the survey. High repeatability means that most coherent noise in the time-lapse data will cancel out in the difference section (when individual surveys are subtracted from each other). This concept does not apply to random ambient noise because this type of noise may not be the same in every time-lapse survey, even if the survey repeatability is high; this noise is called non-repeatable noise (Calvert, 2005). Therefore, since the detectability of a CO₂ plume is governed by the SNR, the ability to model realistic time-lapse noise plays a crucial role in any feasibility study. Hence, the evaluation of seismic monitoring may be achieved by modelling many probabilistic time-lapse signals and noise to represent realistic scenarios of CO₂ plumes in many areas in Australia.

This dissertation will evaluate the use of time-lapse seismic methods for CO₂ monitoring and verification. Studying the possibilities of modelling and examining many CO₂ injection levels with different sizes are required for the detection of CO₂ movement and containment in Australia. Moreover, the modelling of time-lapse noise plays an important role in our understanding of the subsurface processes, in designing surveys and in interpreting recorded data. Thus, accounting for the uncertainties in our understanding of the subsurface is possible by using a statistical approach to many the realistic time-lapse noise models.

1.5 Objectives

It is crucial to establish how effective the use of seismic monitoring is for the purposes of CCS and site characterisation in Australia and for the improvement of CO₂ geosequestration monitoring and verification.

The main objective of this research is to evaluate the use of time-lapse seismic methods to monitor and verify CO₂ subsurface storage. The main problem with using the time-lapse seismic monitoring for this purpose is the presence of noise in the signal. The focus of this thesis is to understand and address the effect of different types of noise on time-lapse seismic monitoring. To this end, I propose the following:

- ☐ Study real time-lapse seismic data to understand and classify the noise.

In this objective, several tasks of interpreting 2D and 3D surface reflection seismic data sets are carried out for three sites around Australia that are suggested targets of CCS and are Australian CCS projects. These are the South West Hub, CarbonNet South and CO₂CRC Otway, respectively. Many different techniques are used to examine the noise and mitigate the uncertainties produced by noise contamination in the observed data sets for each area.

- ☐ Model the time-lapse noise.

This objective applies to the Otway time-lapse data sets. The 4D realistic noise model of the Otway project will be generated from many volumes. A spectral signal decomposition will be applied by implementing an appropriate technique of Short-Time Fourier transform (STFT) to model 3D non-repeatable noise. Many realistic noise models will be produced using this approach to model coherent events in different time-lapse sections and to help in the investigation of CO₂ seismic monitoring.

- ☐ Investigate the time-lapse sensitivity and the detectability of small changes in the CO₂ injection region by building several finite-difference models.

To assess the detectability of CO₂ injection, several numerical models will be based on the interpretation of real data set surface seismic and VSP. In these models, many scenarios of CO₂ plume volumes and sizes will be modelled to assess CO₂ monitoring by seismic time-lapse in Australian onshore and offshore sites. Any estimate or model of a time-lapse seismic response demands an accurate study of the physics of rocks, whether petrophysics or geochemical studies.

- Propose approaches to eliminate the noise in time-lapse seismic data.

1.6 Dissertation Methodology

In this dissertation I first performed a literature review of publications that have focused on the repeatability of 3D time-lapse data, the feasibility of the use of 4D for CO₂ monitoring and ways to model 4D noise. I have divided the methodology into three main categories: data preparation (analysis and interpretation), modelling and finally, the analysis of the results.

First, in the data-preparation stage, I interpreted all the information from the study area, which includes seismic sections, well logs and reports. In the seismic section of the interpretation stage, I mapped all the horizons and geological structures and export them so I can build realistic, finite-difference models, surface and VSP data sets.

In the next stage, several finite-difference models with different scenarios of CO₂ containment were modelled and acquired in both surface and VSP data sets as a baseline section. I began the analysis, processing and testing of the data and produce time-lapse differences. Here, I started by modelling an injection of several volumes of CO₂, then acquire another set of synthetic data after that level of injection (monitor survey) and subtract them. These different sections were utilised to investigate the CO₂ plumes, evaluate the detectability of CO₂ and estimate the level of noise. This stage of the research was described in sections 3 and 4 using the data sets of the South West Hub and CarbonNet projects. In the same stage, I modelled many realistic time-lapse noises from the Otway area by utilising two time-lapse noise

models and comparing them with real, non-repeatable noise. I then repeated these steps to generate various types of realistic time-lapse noises for the Otway area.

Finally, the main result of this thesis shows an evaluation of the use of a time-lapse seismic method and an assessment of the extent to which I can use this method to provide a clear image of a CO₂ plume during and after injection. I also produced noise models for the target area to make the 4D data processing methods more effective in detecting the small changes that occur during CO₂ injection. Figure 1.9 shows an illustrated flow chart of the three main stages that are explained above. This stage of the thesis will be presented in section 6.

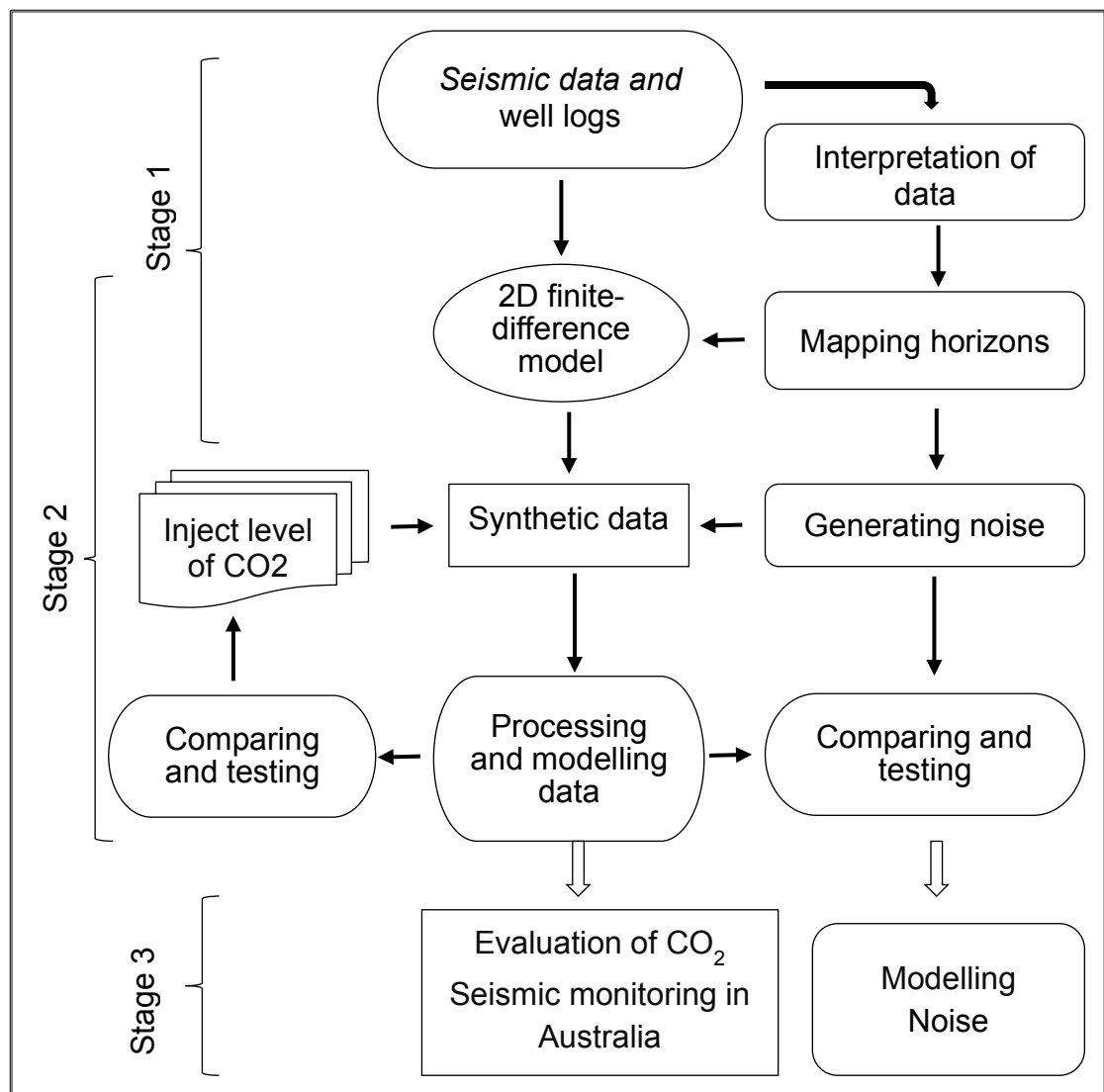


Figure 1.9: Flow chart of the research methodology steps. The research has three main stages that indicate the structure and work methodology of the thesis based on the research objectives.

1.7 References

- Annetts, D., J. Hauser, J. Gunning, B. Gurevich, A. Bona, R. Pevzner, B. Harris, M. Urosevic, M. Alajmi, and J. Cant, 2012, A deployment strategy for effective geophysical remote sensing of CO₂ sequestration: Final report.
- Benson, S. M., and D. R. Cole, 2008, CO₂ Sequestration in Deep Sedimentary Formations: Elements, **4**, 325-331.
- Calvert, R., 2005, Insights and methods for 4D reservoir monitoring and characterization.
- CO₂CRC, 2013, The Cooperative Research Centre for Greenhouse Gas Technologies <http://www.co2crc.com.au/>.
- Cook, P., 2014, Geologically storing carbon: learning from the Otway Project experience: CSIRO PUBLISHING, 2014.
- Cook, P. J., 2009, Demonstration and Deployment of Carbon Dioxide Capture and Storage in Australia: Energy Procedia, **1**, 3859-3866.
- DCCEE, 2012, Department of Climate Change and Energy Efficiency, Commonwealth of Australia.
- EIA, 2013, International Energy Outlook 2013: US Energy Information Administration, Washington, DC.
- Hesse, M. A., F. M. Orr Jr, and H. A. Tchelepi, 2009, Gravity currents with residual trapping: Energy Procedia, **1**, 3275-3281.
- IPCC, 2005, IPCC special report on carbon dioxide capture and storage: Cambridge University Press.
- IPCC, 2007, Climate Change 2007: Impacts, Adaptation and Vulnerability: Working Group II Contribution to the Fourth Assessment Report of the IPCC Intergovernmental Panel on Climate Change: Cambridge University Press.
- Linville, A., and R. Meek, 1995, A procedure for optimally removing localized coherent noise: Geophysics, **60**, 191-203.
- Lumley, D., 2010, 4D seismic monitoring of CO₂ sequestration: The Leading Edge, **29**, 150-155.
- NOAA, 2013, Globally averaged marine surface annual mean data. U.S. National Oceanic and Atmospheric Administration, Earth System Research Laboratory.

Shevalier, M., M. Nightingale, B. Mayer, and I. Hutcheon, 2011, TOUGHREACT modeling of the fate of CO₂ injected into a H₂S containing saline aquifer: The example of the Wabamum Area Sequestration Project (WASP): Energy Procedia, **4**, 4403-4410.

Every reasonable effort has been made to acknowledge the owners of copyright material. I would be pleased to hear from any copyright owner who has been committed or incorrectly acknowledge.

CHAPTER 2: METHODOLOGY

2.1 Introduction

In this chapter, I summarised the main methods used in my research. This chapter is meant to provide the reader with the basic concepts upon which the rest of the thesis builds on.

The focus of the thesis is on using seismic methods for CO₂ monitoring and verification. There are many types of seismic methods with different concepts and applications, whether for near-surface studies or for hydrocarbon exploration and development. Before providing more details about these methods, let us start with the definition of a seismic wave and its motion in the Earth. A seismic wave is ground motion that propagates through the Earth as mechanical energy generated by a source and recorded by an array of receivers. Active seismic exploration methods rely on generating and recording such waves and inverting the recorded data for the elastic properties of the subsurface through which the waves propagate. The layout of the sources and receivers depends on many factors, including the geology, topography and the acquisition purposes. To study the propagation of seismic waves, one of the commonly-used assumptions about the Earth model for sedimentary scenarios is that the Earth consists of homogeneous isotropic layers. Such an assumption is often made because of the difficulty of studying seismic waves in generally heterogeneous media and is in general in agreement with the model of sedimentary deposition (Lowrie, 1997).

To understand the wave propagation, one can invoke the Huygens' Principle, which gives a very important insight into drawing the right position of the wavefronts. The principle states that every point on a wavefront may be regarded as a new source of secondary waves and used to locate the positions of the wavefronts of these waves. By using this principle of raypath reflection and refraction, the waves and the angles on interfaces between the two layers are described by Snell's law. Snell's law can be defined as

$$\frac{\sin\theta_1}{V_1} = \frac{\sin\theta_2}{V_2} = P, \quad 2.1$$

where P is the quantity and is called the raypath parameter, θ_1 is the angle of reflection, θ_2 is the angle of refraction and V_1 and V_2 are the velocities of layer 1 and layer 2, respectively.

In fact, Newton's second law of motion and Hooke's law are the fundamental laws of physics that describe the propagation of seismic waves and from these laws two classes of theories can be inferred: the wave theory (WT) and the ray theory (RT) (Telford et al., 1990). The derivative of Newton's and Hooke's laws gives the wave equation. The general form of the equation can be defined as

$$\nabla^2\psi = \left(\frac{1}{\alpha^2}\right)\frac{\partial^2\psi}{\partial t^2}, \quad 2.2$$

where ∇ is the dilatation (the change in volume per unit volume), ψ represents the wave function (disturbance), t is the travelttime in unit time and ∂ is the partial derivative operator. In this expression, the wave equation relates the spatial derivative (the left side) to the displacement of the temporal derivative (the right side). To describe the wave equation in the spatial part of the 3D coordinates: x-axis, y-axis and z-axis, and in the homogenous isotropic media, the equation can be written as

$$\frac{\partial^2\psi}{\partial x^2} + \frac{\partial^2\psi}{\partial y^2} + \frac{\partial^2\psi}{\partial z^2} = \left(\frac{1}{\alpha^2}\right)\frac{\partial^2\psi}{\partial t^2}. \quad 2.3$$

This expression of the wave equation is called the acoustic wave equation and there are also many general solutions in plane, spherical and harmonic waves. These are discussed in detail by (Telford et al., 1990). As mentioned at the beginning of this chapter, we need this introduction to the seismic wave equation so we can understand the motion of seismic waves and their travelttime through ray tracing and the relationship between elastic properties and velocity.

In this dissertation, two seismic methods are utilised: the reflection surface seismic and VSP. We will also provide insight into these two methods.

Seismic wave propagation depends on the elastic properties of the Earth's layers and is governed by the speed of a compressional wave (P-wave), a shear wave (S-wave) and media density. They are given by these relations:

$$\alpha = \sqrt{\frac{\lambda + 2\mu}{\rho}}, \quad 2.4$$

$$\beta = \sqrt{\frac{\mu}{\rho}}, \quad 2.5$$

$$\lambda = K + \frac{2}{3}\mu, \quad 2.6$$

where α is the P-wave velocity in length per unit time, β is the S-wave velocity in length per unit time, ρ is the density in mass per unit volume, μ is the shear modulus in force per unit area (λ and μ are called Lamè parameters) and K is the bulk modulus. The acoustic impedance (I_P) and shear impedance (I_S) can be given by multiplying the speed of the P- and S-waves and the density and is defined by

$$I_P = \alpha\rho, \quad 2.7$$

$$I_S = \beta\rho. \quad 2.8$$

In the normal case of seismic acoustic wave propagation between two layers separating interface i , the reflection coefficient (R_p) and transmission coefficient (T_p) are given as

$$R_p^i = \frac{I_P^{i+1} - I_P^i}{I_P^{i+1} + I_P^i}, \quad 2.9$$

$$T_p^i = \frac{2I_p^i}{I_p^{i+1} + I_p^i}, \quad 2.10$$

$$R_p^i + T_p^i = 1. \quad 2.11$$

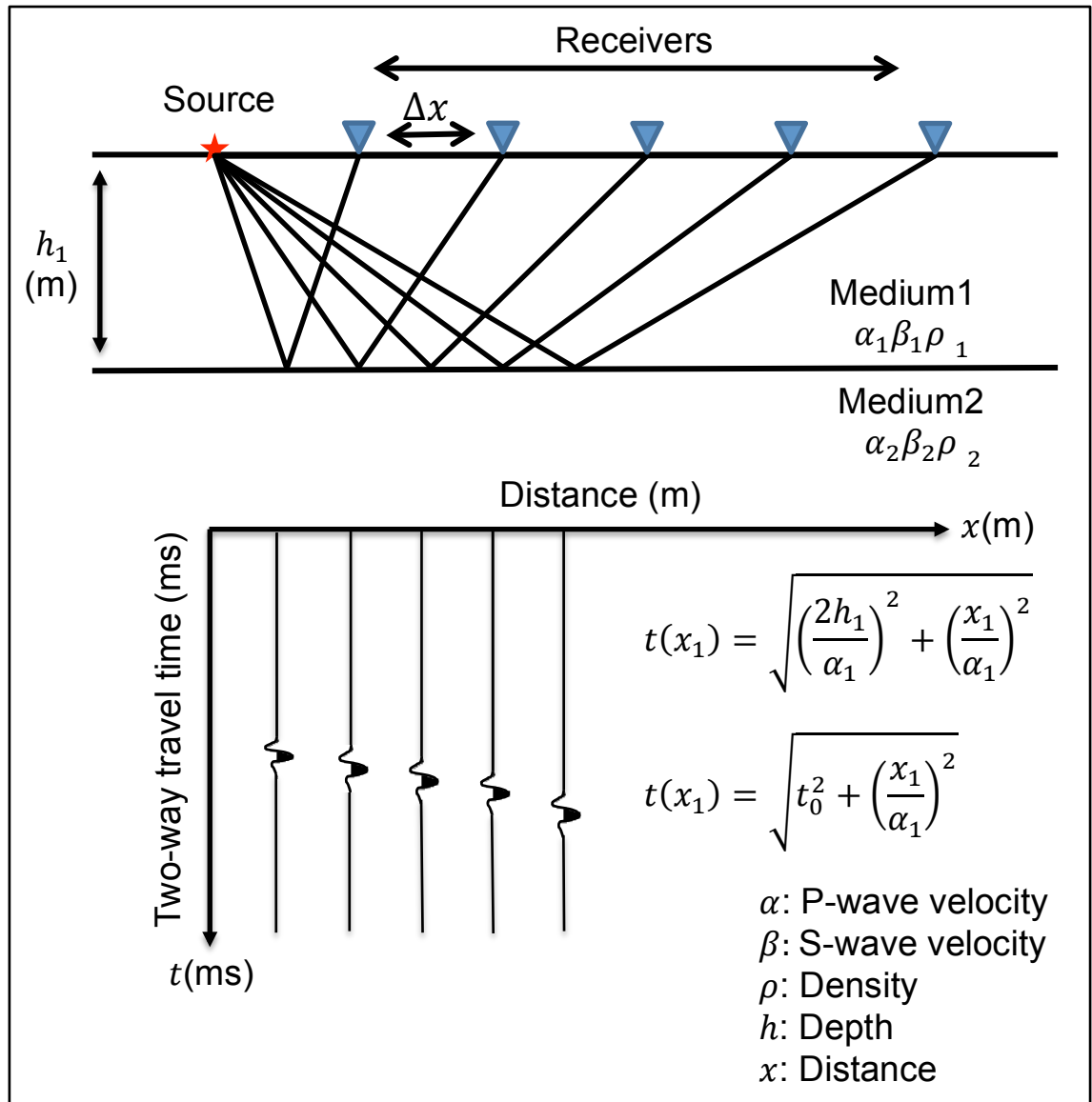


Figure 2.1: An example of the reflection surface seismic end-on spread geometry and the seismic signal record of a P-wave field. In this survey, the depiction of the source (red star) is placed on the left side of the spreading geophones (blue triangles), with a group interval Δx between the geophones, or channels. This experiment's model has

two media, 1 and 2, with a different P-wave velocity, S-wave velocity and density for each medium. A seismic section of two-way traveltimes $t(s)$ and the distance $x(m)$ shows the seismic signal response for each geophone. The delay response of traveltimes is clarified by the hyperbolic relation shown at the bottom of the graphic.

2.2 Seismic Methods

2.2.1 Reflection surface seismic

The purpose of surface reflection seismic experiments is to make 2D or 3D seismic images of the Earth's subsurface. The seismic response of the subsurface is measured by observing the reflected seismic waves from the designed surface geometry of source and receiver arrays (Figure 2.1). There are different layouts of the geometrical design of the source and receiver positions. The location of these positions changes, depending on the main objectives of the survey. Two geometrical layouts are commonly used in 2D field surveys of seismic reflection: the end-on spread and the split spread. These layouts differ in the position of the sources regarding the array of the geophones. In an end-on spread, the source is located on one side of the geophones, or channels; but in the split spread, the source is placed in the middle of the geophone array. Figure 2.1 illustrates a simple example of the end-on survey design and its seismic signal response in a two-way traveltimes record.

In 3D seismic data acquisition, the geometrical design is usually a grid of receiver lines orthogonal on source lines and spread over the study area with same interval space between them. This uniform grid of lines interpolates between these lines to get a 3-D seismic picture of the subsurface. The interpolating uniform grid of any 3-D seismic survey has two types of directions, inline and crossline. A 3D seismic acquisition requires specific conditions to produce an acceptable imaging result; for example, the 3D grid should have sufficient fold, maximum offset distance and azimuthal coverage. These are the basic requirements for any 3D survey. Indeed, any 2D reflection seismic survey may be developed into 3D data if the main geometric requirements are followed (Yilmaz, 2001).

2.2.2 Vertical Seismic Profile

VSP is another seismic method with a special geometrical design. Specifically, a receiver's location is placed inside a well instead of on the Earth's surface. This method provides more details about wave propagation and subsurface layers and helps solve surface analysis data problems, such as multiples and horizons and provides higher SNR. Thus, the VSP and surface seismic methods complement each other. This technique allows for separation of downgoing and upgoing reflected waves (Figure 2.2).

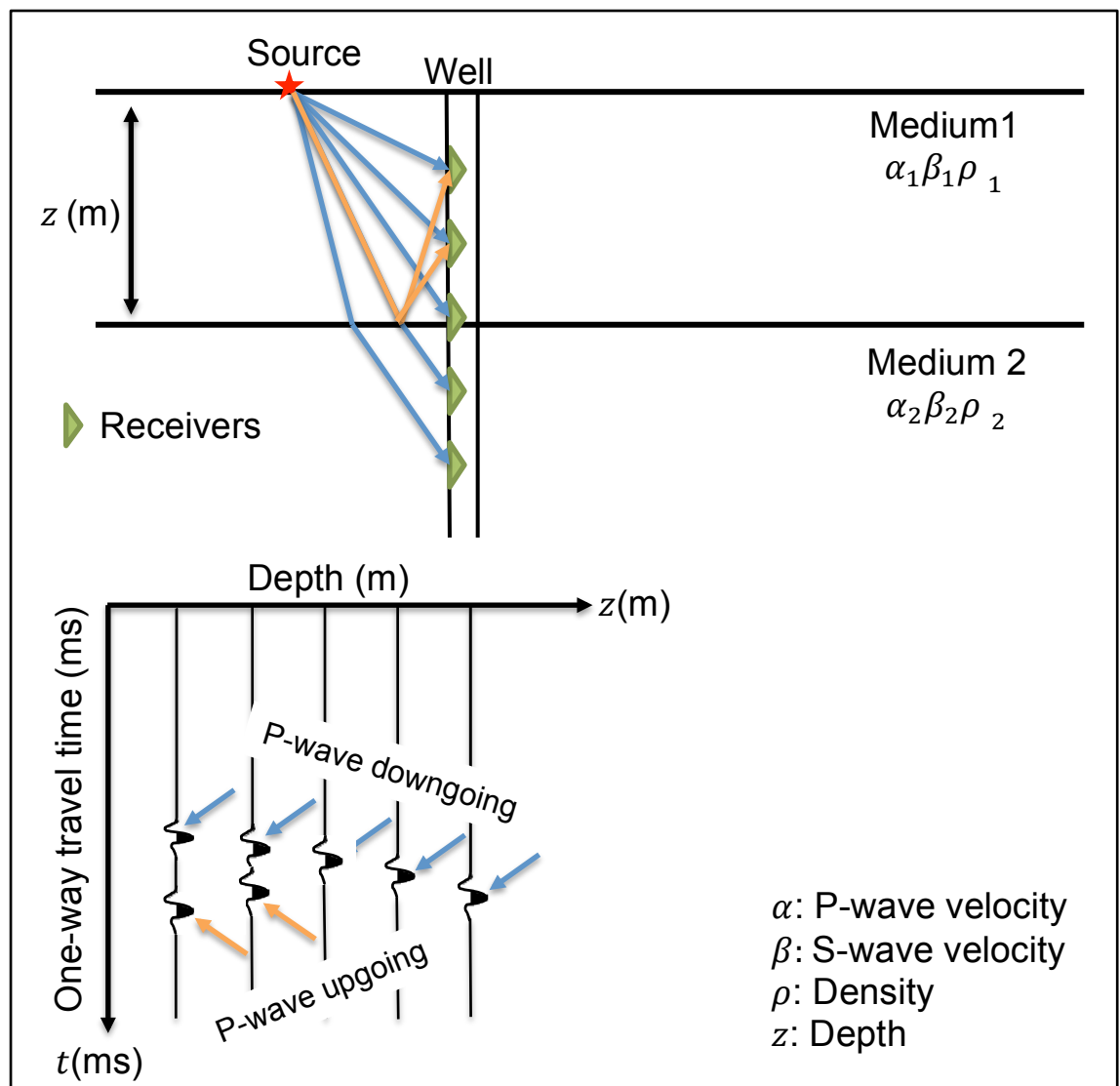


Figure 2.2: An illustration of the vertical seismic profile method, for an Earth subsurface model of two mediums, 1 and 2, with a different P-wave velocity, S-wave velocity and density for each medium. The source (red star) is placed on the surface

and geophones (green triangles) are placed inside the borehole at different depths. The one way traveltime $t(s)$ and the depth $x(m)$ are presented with the depth level for each signal of geophones in the cross-seismic section at the bottom of the figure. A VSP section is made up of the two seismic waves, the upgoing (referred to by blue arrows) and the downgoing (referred to by orange arrows).

Here, I introduced some of the main issues relating to these methods, which provides hints of which seismic methods will be applied in this work. However, much information and the explanation of these methods, their fundamental theories, geometric designs, acquisition equipment used, data processing and data interpretation are discussed in many other references, such as (Telford et al., 1990), (Lowrie, 1997) and (Yilmaz, 2001).

2.2.3 Time-lapse seismic surveys

The time-lapse seismic method is an important tool, which is used to monitor and provide information about the changes in the seismic signal over time. Time-lapse monitoring is the observation of two or more time-lapse seismic data sets, which can produce different images of the reservoir and show fluid flow changes over time when these different data sets are subtracted from each other. 3D and 4D time-lapse monitoring has developed enormously in the past decade in its ability to image the response of fluid flow and movement in a reservoir during production (Cook, 2014). In the oil and gas industry, 3D time-lapse seismic monitoring has been used for hydrocarbon recovery to extend the reservoir's life and to increase production. Globally, the remaining unrecovered oil roughly equals that which has already been produced (Calvert, 2005). In the 1980's in Canada, the United States and Indonesia, 4D was used to monitor the movement of gas and to make images of the heated gas (Lumley, 2001) for enhanced oil recovery (EOR). In general, the time-lapse seismic method can monitor the bypassed hydrocarbon compartments and map hydrocarbon migration. Furthermore, time-lapse seismic monitoring can be used to map oil-water contact over time to help better control the impact of injector wells. However, the repeatability of the 3D time-lapse seismic method plays a key role in

monitoring, whether the data are at the acquisition or the processing level (Jack, 1997).

Many features control the seismic signal response in reservoirs and aquifers. These changes are governed by the rock or the fluid properties and how they change inside the reservoir or aquifer. When supercritical CO₂ is injected into an oil and gas reservoir, it has strong effects on the elastic properties of the reservoir or saline aquifers during and after injection. The density of injected CO₂ is low compared to that of the in situ fluids; however, the density of the oil or water is gradually reduced as CO₂ saturation increases. In the same case, the P- and S-wave velocities (V_p , V_s) are affected by the CO₂ plume and strongly decrease with CO₂ saturation (Lumley et al., 2008). 3D time-lapse seismic monitoring surveys can capture these changes in the signal velocities (V_p , V_s), particularly V_p , and in the densities of the CO₂. Increasing pore pressure is another effect of supercritical CO₂ injection and occurs when the differential pressure (P_d) between the pore pressure (P_p) and the confining pressure (P_c) is increased (Hofmann et al., 2005).

$$P_d = P_p - P_c. \quad 2.12$$

Furthermore, laboratory measurements show that in sandstone samples, V_s is very sensitive to pore pressure and it decreases when the pore pressure is high. Depending on exact conditions, increasing the saturation of CO₂ decreases the acoustic and shear impedance by roughly one order of magnitude because of the sensitivity of V_p to the change in fluid pressure (Nur and Wang, 2001). Figure 2.3 shows a graphic example of how the changes in the elastic properties, V_p , V_s , density, and pressure, may be monitored and recorded using time-lapse seismic signals.

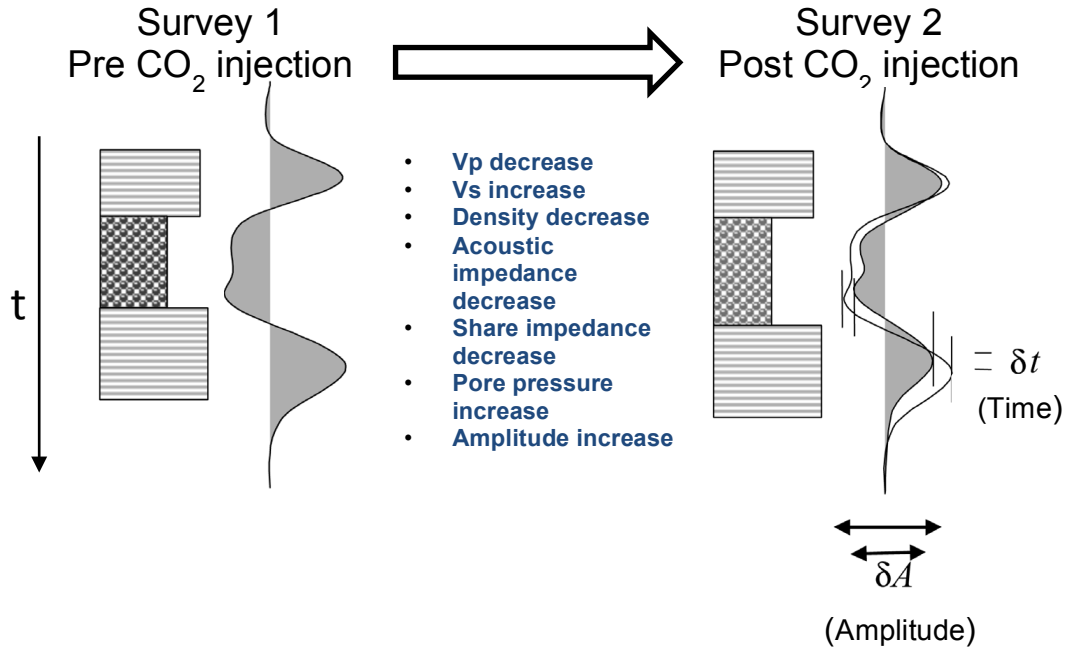


Figure 2.3: The time-lapse seismic signal and its response to the changes in rock and fluid properties V_P , V_S , density and pressure. The graphic shows how the changes in the injection properties of the CO₂ reform the original signal in Survey 1 by decreasing the acoustic and shear impedance and causing shifts in the time and amplitude in Survey 2. These shifts can be monitored using a 4D seismic survey (modified after Calvert, 2005).

Anisotropy can also be affected and changed by CO₂ injection saturation. In the Vacuum field, New Mexico, (Angerer et al., 2000) have observed changes in anisotropy in the S-wave time-lapse data before and after the CO₂ injection, which is 10% larger than those in the P-wave data. That makes multi-component vertical seismic profile (VSP) a good choice to use for monitoring the injected CO₂ in fractures based on the changes in pressure and anisotropy in the reservoir.

In addition, 4D seismic monitoring has been shown to be an important technique for mapping fluid movements and showing changes that may occur due to CO₂ injection in rock to the fluid properties of reservoirs and saline aquifers. Figure 2.4 shows an example of the Sleipner saline aquifer CO₂ project (SACS) for CO₂ injections and storage. This example shows how a CO₂ plume and fluid movement can be captured and mapped over time using 4D seismic monitoring. Consequently,

in this research, the evaluation of using time-lapse seismic data to monitor CO₂ injection and storage will be done by modelling and analysing many data sets from various locations in Australia.

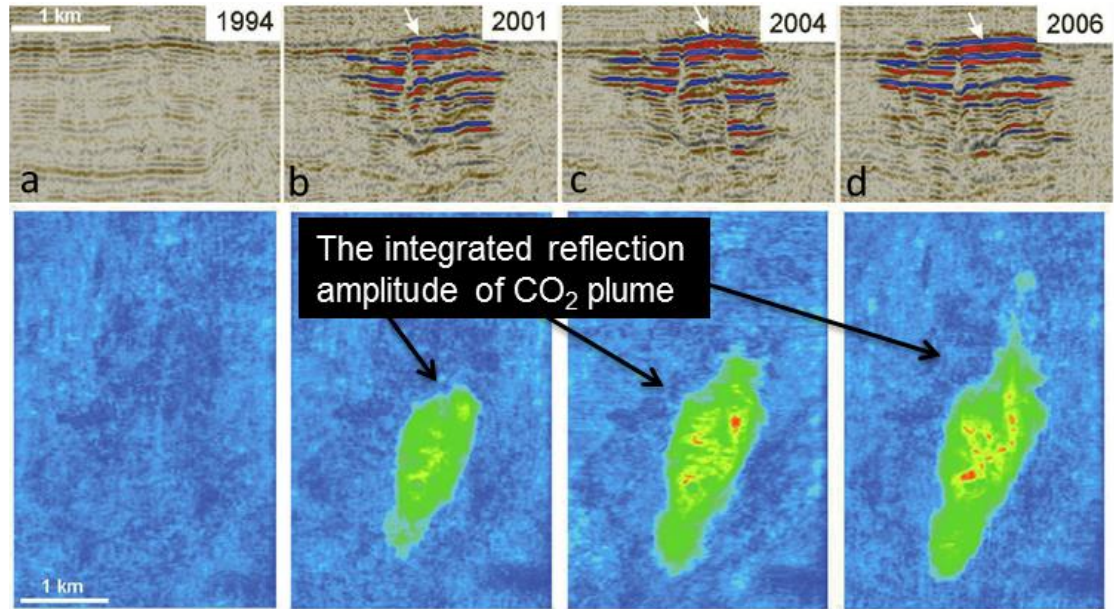


Figure 2.4: A time-lapse seismic image of the Sleipner CO₂ injection project from (a) the baseline pre-injection 1994; (b) the monitoring image 2001; (c) the monitoring image 2004; and (d) the monitoring image 2006. The lower figure shows the integrated reflection amplitude response of the CO₂ plume and its development from 1994, before injection, to 2006, after injection (modified after Chadwick et al., 2009).

2.3 Modelling Methods

2.3.1 Introduction

Seismic modelling is a significant tool that can help in understanding and simulating seismic wave propagation and the response through a subsurface geological structure model. This technique is very important for many reasons. One reason is that if the details of subsurface seismic environment are unknown, then seismic modelling is the best option to build a good geometric and acquisition design. Another important reason is that modelling the responses of Earth's physical

properties plays an essential role in seismic interpretation and inversion algorithms (Cook, 2009). There are many approaches to seismic modelling and all are based on two main concepts, the physical or the mathematical (Lines and Newrick, 2004).

Mathematical, or numerical modelling can be divided into three main categories: the direct method, the integral method, and the ray tracing method. These categories are proposed to simulate the seismic response of the synthetic geological model. Finite-difference modelling is one of the direct numerical methods. Since I used only finite-difference modelling in the thesis, I will not touch on the other modelling methods when discussing wave propagation.

Since seismic modelling is generally very resource intensive, I need to simplify the subsurface models. One of the most common ways of such simplification is to use an effective media to replace a collection of more complex media. To determine the proper physical properties of such effective media, I used rock physics modelling.

The rock physics method is a modelling approach that is conceptual and based on the physics of the subsurface properties of the physical model. All models will be discussed later.

2.3.2 Finite-difference methods

The finite-difference (FD) method is a mathematical forward model used to simulate a seismic wavefield by using a realistic geological model. This technique uses the wave theory in modelling seismic response. As mentioned, the FD model uses a direct method and requires a discretisation of time and space. A realistic geological model can be created by using a finite number of points in a space-time grid. This grid is used to solve the wave equation numerically and then to model the full wavefield using spatial ∂x and temporal ∂t steps.

For simplicity, the acoustic wave equation (equation 2.11), which is written based on homogenous isotropic media, may describe the pressure wave travelling along the x-axis and is given by

$$\frac{\partial^2 \psi}{\partial x^2} = \left(\frac{1}{\alpha^2}\right) \frac{\partial^2 \psi}{\partial t^2}. \quad 2.13$$

The first derivative of the wave function was denoted by (Smith, 1985) and is defined as

$$\frac{d\psi(x)}{dx} = \lim_{\Delta x \rightarrow 0} \frac{\psi(x + \Delta x) - \psi(x)}{\Delta x}, \quad 2.14$$

where Δx is the spatial change in the grid.

The approximation derivative of the wave equation was done by (Margrave, 2003), who rewrote the equation (2.14) of the first derivative to find the best approximation in the following equation:

$$\frac{d^{+1}\psi}{dx} \approx \frac{d^{+1}\psi(x)}{dx} = \frac{\psi(x + \Delta x) - \psi(x)}{\Delta x}. \quad 2.15$$

This expression represents the forward FD. The backward difference approximation of the FD grid spatial step is given by

$$\frac{d^{-1}\psi}{dx} = \frac{\psi(x) - \psi(x - \Delta x)}{\Delta x}. \quad 2.16$$

The centred FD grid shows the best approximation of the first derivative (Margrave, 2003). This value can be computed by taking the average of both sides of the equations forward (2.15) and backward (2.16) and can be defined as

$$\frac{d\psi}{dx} \approx \frac{\psi(x + \Delta x) - \psi(x - \Delta x)}{2\Delta x}. \quad 2.17$$

The simplified mathematical model of how the FD method can calculate this approximation along the x-axis is shown in Figure 2.5. Apparently, the acoustic wave equation 2.11 is written in terms of the second derivative. Therefore, the approximation solution of the centred spatial difference equation can be written in the terms of second derivative as

$$\frac{d^2\psi}{dx^2} \approx \frac{\psi(x + \Delta x) - 2\psi(x) + \psi(x - \Delta x)}{\Delta x^2}. \quad 2.18$$

The grid temporal step value Δt can be involved in this approximation by rewriting equation (2.18) as

$$\begin{aligned} & \frac{\psi(x + \Delta x) - 2\psi(x) + \psi(x - \Delta x)}{\Delta x^2} \\ &= \frac{1}{\alpha^2} \frac{\psi(t + \Delta t) - 2\psi(t) + \psi(t - \Delta t)}{\Delta t^2}, \end{aligned} \quad 2.19$$

To make this solution or other mathematical solutions of the wave equation in the FD model applicable, there are concepts of concern that should be taken in account in the modelling process: time integration, derivatives calculation in space, execution of the source, and the model boundaries (Carcione et al., 2002).

This is a general introduction to the finite-difference modelling method, which can provide a background to understanding the computer software algorithm that uses it. In this work, highly accurate full wavefield modelling software was used: the software packages Tesseral 2D and Tesseral Professional. The FD model and the synthetic data of the surface seismic and VSP experiments will be discussed in chapters 3 and 4. Good detailed discussion of these and other modelling methods of forward seismic modelling are given in Wason et al. (1984), Kelly and Marfurt (1990), Carcione et al. (2002), Gjøystdal et al. (2002), Margrave (2003) and Krebs (2004).

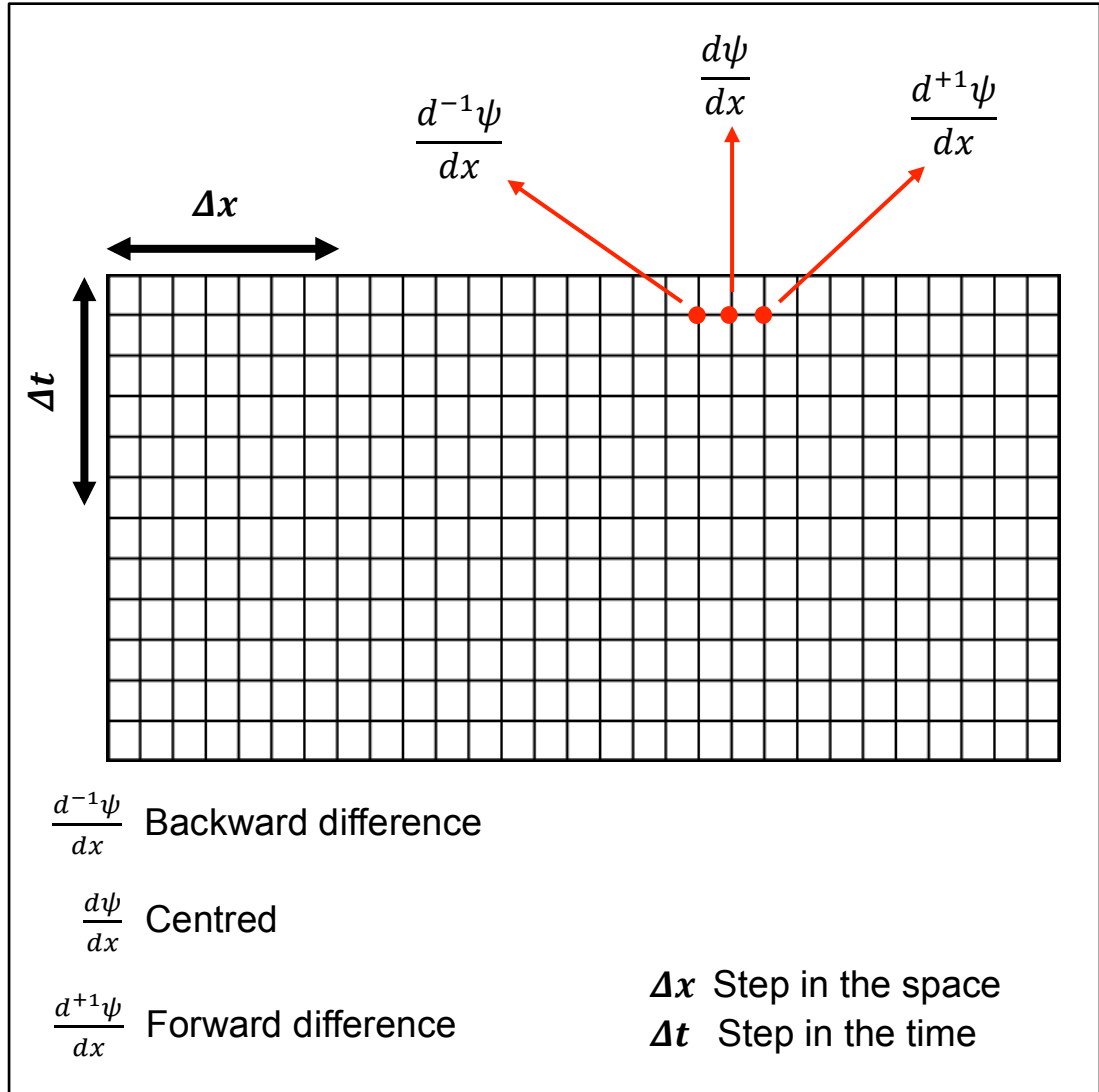


Figure 2.5: The model of the 2D finite-difference method. This mathematical model is represented by a grid of different time Δt and space Δx steps. The node's backward, centred and forward difference steps, respectively (three dots) explain how the wavefield is calculated by FD in space. Simply, the first derivative approximation of a spatial value step is used and is represented by three steps (red dots).

2.3.3 Rock physics methods

In seismic modelling and attributes (e.g., amplitude variation with offset AVO and 4D analysis), the rock physics method and fluid substitution provide a good way to model and quantify several scenarios of fluid in a reservoir (Smith et al., 2003). Herein, I provided a general insight into the rock physics method and

Gassmann's equation for fluid substitution, which will be used in CO₂ plume modelling in sections 3 and 4 of the dissertation. More information and a discussion of the Gassmann method can be found in (Gassmann, 1951), (Smith et al., 2003) and (Russell et al., 2003).

Based on assumptions of homogeneous and isotropic media, connected pore space and low-enough frequencies of pore pressure, Gassmann's equation relates the saturated bulk modulus of the rock to its porosity, frame, mineral matrix and fluid properties (Gassmann, 1951), namely,

$$K_{sat} = K_{frame} + \frac{\left(1 - \frac{K_{frame}}{K_{matrix}}\right)^2}{\left(\frac{\phi}{K_{fluid}} + \frac{(1 - \phi)}{K_{matrix}} - \frac{K_{\phi}}{(K_{matrix})^2}\right)}, \quad 2.20$$

where K_{sat} , K_{frame} , K_{matrix} and K_{fluid} are the bulk moduli of the saturated medium, porous medium (drained of any fluid), mineral matrix and pore fluid, respectively and ϕ is the porosity. Figure 2.6 illustrates the separation of the material into the above mentioned constituents. The shear modulus in the Gassmann formulation is assumed to be mechanically independent of any medium fluids and can be defined as

$$\mu_{sat} = \mu_{frame}, \quad 2.21$$

where μ_{sat} is the shear modulus of the saturated medium and μ_{frame} is the shear modulus of the porous medium drained of any fluids. The moduli (K and μ) will be measured in gigapascals (GPa). To estimate the relationship between the elastic bulk modulus, shear modulus, seismic velocities (α and β) and density (ρ), we can rewrite equations 2.1, 2.2 and 2.3 as

$$K_{sat} = \rho \left(\alpha^2 - \frac{4}{3} \beta^2 \right), \quad 2.22$$

$$\mu = \rho \beta^2. \quad 2.23$$

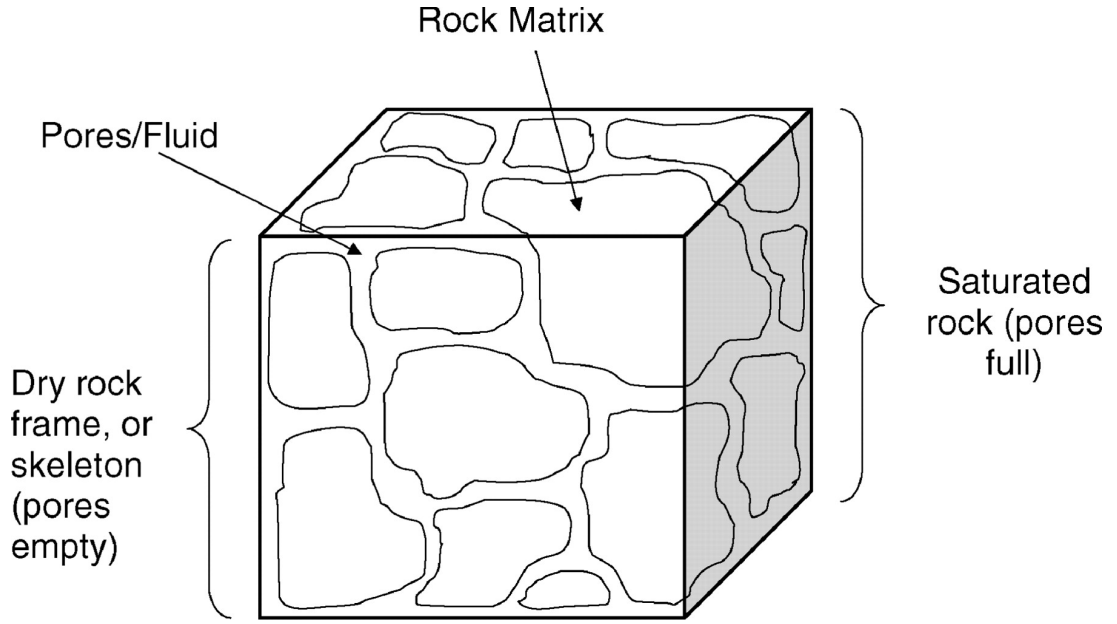


Figure 2.6: A depicted cube of rock characterising four major geological components, according to the Gassmann theory: the saturated frame, dry frame, rock matrix and fluid system (Russell et al., 2003).

2.3.4 Fourier transform

The Fourier transform is the main tool for analysing the frequency content of signals. The transform can be used not only for data analysis, filtering and processing, but also for modelling data sets based on the observed data, as I will discuss in Chapter 6.

The sinusoids Fourier series can express the seismic signal as a periodic time series with period T . This series was expressed by (Sheriff and Geldart, 1995) as

$$s(t) = \frac{1}{2}b_0 + \sum_{i=1}^{\infty} b_i \cos(i\omega_i t) + \sum_{i=1}^{\infty} c_i \sin(i\omega_i t), \quad 2.24$$

where $s(t)$ is the seismic signal, i is a positive integer, ω_i is the discrete angular frequency and b_i and c_i are the Fourier coefficients of the signal. The angular frequency is given by

$$\omega_i = 2\pi f_i, \quad 2.25$$

where f_i is given by

$$f_i = \frac{i}{T}, \quad 2.26$$

where f_i is the fundamental frequency in Hertz and T is the period time in seconds.

The Fourier coefficients b_i and c_i can be computed as the following functions:

$$b_i = \frac{2}{T} \sum_{k=1}^T s(t) \cos(\omega_i t), \quad 2.27$$

$$c_i = \frac{2}{T} \sum_{k=0}^T s(t) \sin(\omega_i t). \quad 2.28$$

By applying the functions 2.25 and 2.26 in these relationships, they can be written as

$$b_i = \frac{2}{T} \sum_{k=1}^T s(t) \cos\left(\frac{2\pi tk}{T}\right), \quad 2.29$$

$$c_i = \frac{2}{T} \sum_{k=1}^T s(t) \sin\left(\frac{2\pi tk}{T}\right). \quad 2.30$$

This analysis of the Fourier transform can be represented as the signal for each frequency component by the amplitude $A(\omega)$ and the phase $\varphi(\omega)$, which are expressed as

$$A(\omega) = |X(f)| = \sqrt{a_i^2 + b_i^2}, \quad 2.31$$

$$\varphi(\omega_i) = \tan^{-1}\left(\frac{b_i}{a_i}\right), \quad 2.32$$

As mentioned previously, the seismic signal can be decomposed by the Fourier analysis by crosscorrelating the signal with the sines and cosines of the frequency components. Therefore, the Discrete Fourier Transform (DFT) can be written by using this Fourier analysis but in a complex expression of a seismic signal in a frequency domain as

$$X(f) = \sum_{i=1}^{\infty} s(t_i) e^{-j(\omega t_i)} = |X(f)| e^{-j(\varphi)}. \quad 2.33$$

where $X(f)$ is the complex representation of the seismic signal in the Fourier domain and $s(t_i)$ is the seismic signal.

I can analyse the signal as a whole, or split it into subsignals by using windows. Such spectral decomposition can be done in two ways, either by using systemically variable windows or fixed-length windows (Reine et al., 2009). The standard Fourier transform corresponds to a single window covering the entire period. Therefore, this technique transforms the signal from the time to the frequency domain without showing how the signal frequencies change over time. This method leads to the loss of diversities in constructing frequencies in the seismic data (Figure 2.7). However, the windowing approach (with a relatively short temporal window) decomposes the seismic signal in a narrow or short window to delineate the response frequencies that are associated with lithology or coherent events in seismic signals to observe a better result of seismic data analysis, as shown in Figure 2.8.

In this dissertation, I applied the technique of the fixed window (short window) by using the most commonly used technique, called the Short-Time Fourier Transform. To implement this technique in the case of continuing time, the Fourier transform in function 3.33 will be multiplied by a nonzero short window function. This function of STFT was first introduced by (Allen and Rabiner, 1977) and is defined by

$$STFT(\tau, f) = \int_{-\infty}^{\infty} w(t - \tau) s(t) e^{-i2\pi f t} dt, \quad 2.34$$

where $STFT(\tau, f)$ is the STFT spectrum, f is the frequency, t is the time, w is the time window and τ is the time at which I inspect the seismic signal $s(t)$. The STFT inverse is given by

$$s(t) = \frac{\sum_{i=1}^N \int_{-\infty}^{\infty} STFT(\tau_i, f) e^{i2\pi f t} df}{\sum_{i=1}^N w(t - \tau_i)}, \quad 2.35$$

where I assumed that the sum of the shifted time windows in the denominator is nonzero for all t ; in other words, the shifted time windows have to overlap.

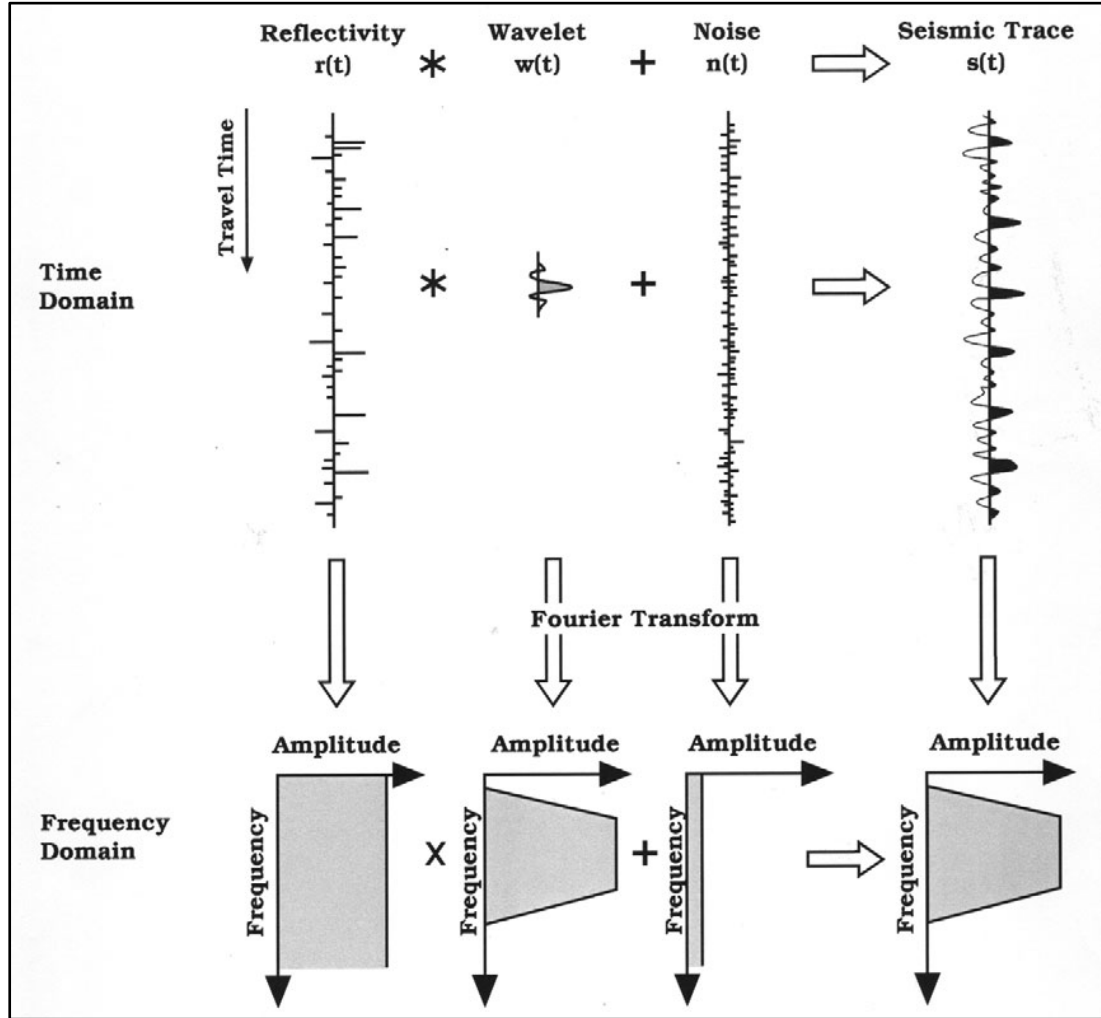


Figure 2.7: The conventional model of the Fourier transform with a long window. In this conventional transform (symmetrical variable window), the Fourier analysis is done by encompassing all frequencies of the seismic signal in a long window in a time domain. As a result, a band-limited white amplitude spectrum is observed in the frequency domain, which makes seismic data interpretation very complicated (Partyka et al., 1999).

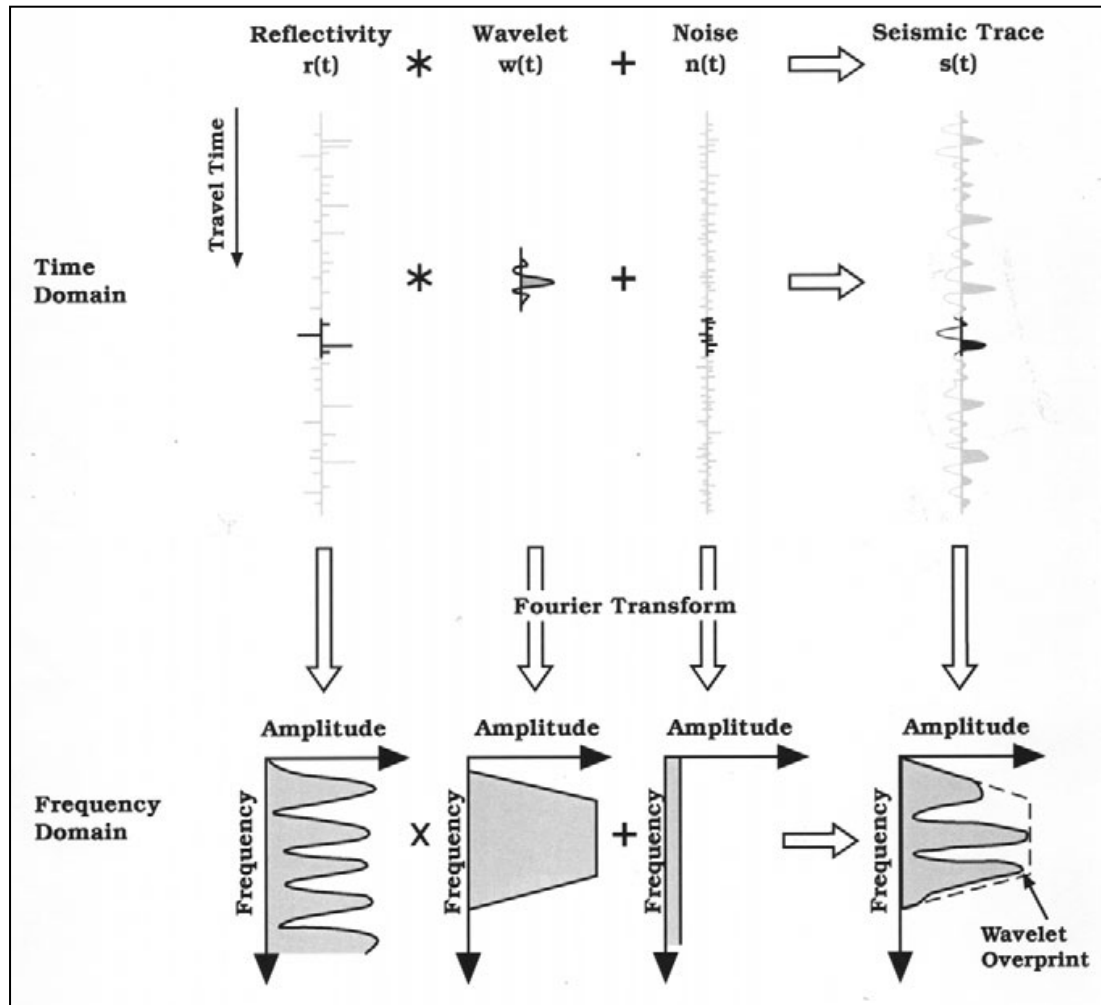


Figure 2.8: The short window spectral decomposition, or the fixed window analysis of Fourier transform. It can be seen how the short window technique addresses the seismic signal in the details to help in the interpretation of the small and thin events shown in the data. The fixed time of the short time of the Fourier analysis is done by decomposing a short temporal window of the seismic signal for a small group of frequencies. This short window in the frequency domain shows a series of chirp frequencies in the coloured spectrum and gives a band-limited coloured spectrum of the seismic signal. This technique of the Fourier transform is a good way to reduce the randomness of geological interpretation in seismic signal processing (Partyka et al., 1999).

In general, the implementation of STFT is analysed by using a series of short time windows with a certain overlap shifting between these windows. A simple illustration of STFT and its overlapping sliding windows is shown in Figure 2.9. In this graphic, I can see the first short red window, $w(t)$, which starts from the beginning of the seismic signal $s(t)$ and extends to the fixed time length of the designed STFT window. That means the frequencies in the time of this short red window will be allowed to analyse and transform to the frequency domain and the rest of the record will be zero. Then, the STFT operator will move and pick up the next overlapping black window $w(t-\tau)$ and transform it with zeroes for the rest of the windows and so on. This overlapping technique continues with same window time length, but overlaps with the sliding window over all seismic records. Depending on that, the STFT resolution is governed by two features, the type of window and the width of the window function.

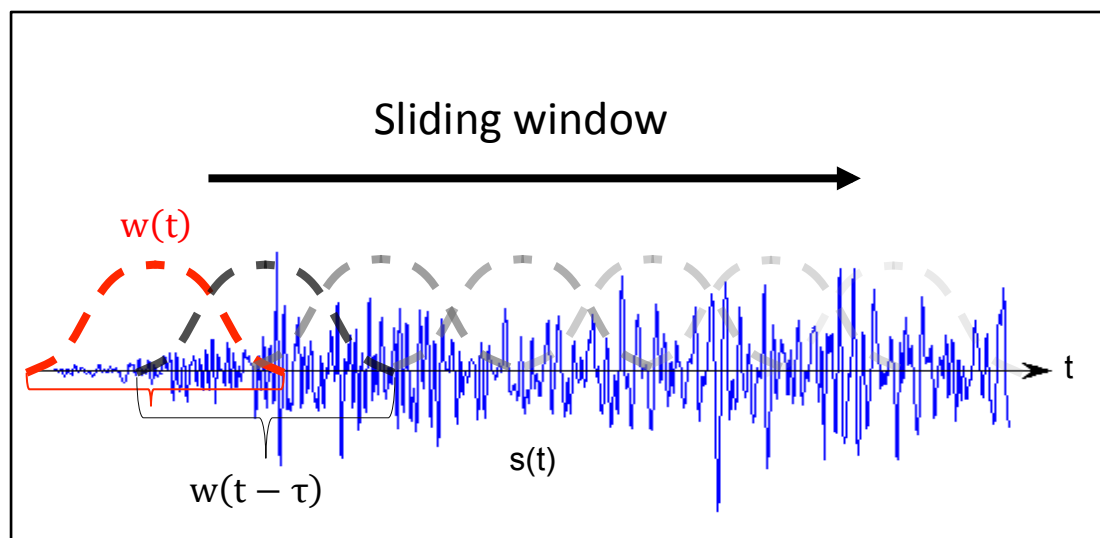


Figure 2.9: A simple example of the STFT windows' moving and overlapping technique. STFT analysis transforms the window individually by making the rest have a value (out of the window) of zero and then moves to the next window. The time to frequency transform technique continues to cover the entire seismic signal.

There are many types of STFT windows with different purposes and working mechanisms. Here, I found that the appropriate window that can give a promising result is a Hann window (Hanning window). (Harris, 1978) stated that, typically, applying a sine window (Hann window) with a 50% overlap in time length in fast Fourier transform (FFT) decomposition decreases the leakage of spectral amplitude in the main lobe and shows a side lobe with a lower amplitude and far from the main lobe Figure 2.10. Hence, the window will chirp smoothly and preserve the amplitude distribution in the main lobe of windowed signal. In contrast, the sharp windows, for instance a rectangle window, may cause some frequency interferometry, particularly at the boundaries of the windows and show a modelled signal with some unreal high frequencies. Relying on this conception, I utilised a Hann window function with a 50% overlap, which is defined as

$$w(\tau) = \sin^2 \left[\frac{\tau}{N} \pi \right], \quad 2.36$$

where $w(\tau)$ is the function of the Hann window and N is the windowing time length.

Another tool that controls window function resolution is the selection of the window length. An STFT window's width should be carefully fixed in the time and frequency domain. This is done because, for example, if the window is wider, STFT will show a good frequency resolution but a poor time resolution and if it is a narrow window the time resolution will be better than the frequency.

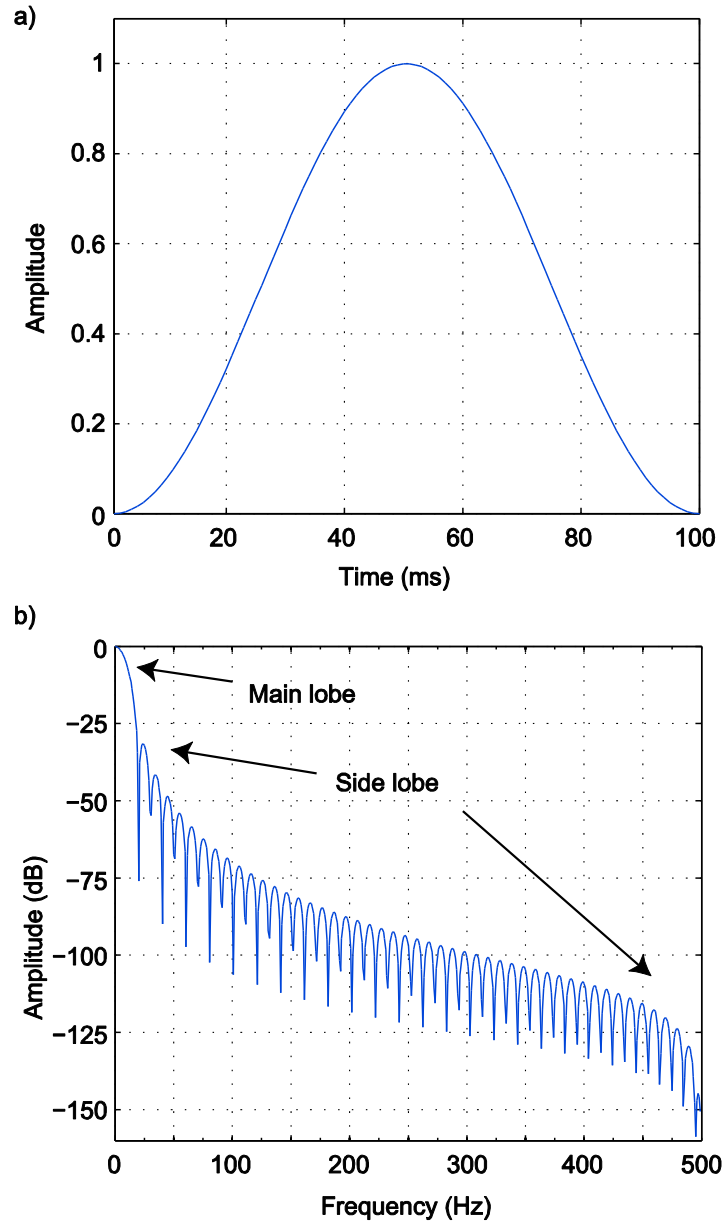


Figure 2.10: The Hann window in (a) time and (b) frequency domains. The smoothness shown in the Hann window is reflected in the transform frequency window by reducing the level of the side lobe and in contrast, increasing the width of the main lobe. This effect causes a decrease in the leakage of spectral amplitude in a time-frequency transform decomposition.

More discussion of SFTF and its application can be found in (Harris, 1978), (Allen and Rabiner, 1977), (Reine et al., 2009) and (Partyka et al., 1999). In Chapter 5, STFT will be utilised to model 3D time-lapse seismic noise and evaluate CO₂ injection by using the 3D seismic time-lapse signal in the Otway project.

2.4 Seismic Noise

Noise plays fundamental role in quality of seismic processing, interpretation and inversion. As such, it is important to be able to quantify the presence of noise in the data. To this end, I summarised the basic concepts about the noise level measurements.

2.4.1 Seismic repeatability

The normalised root mean square (NRMS) is a tool used to estimate the deviation error between two repeated sets of values. In seismic monitoring, NRMS is a common function used to measure the similarities or differences in the seismic signals of two repeated traces from two time-lapse surveys (Kragh and Christie, 2002). Therefore, this measured function is an important tool when used to examine the non-repeatability of noise effects in a time-lapse seismic data set (Spetzler, 2004). The differences in time-lapse data are usually caused by changes in reservoir production, fluid/gas injection (CO₂ plume) or other reasons, for example, survey geometry or noise.

The NRMS values for two traces can be computed by applying the average repeatability metrics of the two traces, a and b, which are defined as

$$NRMS = 200 \times \frac{RMS(a_t - b_t)}{RMS(a_t) + RMS(b_t)}, \quad 2.37$$

where the root mean square (RMS) is defined as

$$RMS(x_t) = \sqrt{\frac{\sum_{t_2}^{t_1} (x_t)^2}{N}}, \quad 2.38$$

where a_t and b_t are the seismic traces from two surveys and N is the number of samples within the time windows between t_1 and t_2 . In general, time shifts, amplitude and phase changes significantly affect the NRMS values. A small value of NRMS shows good repeatability, whereas a high value represents poor repeatability or a large value of non-repeatable noise. Typically, a good value of NRMS for a

time-lapse seismic signal is less than 20% and it is reasonable if it is in the range of 40% to 60%. Theoretically, NRMS is not limited by 100%; it may reach 140% if the two time-lapse traces contain uncorrelated random noise and may reach 200% if their polarity is reversed (Kragh and Christie, 2002).

2.4.2 Signal-to-noise ratio estimation

The signal-to-noise ratio (SNR) is a seismic attribute to quantify the amount of noise corresponding to the seismic signal. Initially, we do not know what is signal and what is noise. Thus, I commonly assumed that any coherent event in the seismic record corresponds to signal and everything else is noise. Using this assumption, I can define SNR as the percentage of primary P-wave reflection signals of all other unwanted noise. Mathematically, this definition is established by (Hatton et al., 1986) and given by

$$(SNR)_i = \sqrt{\frac{[g_{i,i+1}]_{max}}{1 - [g_{i,i+1}]_{max}}}, \quad 2.39$$

where $(SNR)_i$ the signal-to-noise ratio and $[g_{i,i+1}]_{max}$ the maximum of normalised crosscorrelation between two sequential traces i and $i + 1$ of the time window.

In Chapters 3, 4 and 5 the detectability of CO₂ and the noise level will be observed by utilising this estimation tool.

2.5 References

- Allen, J. B., and L. Rabiner, 1977, A unified approach to short-time Fourier analysis and synthesis: Proceedings of the IEEE, **65**, 1558-1564.
- Angerer, E., S. Crampin, X. Li, and T. Davis, 2000, Time-lapse seismic changes in a CO₂ injection process in a fractured reservoir, SEG Technical Program Expanded Abstracts 2000, 1532-1535.
- Calvert, R., 2005, Insights and methods for 4D reservoir monitoring and characterization.
- Carcione, J. M., G. C. Herman, and A. P. E. ten Kroode, 2002, Seismic modeling: Geophysics, **67**, 1304-1325.
- Chadwick, R. A., D. Noy, R. Arts, and O. Eiken, 2009, Latest time-lapse seismic data from Sleipner yield new insights into CO₂ plume development: Energy Procedia, **1**, 2103-2110.
- Cook, P., 2014, Geologically storing carbon: learning from the Otway Project experience: CSIRO PUBLISHING, 2014.
- Cook, P. J., 2009, Demonstration and Deployment of Carbon Dioxide Capture and Storage in Australia: Energy Procedia, **1**, 3859-3866.
- Gassmann, F., 1951, ELASTIC WAVES THROUGH A PACKING OF SPHERES: Geophysics, **16**, 673-685.
- Gjøystdal, H., E. Iversen, R. Laurain, I. Lecomte, V. Vinje, and K. Åstebøl, 2002, Review of Ray Theory Applications in Modelling and Imaging of Seismic Data: Studia Geophysica et Geodaetica , **46**, 113-164.
- Harris, F. J., 1978, On the use of windows for harmonic analysis with the discrete Fourier transform: Proceedings of the IEEE, **66**, 51-83.
- Hatton, L., M. H. Worthington, and J. Makin, 1986, Seismic data processing: Theory and practice.
- Hofmann, R., X. Xu, M. Batzle, M. Prasad, A.-K. Furre, and A. Pillitteri, 2005, Effective pressure or what is the effect of pressure?: The Leading Edge, **24**, 1256-1260.
- Kragh, E., and P. Christie, 2002, Seismic repeatability, normalized rms, and predictability: The Leading Edge, **21**, 640-647.
- Krebes, E., 2004, Seismic Forward Modeling: CSEG RECORDER , April, 28-39.

- Kelly, K. R., and K. J. Marfurt (eds), 1990, Numerical modeling of seismic wave propagation: Geophysical Reprint Series, Society of Exploration Geophysicists, 520 p.
- Lines, L. R., and R. T. Newrick, 2004, Fundamentals of geophysical interpretation: Society of Exploration Geophysicists.
- Lowrie, W., 1997, Fundamentals of geophysics: Cambridge University Press.
- Lumley, D., D. Adams, R. Wright, D. Markus, and S. Cole, 2008, Seismic monitoring of CO₂ geo - sequestration: realistic capabilities and limitations.: SEG Technical Program Expanded Abstracts 2008, 2841-2845.
- Lumley, D. E., 2001, Time-lapse seismic reservoir monitoring: Geophysics, **66**, 50-53.
- Margrave, G. F., 2003, Numerical Methods of Exploration Seismology with algorithms in MATLAB: CREWES.
- Nur, A. M., and Z. Wang, 2001, Seismic and Acoustic Velocities in Reservoir Rocks: Recent developments: Society of Exploration Geophysicists.
- Partyka, G., J. Gridley, and J. Lopez, 1999, Interpretational applications of spectral decomposition in reservoir characterization: The Leading Edge, **18**, 353-360.
- Reine, C., M. van der Baan, and R. Clark, 2009, The robustness of seismic attenuation measurements using fixed- and variable-window time-frequency transforms: Geophysics, **74**, WA123-WA135.
- Russell, B., K. Hedlin, F. Hilterman, and L. Lines, 2003, Fluid - property discrimination with AVO: A Biot - Gassmann perspective: Geophysics, **68**, 29-39.
- Sheriff, R. E., and L. P. Geldart, 1995, Exploration seismology: Cambridge university press Cambridge.
- Smith, G. D., 1985, Numerical solution of partial differential equations: finite difference methods: Oxford University Press.
- Smith, T. M., C. H. Sondergeld, and C. S. Rai, 2003, Gassmann fluid substitutions: A tutorial: Geophysics, **68**, 430-440.
- Spetzler, J., 2004, On the sensitivity of the NRMS function to non - repeatability causes and production: Presented at the SEG Technical Program Expanded Abstracts 2004.

Telford, W. M., L. P. Geldart, and R. E. Sheriff, 1990, Applied geophysics: Cambridge university press.

Wason, C. B., Black, J. L., & King, G, 1984, Seismic modeling and inversion: Proceedings of the IEEE, 72(10), 1385-1393.

Yilmaz, Ö., 2001, Seismic data analysis: Society of Exploration Geophysicists Tulsa.

Every reasonable effort has been made to acknowledge the owners of copyright material. I would be pleased to hear from any copyright owner who has been committed or incorrectly acknowledge.

CHAPTER 3: QUANTIFYING TIME-LAPSE SEISMIC SIGNAL DETECTION FOR CO₂ MONITORING AND VERIFICATION AT THE SOUTH WEST HUB

3.1 Introduction

The South West Hub (SW Hub) project, one of the Australian CO₂ capture and storage projects, is located 160 km south-southeast of Perth in the Collie Basin, Western Australia (Figure 3.1).

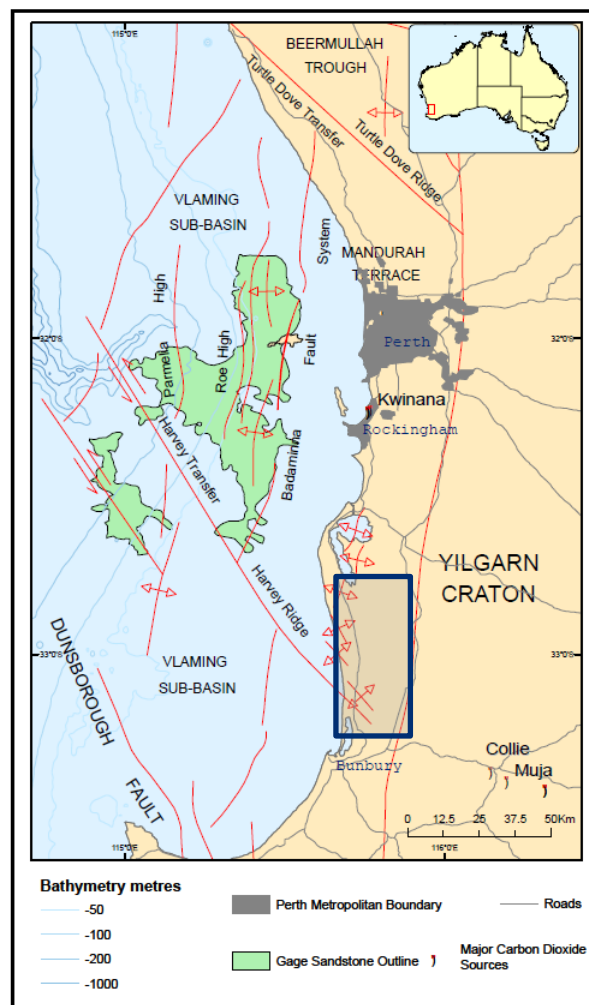


Figure 3.1: Map showing the location of the South West Hub project for CO₂ capture and storage. The blue rectangle shows the area within which the project expects to inject the gas (Modified after Dance and Tyson, 2006).

The Australian CCS projects have been chosen on the basis of numerous studies and reports that have considered a great number of scientific and environmental aspects. There are many sources of CO₂ emissions in Western Australia such as those from high CO₂ natural gas fields, liquefied natural gas, mineral processing plants and coal-fired power stations. The number of these sources is increasing as these industries expand. However, the largest CO₂ emission source is the Collie power station, which is found in the area shown in the blue rectangle in Figure 3.1. That makes the location of Collie power station an interesting suggested location for Australian CCS projects (Varma et al., 2009). On that basis, Varma et al. (2009) studied the possibility of injecting the CO₂ into the subsurface in the Collie area by conducting many rock physics modelling and well log experiments. They found that CO₂ injection is feasibly applicable, especially into the deep highly permeable Lesueur formation. The trapping system in the SW Hub is a physical residual trapping mechanism in the lower leasure formation. The reservoir properties were tested in lab measurements and show promising porosity and significant permeability anisotropy in injection level of the formation (Stalker et al., 2013). The examination presented physical residual trapping mechanism (25–45%) in the lower leasure formation.

The feasibility of using the SW Hub for CCS has been investigated from many points of view, including geological, geomechanical and geochemical. The findings from these studies have been published in many reports to help ensure the feasibility and safety of CO₂ storage at this site. However, there has not been any work done on seismic monitoring and verification for the site. In this chapter, I assessed the seismic signal detectability for CO₂ monitoring in the SW Hub project. First, I identified the noise level in real data from the area. Second, I modelled different injection scenarios and monitoring geometries (surface and VSP), add the expected amount of noise, and then examine the seismic detectability of the CO₂ plumes. To create a realistic finite-difference model for several volumes of CO₂ plumes, I need to simulate the rock physics properties of the CO₂ saturated reservoir from expected brine salinity, CO₂ temperature and pressure.

3.2 Study Area and Geology

The SW Hub project is located in the Southern Perth Basin (the Collie basin), which was formed by a Precambrian basement underneath the Permian succession to recent Holocene sediments (Varma et al., 2009). This basin is trending along the southern end of the Western Australian coast and is bordered onshore from the east by the Darling Fault and the Yilgarn Craton of Proterozoic rocks. From the west it is bordered by the Dunsborough Fault, with decreasing sedimentary thickness towards the Indian Ocean crust. The other two major boundaries of the Southern Perth Basin are the Harvey Ridge in the south and the Busselton Fault, with trending filling the sedimentary Bunbury Trough in the northern part of the basin. As shown in Figure 3.2, the Southern Perth Basin has a complex tectonic structure as a result of the early continental separation between Australia and greater India (Crostell and Backhouse, 2000).

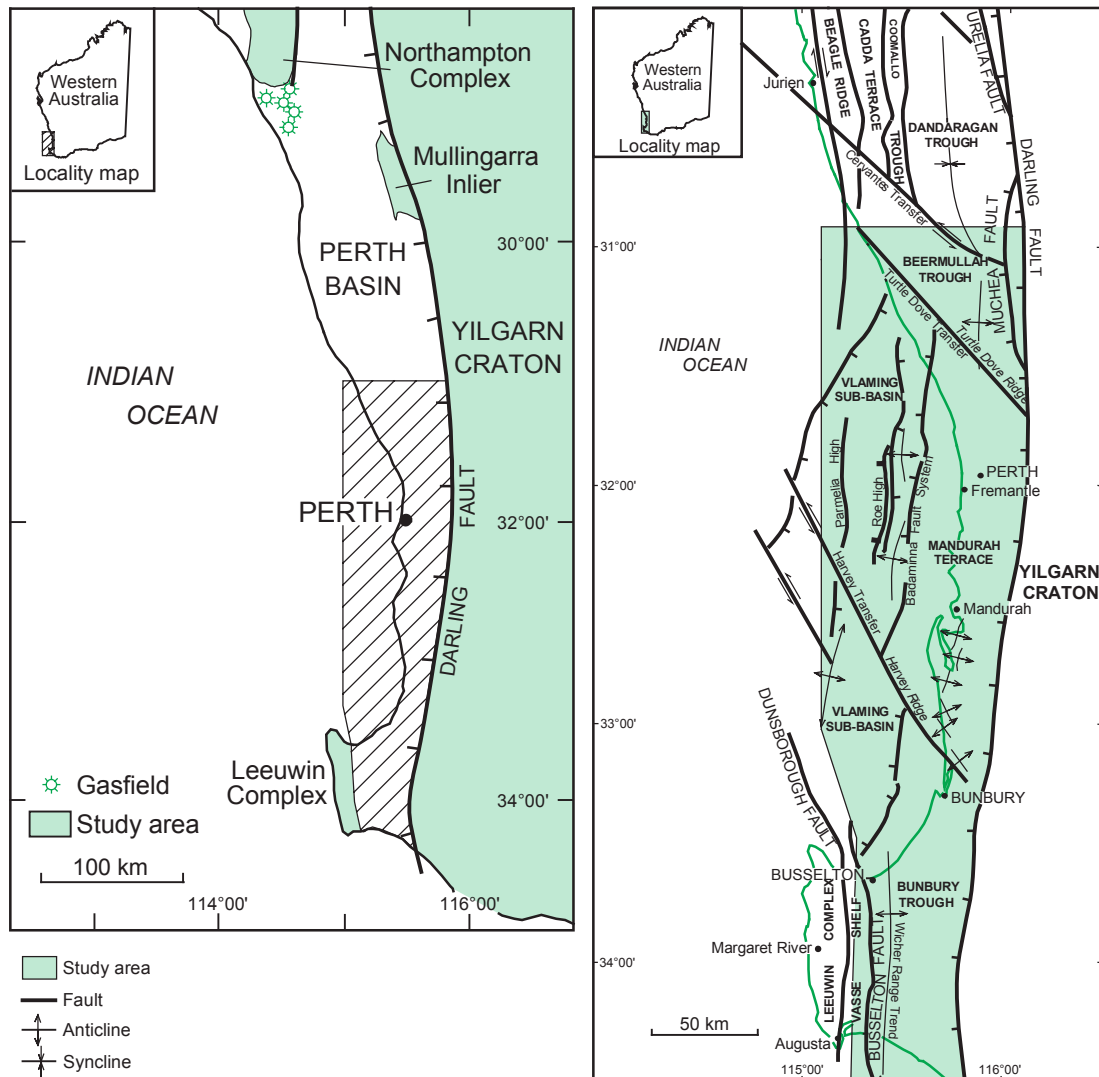


Figure 3.2: Simplified geological maps of the Southern Perth Basin. On the left is a general map of the study area, showing the major fault in the Darling Fault in the east of the Perth Basin. The geological structure, faults, anticline and syncline are presented in the map on the right. The boundaries of the Southern Perth Basin are clarified in this map, with the subdivisions and tectonic lineament of the basin. The target area for the South West Hub CCS project falls to the east of the apex of the Harvey Ridge (after Crostella and Backhouse, 2000).

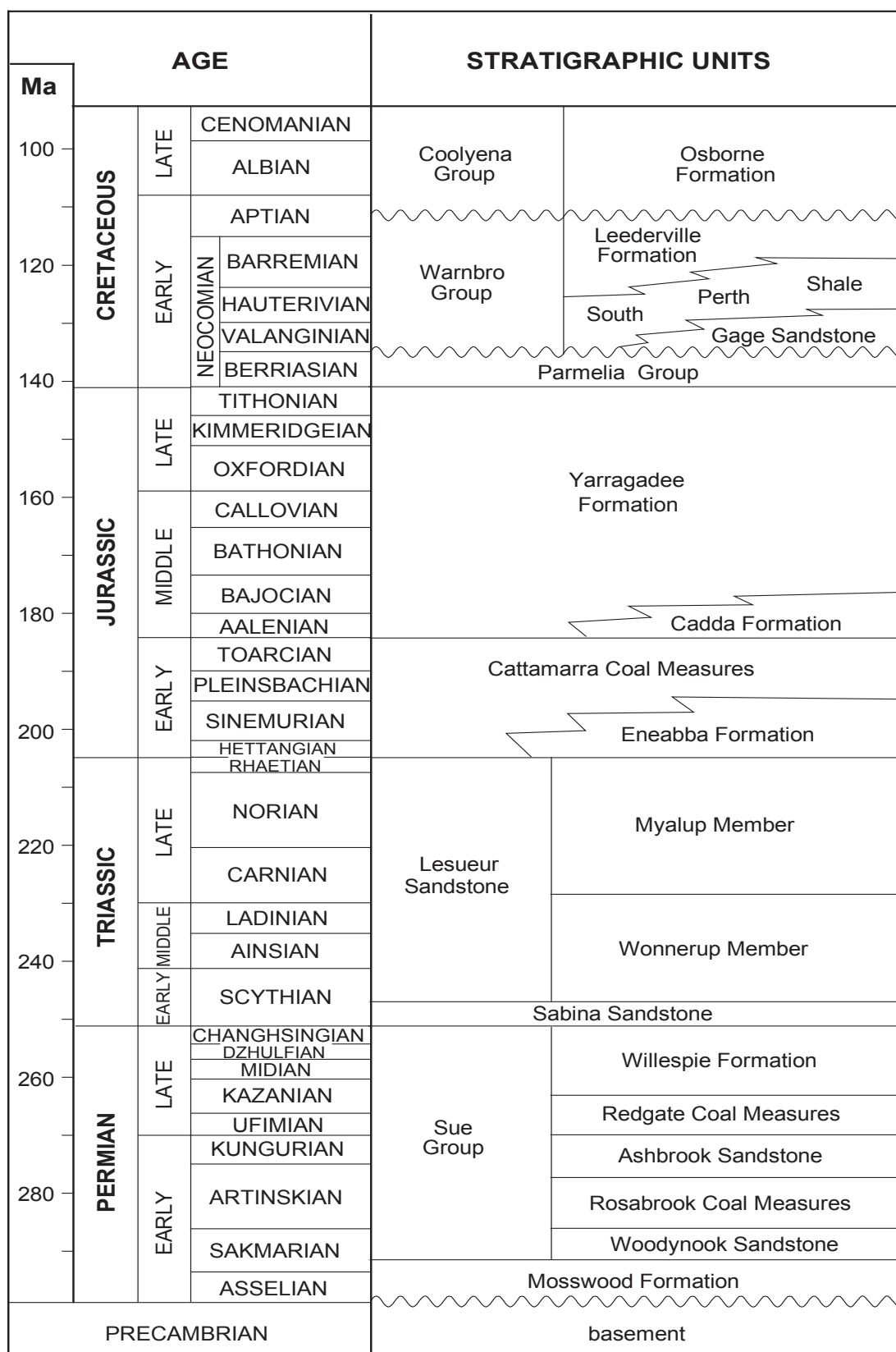


Figure 3.3: Stratigraphy of the Southern Perth Basin (Crostella and Backhouse, 2000).

According to Crostella and Backhouse (2000), the geological stratigraphy sequence of the Southern Perth Basin is composed of many formations, as shown in Figure 3.3. They used many wells to describe the geological segment and units for the whole basin. However, only two of those wells (Lake Preston 1 and Pinjarra), which are marked by the red rectangle in Figure 3.4, are located in the area of the SW Hub project. The insufficient number of wells in the area may add extra uncertainty to the expected geological structure of the site.

The stratigraphy of the Southern Perth Basin was initially formed during the Permian age, extending to the beginning of the Cretaceous period (Figure 3.3). The Sabina sandstone is from the earliest Triassic age and overlies the Sue Coal Measures unit of the basement rocks of the Southern Perth Basin. In general, the Sabina sandstone was filled from the south and consists of sorted fine to medium coarse-grained and clayey-grained sandstone. The Lesueur sandstone Formation was the next formation in the Triassic period and it overlies the Sabina sandstone. It is the suggested CO₂ injection formation for the SW Hub project. The average depth of the Lesueur sandstone varies from 1600 m in Bunbury, to 2556 m in Whicher Range 3 and to over 3000 m in the northern part of the Southern Perth Basin (Iasky, 1993). The Lesueur sandstone formation is divided into upper and lower members (Crostella and Backhouse, 2000). The upper Lesueur (Wonnerup Member) is described as a regional marine transgression in the early Triassic age and is formed of very coarse-grained gravelly sandstone. The lower Lesueur (Myalup member) is a regression to deltaic and fluvial facies and was formed in the middle to late Triassic. This member forms from a fine inter-beds sandstone rock with siltstone (Iasky, 1993). It is assumed that the Southern Perth Basin and other parts of Western Australia that formed in the early Triassic were once covered by huge flowing Triassic rivers. The early and middle Jurassic fluvial and marshy sedimentation of the Cockleshell Gully formation overlies the Lesueur sandstone formation in the Southern Perth Basin. It includes the Cattamarra Coal Measure and Eneabba Formation and its thickness increases towards the eastern part of the basin under the Darling Fault (Iasky, 1993). The formation consists of sand and interbedded shale; the sand ranges from middle to poor fine coarse-grained. In the middle and late Jurassic period, continental sedimentation was again widespread and led to the Yarragadee Formation in the Southern Perth Basin. This formation overlies the Cattamarra Coal Measure in the

southern part of the basin and on the Cadda formation in the north. The ongoing northwest-southeast extension from the middle Jurassic to the earliest part of the Cretaceous age culminated in the break-up of Australia and greater India. In the early Cretaceous period the Parmelia, Warnbro and Coolyena groups were broken up by unconformity (Varma et al., 2009). The break up in the early Cretaceous was associated with widespread uplift and erosion and possibly also with volcanism. The lower early group, Parmelia, overlies the Yarragadee formation. A renewed phase of subsidence followed in which localised sagging allowed for the deposition of submarine sediments, including turbidites.

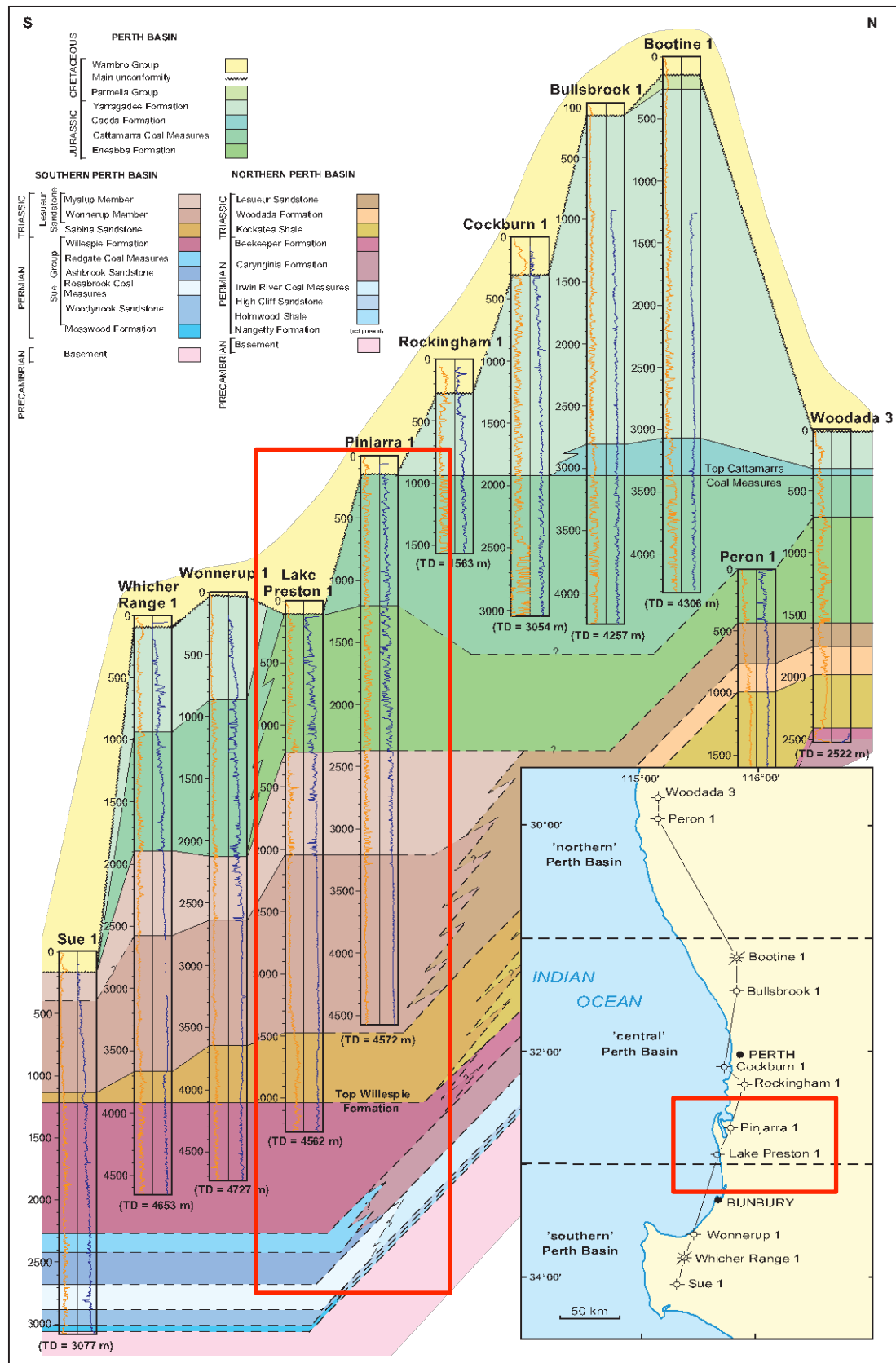


Figure 3.4: South-to-north strata correlation and a map of the wells over the Southern Perth Basin. The geological formations of the Southern Perth Basin within many wells in the area are shown with their depth in meters. The CO₂ trapping sequence of

interleaved sands and shale, which extends to at least 2600 m below the surface, is shown. The closest wells to the SW Hub project are Lake Preston 1 and Pinjarra 1, which are marked with the red rectangle. The Lesueur sandstone, the suggested formation for CO₂ injection, is located at a depth of 1520 m in Preston 1 and at a depth of 2400 m in Pinjarra (after Crostella and Backhouse, 2000).

3.3 Data and Site Characterisation

Many 2D surface seismic data and vertical seismic profiles have been acquired for the Southern Perth Basin over the years. In the early 1960's and 1970's, the first 2D seismic surveys were acquired and processed with the earliest processing tools. With the development of new processing techniques in the early 1990's, most of these data were reprocessed and analysed to try to improve the quality of the seismic sections (Annetts et al., 2012). However, the resolution of the data was still very poor despite repeated data processing, due to a combination of numerous problems: a low survey fold and large distance between source and receiver, the level of noise, which showed low SNRs in the data, and the survey equipment tools.

In 2011, six 2D surface seismic data lines were acquired in the onshore Perth Basin of the SW Hub project (Figure 3.5). This was accomplished using a vibrator source (VS) with a 25 m station interval, a 25 m shot interval and nominal 300 channels pre-shot with symmetrical spread geometry (split spread). The survey elevation is in the range of 6 m and 46 m, the nominal far offset is 3700 m. The lines have all been given a prefix number, 11GA-LL and their geometry is summarised in Table 3.1. The data were processed using the Landmark ProMax[®] 2D processing software and migrated using Tsunami software. Common offset binned data were migrated by utilising the Prestack Kirchhoff 2D time migration algorithm for all lines, with the parameters shown in Table 3.2. The reprocessing data of 11GA-LL2 was basically implemented in the following steps:

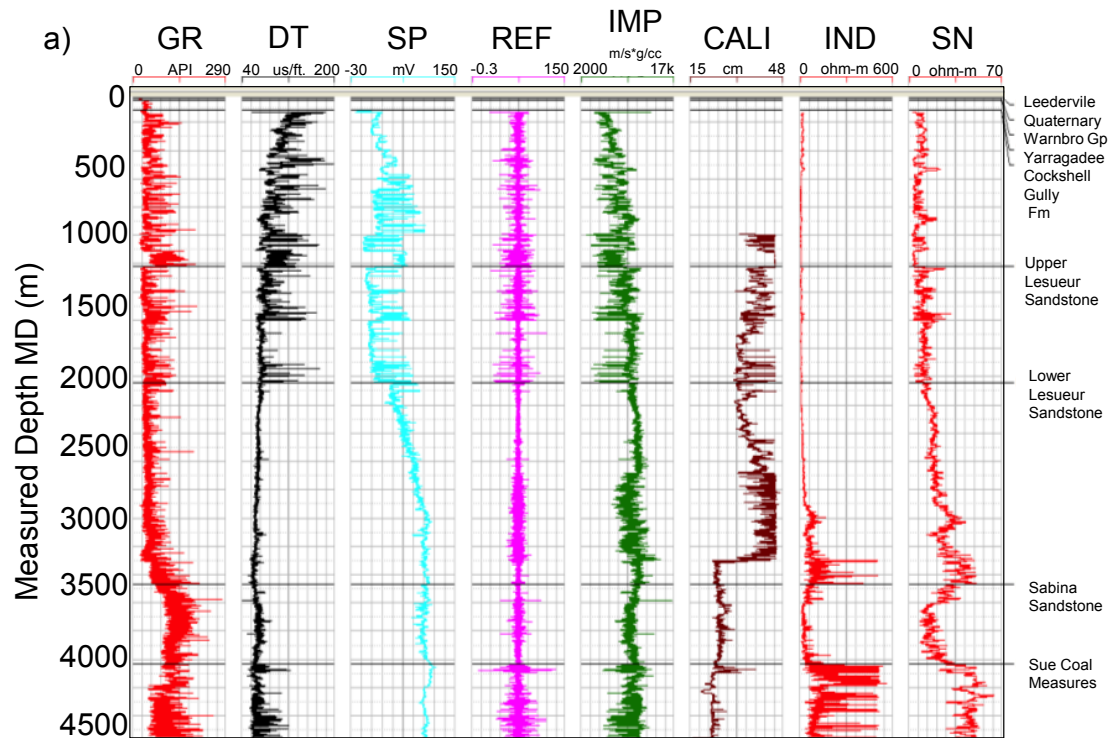
- Data load, geometry
- Trace editing (manual trace kill/reverse)
- Elevation statics
- Predictive de-convolution
- F-K filter to suppress source-generated noise
- Auto gain control (AGC) applied and saved (500 ms)

- Forward linear move-out (LMO)
- F-K domain filtering (rejection)
- Inverse LMO
- Remove saved AGC (500 ms)
- Velocity analysis
- Brute stack
- Max-power auto statics
- Velocity analysis
- Stack
- Post-stack migration
- Post-processing (FX deconvolution)

Many logged wells are distributed around the Southern Perth Basin area, for example, Wonnerup 1, Lake Preston 1, Preston 1, Pinjarra 1, Rockingham 1 and Cockburn 1. As mentioned in section 3.2, two of these wells are near to the SW Hub project area; Lake Preston 1 and Pinjarra 1 (Figure 3.5). However, none of these well logs intersect the seismic lines. Indeed, Lake Preston 1 is the closest well to the SW Hub project in the eastern area, but Pinjarra 1, which is located several kilometres north of the SW Hub Project, is very important in this study because it is the nearest cored well and is therefore helpful in providing a great deal of information and accurate rock properties of the subsurface formations (Figure 3.6).



Figure 3.5: The location of the six 2D surface seismic data lines. These lines were utilised to evaluate the CO₂ seismic monitoring for the SW Hub project for CO₂ capture and storage. The available well logs in the area are from wells Pinjarra 1 and Lake Preston 1, which are also shown. No wells intersect any of the lines.



b)



Figure 3.6: The various log types of Lake Preston 1 (a) and some core samples of the Pinjarra 1 well (b). The photographs of core samples 1, 2 and 3 present the cores at depths of 625 m, 2587 m and 1385 m, respectively. The lithology of these cores shows fine-grained sandstone (2) and shale (1), fine-grained sandstone overlying shale and shale overlying very fine-grained sandstone (3).

All seismic lines, shown in Figure 3.7, were interpreted for the geological structure, faults, layers horizons and the majority dipping of the area. The complexity in the near-surface conditions of the Southern Perth Basin (Figure 3.7) reduces the quality of the seismic data, which in turn hinders the interpretation. Annetts et al. (2012) attributed this complexity of the shallow layers to coastal limestones and sand dunes. Figure 3.7, based on the area geology of Section 3.2, clearly shows that the general layer dipping is in the east-west direction and the major north-south fault, the Darling fault, is located in the eastern border of the study area. In addition, the interpretation of basement modelling of potential field results obtained in the Southern Perth Basin (Figure 3.8) shows an estimation of the depth of the basement beneath the basin (Iasky and Lockwood, 2004). On the basis of the exact description, the best data option was used to derive a realistic finite-difference model for the SW Hub for CCS and was one of these lines, 11GA-LL1, 11GA-LL2 or 11GA-LL3, along the major fault (Figure 3.7).

Table 3.1: A summary of the seismic lines geometry parameters for SW Hub project.

Line	1st	Last	Station			Max	1st	Last
LLGA-	VS	VS	int., m	2D km	Shots	Fold	CDP	CDP
LL1	1000	1709	25	17.73	658	150	2000	3409
LL2	2000	2610	25	15.25	537	150	4051	5220
LL3	3000	3595	25	14.88	494	140	6000	7190
LL4	4000	5066	25	26.65	1010	150	8000	10132
LL5	5000	5626	25	15.65	529	144	10004	11252
LL6	6000	6418	25	10.45	378	146	12000	12837

Table 3.2: The parameters of the Prestack Kirchhoff 2D time migration, which was applied in the imaging of processed seismic data lines.

Migration velocity	At 500 m intervals (40 CDPs)
Aperture	4000 m
Dip limit	45 degree
Bin size	50 m
Number of offsets	75
Output CDP interval	12.5 m

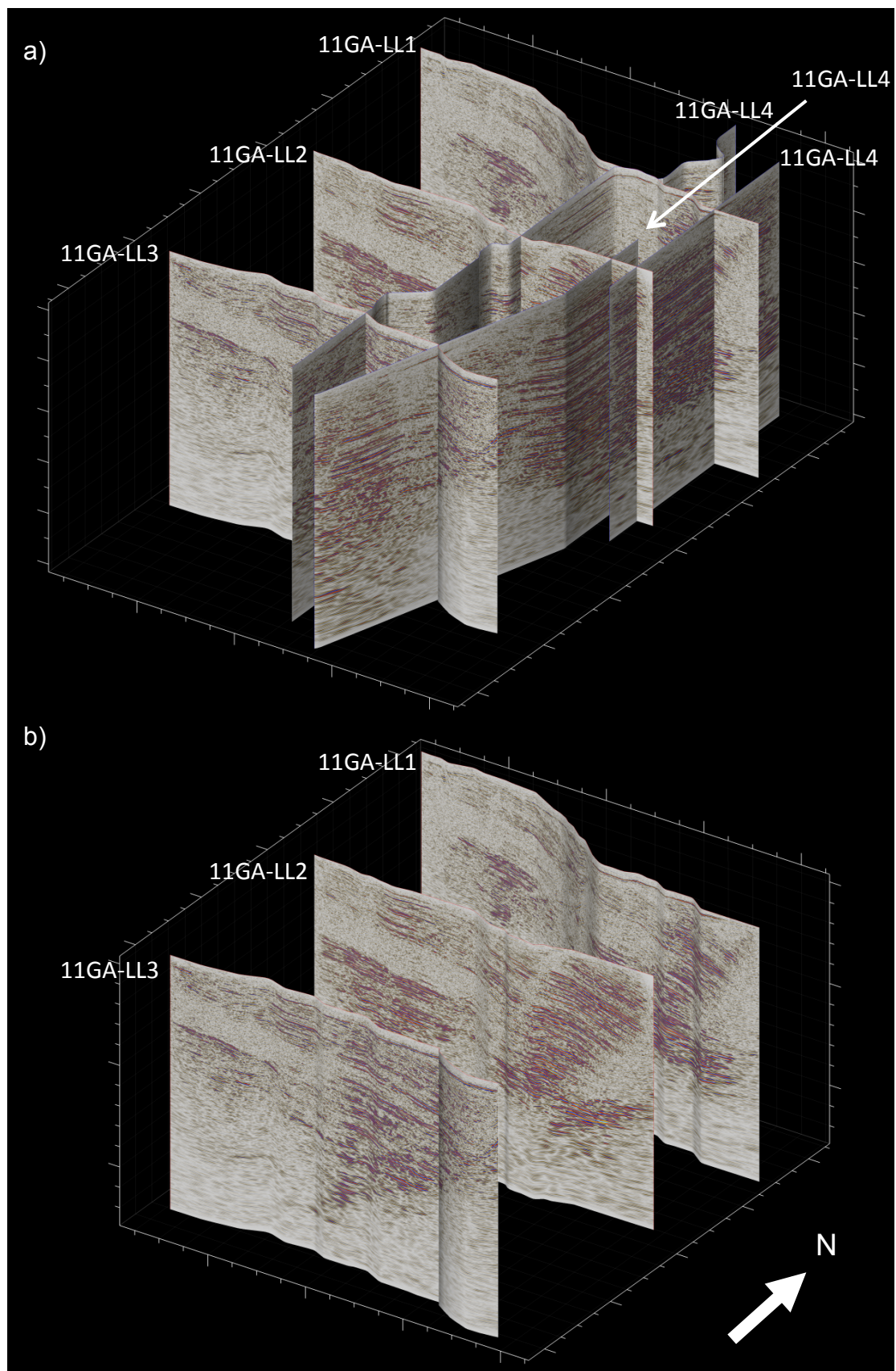


Figure 3.7: The 3D interpretation view of 11GA_LL2. The interpreted section shows the geological structure of the southern Perth Basin, with collared horizons of the

subsurface formation from lower to upper: Wonnerup Member (Lower Lesueur formation), Myalup Member (Upper Lesueur formation), Eneabba Member, Cattamarra Member, Cadda Formation, Warnbro Group and the near-surface superficial sediments. It also shows the fault system in the area (marked in black) and how the seismic line is crooked in the faulting area.

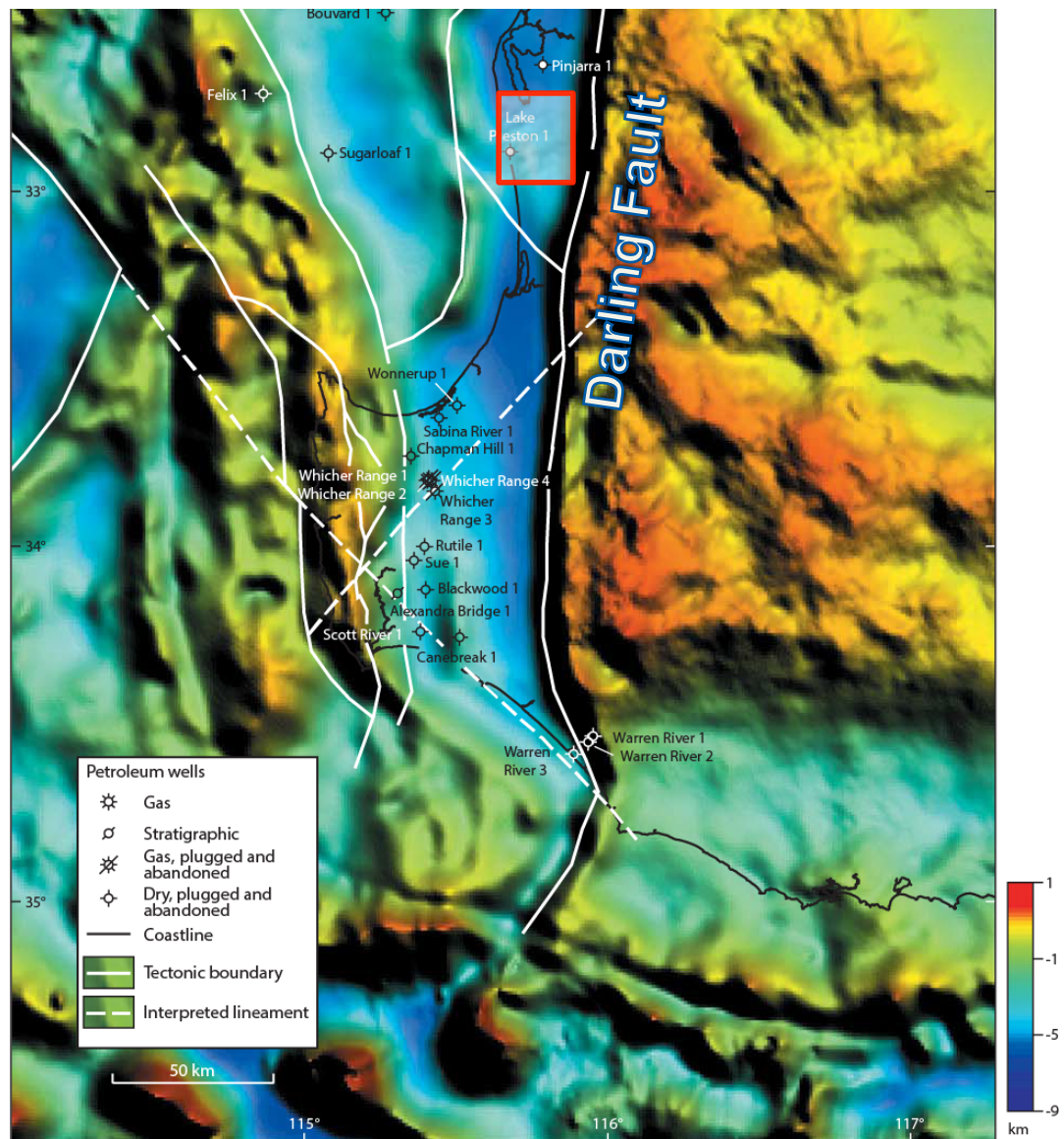


Figure 3.8: Gravity anomaly map of the basement depth of the Southern Perth Basin. The South West Hub project area (red square) is located near the Harvey Ridge, south of the study area (after Iasky and Lockwood, 2004).

3.4 Time-Lapse Seismic Monitoring Feasibility Analysis

3.4.1 Overview

This investigation is a feasibility study of the detection of several amounts of CO₂ by seismic monitoring in the SW Hub project. In section 3.3, I discussed the site and the appropriate data that can be used in a feasibility study of CO₂ monitoring and verification in this project. On the basis of the area geology and the structure dipping, three seismic lines, 11GA-LL1, 11GA-LL2 and 11GA-LL3, were chosen for interpretation to create a geological model of the area. To create a 2D model we chose to use line 11GA-LL2. This model was then used for synthetic modelling of the time-lapse response of CO₂ injection in the onshore SW project area. The results from the modelling were analysed in terms of plume detectability in estimated signal to noise conditions. The main elements of the workflow are shown in Figure 3.9. In this section, I described this workflow in detail.

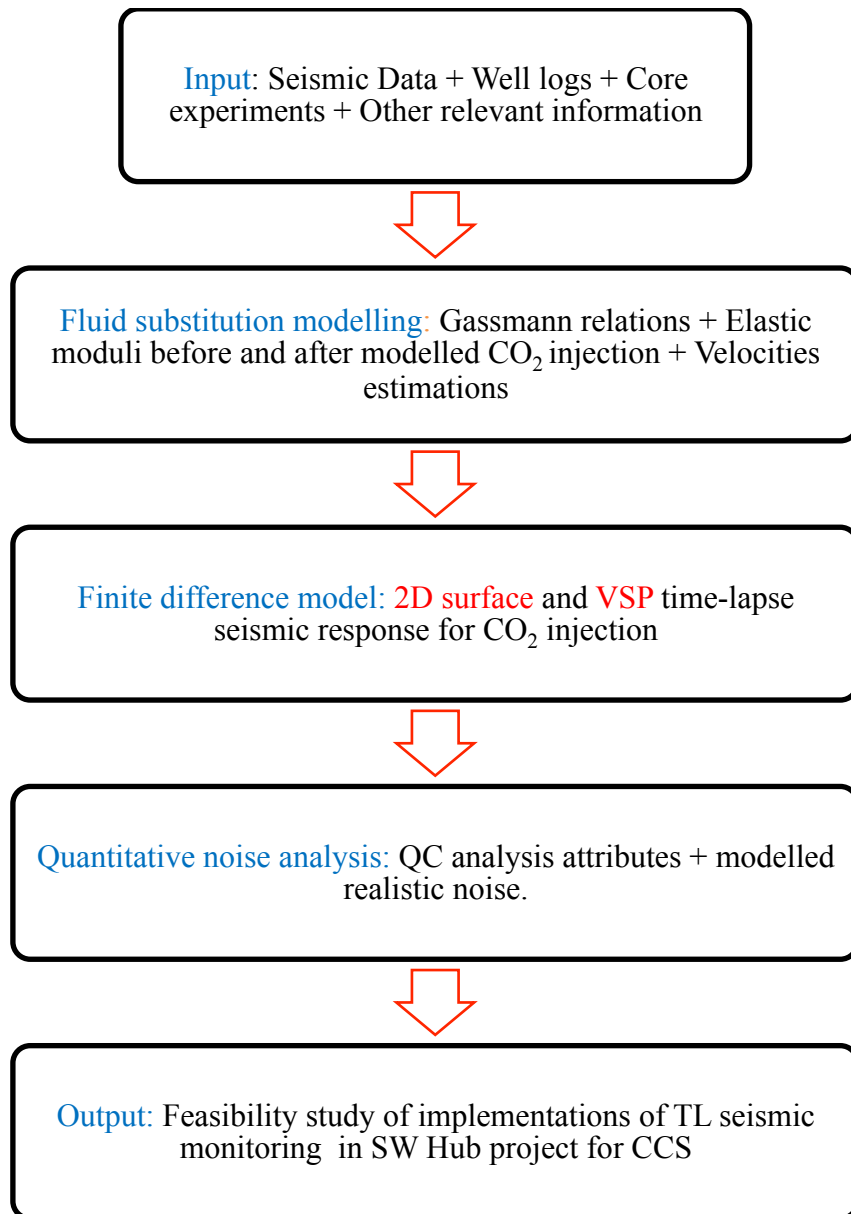


Figure 3.9: A flowchart of the main experimental steps of a feasibility analysis for the CO₂ capture and storage South West Hub project. Some hints into insights that were applied through the investigation in time-lapse seismic signal response for CO₂ injection are also shown.

3.4.2 Rock Physics and Fluid Substitution Modelling

In order to study the time-lapse seismic response of CO₂, an understanding of fluid changes through the suggested CO₂ sequestration area is required. Therefore, rock physics and fluid substitution modelling are highly important to study CO₂ replacement of brine in the reservoir. The resulting changes in the elastic properties of the plume can be then input into the seismic modelling of the time-lapse seismic signal.

The common relationship between density, elastic-wave velocity properties and the replacement of the pore fluid and matrix properties of rocks is calculated using the Gassmann equation (1951). This equation computes the bulk and shear moduli of a fluid-saturated isotropic porous medium and relates them to the bulk and shear moduli of the same medium in the drained case. The discussion around use of this equation for reservoir monitoring and the changes in fluid saturation and seismic velocities was the subject of an excellent review by (Smith et al., 2003) and is generally described in section 2.3.

As mentioned previously, the model of rock physics and fluid substitution was based on the interpretation of 11GA_LL2. The interpretation of this line shows many geological formations and members structures, which were modelled in the FD model with appropriate velocities and CO₂ plumes as shown in Figure 3.10. The interval velocities (P-wave velocities) of these formations were observed in correlation with log data from the Lake Preston 1 well and are shown in Table 3.3. The prediction densities of these formations were derived by using the interval P-wave velocities and applying Gardner's empirical relation (Gardner et al., 1974):

$$\rho = 0.174V_p^{0.25}, \quad 3.1$$

where ρ is the bulk density in grams per cubic centimetres (g/cm³) and V_p is the P-wave velocity in kilometres per second (km/s).

I also computed the S-wave velocities because the direct measurements of these velocities *in situ* are not available. I applied Castagna's equation (mud rock line) to derive S-wave velocities from P-wave velocities in the *in situ* data (Castagna et al., 1985):

$$V_s = 0.86V_p - 1.17, \quad 3.2$$

where V_s is the S-wave velocity in kilometres per second (km/s), and V_p is the P-wave velocity in kilometers per second (km/s).

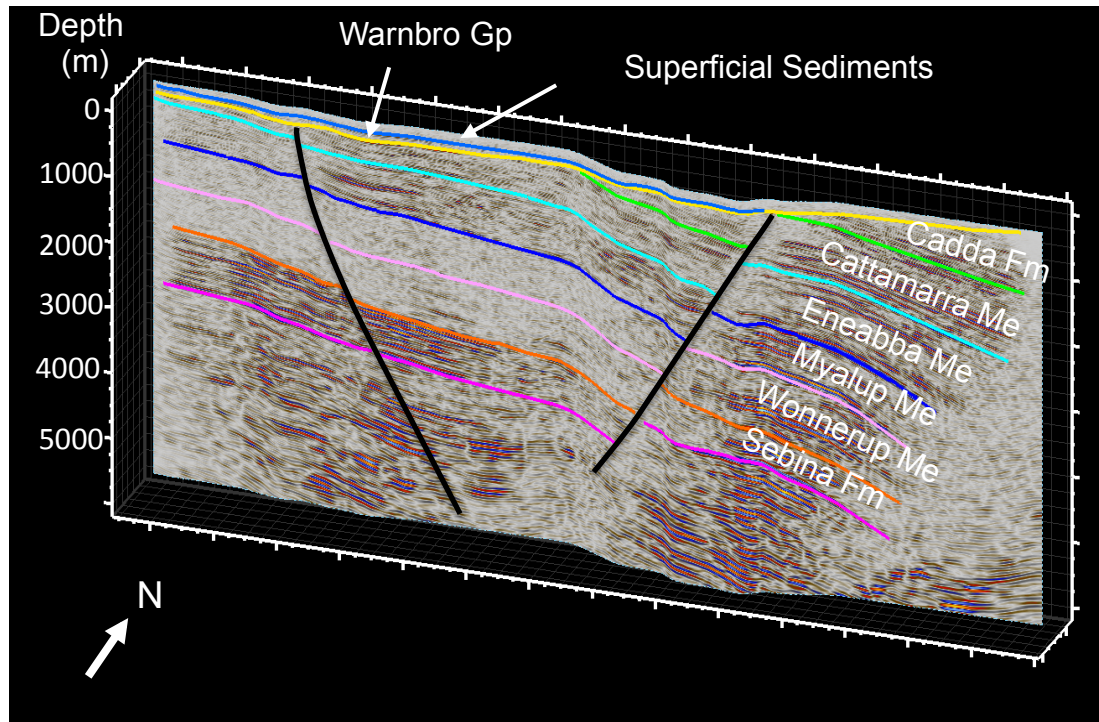


Figure 3.10: The interpretation of 11GA_LL2. The interpreted section shows the geological structure of the Southern Perth Basin, with collared horizons of the subsurface formation from lower to upper: Wonnerup Member (Lower Lesueur formation), Myalup Member (Upper Lesueur formation), Eneabba Member, Cattamarra Member, Cadda Formation, Warnbro Group and the near-surface superficial sediments. It shows also the fault system in the area, which is marked in black.

Table 3.3: The observed interval velocities (P-wave velocities) V_p from the Lake Preston 1 well log for the Southern Perth Basin undersurface geological formations. The table also shows the calculated S-wave velocities V_s and densities ρ calculated using Gardner's empirical relation and Castagna's equation, respectively.

Formation	V_p (km/s)	V_s (km/s)	Density (kg/m ³)
<i>Sedimentary</i>	2.200	0.7241	2120.3
<i>Warnbro Gp</i>	2.250	0.7650	2132.3
<i>Cadda Fm</i>	2.400	0.8940	2167.0
<i>Cattamarra Me</i>	2.670	1.1266	2225.6
<i>Eneabba Me</i>	3.429	1.7793	2369.2
<i>Myahup</i>	4.333	2.5564	251.2
<i>Wonnerup</i>	4.983	3.1154	2601.2

The estimated effective porosity was calculated from the log data from the well Lake Preston 1 in the lower Lesueur Sandstone formation at a depth of 2500 m as 11%.

The elastic properties of the subsurface rocks replacing brine by CO₂ injection are based on the Gassmann fluid substitution. The properties of CO₂ that will replace the brine in rock pore are:

- Moduli of dry rock K_{Dry}
- Brine-saturated rock (K_{Sat}, μ)
- Bulk moduli (incompressibilities) of brine and CO₂ (K_B, K_{CO_2})
- Porosity (ϕ)
- CO₂ saturation (S)
- Bulk modulus of the solid grain material (K_G).

Density (ρ), P-wave velocity (V_p) and S-wave velocity (V_s) were used to derive the brine-saturated rock moduli (K_{Sat}, μ) using the functions (see section 2.1)

$$\mu = V_s^2 \rho, \quad 3.3$$

$$K_{Sat} = V_s^2 \rho - \frac{4}{3} \mu. \quad 3.4$$

The dry bulk modulus (K_{Dry}) value is obtained by using the values of the properties of porosity, brine modulus and grain modulus. Moreover, the volume fractions of the minerals can be observed from well logs or core samples. These volume fractions can be used to calculate the bulk modulus of the solid grain material. The moduli of the grain mixture was calculated by using the average of the upper and lower Hashin-Shtrikman bounds (Hashin and Shtrikman, 1962). In a clean sandstone situation, the bulk modulus and density of the grain material of the Quartz-rich are identical values of the sandstone. On that basis, the bulk modulus and density of Quartz will be:

- $K_G = K_{Quartz} = 36.6 \text{ GPa}$
- $\rho_G = \rho_{Quartz} = 2.65 \text{ g/cm}^3$

Depending on the previous discussion and using the Gassmann equation shown in section 2.3, the K_{Dry} can be given by:

$$K_{Dry} = \frac{K_{Sat} \left(\phi \frac{K_G - K_B}{K_B} + 1 \right) - K_G}{\phi \left(\frac{K_G - K_B}{K_B} \right) - 1}. \quad 3.5$$

Wood's equation of mixing fluid rules was implemented to calculate the bulk modulus of the brine and CO₂ mixture K_W and this is given by:

$$\frac{1}{K_W} = \frac{1 - S}{K_B} + \frac{S}{K_{CO_2}}. \quad 3.6$$

This equation was first introduced by (Wood, 1955) and later represented by (Mavko et al., 2009) and it computes uniform saturation of the mixture. The applicability of this assumption for sandstone at seismic frequencies was justified by (Johnson, 2001;

Caspari et al., 2011). For the Southern Perth Basin, we assume that approximate maximum residual of CO₂ saturation for sandstones is 50% brine and 50% gas mixture (IPCC, 2005; Benson et al., 2012). In addition, the modelling effect results have indicated that saturations between 30% and 50% do not cause large seismic impedance changes (Annetts et al., 2012) (Figure 3.11).

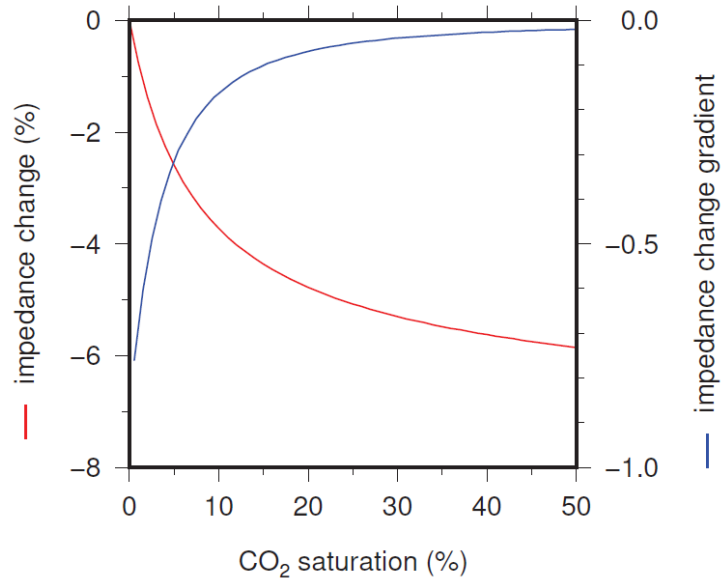


Figure 3.11: The percentage and gradient changes in impedance crossplot with the CO₂ saturation percentage in the South West Hub project for CO₂ capture and storage. Impedance will decrease with high changes of CO₂ saturation, which means that injection procedures have less of an effect on seismic response (Annetts et al., 2012).

After calculating K_{Dry} and K_W , based on the assumption of a 50% brine and gas mixture, K_W can be substituted for K_B in order to calculate K_{CO_2Sat} , the bulk modulus of the rock, after CO₂ injection by modifying equation 3.5:

$$K_{CO_2Sat} = \frac{K_{Dry} \left(\phi \frac{K_G - K_W}{K_W} + 1 \right) - K_G}{\phi \left(\frac{K_G - K_W}{K_W} \right) - 1}. \quad 3.7$$

The thermophysical properties of fluid systems from material laboratory measurements are utilised to estimate the properties of the bulk modulus and density of brine and CO₂, based on the *in situ* well logs data of temperature and pressure (Lemmon et al., 2012). Based on the temperature gradient in the area of 2.1 °C/100 m, and the temperature on the surface of 18 °C, the temperature at the injection depth is around 70 °C. The pore pressure in the Lesueur Formation was also computed from the pressure gradient of 9.8 kPa/m and the hydrostatic pressure of water with salinity was 30,000 ppm, with a density of 99985x10⁴ kg/m³. The results of Gassmann fluid substitution methods are with the CO₂ and brine properties pre- and post-injection in Table 3.5.

Table 3.4: The Lesueur properties for bulk modulus and density of brine and CO₂. These were computed by using the thermophysical properties of fluid systems calculations (Lemmon et al., 2012) and were based on the *in situ* well logs data of temperature and pressure.

Pore pressure	24.5 MPa
Temperature	70 °C
V_P	441.82 m/s
K_{CO_2}	0.143 GPa
ρ_{CO_2}	0.731 g/cm ³
K_{Brine}	2.502 GPa
ρ_{Brine}	0.999 g/cm ³

Table 3.5: The Gassmann fluid substitution performance results using interval P-wave velocities as input. The P-velocities were observed from borehole measurements in the area. S-wave velocities V_S and densities ρ were estimated by using Gardner's empirical relation and Castagna's equation (mud rock line), respectively. For the same modelled injection interval, this gave 100% brine pre-injection and a 50% brine 50% gas post-injection composition, which is the approximate residual CO_2 saturation for sandstone (IPCC, 2005; Benson et al., 2012).

% saturation	Pre- CO_2 injection (100% brine)	Post- CO_2 injection (50% brine and 50% CO_2)
V_P	4333 m/s	4225 m/s
V_S	2556 m/s	2564 m/s
ρ	2.512 g/cm ³	2.497 g/cm ³

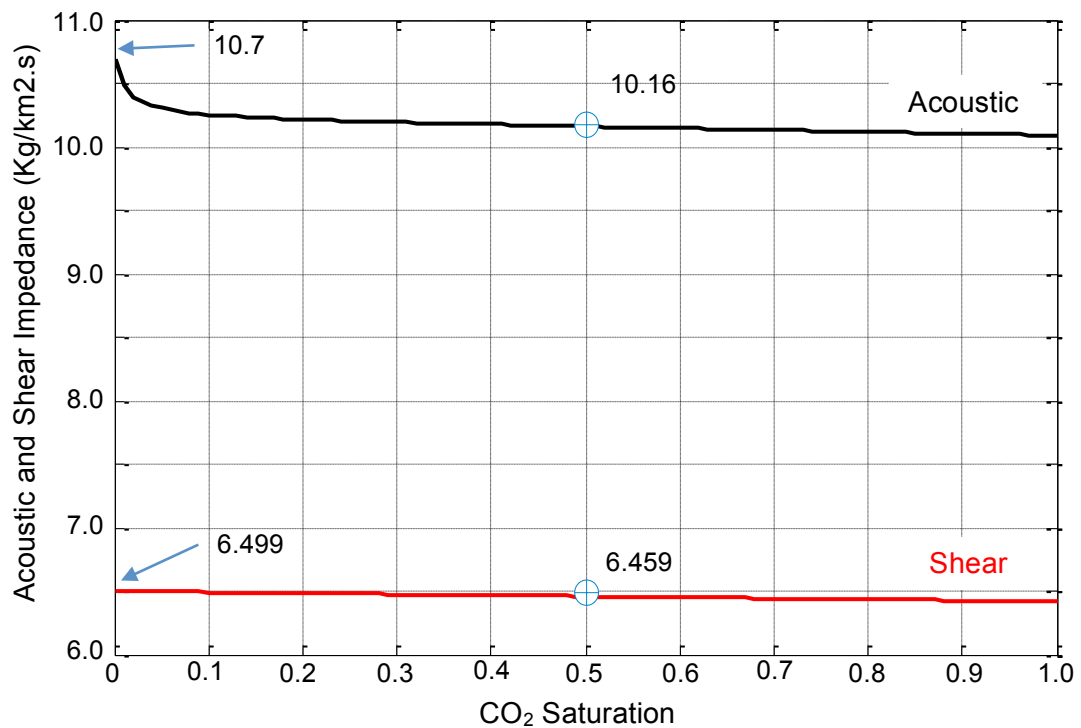


Figure 3.12: The acoustic and shear impedance changes of CO_2 saturation before and after injection into the Lesueur formation.

3.4.3 Numerical Forward Seismic Modelling

To investigate the seismic response of CO₂ injection and to image the difference in seismic sections, I chose to use finite difference modelling due to its availability and proven accuracy. I used a geological model discussed in the previous section as input to the Tesseral modelling software. The subsurface geological model is shown in Figure 3.10. In this numerical experiment, two 2D synthetic data sets were generated. These data sets were baseline for the pre-injection model and monitor for the post-CO₂ injection, based on the results described in the rock physics section (section 3.4.1). The synthetic models consisted of a series of surface shots with the receivers located both on the surface and in boreholes to simulate VSP experiments.

Before describing the numerical surface and VSP models, I will introduce some points regarding the first stage of this experiment, which was explained in the previous section. On the basis of the rock physics estimations results, the pre- and post-injection acoustic impedance (I_p) differences were around -0.540 (kg/km²*s), which is an approximately -3% change (Figure 3.12). Depending on the exact impedance change, the reflectivity for normal incident waves was approximately 0.016, which is almost 0.026% of the plume energy response. This response of reflection coefficient shows that low levels of seismic energy is reflected from the CO₂ plume. The small seismic response is mostly controlled by the effective porosity of the reservoir, which is 11%. In my modelled baseline and monitor line I investigated how the time-lapse signal can detect this small amount of energy of the reflected waves from the subsurface changes due to the injection of CO₂.

The respective volumes of the CO₂ saturated rock were calculated as in section 3.4.1, based on the pore pressure, temperature, effective porosity and saturation at the injection interval. To investigate detectability of different CO₂ plumes, I injected and modelled several CO₂ plume sizes and distributions. These variations in the CO₂ plume helped in establishing the level of CO₂ detectability. As mentioned previously, after the injection the gas saturation is assumed to be 50% CO₂ and 50% brine, with the elastic properties shown in Table 3.5. The suggested CO₂ volumes are 2, 5, 10, 20, 40 and 80 thousand tonnes of CO₂. In order to inject these volumes of CO₂ into the numerical model, the specific shape that can simulate the injected CO₂ under the surface should be identified. Since I did not perform any

fluid flow simulations, I assumed that the shape of plume is cylindrical. Even if I fix the cylindrical shape of the plume, the ratio of the cylinder thickness to diameter needs to be determined. To do so, I considered the detectability of the CO₂ plume. I expected to detect an injection of CO₂ into a deep reservoir when the diameter of the simulated plume shape is larger than the first Fresnel zone and the thickness is greater than that of the tuning thickness shape (Figure 3.13). I chose all the plume volumes to have the ratio of the thickness to diameter the same as the tuning thickness to the first Fresnel zone. Another reason for this assumption is that the thickness of the plume will increase with its volume. Moreover, the numerical modelling is expensive and thus I modelled only a limited number of plume sizes and shapes. In the finite difference model, and based on the suggested shape of plume CO₂, the injection was performed and distributed along a line with a slope given by the quotient of the first Fresnel zone and the tuning thickness. The six different volumes of CO₂ plumes and their respective rock volumes, with the dimensions, diameters and thickness, are given in Table 3.6. These variables were measured based on 50% CO₂ saturation, with pore pressure of 24.5 MPa, temperature of 70 °C and effective porosity of 11%.

Table 3.6: The calculated CO₂ plumes of six different volumes with their respective rock properties and shaping plume dimensions.

Injected CO ₂ (k tonnes)	2	5	10	20	40	80
Rock volume (10 ² m ³)	49.75	124.36	248.73	497.45	994.90	1989.8
Plume thickness (m)	3.62	4.92	6.19	7.80	9.83	12.39
Plume diameter (m)	132.24	179.48	226.13	284.91	358.97	452.27

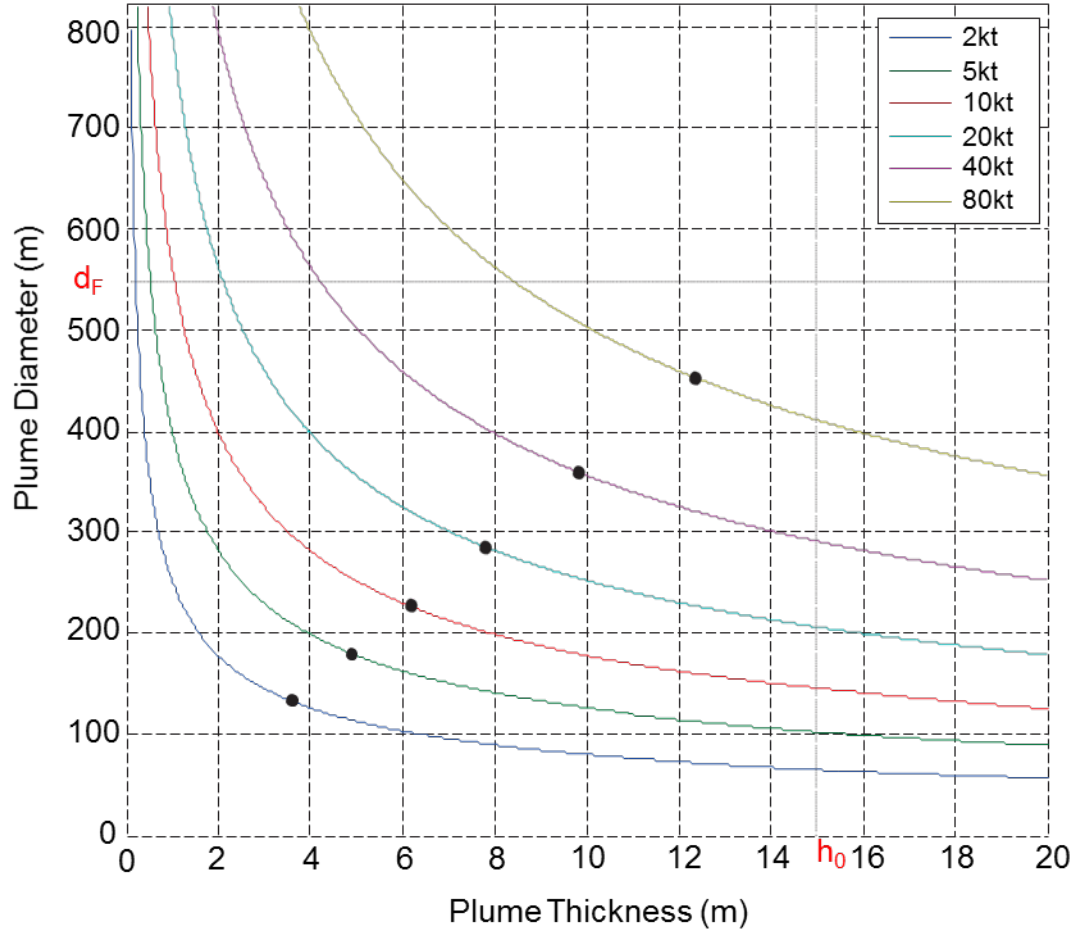


Figure 3.13: A cross-section of shape dimensions, diameters and thicknesses for the volumes of the six different plumes. The black dots show the selection of diameter/thickness pairs. The d_F indicates the diameter of the first Fresnel zone in the injection area in the Lesueur formation. h_0 refers to the tuning thickness for a wavelength of 60 m.

3.4.3.1 Quantitative Noise Analysis

CO₂ seismic monitoring is the tool used to observe time changes in seismic signals and then to help us understand the causes that contribute to these changes. These changes usually occur as a response to something in the reservoir or around it and can be attributed to, for example, CO₂ injection, seismic noise or the repeatability of the survey geometry. In my experiment, the CO₂ injection and survey

geometry were designed on the basis of the project plan and field dataset. Noise is the limiting factor in seismic monitoring of CO₂ detectability. However, the effect of noise required further investigation to study and model the relative level of noise that should apply in the finite difference model of the SW Hub area.

The most common seismic interpretation attribute used to quantify the amount of noise corresponding to the seismic signal is SNR. In the quantitative noise analysis, I estimated the amount of noise in the field data by using this technique to investigate the genuine detectability of CO₂ plumes. Since in field data I usually cannot determine the level of noise independently from the data, I need to decide which part of the data is signal and which part is noise. The usual distinction is that the signal is anything that is spatially correlated while noise is considered uncorrelated. This assumption leads to the following definition of SNR, which was established by Hatton (1986):

$$(SNR)_i = \sqrt{\frac{[g_{i,i+1}]_{max}}{1 - [g_{i,i+1}]_{max}}}, \quad 3.8$$

where $(SNR)_i$ is the signal-to-noise ratio and $[g_{i,i+1}]_{max}$ is the maximum of normalised crosscorrelation between two sequential traces i and $i + 1$ of the time window.

As mentioned above, SNR is a reliable measurement in evaluating the level of noise that is observed in seismic field data. I used this attribute to model a realistic amount of noise and then applied it to synthetic data to examine the detectability of CO₂ injection in the SW Hub area. As discussed earlier, the dataset that was selected to investigate CCS in the SW Hub was 11GA-LL2. Figure 3.14 shows that the horizontal axis is oriented east-west along the migrated section of 11GA-LL2 at the top, and the result of SNR attribute with time window length is 100 ms at the bottom. The values of SNR are presented in \log_{10} scale. The low SNR that is shown in the marked area in the west, the ‘mute zone’ of the SNR result, may be due to the subsurface geology or the surface conditions altering recorded signal levels. Therefore, in an attempt to understand this event in the west, I conducted some data

analysis with regard to the seismic line to elucidate the main reasons for this decrease in SNR before moving forward with my numerical model.

The quality control (QC) attributes, for example, the QC SNR (SNR_{QC}), were required to explain the reasons behind the variation in the SNR result that was specific to the western part of 11GA-LL2.

This QC attribute helped to divide the different couplings of the sources and receivers. Measuring the entire signal, ground roll and noise in the raw data requires separation of the source and receiver gathers into independent windows. Figure 3.15 depicts the meaningfulness of using this technique. As shown, this attribute basically analysed the raw seismic signal into three main windows; noise (including the direct arrival), ground roll and signal. I computed the QC attributes for these windows and obtained three windows. The results are represented in Figure 3.16. The windows show the mean absolute amplitude in the SNR_{QC} (signal and noise) window, in the ground roll window and in the centroid frequency (signal) window. All of these attributes were plotted versus the shot-receiver offset (station number). The SNR_{QC} dramatically increased in the common receivers gathers, as shown in Figure 3.16, while it was stable in the common source gathers. Therefore, the potential reason behind an increase in the SNR_{QC} values may be changes in near-surface conditions. As shown in Figure 3.17, the huge change in SNR_{QC} in common receivers gathers was correlated with the area of low SNR_{QC} in the western region ‘mute zone’, which is the location of the Lesueur formation. I concluded that the results of this analysis mean that any reflectors or events in this ‘mute zone’ will be hidden by a high level of noise. Moreover, this should be considered when building the SW Hub model to evaluate CO₂ detectability in the area.

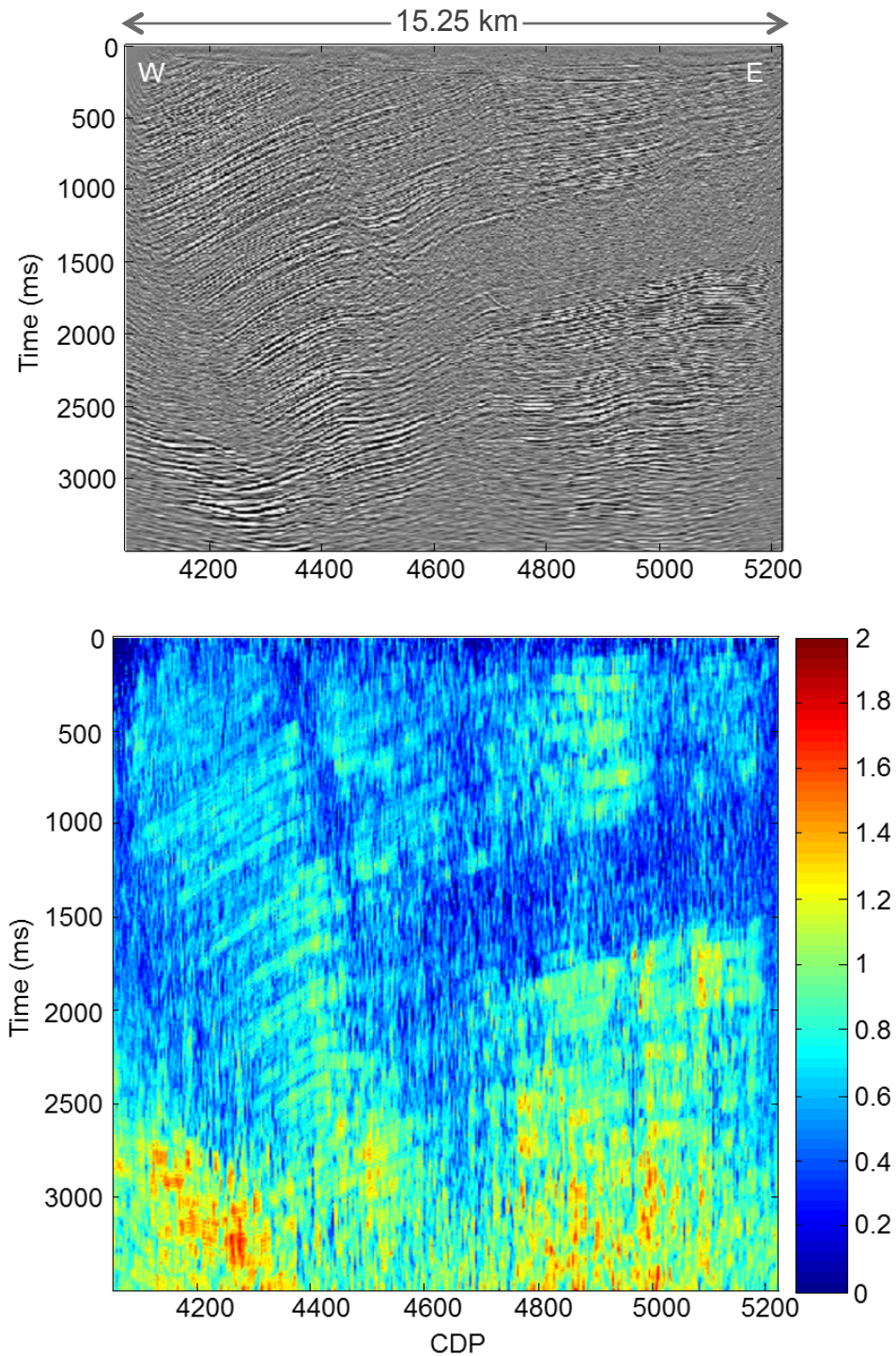


Figure 3.14: The horizontal axis is oriented east-west along 11GA-LL2 (top) and the values of signal-to-noise ratio (SNR) are shown in \log_{10} scale (bottom). The amount of noise, as shown in the SNR result, is low in the deep and that may have been caused by the source energy or the attenuation of the seismic wave. However, the unusual values that are shown in the area are in the western region—the ‘mute zone’.

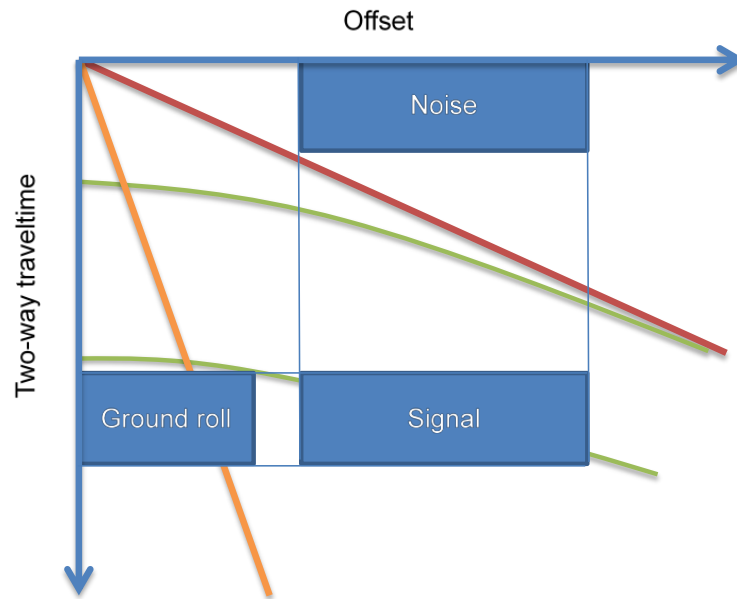


Figure 3.15: Depiction of the noise attributes analysis windows of common source and receivers gathers. The analysis windows are divided into three main windows; signal, ground roll and noise, and direct arrival. They display shot and receiver offset in the horizontal axis and two-way traveltme in the vertical axis. The red line indicates the direct arrival waves, the green curves indicate the range of reflected signals and the orange line indicates the ground roll.

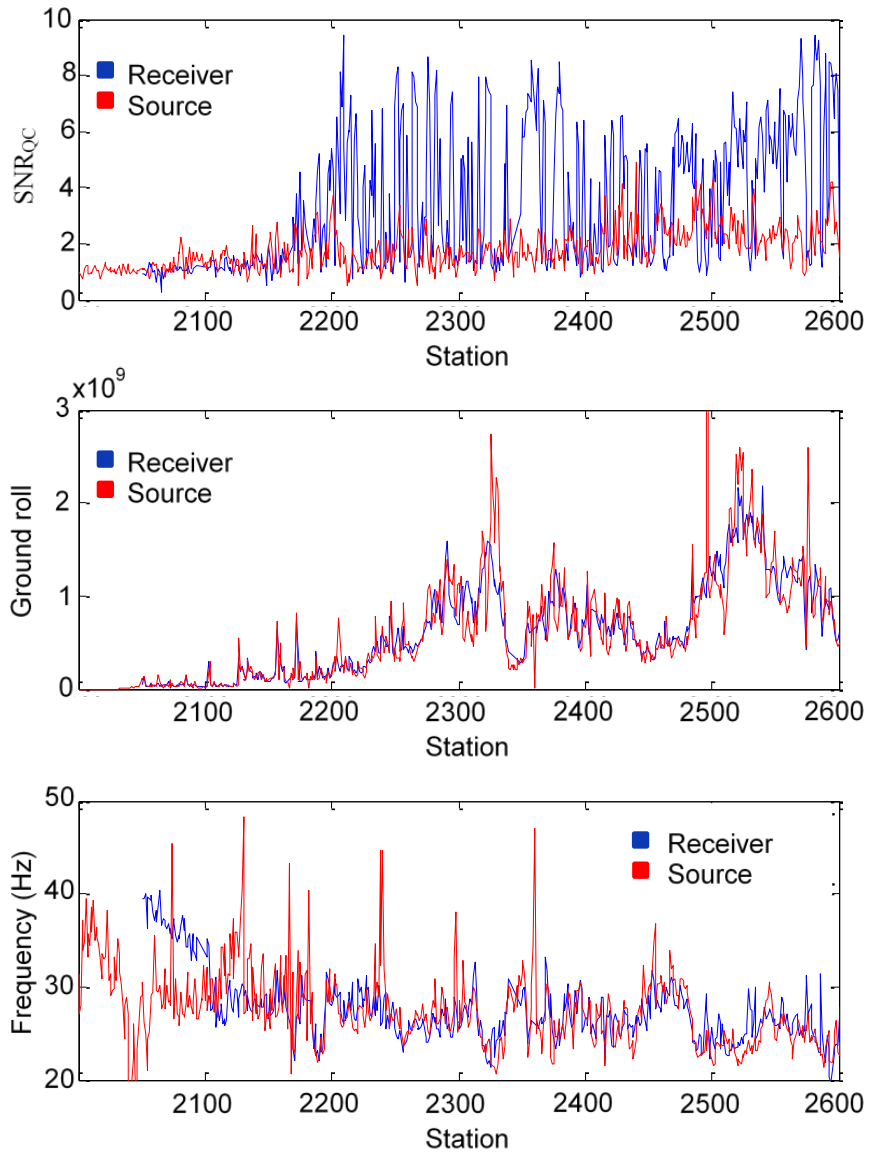


Figure 3.16: The results of the quality control (QC) attributes: the mean absolute amplitudes in ‘signal’ and ‘noise’ windows (SNR_{QC}), in the ‘ground roll’ window, and centroid frequency in the ‘signal’ window. These analysis windows are computed by using common source and receivers gathers. In the SNR_{QC} attribute, it is clear that there is a large increase in the receiver’s gathers, while the source’s gathers remain relatively unchanged.

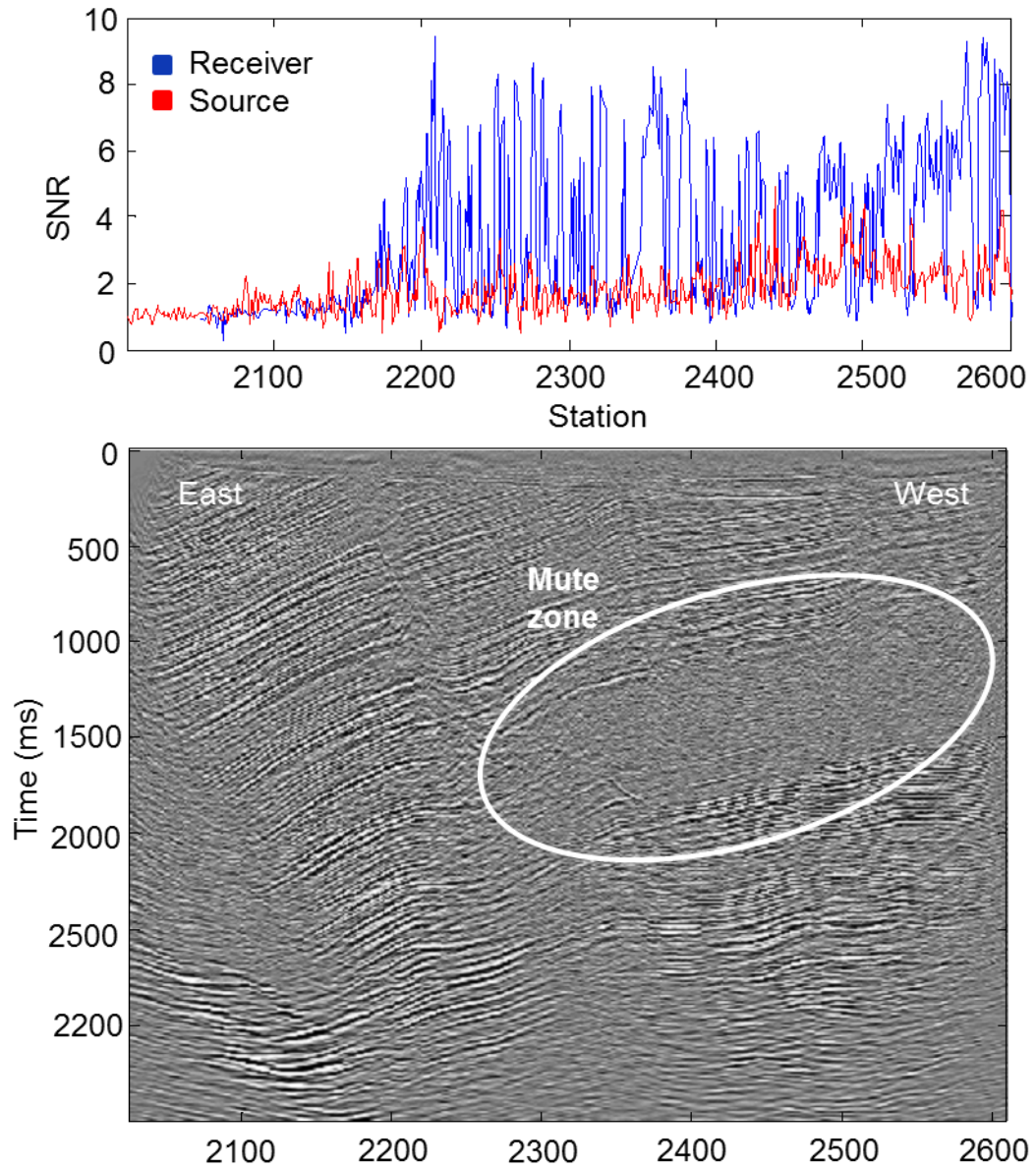


Figure 3.17: Quality control signal-to-noise (SNR_{QC}) attribute (top) and 11GA-LL2 (bottom). The horizontal axis is oriented east-west along 11GA-LL2 (top), with increasing station numbers that are related to the geometry of the seismic acquisition. The marked area on the seismic section represents the ‘mute zone’, which hides the most reflected waves and layer interfaces inside this area (the location of the Lesueur formation). In the ‘mute zone’, the SNR_{QC} attribute shows a great increase in receivers gathers, while the sources are stable without observed changes. The suggested reason behind these variations is changes in the near-surface conditions.

3.4.3.2 Surface Seismic Reflection Processing and Imaging

The finite difference model of the surface seismic was modelled on the basis of all the experiments and studies that have previously been discussed in this chapter. The layout geometry was designed to simulate the actual field survey with realistic modelling parameters (Table 3.7). The dominant frequency for the modelling results both from the typical land data and the limitations of the constraints for the finite difference modelling. The modelling was 2D elastic model with dominant wavelength namely 50Hz. The final finite difference model, including six plumes, is shown in Figure 3.18. The plumes were placed at different depths on the interface or between the layers (Figure 3.18) and others were injected inside. The positioning of the plume at the interface has two main reasons: one would expect CO₂ to accumulate at the interface of the reservoir seal and also from the point of view to study detection limit, the plume located at the interface is more obscured by the interface than the plume located within the reservoir. I simulated the six CO₂ injection volumes in one finite difference model by distributing them around the suggested injection area. The first reason for doing this is the modelling run time. Each CO₂ volume of the finite difference model requires one generation of data, which means a significant amount of time is needed to generate the data for entire volumes. Another reason for gathering all the different plumes in one model is that it is easier to compare them directly in one seismic section. The compression of the final results, which were generated by modelling the placement of the plumes in one section, meant that it was far easier to obtain genuine insight regarding CO₂ injection detectability in the SW Hub project area.

Table 3.7: The parameters of the finite difference model and other pertinent information relating to the wave propagation method.

Simulation method	Finite-difference using an explicit solution to the acoustic wave-equation
Modelling method	2D-Elastic
Source type	Omnidirectional source
Source position	Surface
Seismic wavelet	Zero phase Ricker wavelet
Frequency	50 Hz
Number of sources	141
Source interval	50 m
Number of receivers	705
Receiver interval	10 m
Sampling rate	2 ms
Minimum offset	10
Maximum offset	7000
Modelling depth	3500
The grid size (dx,dz)	1.5 m
The grid time step (dt)	0.54 ms

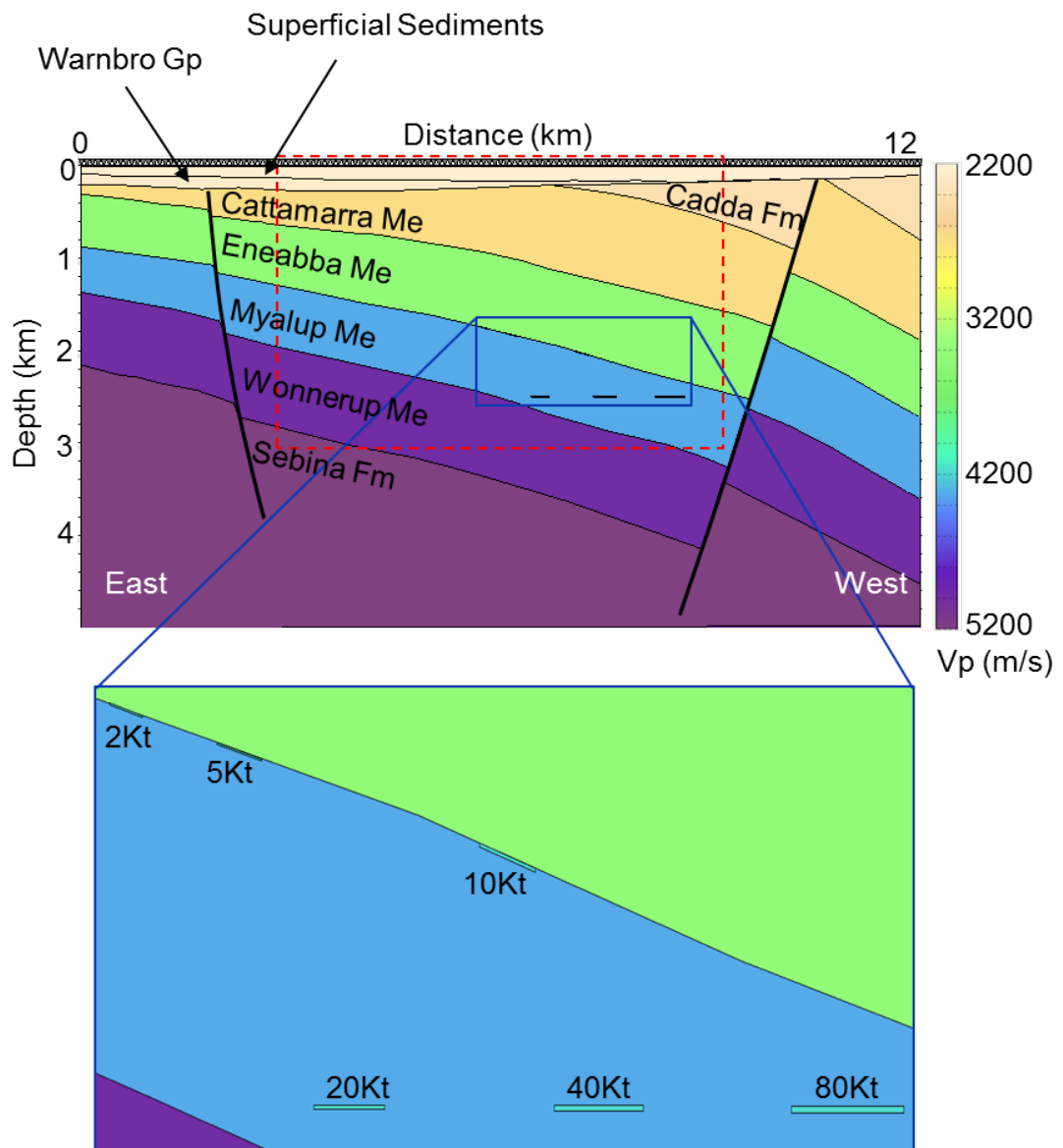


Figure 3:18: The model of the South West Hub area with six difference volumes of CO₂ plumes; 2, 5, 10, 20, 40 and 80 Kt. The model is driven on the basis of seismic line 11GA-LL2. The enlarged figure shows the locations of the suggested plumes, which are placed on the interface at the top of Myalup (the top of the Lesueur formation) and inside the formation to assess the CO₂ detectability in the plumes area and after CO₂ migration. The red dashed rectangle indicates the subset of the model, which was used to present the remainder of the work and results.

The noise-free seismic response of the model showed high detectability of the CO₂ injection for all the plumes (Figure 3.19). In this figure, the migrated sections of the red rectangle of the model are presented for time-lapse data (baseline and monitor lines) and their difference. It is clear that the CO₂ plumes that were placed on the interface or inside the layer are detectable in difference sections. Thus, this result is not sufficient to evaluate the CO₂ detectability in the SW Hub CCS; as mentioned previously, the response of the seismic signal must be simulated with a realistic noise in order to assess the genuine detectability of the CO₂ plumes.

In section 3.4.2.1, I analysed and estimated a realistic amount of noise that can be observed in 11GA-LL2. To do that, I filtered the amount of noise that was observed in the SNR result to match the frequency spectrum of real data and added the estimated real noise to the synthetic data (Figure 3.20). The figure shows histograms of the SNR of the real noise (a), synthetic noise and the high count of selected SNR value at a given time of synthetic data (c). Indeed, the addition of realistic noise to the synthetic data (Figure 3.20) was selected corresponding to the amount of noise at the interface close to the modelled plume.

The matching SNR value at the interface of the Lesueur formation was approximately 5. The CO₂ detectability was very low in the difference section after addition of the modelled realistic noise to the base and monitor lines (Figure 3.21). The large plumes of CO₂, 40 and 80 kt, were detected, but the small plumes were undetectable. The low level of seismic CO₂ detectability can be explained by the relatively low effective porosity of the Lesueur formation, which was 11% in the injection interval. Another reason behind the low detectability is that the detectability of plumes of 40 and 80 kt was in fact more visible in the monitor line than in the difference section. That is because the amount of realistic noise in the difference section was formed by combining two realisations of the modelled noise from the base and monitor lines, while the monitor line contained just one realistic model of noise. Therefore, in the real-life scenario, the plumes in the difference section will contain the same level of noise, which represents a promising opportunity to detect at least the largest amount of CO₂ undersurface, which is represented by the volume, thickness and diameter of CO₂ plume in the storage. Note that it would be difficult to detect the plumes on the monitor section in cases where the plume is located at an interface, as can be seen in Figure 3.21 for the plumes located at the interface. Also

note that one could add band-limited noise only to the difference section by suitably scaling it.

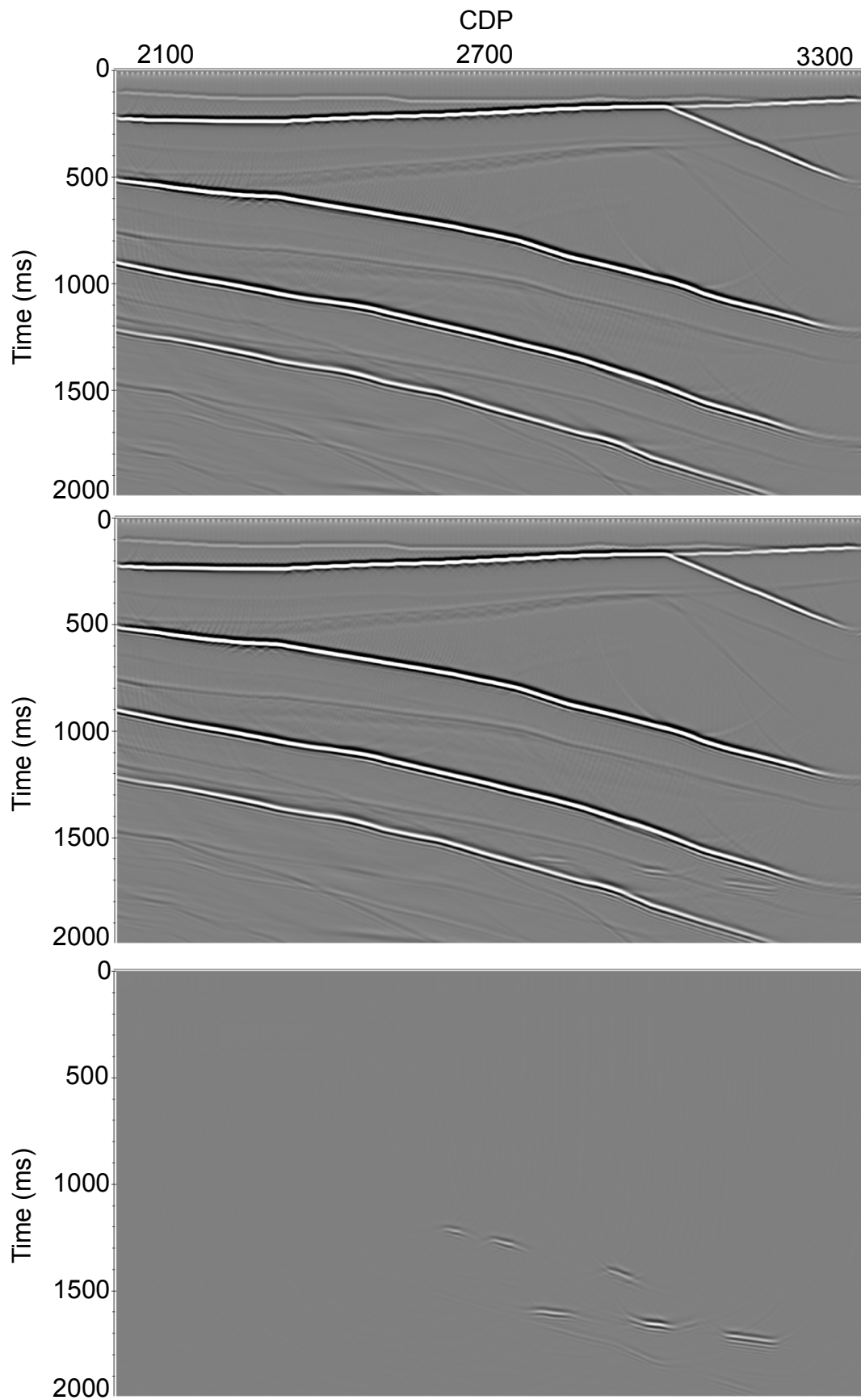


Figure 3.19: Noise-free seismic response sections of baseline, monitor line, and difference of the synthetic data. The six CO₂ plumes are clearly detectable in the

difference section. Realistic noise should be modelled and added to evaluate the detectability of CO₂.

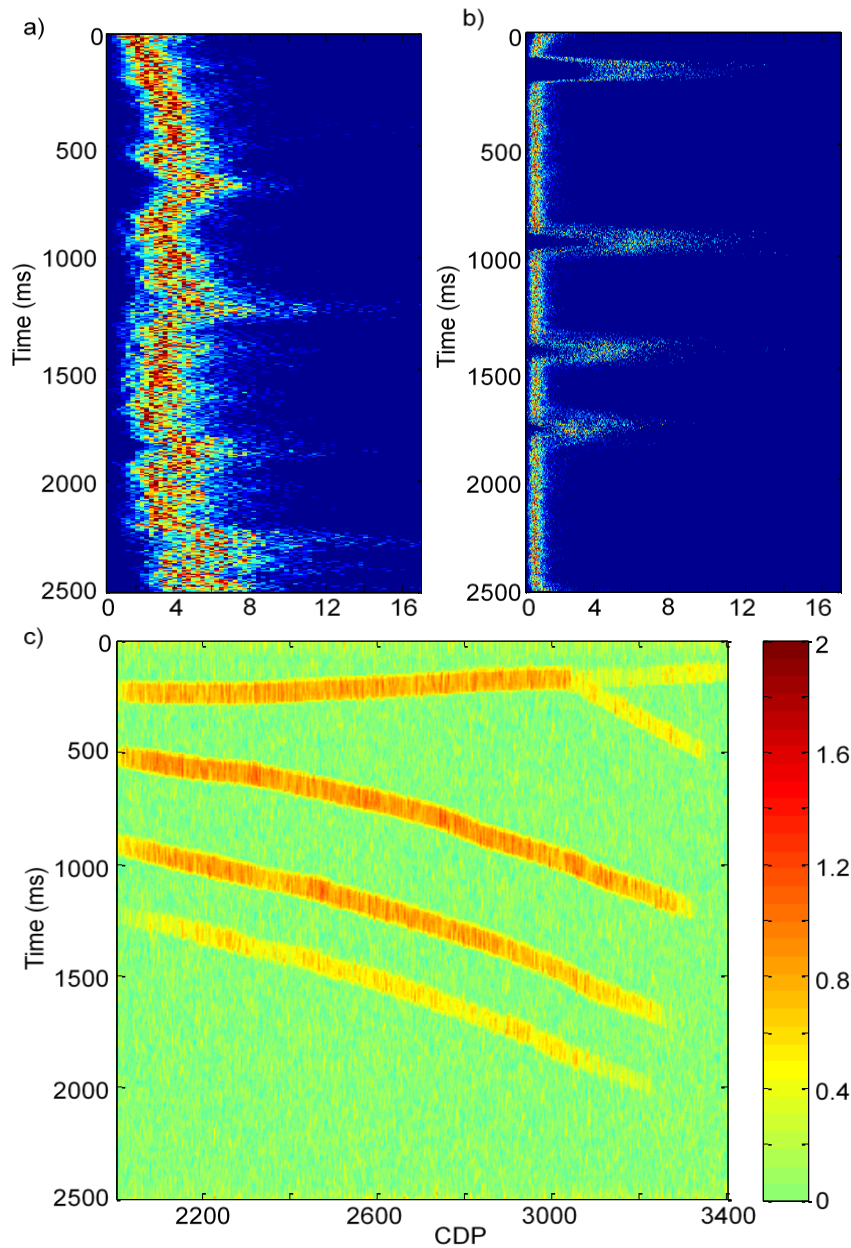


Figure 3.20: The signal-to-noise ratio (SNR) histograms for (a) real and (b) synthetic sections, according to the modelled injection location. A high SNR count is shown on the interface layers of synthetic data at the given time. (c) The synthetic section of the SNR result is shown with a log₁₀ scale. The amount of noise that was added approximately a SNR of 5 to match the measured SNR at the reflector corresponding to the interface between the formations of the finite difference model of the Eneabba Me and Myalup formations.

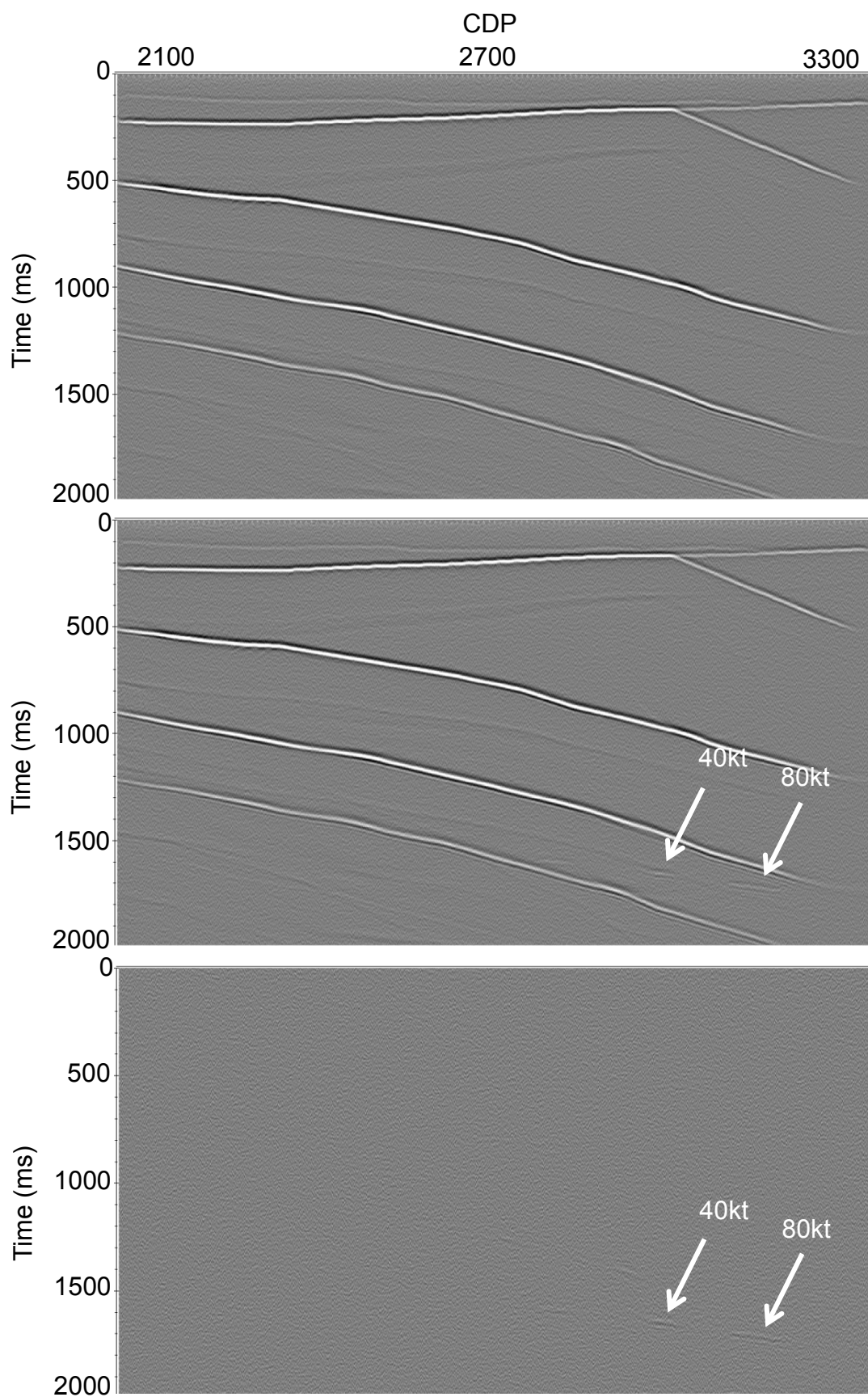


Figure 3.21: The results of the migrated baseline, monitor line and difference

synthetic section, with added filtered realistic noise. The CO₂ detectability is low in the difference section. The detectability of the plumes is higher in the monitor section than in the difference section. That is because the difference section contains noise from both the monitor and baseline surveys, while the monitor only contains one realistic noise. However, plumes located at an interface would not be visible in the monitor section.

3.4.3.3 Vertical Seismic Profiling

Another seismic survey technique that has been suggested for evaluation of the seismic monitoring of the SW Hub CCS is VSP, using either traditional well geophones or via burying numerous permanent geophones in the subsurface.

This approach was modelled by installing permanent receivers inside several wells of different depths. The previously described 2D finite difference model was utilised to model this geometry, but by using vertical wells to place the receivers instead of the surface layout geometry. Many potential benefits are promised by using the permanently installed receivers:

- Increasing the value of SNR that is affected by surface-related noises.
- Decreasing the problems that are related to time-lapse acquisition changes and that cause the weakness of time-lapse repeatability.
- Reducing the impact of time-lapse repeating surveys on land owners and communities around the field.

The advantages emphasise further motivation to model the VSP surveys with permanently installed receivers in order to provide sufficient CO₂ detectability in the SW Hub project.

I modelled six wells (w1, w2, w3, w4, w5 and w6) and placed them at intervals of 1000 m in the previous surface 2D finite difference model, with six CO₂ plumes (Figure 3.22). The wells are located from left (west) to right (east) with different depths, 2 and 3 km. I chose these deep wells in order to be able to simulate acquisition geometries with varying well depths. The receivers' depth interval in the

wells is 10 m and the sources surface interval is 50 m. The modelling parameters, with further details of the wave propagation method, are presented in Table 3.8.

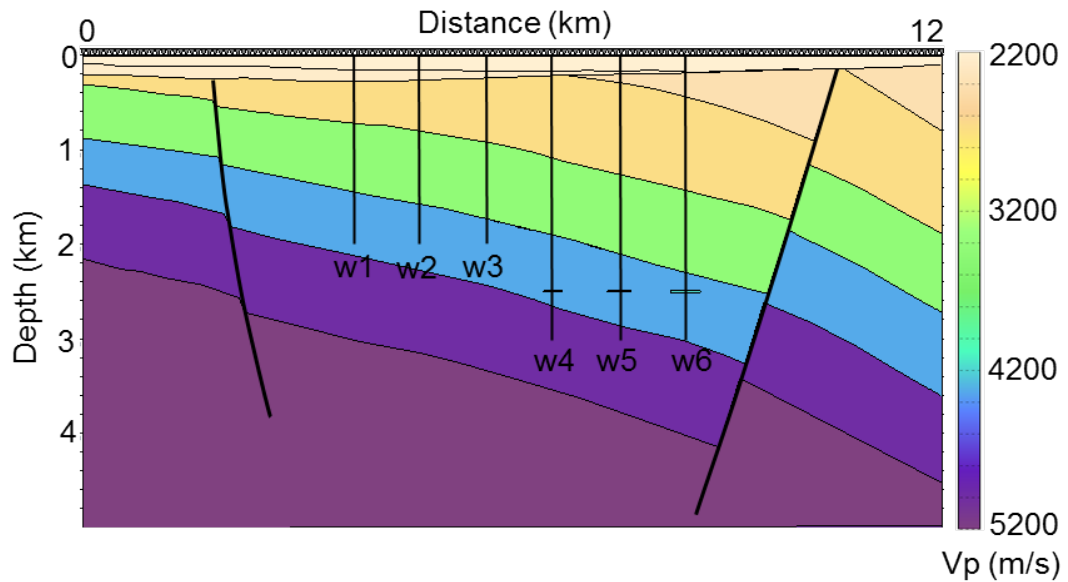


Figure 3.22: The distribution of the CO₂ plumes within the model. The location of the six plumes is distributed in the Myalup formation as show in figure 3.18. The black vertical lines indicate the location of the modelled monitoring and/or injection wells. The grid size is 0.5 km×0.5 km.

Table 3.8: The parameters of the finite difference model and other pertinent information relating to the wave propagation method.

Simulation method	Finite-difference using an explicit solution to the acoustic wave-equation
Modelling method	VSP-elastic
Source type	Omnidirectional source
Source position	Surface
Seismic wavelet	Zero phase Ricker wavelet
Frequency	50 Hz
Number of sources	141
Source interval-surface	50 m
Number of receivers	705
Receiver interval - depth	10 m
Sampling rate	2 ms
Number of wells	6
Surface location of wells	21,41,61,81,101,121 m
The wells depth	2000 m (wells 1,2,3) and 3000 m (wells 4,5,6)
The grid size (dx,dz)	1.5 m
The grid time step (dt)	0.54 ms

The noise-free seismic response of the zero-offset (100 m offset) VSP model shows a good detectability of the CO₂ injection for all plumes in all wells. An example of this can be seen in Figure 3.23 for well 6 and Figure 3.24 for well 5, which show the migrated sections of VSP time-lapse data at baseline and monitor lines and their difference. Kirchhoff migration with an aperture of 10 degrees was performed in the imaging processing, based on an assumption of a reflector dip of 10 degrees. The difference section is approximately 10% of the baseline amplitude main reflector (Figure 3.24). As a result, the CO₂ plumes on the interface are hidden by the strength of the reflected wave and they are only detectable in the difference section in the VSP model. Figure 3.25 shows the enlarged plume zone in migrated, monitored and difference sections of well 5, which were achieved by utilising all well depth receivers ranging between 50–2950 m. An example of the detectability in the difference section is shown, as well as how the plumes on the layer interface are covered by the strong amplitude of the reflected wave in the monitor section. Unfortunately, there is no VSP field data in SW Hub area to estimate the SNR, therefore, the test for modelling time-lapse noise is not possible. Regardless, the CO₂ plume will be only detectable in the difference section, due to the reflector strength in the monitor line.

The last experiment for use in VSP modelling to investigate the detectability of CO₂ injection is walkaway VSPs. It is crucial to note that in ordinary processing of walkaway VSPs, a very large offset is not practical. However, for difference sections the use of large offsets might be beneficial as the issues associated with the long offsets are repeatable and will subtract out. In this investigation I conducted the walkaway VSPs experiment, but with a slight change in the main model to achieve some goals associated with the drilling cost of the SW Hub project. I studied the effect of decreasing depth on result quality. That was achieved by decreasing the depth of some the wells and limiting the range of receivers in the modelled data, and then comparing the results of the deep and shallow wells. The monitoring wells depth was approximately 3000 m, 1000 m and 500 m. The results of plume detection for these varied well depths are shown in Figure 3.26. The migration results present a very slight change in the degradation quality between the depths, which is irrelevant compared to the advantage to well-drilling costs of reducing the depth. To this end, the permanent installation of receivers based on these results can be mapped as a

relatively dense array of shallow wells of between 500 m and 1000 m in depth, as supported by Figure 3.26.

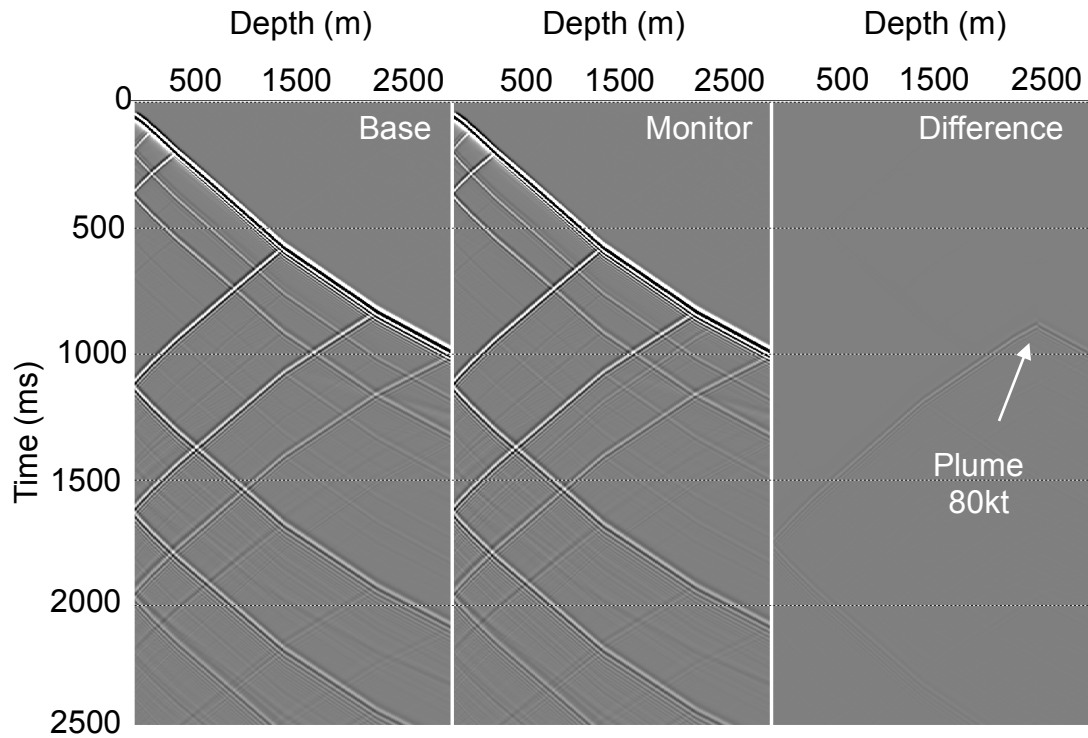


Figure 3.23: The well six VSP zero-offset (100 m offset) noise-free sections for baseline, monitor line and difference. In VSP modelling, the plumes are detectable because they are not placed on the interface. Therefore, any modelled plumes placed on the interface will be covered by the strength of the interface reflected wave. Here, the plume seismic response is apparent in the difference section, which is indicated by the arrow.

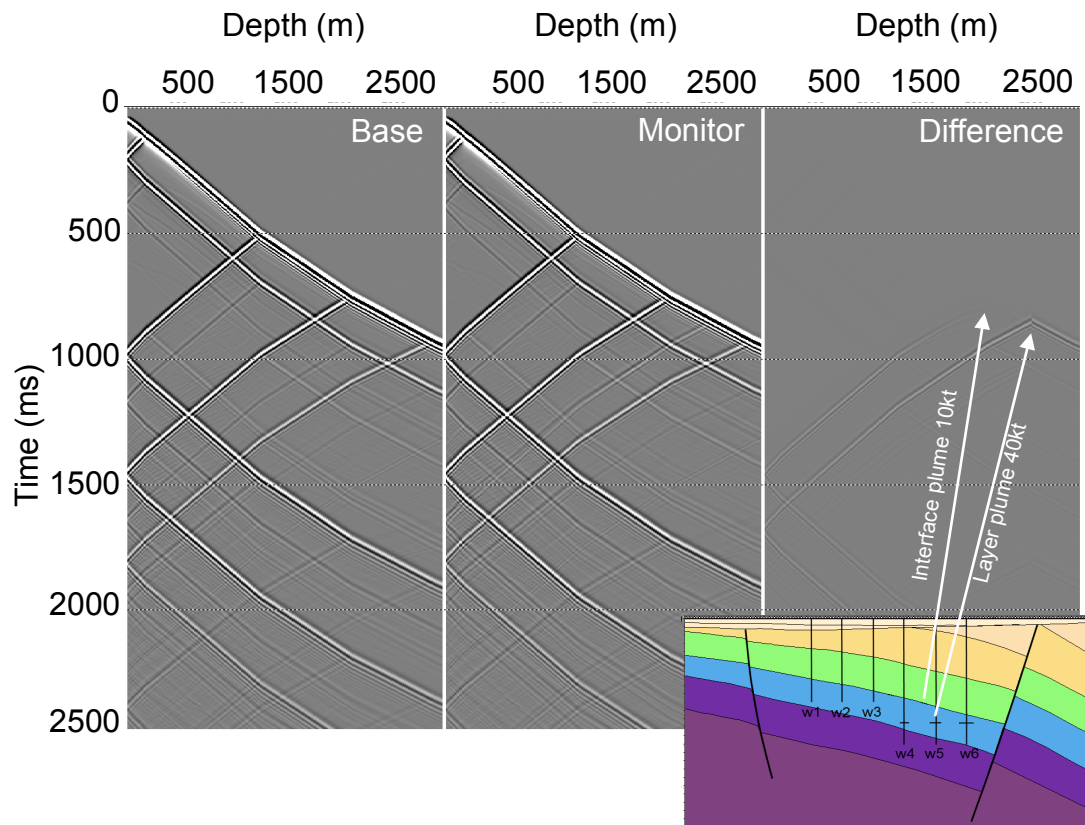


Figure 3.24: The well five VSP zero-offset (100 m offset) noise-free sections for baseline, monitor and difference. Again, the CO₂ detectability is high in the difference section and low in the monitor section, due to the reflected wave strength. The arrows indicate the locations of the injected CO₂ on the interface and inside the layer in the difference section.

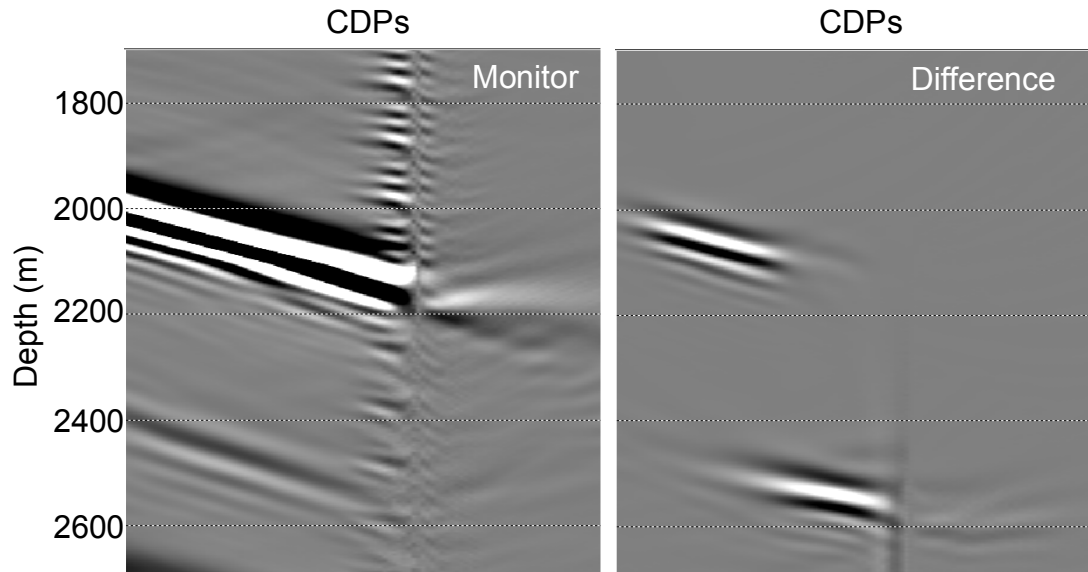


Figure 3.25: The zoom plume location of the migrated VSP zero-offset (100 m offset) noise-free migrated monitor and difference sections of well five. The amplitude of the difference signal is only approximately 10% of the amplitude of the reflector in the monitor section.

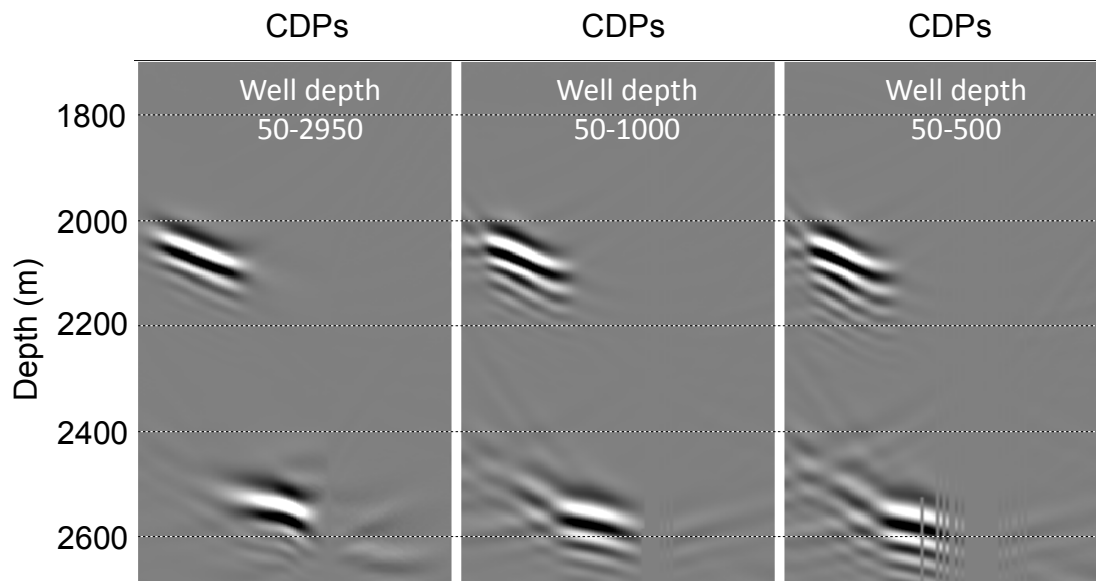


Figure 3.26: The enlarged plumes zone of the walkaway VSP migrated difference sections for receiver depth ranges of 50–2950 m, 50–1000 m and 50–500 m. The source-offset range is ± 1500 m. These results show a very slight change in the degradation quality between the depths. This change is considered irrelevant if we compare the advantage of the well-drilling cost between shallow and deep wells.

3.5 Conclusion

In this chapter, I presented a feasibility study to evaluate the use of time-lapse seismic methods in CO₂ monitoring and verification in the Lesueur formation in the SW Hub project. I utilised the available seismic datasets in the area as the basis of modelling many numerical models of the SW Hub area sub-surface. There were six 2D seismic lines available from the area. The line 11GA-LL2 was chosen to use in this seismic time-lapse monitoring feasibility study. Many geological and lithological reports were used to make the model more realistic. The estimation of effective porosity was calculated from the log data from the well Lake Preston 1 in the lower Lesueur sandstone formation at a depth of 2500 m and is given 11% effective porosity. The properties of a CO₂ saturated reservoir were simulated by applying the Gassmann fluid substitution, while to calculate the velocities and densities of subsurface geological layers, I used the mudrock line and Gardner's empirical relations.

Two numerical forward models, surface and VSP, were modelled to investigate the detectability of six CO₂ plumes located on the interface of, and inside, the Lesueur formation. Time-lapse seismic baseline and monitor data after CO₂ injection were acquired and processed for these models. In the case of noise-free time-lapse, the difference migration sections show a high detectability for all plumes. Realistic noise modelling was generated by adding band-limited random noise with SNR obtained from the field data and using a series of quality control analysis tools. The 'mute zone', which is apparent in the western part of the seismic section, hides the Lesueur formation interfaces and may be related to near-surface condition changes. The noise model was applied in the base and monitor migrated data. The difference section, including modelled noise, showed a low detectability, particularly with regard to the small plumes; 2, 5, 10 and 20 kt. The large plumes, 40 and 80 kt, were detectable in both the difference and monitor sections, but they were more visible in the monitor section due to the fact that they were not located on the interface. That indicates that the modelled noise, which was added in the base and monitor sections, all combined in the difference section. Therefore, the noise level in the difference, which hides the most plumes, appears higher than as presented in the individual base or monitor sections.

The VSP numerical forward model was another experiment to assess CO₂ time-lapse seismic monitoring by using permanent seismic receivers arrays. I used the same base and monitor model as was generated in the surface finite difference model. Six wells were placed in the model at intervals of 1000 m. The wells were located from left (west) to right (east) with different depths of 2 and 3 km. In normal time-lapse monitoring, the plumes should be detectable in both the monitor and difference sections. Here, in the noise-free result, the plumes were detectable in only the difference section for the entire wells, which were specifically placed on the formation interface. This is because the amplitude of the signal in the difference section was approximately 10% of the amplitude of the main reflector in the baseline section. Therefore, the CO₂ plumes on the interface were hidden by the strength of the reflected wave and, as a result, they were only detectable in the difference section in the VSP model. As mentioned, in the surface model, modelling time-lapse noise is unworkable here due to unavailability of real VSP data.

The VSP survey will be significantly useful in solving the variations in the near-surface condition and helpful in interpretation. Designing a walk-away VSP geometry with shallow wells and a large offsets will give a good and sufficient detectability for CO₂ seismic monitoring.

In this chapter, I evaluated the seismic signal detectability for CO₂ monitoring in the SW Hub project by following several steps. First, I identified the noise level in real data from the area. Second, I modelled different injection scenarios and monitoring geometries (surface and VSP), added the expected amount of noise and then examined the seismic detectability of the CO₂ plumes. To create a realistic finite-difference model for several volumes of CO₂ plumes, I simulated the rock physics properties of the CO₂ saturated reservoir from expected brine salinity, CO₂ temperature and pressure. In this evaluation, I utilised six 2D seismic field data lines, which were processed and migrated by an Australian seismic exploration company Velseis Pty. Ltd. The high repeatability of time-lapse surveys in the base and monitor lines after CO₂ injection will be most helpful in obtaining high detectability of CO₂ plumes and decreasing time-lapse noise. Moreover, the high repeatability survey will be significantly supportable in solving the variations in the near-surface condition and helpful in interpretation.

3.6 References

- Annetts, D., J. Hauser, J. Gunning, B. Gurevich, A. Bona, R. Pevzner, B. Harris, M. Urosevic, M. Alajmi, and J. Cant, 2012, A deployment strategy for effective geophysical remote sensing of CO₂ sequestration: Final report.
- Benson, S. M., B. Li, M. Krause, S. Krevor, C.-W. Kuo, R. Pini, and L. Zuo, 2012, Investigations in Geologic Carbon Sequestration: Multiphase Flow of CO₂ and Water in Reservoir Rocks Annual Report 2012.
- Caspari, E., T. M. Müller, and B. Gurevich, 2011, Time-lapse sonic logs reveal patchy CO₂ saturation in-situ: *Geophysical Research Letters*, **38**, L13301.
- Castagna, J., M. Batzle, and R. Eastwood, 1985, Relationships between compressional-wave and shear-wave velocities in clastic silicate rocks: *Geophysics*, **50**, 571-581.
- Crostella, A., and J. Backhouse, 2000, Geology and petroleum exploration of the central and southern Perth Basin, Western Australia: Geological Survey of Western Australia.
- Dance, T., and S. Tyson, 2006, Geological reservoir characterisation and modelling of the offshore Perth Basin.
- Gardner, G., L. Gardner, and A. Gregory, 1974, Formation velocity and density—the diagnostic basics for stratigraphic traps: *Geophysics*, **39**, 770-780.
- Hashin, Z., and S. Shtrikman, 1962, A Variational Approach to the Theory of the Effective Magnetic Permeability of Multiphase Materials: *Journal of Applied Physics*, **33**, 3125-3131.
- Iasky, R., and A. Lockwood, 2004, Gravity and magnetic interpretation of the Southern Perth Basin, Western Australia.
- Iasky, R. P., 1993, A structural study of the southern Perth Basin, Western Australia: Geological Survey of Western Australia.
- IPCC, 2005, IPCC special report on carbon dioxide capture and storage: Cambridge University Press.
- Johnson, D. L., 2001, Theory of frequency dependent acoustics in patchy-saturated porous media: *Journal of the Acoustical Society of America*, **110**, 682-694.
- Lemmon, E., M. McLinden, S. Klein, and A. Peskin, 2012, "Thermophysical Properties of Fluid Systems" in NIST Chemistry WebBook, NIST Standard Reference Database Number 69: Linstrom and W.G. Mallard, National

Institute of Standards and Technology, Gaithersburg MD, 20899, <http://webbook.nist.gov>, (retrieved May 12, 2012).

Mavko, G., T. Mukerji, and J. Dvorkin, 2009, The rock physics handbook: Tools for seismic analysis of porous media: Cambridge University Press.

Smith, T. M., C. H. Sondergeld, and C. S. Rai, 2003, Gassmann fluid substitutions: A tutorial: *Geophysics*, **68**, 430-440.

Stalker, L., S. Varma, D. Van Gent, J. Haworth, and S. Sharma, 2013, South West Hub: a carbon capture and storage project: *Australian Journal of Earth Sciences* 60, no. 1 (2013): 45-58.

Varma, S., J. Underschultz, T. Dance, R. Langford, J. Esterle, K. Dodds, and D. van Gent, 2009, Regional study on potential CO₂ geosequestration in the Collie Basin and the Southern Perth Basin of Western Australia: *Marine and Petroleum Geology*, **26**, 1255-1273.

Wood, A. B., 1955, A Textbook of sound: THE PHYSICS OF VIBRATIONS: Bell and Sons.

CHAPTER 4: QUANTIFYING TIME-LAPSE SEISMIC SIGNAL DETECTION FOR CO₂ MONITORING AND VERIFICATION AT THE CARBONNET PROJECT (GIPPSLAND BASIN)

4.1 Introduction

The CarbonNet Project is one of the Australian CCS projects and is located in south-eastern Australia in an east-west trending rift basin, which is called the Gippsland basin (Figure 4.1). The Gippsland basin is one of the earliest Australian oil production fields and is the first onshore field explored during the 1920's with production starting in the 1960's (Gibson-Poole et al., 2006). There are many depleted hydrocarbon reservoirs and others deep saline formations in the Gippsland basin, which are suggested to be used for CO₂ Storage (Gibson-Poole et al., 2006). However, the Latrobe group, which is located offshore of the Gippsland basin and has a conventional reservoir seal, is nominated for the CarbonNet CCS Project.

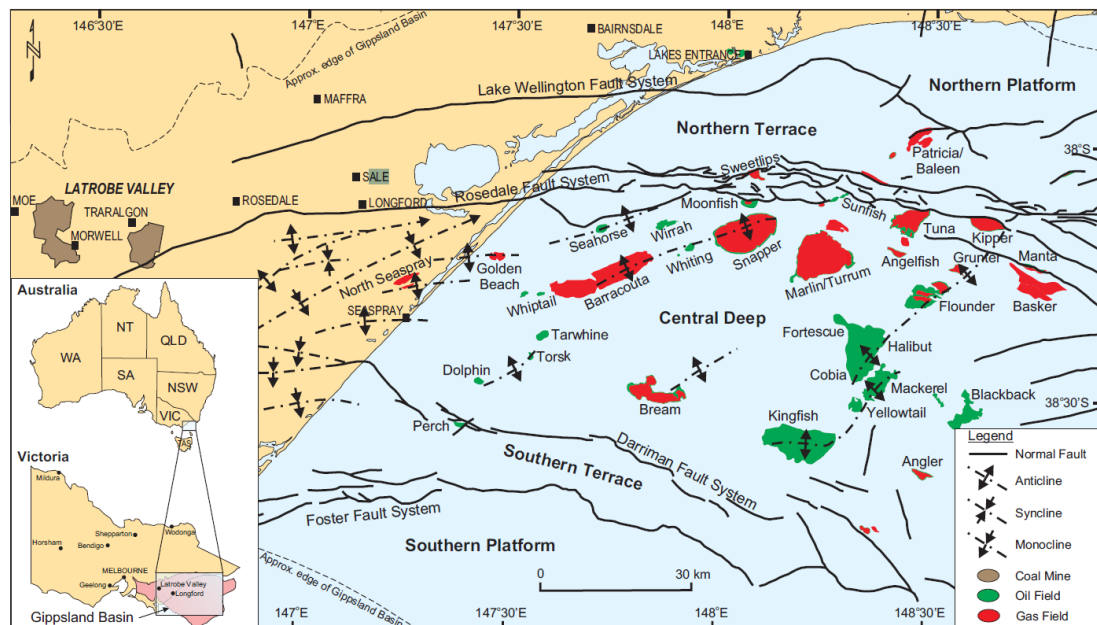


Figure 4.1: Map showing the location of the CarbonNet project for CO₂ capture and storage. The location of the project in the south-east of Australia in the Gippsland basin, which represents the major tectonic elements in the area and the oldest produced hydrocarbon fields in Australia (after Power, Hill, Hoffman, Bernecker and Norvick, 2001).



Figure 4.2: The map of the Gippsland basin, which extends onshore and offshore of the south-east of Australia. The oil and gas field spreads throughout the basin. The offshore depleted fields are suggested for use in investigating CO₂ geosequestration for the CarbonNet project (Geoscience Australia, 2013).

4.2 Study Area and Geology

The wide Gippsland basin extends from onshore in the Mornington Peninsula from the west to the Gippsland Rise offshore to the east. This extension is roughly one-third onshore and the rest offshore in a water depth of between 100 m near the shore to 4 km in the deepest point of the basin offshore (Figure 4.2). The basin is bounded in the north and the south by faulted terraces—the Northern Terrace and the Southern Terrace, respectively (Figure 4.1).

According to the geological studies, the Gippsland basin was formed during the early Cretaceous by the breaking up of Gondwana in the southern margin of Australia (Holdgate et al., 2003), (Figure 4.3). The earliest sediments of the Latrobe group were deposited in the late Cretaceous. These sequences of depositions in the basin from early Cretaceous to Neogene were bounded under the Tasman Sea by angular unconformities (Gibson-Poole et al., 2006). Several unconformities and disconformities were deposited from the Palaeocene to Eocene along the shoreline as a range of interbedded of sandstone, shale and coal (Rahmanian et al., 1990). The

upper Latrobe Group consists of a complex sedimentary sequence. The angular Latrobe unconformity was deposited at the top of these unconformities and formed the transition from Eocene to Oligocene (the Latrobe Group to the Seaspray Group) (Figure 4.3). Afterwards, a compressional period from Latest Eocene to Middle Miocene formed a wide range of hydrocarbon traps of anticlines and other structures in the northern trend (Gibson-Poole et al., 2006). Beneath the Lake Entrance formation seal, the coarse clastic top of the Latrobe group trapped up to 90% of the oil and gas produced there (Driscoll, 2006). Figure 4.3 shows a stratigraphic column summary of the Gippsland basin onshore and offshore with a description of the age sequence of the geological units.

The potential for CO₂ storage onshore in the deep depleted reservoirs or saline formations has been evaluated by (Driscoll, 2006). In his study, he recommends that the suggested undersurface formation for CO₂ geosequestration is the Latrobe Group. However, the Latrobe Group is sealed by the very shallow Lakes Entrance formation of the Seaspray Group at a depth 800 m, which makes a potential injection less desirable (Driscoll, 2006). The offshore of the Lakes Entrance Formation support the potential of CO₂ geosequestration with a good lithological seal consisting of glauconitic, slightly calcareous and mud-rich sediments at depth more than 1000 m and average thickness 390 m (Gibson-Poole et al., 2006).

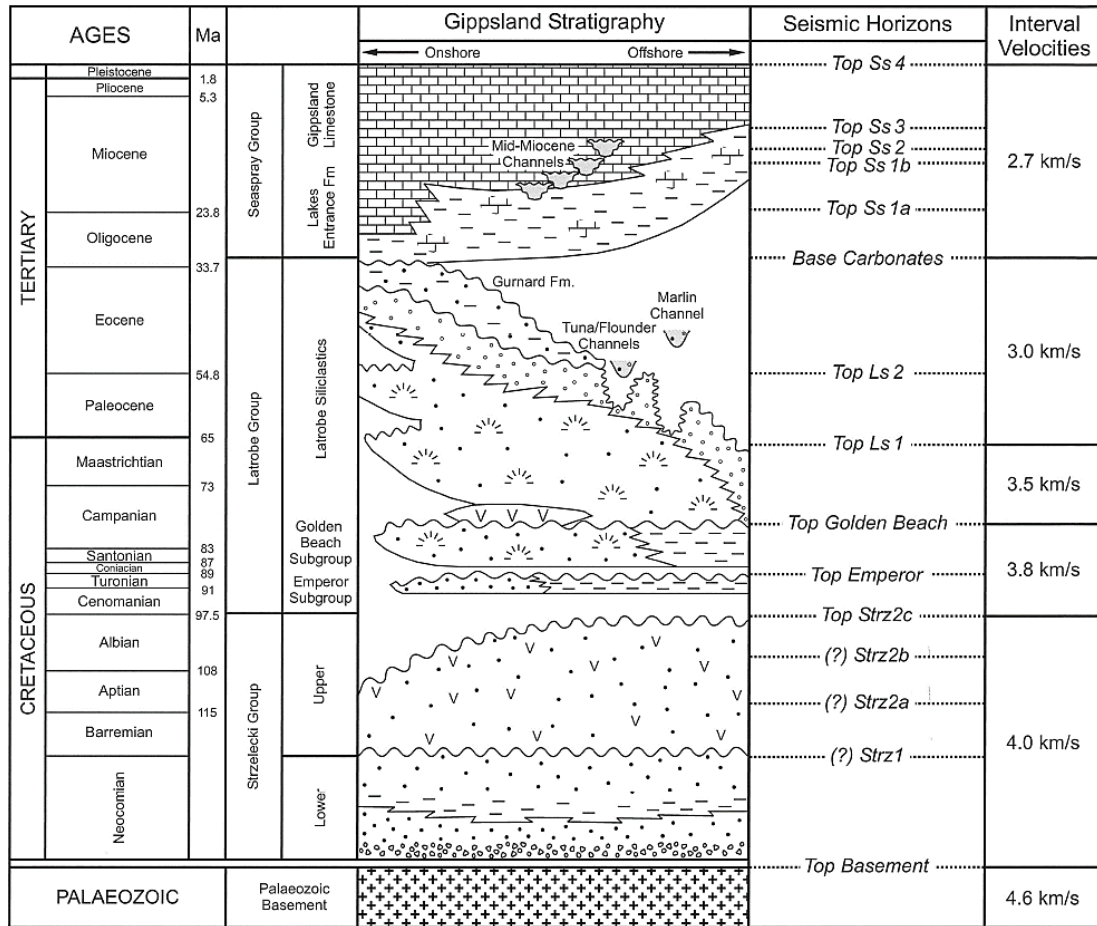


Figure 4.3: Stratigraphy column of Gippsland onshore and offshore (after Power, Hill, Hoffman, Bernecker and Norvick, 2001).

4.3 Data and Site Characterisation Approach

As mentioned previously, the Gippsland basin extends from onshore to offshore and covers approximately 56,000 km². The offshore part of the Gippsland basin is covered by roughly 100 m of water in the oil and gas producing area. The basin is one of the most productive oil and gas fields in Australia and is a mature hydrocarbon basin (Driscoll, 2006). Recently, many offshore 2D and 3D seismic lines were acquired to cover more than 80,000 km² of the Gippsland Basin with approximately 300 drilled wells within the area (Bernecker et al., 2006). Many of these oil producing fields have been depleted and are now ready to be used for CO₂ storage.

By evaluating most of these data, I found an appropriate seismic line that could serve as basis for a realistic finite-difference model for the CarbonNet project for CCS; this line is G92A-3000 (Figure 4.4). One of the reasons behind choosing this seismic line for a feasibility study was its use in many previous studies and

interpretation models of the area. The line is intersected by logged well Kyarra-1 (Figure 4.5). This line was used as a base to interpret and construct the geological model in order to investigate the CO₂ detectability.

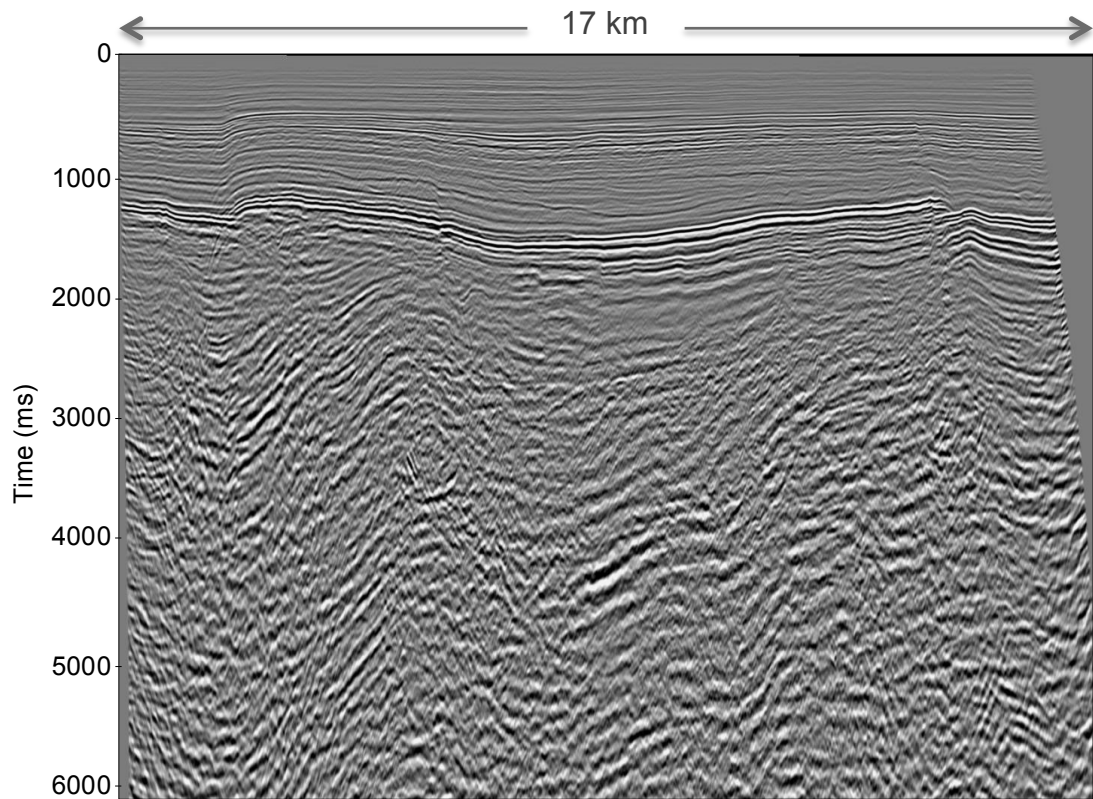


Figure 4.4: Seismic section G92A-3000, the basis of a 2D geological model to assess the CO₂ detectability for the CarbonNet project.

Many of the depleted hydrocarbon reservoirs and other deep saline formations in the Gippsland Basin were suggested for use as CO₂ storage (Root et al., 2004). One of these suggested locations, shown in Figure 4.6, was modelled based on the seismic line GGS185B-17a in nearshore Gippsland. This model simulates CO₂ injection into the Latrobe Group, which is sealed by the Seaspray Depression. The location of this interpreted line is near the seismic line G92A-3000, which will help with my interpretation of this line. Moreover, other geological models were interpreted and constructed by Moore and Wong (2002) and Power et al. (2001) based on many seismic lines (Figure 4.7) These previous works are most helpful for constructing a realistic geological model of this area (Figure 4.7).



Figure 4.5: The location of seismic line G92A-3000 shown in red, the line GGS185B-17a shown in yellow and the intersection well, Kyarra-1. The line GGS185B-17a is used as guide in constructing the geological model of G92A-3000 for the CarbonNet project.

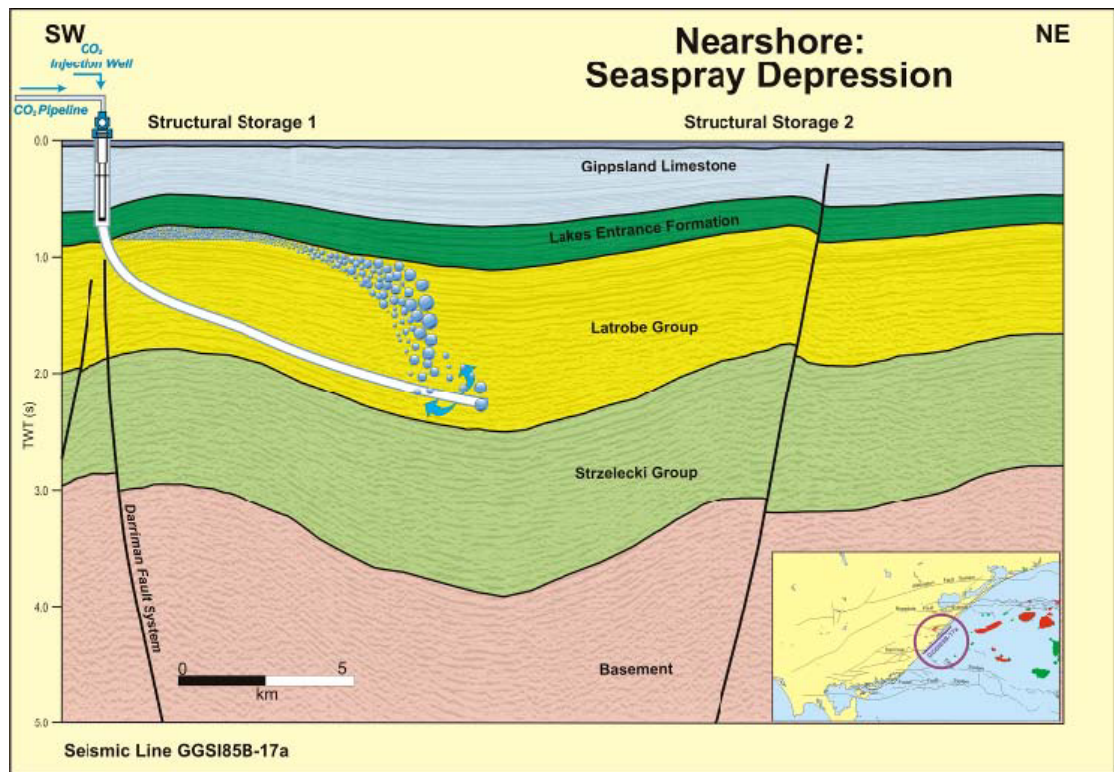


Figure 4.6: The Nearshore Gippsland concept for CCS of CarbonNet project. This simulation is a one of several opportunities that are suggested by Gibson-Poole et al., (2006).

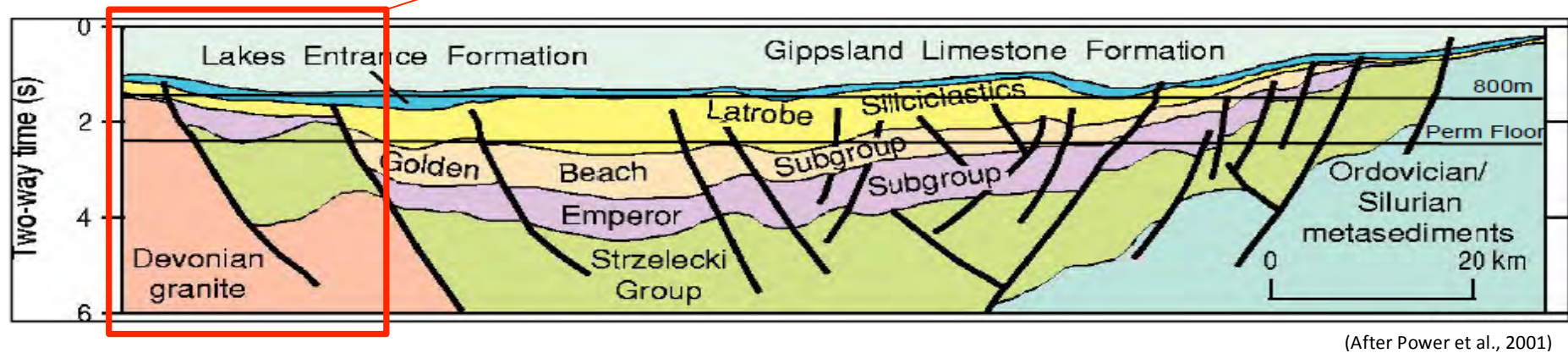
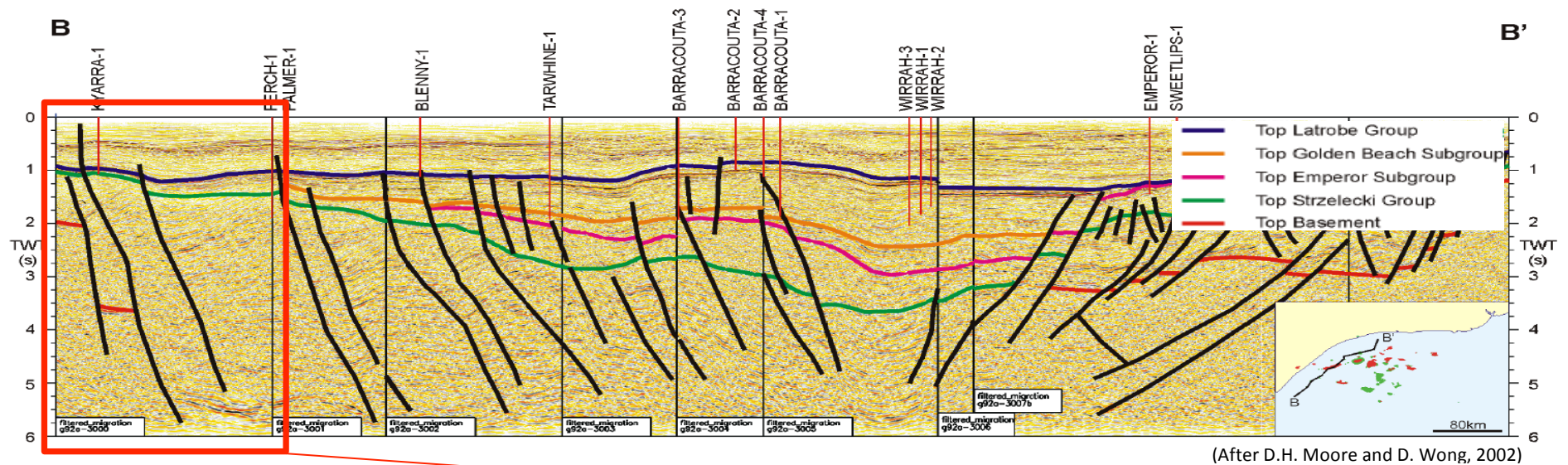


Figure 4.7: Two examples of seismic lines interpreting the geological structure in the onshore Gippsland Basin (after Moore and Wong, 2002) and (after Power et al., 2001). The location of the line G92A-3000 is roughly located near the area in red box.

4.4 Time-Lapse Seismic Monitoring Feasibility Analysis

4.4.1 Overview

The main aim of this investigation is to study the feasibility of seismic monitoring several plumes of injected CO₂ in the CarbonNet project. All of these geological structures need to be modelled in order to investigate the time-lapse response of CO₂ injection in the offshore CarbonNet project area. Several investigations were required to ensure the feasibility of applying time-lapse seismic monitoring by injecting different volumes of CO₂ and modelling their plumes (Figure 4.8). In this section, I assessed CO₂ seismic monitoring using a finite difference model with streamer cable and ocean bottom cable geometries of reflection seismic surveys. Different amounts of CO₂ are simulated and injected into the realistic finite difference model of the CarbonNet area.

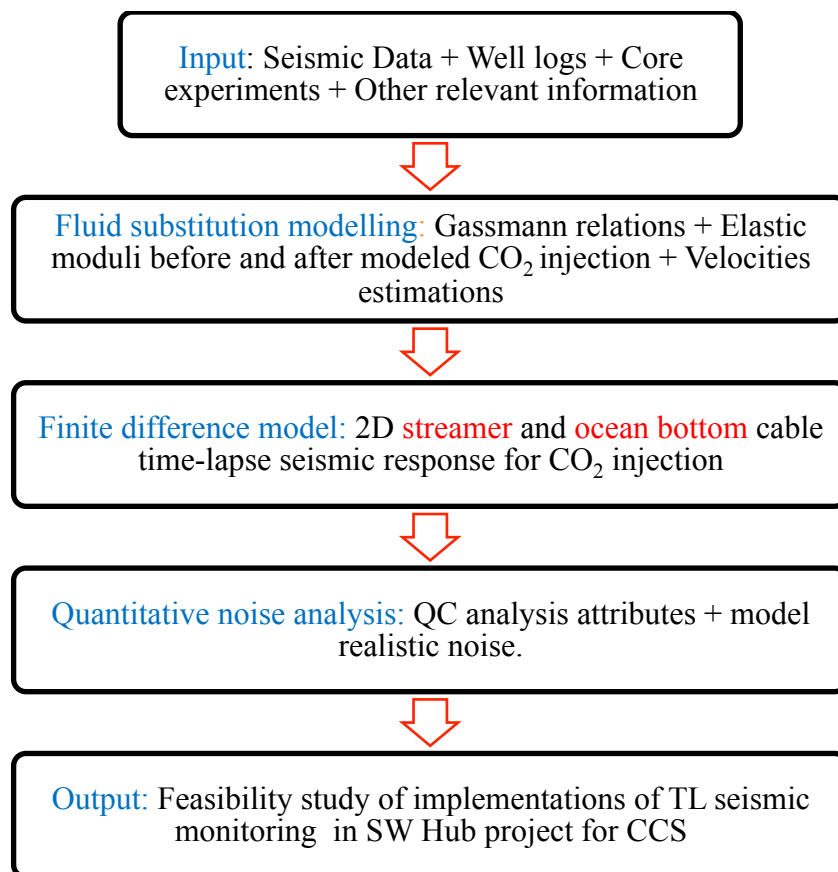


Figure 4.8: A flowchart of the main experimental steps of a feasibility analysis for the CO₂ capture and storage CarbonNet project. Some hints into insights that were applied through the investigation in time-lapse seismic signal response for CO₂ injection are also shown.

4.4.2 Rock Physics and Fluid Substitution Modelling

Investigating the detectability of CO₂ using seismic time-lapse is accomplished by monitoring the response of fluid changes through the suggested sequestration area. Modelling the fluid replacement by CO₂ injection is required in the feasibility study of CO₂ geosequestration for the CarbonNet project. Therefore, studying the rock physics properties and fluid substitution modelling is necessary in order to study the CO₂ saturation in the brine and then relate them to their response in the time-lapse seismic signal.

In the CarbonNet project, the interpretation of seismic line G92A-3000 (shown in Figure 4.9) was used as basis for the rock physics and fluid substitution model. The well data is unavailable and I used the velocities from borehole measurements in the area, which were done by Moore and Wong (2001). The interval P-velocities were obtained as an average of velocities as shown in Table 4.1. The table shows also the prediction densities and the S-wave velocities of these formations that were derived from the interval P-wave velocities *in situ* by applying the Gardner's empirical relation and Castagna's equation (mud rock line), respectively (see section 3.4.2).

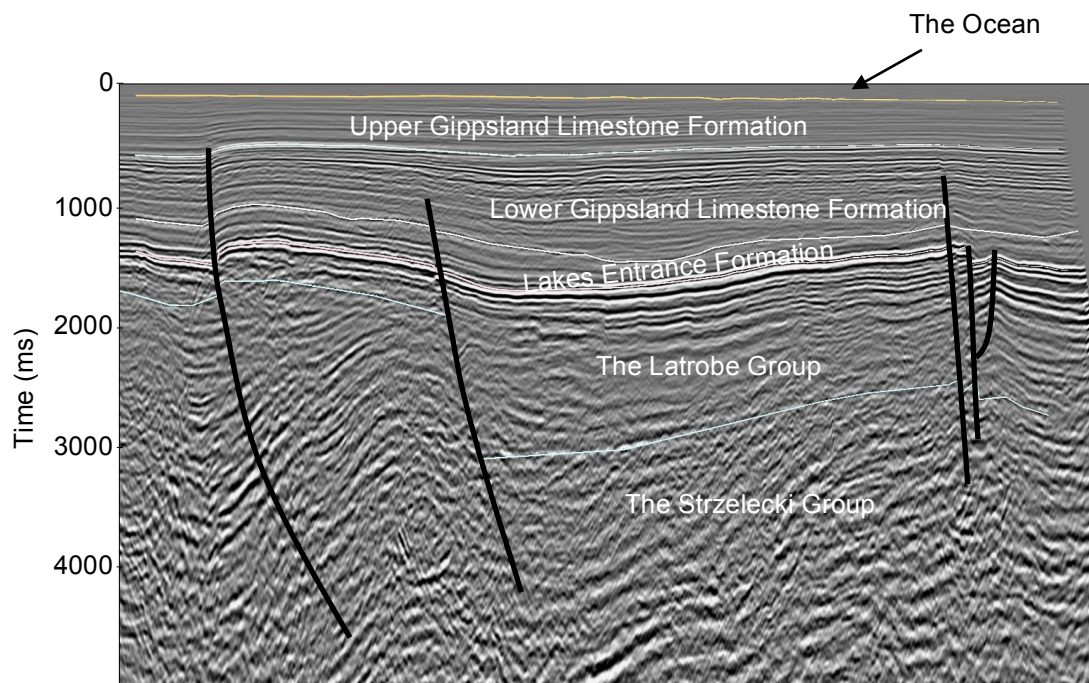


Figure 4.9: The interpretation of seismic line a G92A-3000 shows the subsurface geological structure of Gippsland Basin offshore. The geological structures are

shown with marked horizons of the subsurface formation from lower to upper: The Strzelecki Group, The Latrobe Group, Lakes Entrance Formation, Lower and Upper Gippsland Limestone and the nearshore of the ocean. It shows also the fault system in the area, which is marked in black.

Table 4.1: The observed interval velocities (P-wave velocities) V_p from Kyarra 1 well log measured by Moore and Wong, (2001). The table also shows the calculated S-wave velocities V_s and densities ρ calculated using Gardner's empirical relation and Castagna's equation, respectively.

Formation	V_p (km/s)	V_s (km/s)	Density (kg/m ³)
<i>Ocean Water</i>	1.480	0	1000
<i>Upper Gippsland limestone</i>	2.291	0.800	2000
<i>Lower Gippsland limestone</i>	2.571	1.041	2100
<i>Lank Entrance</i>	2.800	1.238	2200
<i>Latrobe Group</i>	3.400	1.754	2100
<i>Strzelecki Group</i>	3.900	2.184	2300

As mentioned previously in section 3.2.4, the Gassmann equation relates density, elastic-wave velocity properties, the replacement of the pore fluid and matrix properties of rocks. This relationship also computes the bulk and shear moduli of a fluid-saturated isotropic porous medium and relates them to the bulk and shear moduli of the same medium in the drained case.

In the CarbonNet project, the suggested geological formation for CO₂ injection is the Latrobe Group at a depth of 1100 m. *In situ* properties of the bulk modulus and density of brine and CO₂ based on temperature and pressure estimates are calculated by utilising the thermophysical properties of fluid systems for material laboratory measurement (Lemmon et al., 2012), as shown in Table 4.2. The moduli of the grain mixture for the Latrobe Group was calculated based on the Hashin-Shtrikman bounds (Hashin and Shtrikman, 1962). In a clean sandstone situation, the bulk modulus and density of the grain material of the Quartz-rich are identical to the

values of the sandstone. On that basis, the bulk modulus and density of the grain is that of Quartz:

- $K_G = K_{\text{Quartz}} = 36.6 \text{ GPa}$
- $\rho_G = \rho_{\text{Quartz}} = 2650 \text{ kg/m}^3$

Table 4.2: The Latrobe Group elastic properties for bulk modulus and density of brine and CO₂. These were computed using the thermophysical properties of fluid systems calculation (Lemmon et al., 2012) and were based on the *in situ* well logs data of temperature and pressure.

Pore pressure	11.6 MPa
Temperature	57 °C
Effective Porosity	32%
$V_{P_{CO_2}}$	237.1 m/s
K_{CO_2}	0.0248 GPa
ρ_{CO_2}	0.441 g/cm ³
K_{Brine}	2.438 GPa
ρ_{Brine}	989 kg/m ³

By performing the Gassmann fluid substitution using all the values in Table 4.2, the results of interval P-velocities and S-velocities, densities and based on the assumption of 50% brine and gas mixture, I estimated the seismic velocities and density for pre- and post-injection shown in Table 4.3. I noted that this result shows the acoustic impedance (AI) pre-injection (100% brine saturation) is 7.203 kg/(km².s), which became (50% brine, 50% CO₂) 6.639 kg/(km².s) post-injection. That means the change of acoustic impedance (AI) is approximately - 0.564kg/(km²/s), or -8%. There was a slight change in shear impedance (SI). Moreover, the reflection coefficient for incident waves normal to the plume is approximately 0.0407, which means that 0.19% of the seismic energy is reflected from the plume. This indicates that seismic monitoring should be applicable in this situation, as will be demonstrated in the next part of this feasibility study.

4.4.3 Numerical Forward Seismic Modelling

The interpretation of the seismic line G92A-3000 was utilised to build a realistic numerical model. I believe that this model was characteristic for the wider area and captures the main geological features important for the purpose of evaluating the CO₂ seismic monitoring in the CarbonNet area. The interpretation of the seismic line was supported by the data from the well log of Kyarra-1. The numerical forward model was established by including the major subsurface geological structures: The Strzelecki group, The Latrobe Group (the suggested formation for CO₂ plumes), Lakes Entrance Formation, Lower and Upper Gippsland formation and on top of the nearshore of the Ocean (Figure 4.11). The interval velocities, which were obtained from the well logs data, were utilised to convert the seismic line section from time to depth in order to export interned mapping horizons in the depth domain. In figure 4.11, the yellow dashed box indicates the area of interest for the model, which is used in the remainder of this experiment. The zoomed-in area indicated by the solid red rectangle, shows the CO₂ plumes placed on the top of the Latrobe Group and sealed with the Lakes Entrance formation.

Table 4.3: The Gassmann fluid substitution performance results using interval P-wave velocities as input. The P-wave velocities were observed from borehole measurements in the area. S-wave velocities V_s and densities ρ were estimated by using Gardner's empirical relation and Castagna's equation (mudrock line), respectively. For the same modelled injection interval, this gave 100% brine pre-injection and a 50% brine, 50% gas post-injection composition, which is the approximate residual CO₂ saturation for sandstone for the Latrobe Group (IPCC, 2005; Benson et al., 2012).

% saturation	Pre- CO ₂ injection (100% brine)	Post- CO ₂ injection (50% brine and 50% CO ₂)
V_p	3400 m/s	3256 m/s
V_s	1754 m/s	1791 m/s
ρ	2.11 g/cm ³	2.03 g/cm ³

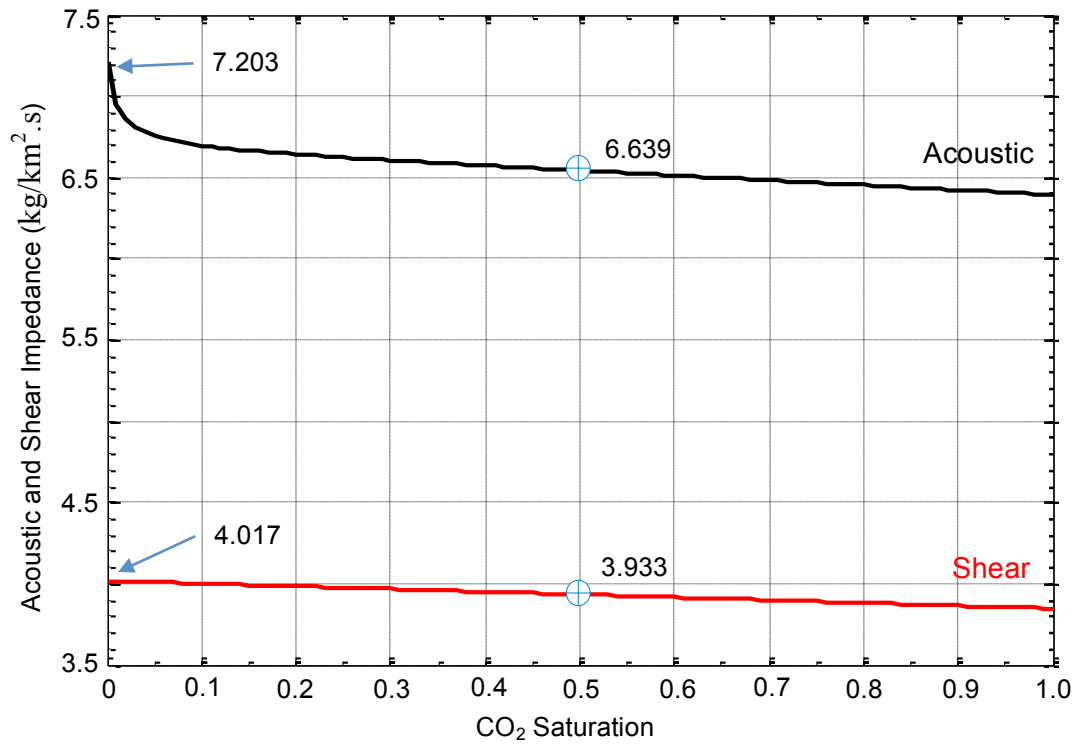


Figure 4.10: The acoustic and shear impedance changes of CO₂ saturation into the Latrobe Group of the Gippsland Basin. The blue arrows show the acoustic and shear impedance for the pre-injection case of 100% brine saturation of 7.203 and 4.017, respectively. The post-injection results of acoustic and shear impedance on a 50% CO₂ saturation are 6.639 and 3.933 kg/(km².s), respectively. These differences between pre- and post-injection indicates that approximately 0.19% of the seismic energy is reflected from the CO₂ plume.

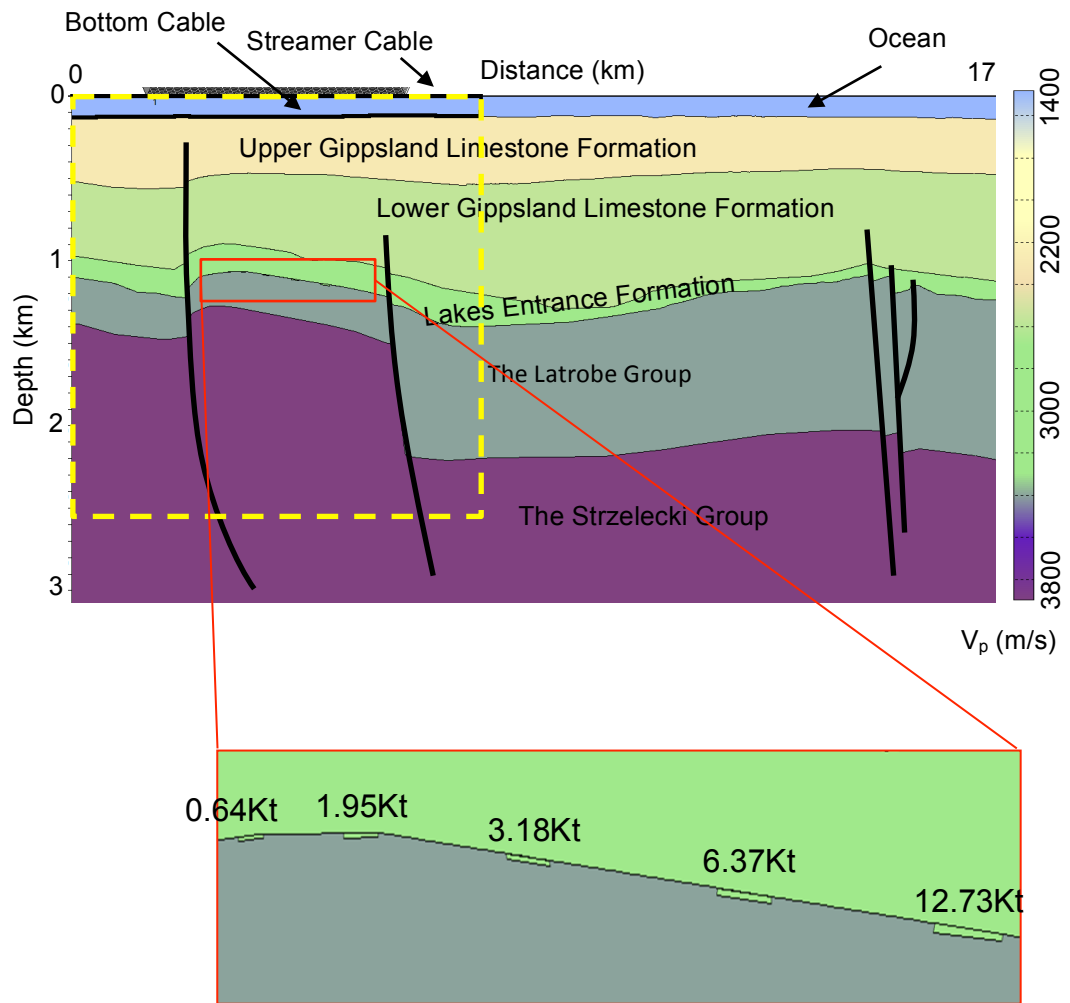


Figure 4:11: The finite difference model on the basis of interpreted seismic line G92A-3000 with five difference volumes of CO₂ plumes; 0.64, 1.95, 3.18, 6.37 and 12.73 Kt. The size of the plumes gradually increases from left to right and all sizes are listed in Table 4.4. The model is used to investigate the CO₂ detectability in CarbonNet project area. The enlarged figures in red rectangle shows the locations of the suggested plumes, which are placed on the interface at the top of Latrobe Group sealed by Lakes Entrance formation. The yellow dashed rectangle indicates the subset of the model, which was used to present the remainder of the work and results.

I modelled several CO₂ plume sizes and distributions. The suggested CO₂ volumes are 0.64, 1.59, 3.18, 6.37 and 12.73 thousand tonnes (k tonnes) of CO₂. As done in previous work in the SW Hub project (see section 3.4.3), the shape of the plumes are cylinders with a suitable constrain on the diameter and thickness. All plumes were distributed along the top of the Latrobe Group. The reasons for including all the plumes in one model are two-fold. First, the simultaneous placement of the different plumes requires computing only one forward model, which significantly saves on the time needed to generate the data. Second, the placement of the plumes in one section allows for easier comparison of detectability of the different CO₂ volumes. The volumes of the CO₂ plumes are $9.02 \times 10^3 \text{ m}^3$, $22.56 \times 10^3 \text{ m}^3$, $45.11 \times 10^3 \text{ m}^3$, $90.22 \times 10^3 \text{ m}^3$ and $180.45 \times 10^3 \text{ m}^3$ (Figure 4.12). In the figure, the dimensions of the volumes are shown as black dots on graphs of possible diameter/thickness values for given volume and the d_f indicates the diameter of the first Fresnel zone in the injection level on the top of Latrobe Group. h_0 refers to the tuning thickness for the wavelength. The dominant wavelength is related to the model properties, namely the interval velocity of the reservoir of 3400m/s, and the dominant wavelength that was used in the modelling, namely 60Hz, which results in approximately 60m and the modelling was 2D elastic model. Table 4.4 summarises the dimensions of the modelled CO₂ plumes for calculated CO₂ plumes of five different volumes with their respective rock properties and shaping plume dimensions.

The location of the injection well of the CarbonNet project, which is in nearshore of the Gippsland Basin, encourages us to drive two different seismic applications of numerical forward model marine streamer and ocean-bottom cable, as shown in Figure 4.11. Therefore, in the next section I will show and discuss these two experiments and the possibilities of CO₂ detectability in the CarbonNet project area by using time-lapse seismic monitoring.

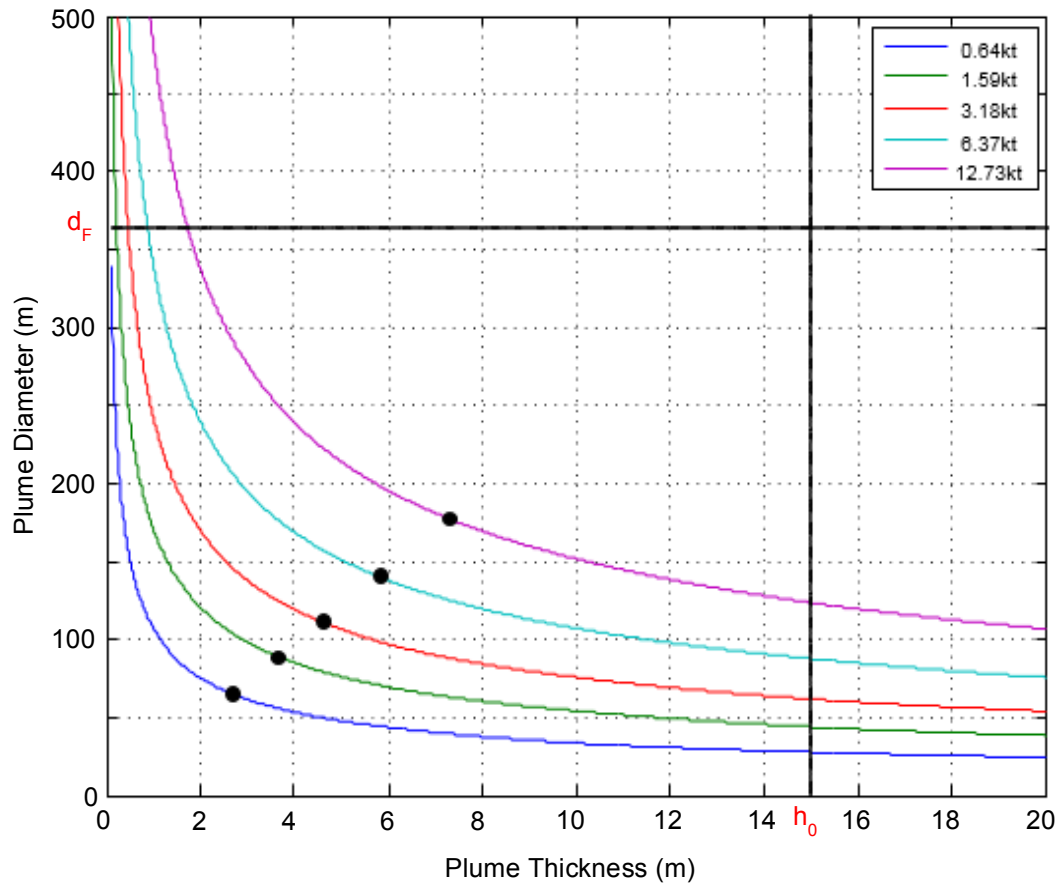


Figure 4:12: A cross-section of shape dimensions, diameters and thickness for the volumes of five different plumes. The black dots show the selection of diameter/thickness pairs. The d_F indicates the diameter of the first Fresnel zone in the injection level on the top of Latrobe Group. h_0 refers to the tuning thickness for a wavelength of 60 m.

Table 4.4: The calculated CO₂ plumes of five different volumes with their respective rock properties and shaping plume dimensions.

Injected CO ₂ (k tonnes)	0.64	1.59	3.18	6.37	12.73
Rock volume (10 ² m ³)	9.02	22.56	45.11	90.22	180.45
Plume thickness (m)	2.70	3.66	4.61	5.81	7.32
Plume diameter (m)	65.23	88.58	111.62	140.61	177.16

4.4.3.1 Ocean streamer model

As shown in Figure 4.11, the first evaluation of CO₂ detectability in the Gippsland nearshore is applied by using streamer cable in the finite difference model when the cable is located on the Ocean surface. The layout geometry was designed to simulate the appropriate field survey (Table 4.5). The plumes were placed on the interface of Latrobe group layers at a depth of between 1000 and 1100 m.

Table 4.5: The geometry parameters of the finite difference model for streamer and bottom cables. The pertinent information relating to the wave propagation method and reordered offices range are shown.

Simulation method	Finite-difference using an explicit solution to the acoustic wave-equation
Modelling method	2D-Elastic
Source type	Omnidirectional source
Source position	Surface
Seismic wavelet	Zero phase Ricker wavelet
Frequency	60 Hz
Number of sources	200
Source interval	25 m
Number of receivers	630
Receiver interval	12.5 m
Sampling rate	2 ms
Minimum offset	12.5
Maximum offset	7875
Modelling depth	3000
The grid size (dx,dz)	1.5 m
The grid time step (dt)	0.54 ms

The noise-free migrated time-lapse seismic results (baseline and monitor lines) and their difference are shown in Figure 4.13. The results from the streamer model showed high detectability for all five CO₂ injection plumes. This alone is not enough to evaluate the CO₂ detectability. I should also create a more accurate model by adding a realistic amount of noise to simulate the real, observed noise in the post-stack migrated section of line G92A-3000.

To do that, I utilised the SNR estimation, discussed in section 3.4.3.1, with a window of 100 m in the seismic section to measure the level of noise that can be observed in the real data. The best option is to present the SNR values at different depths to estimate the actual SNR result for real data (Figure 4.14). In the streamer field survey, I commonly observed some amount of ghost noise. Herein, I did not simulate this because the real data I used for the SNR estimates had them already removed. In Figure 4.14 I plotted histograms of the SNR values opposite SNR values of the real data, which appear as hot colours correspond to high counts of SNR estimation. The matching SNR value at the interface of the Latrobe group was approximately 10 at the depth of the plumes.

To simulate this amount of random noise I filtered the amount of noise that was observed in the SNR result to match the frequency spectrum of the real data and then added the estimated real noise to the synthetic data (Figure 4.15). In this figure is the result of matching 10 SNR with synthetic data computed with a 100 ms window. The hot colours, shown in the figures in a log₁₀ scale (left) and in histograms (right), correspond to high counts of SNR values. The white circles, as shown in the figure, show the level of noise, which was added to synthetic data to match the level noise in the injection zone so the detectability of CO₂ plumes at the top of Latrobe Group formation could be investigated. The time-lapse synthetic migrated base, monitor and difference sections including the added noise, which I observed in the SNR estimation, are shown in Figure 4.16. The CO₂ plumes are obviously detectable for the largest volumes 6.37 and 12.73 k tonnes as marked with white arrows. The result indicates that the CO₂ plumes size of more than approximately 3 kt tonnes is possible to detect for the CarbonNet project area.

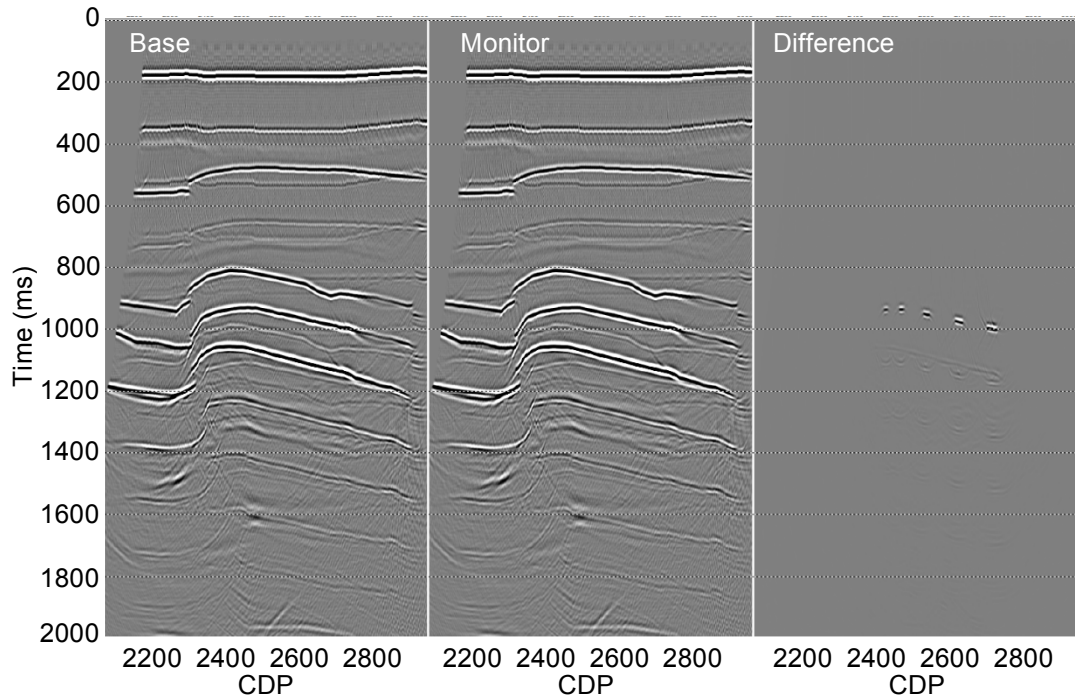


Figure 4.13: Noise-free seismic response sections of baseline, monitor line, and difference of the synthetic data. The five CO₂ plumes are clearly detectable in the difference section. Realistic noise should be modelled and added to evaluate the real detectability of CO₂.

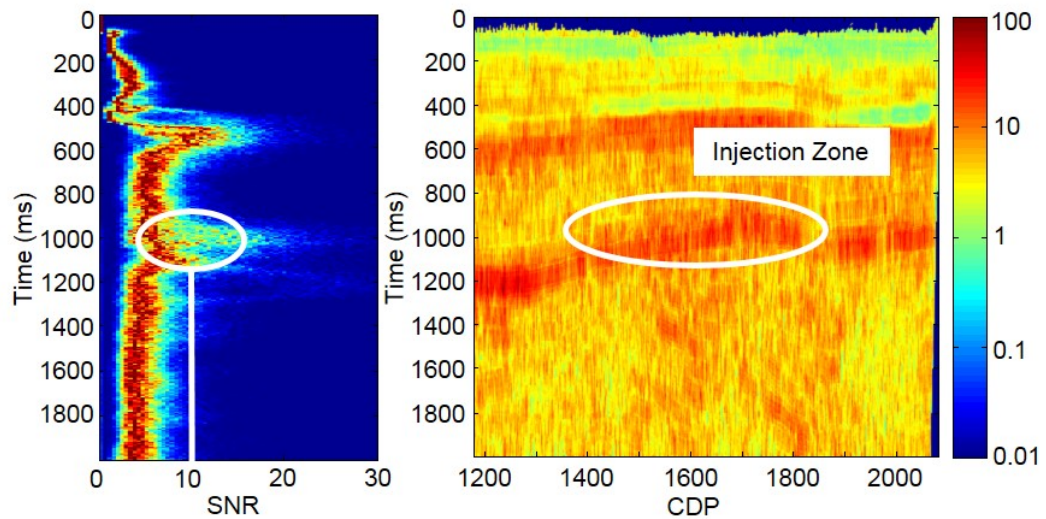


Figure 4.14: The SNR for real data computed with 100 ms window in a log₁₀ scale (right) and in histograms for each time slice (left) where the hot colours correspond to high count of SNR values. In the white circles show the suggested location for CO₂ plumes. The amount of noise in plume zones approximately matches a SNR of 10, which is located at the top of Latrobe Group subsurface formation.

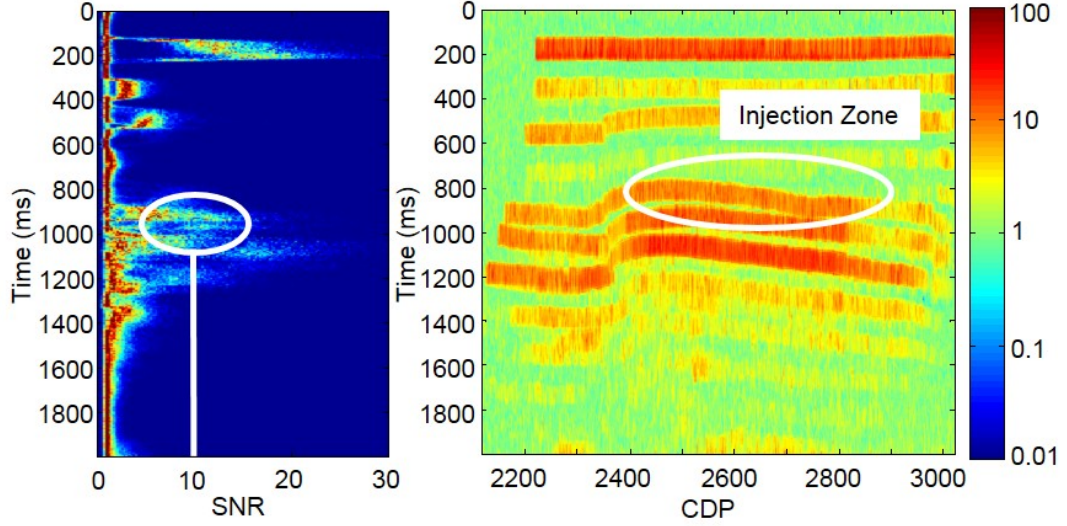


Figure 4.15: The result of matching 10 SNR for synthetic data computing with 100 ms window in a log10 scale (right) and in histograms for each time slice (left) where the hot colours correspond to high count of SNR values. The white circles show the level of noise, which was added to synthetic data to match the level noise in the injection zone to investigate the detectability of CO₂ plumes at the top of Latrobe Group subsurface formation.

I applied another level noise measurement, which corresponds to the change in the time-lapse signal to noise. This measurement is the NRMS. The NRMS values for two traces can be computed by applying the average repeatability metrics of two traces a and b, which is defined by (Kragh and Christie, 2002) as:

$$NRMS = 200 \times \frac{RMS(a_t - b_t)}{RMS(a_t) + RMS(b_t)}, \quad 4.1$$

where the RMS is defined as

$$RMS(x_t) = \sqrt{\frac{\sum_{t_2}^{t_1} (x_t)^2}{N}}, \quad 4.2$$

where a_t and b_t are the seismic traces from the two surveys baseline and monitor and N is the number of samples within the time windows t_1 and t_2 .

In general, time shifts, amplitude and phase changes significantly affect the NRMS values. A small value of NRMS shows good repeatability, whereas a high

value represents poor repeatability or a large value of non-repeatable noise (see section 2.4.1).

In Marine data, the normal values of NRMS are placed between 20 and 50% (Calvert, 2005). Based on that, I add one realisation of matching time-lapse noise frequencies to the baseline and monitor section to compute the NRMS vales. I simulated NRMS values of the realistic noise by changing and adjusting the strength of added noise. The NRMS values are shown in a histogram and on the synthetic section in Figure 4.17. Approximately 50% of NRMS is very similar to the level of noise that I observed in SNR, as shown in Figure 4.15, of a value of 10. The result of the baseline, monitor and their difference sections are shown in Figure 4.18 contaminated by 50% of NRMS to match the amount of noise in the real data. Based on the similarity of matching noise levels of SNR and NRMS, shown in Figure 4.16 and 4.18, the CO₂ plumes are detectable for sizes of approximately 3 k tonnes or more.

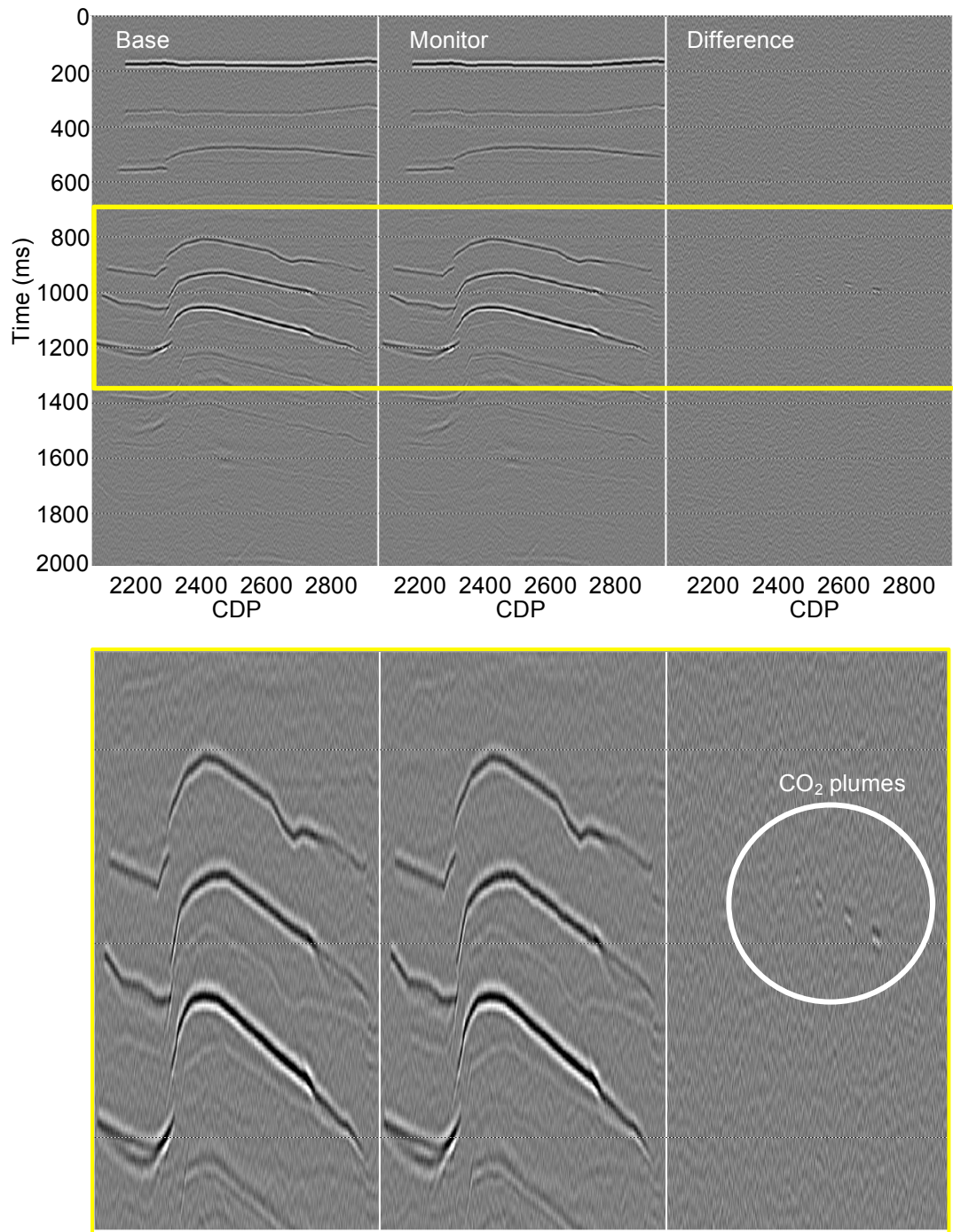


Figure 4.16: The results of the synthetic migrated baseline, monitor line and difference synthetic section, with added filtered realistic noise from SNR estimation. In the enlarged figure (below) the CO₂ plumes are detectable for the largest volumes 6.37 and 12.73 kt, as marked with a white circle.

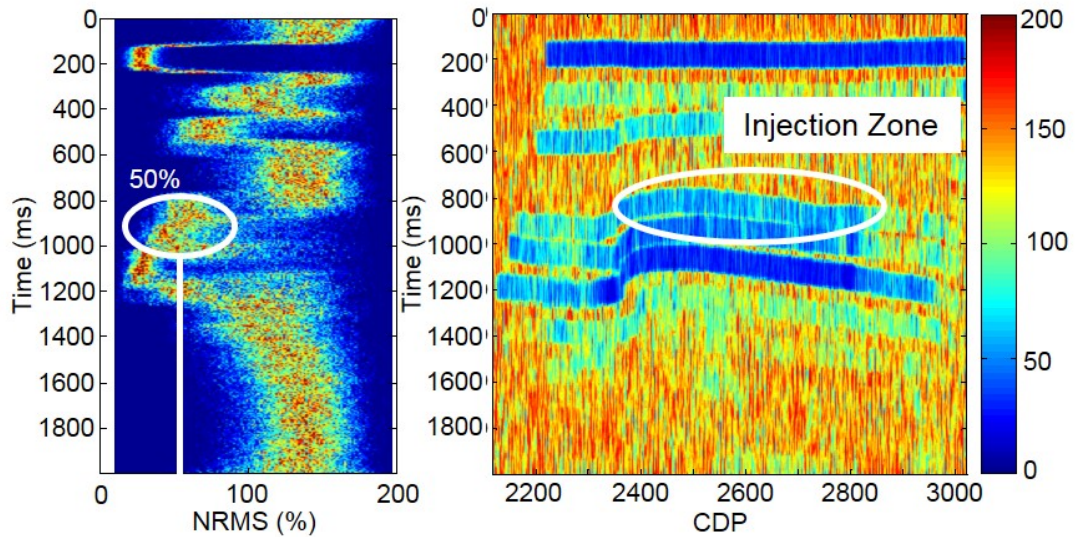


Figure 4.17: The result of the NRMS attribute for the synthetic data in the histogram (on the left) and the synthetic section (on the right). Hot colours refer to the high count values of NRMS. The produced NRMS is 50%, which was chosen to match the noise in the injection zone (the top of Latrobe Group subsurface formation).

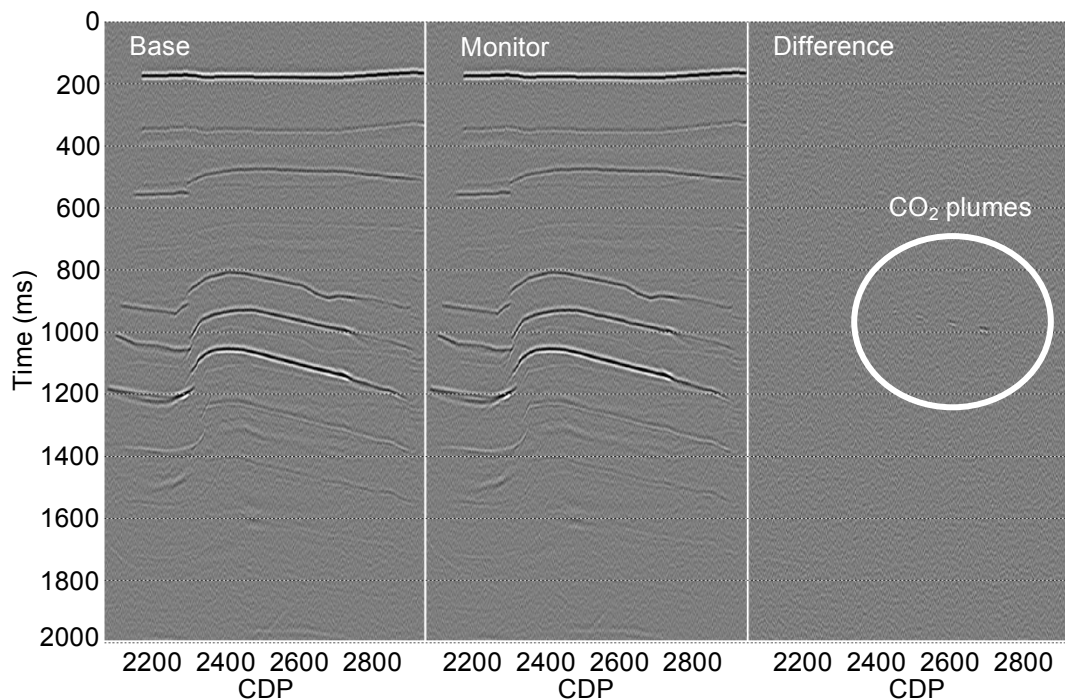


Figure 4.18: The results of the synthetic migrated baseline, monitor line and difference synthetic section with added noise matching roughly 50% NRMS. The observed amount of noise is very similar to what I had observed in the SNR estimation. The CO₂ plumes are detectable for approximately 3 kt and more.

4.4.3.2 Ocean bottom cable model

The second marine seismic time-lapse option of CO₂ detectability evaluation for the CarbonNet project is an ocean bottom cable (OBC). The OBC concept is a development from the ocean bottom seismometer technique. In OBC acquisition, the geophone receivers are attached to the bottom ocean instead the conventional marine streamer, which are floated on sea surface. This method has been used for several decades. The first use of OBC was in 1930s by Mobil Oil Co but the first academic application of OBS designs was in 1975 for refraction studies (Zachariadis et al., 1983). The method was used to map structures below volcanic rocks (basalt) in northern Norway (Mjelde et al., 1991) and to image and model the possible existence of hydrocarbons source rocks (Hughes et al., 1995). Recently, the technique has been used in wider seismic applications, which makes it a good solution for enhancing the data resolution, particularly in near-shore surveys. The quieter environment around the OBC layout provides high signal-to-noise ratio when compared to the conventional marine streamer on the surface. The cost and the difficulty of velocity analysis are the main drawbacks of OBC.

For a bottom cable of the Gippsland nearshore, I do not have any real data in order to estimate the level of noise; however, the NRMS value can be shown to be approximately in the range of 10–20% in the difference section based on the source position matching between the repeatable surveys (Reine et al., 2009). Shell's Shearwater project in 2002/2004 achieved 7% NRMS, which represents the actual noise of a 4D streamer (Shulakova et al., 2012). Based on that, I added two noise representations to the baseline and monitoring surveys matching 17% NRMS (Figure 4.19). In this figure, a histogram of the NRMS attributes are shown for the synthetic data (on the left) and for the synthetic section (on the right).

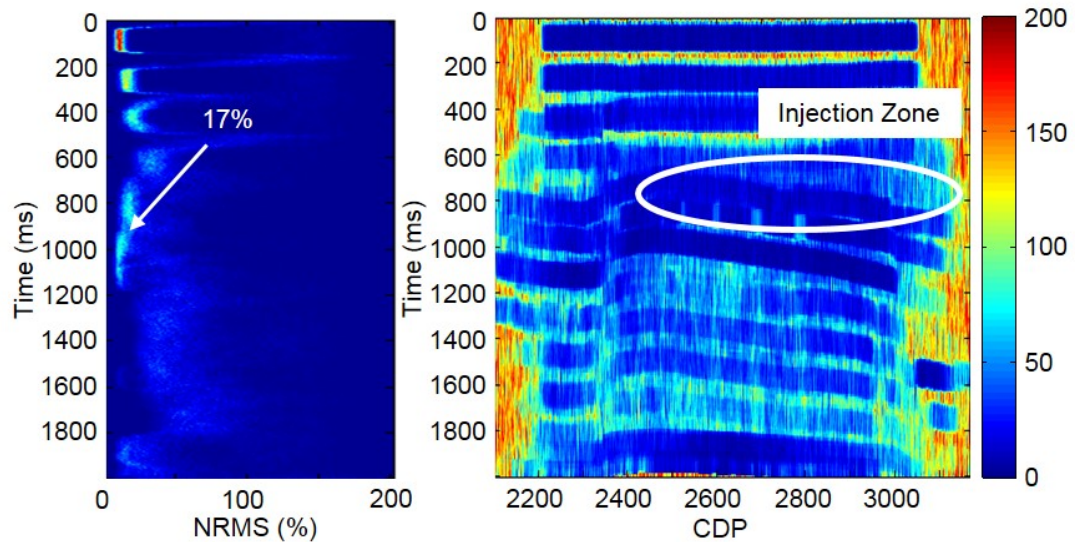


Figure 4.19: The result of the NRMS attribute for the synthetic data in the histogram (on the left) and the synthetic section (on the right). Hot colours refer to the high count values of NRMS. The produced NRMS is 17%, which I chose to match the noise in the injection zone.

The matching amount of noise of 17% of NRM is shown in Figure 4.20 for the synthetic baseline, monitor and difference sections. In the migrated section of the baseline and monitor I can see the effect of the multiples, which produce a high amount of wide-spread multiple noise. I decided not to remove this modelling artefact, since in real data one could observe similar repeatable multiples noise corresponding to the variation in the temperature and / or tide. However, the CO₂ detectability of the OBC in the Gippsland nearshore is high for all plumes, which makes this a good option for CO₂ monitoring for the CarbonNet project.

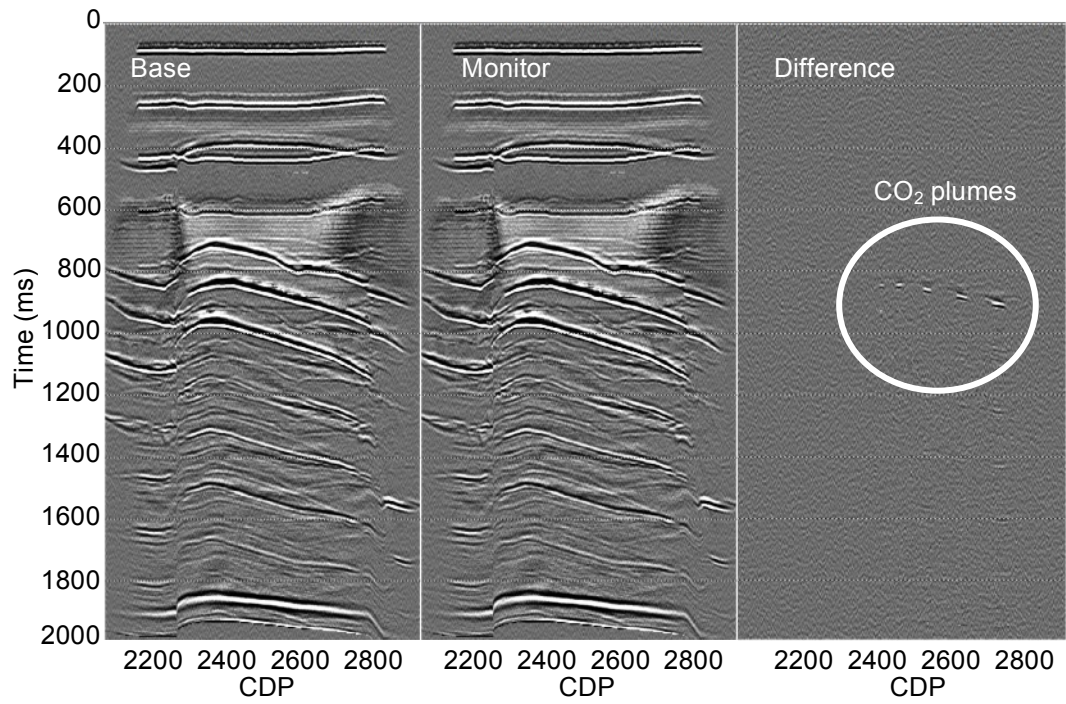


Figure 4.20: The results of the synthetic migrated baseline, monitor line and difference synthetic section with added noise matching roughly 50% NRMS.

4.5 Conclusion

In this chapter I presented a feasibility study to evaluate the use of time-lapse seismic methods in CO₂ monitoring and verification in the CarbonNet project in the nearshore Gippsland Basin. I used the field data G92A-3000 baseline to simulate many realistic finite difference models and to investigate a time-lapse monitoring feasibility study of CO₂ injection of the CarbonNet project area. Many geological and lithological reports were used to make the model more realistic. The estimation of effective porosity was calculated from the log data from the well Kyarra 1, measured by Moore and Wong, (2001) for the Latrobe Group Sandstone formation and is given at 32% effective porosity. Properties of a CO₂ saturated reservoir were simulated by applying the Gassmann fluid substitution, while to calculate the velocities and densities of subsurface geological layers, I used the mudrock line and Gardner's empirical relations.

Two numerical forward models, the streamer cable model and OBC model, were generated to investigate the detectability of a spread of five CO₂ plumes injected at the top of Latrobe Group Sandstone formation. Synthetic time-lapse seismic data baseline and monitor after CO₂ injection were acquired and processed for these models. The noise-free difference migration sections of the streamer model shows high detectability for all plumes. I implemented two different noise measurements to simulate a realistic level of noise: SNR and NRMS. The results of these measurements show a very similar amount of noise, which were 10 SNR and 50% NRMS. The CO₂ plumes in the difference section with added filtering noise were detectable for the volumes of approximately more than 3 k tonnes. Herein, I can state that the CO₂ detectability in the CarbonNet project is satisfactory when using the streamer acquisition.

The OBC numerical forward model is another method used to assess the CO₂ detectability by using layout seismic receiver arrays placed on the ocean-bottom. I used the same model as for the streamer model with five CO₂ plumes. Since we do not have any baseline data from the area, I could not do direct noise-level measurements. Therefore, I added two band-limited random noise realisations to the baseline and monitoring surveys matching 17% of NRMS, which is reported by many sources for OBC time-lapse data. The difference migrated sections show a high CO₂ detectability for all plumes including the small volumes 0.64 k tonnes.

In summary, synthetic OBC shows high effective time-lapse methods for CO₂ verification and monitoring, which make it the first recommended method in the CarbonNet project. Indeed, the high repeatability of a time-lapse survey after CO₂ injection will be most helpful in obtaining high detectability of CO₂ plumes and decreasing the time-lapse noise. Again, the lack of real time-lapse data in the area limited this feasibility study because all the models were based only on one vintage of seismic line and reported noise levels from different areas. In the next chapter I will use real time-lapse data and methods to assess CO₂ detectability for CCS stage 2 of Otway project.

In this chapter, I assessed CO₂ seismic monitoring in the near-shore location of the CarbonNet project using a finite difference model with streamer cable and ocean bottom cable (OBC) geometries of reflection seismic surveys. Different amounts of CO₂ were simulated and injected into the realistic finite difference model of the CarbonNet area. I modelled a more accurate noise model by adding a realistic amount of noise to simulate the real noise. The lack of real shot-gather time-lapse data in the area limited this feasibility study because all the models were based only on one vintage of migrated data and reported noise levels from different areas. In this assessment, I utilised a processed and migrated near-shore 2D seismic data line GGS185B-17a. In the next chapter, I will use real shot-gather 2D data to evaluate CO₂ detectability for CCS stage 2 of Otway project and model more realistic noise models.

4.6 Reference

- Australia, G., 2013, The Gippsland Basin: Geoscience Australia, <http://www.ga.gov.au>, (retrieved May 21, 2013).
- Bernecker, T. Tom, J.H. , and G. W. O'Brien, 2006, Hydrocarbon prospectivity of areas V06-2, V06-3 and V06-4, southern offshore Gippsland Basin, Victoria, Australia Department of Primary Industries, Report 88.
- Calvert, R., 2005, Insights and methods for 4D reservoir monitoring and characterization.
- Driscoll, J., 2006, Geothermal Prospectivity of Onshore Victoria, Australia. Victorian Initiative for Minerals and Petroleum Department of Primary Industries, Report 85.
- Gibson-Poole, C. M., L. Svendsen, J. Underschultz, M. N. Watson, J. Ennis-King, P. J. Van Ruth, E. J. Nelson, R. F. Daniel, and Y. Cinar, 2006, Gippsland Basin geosequestration: A potential solution for the Latrobe Valley brown coal CO₂ emissions.
- Hashin, Z., and S. Shtrikman, 1962, A Variational Approach to the Theory of the Effective Magnetic Permeability of Multiphase Materials: Journal of Applied Physics, **33**, 3125-3131.
- Holdgate, G., C. Rodriguez, E. Johnstone, M. Wallace, and S. Gallagher, 2003, The Gippsland Basin top Latrobe unconformity, and its expression in other SE Australia basins: APPEA Journal, **43**, 149-173.
- Hughes, J. K., 1998, Examination of Seismic Repeatability as a Key Element of Time-Lapse Seismic Monitoring: Presented at the European Petroleum Conference.
- Kragh, E., and P. Christie, 2002, Seismic repeatability, normalized rms, and predictability: The Leading Edge, **21**, 640-647.
- Lemmon, E., M. McLinden, S. Klein, and A. Peskin, 2012, "Thermophysical Properties of Fluid Systems" in NIST Chemistry WebBook, NIST Standard Reference Database Number 69: Linstrom and W.G. Mallard, National Institute of Standards and Technology, Gaithersburg MD, 20899, <http://webbook.nist.gov>, (retrieved May 12, 2012).
- Mjelde, R., Sellevoll, M.A. and Berg, E.W., 1991, Shear-waves from 3-C ocean bottom seismographs indicative of anisotropy in the lower crust: 53rd EAEG Meeting, Expanded Abstracts, paper D034, pages 382-383.
- Moore, D., and D. Wong, 2002, Down and out in gippsland: Using potential fields to look deeper and wider for new hydrocarbons: Presented at the Proceedings of

the PESA Eastern Australasian Basins Symposium, Petroleum Exploration Society of Australia.

- Power, M. R., K. Hill, N. Hoffman, T. Bernecker, and M. Norvick, 2001, The structural and tectonic evolution of the Gippsland Basin, results from 2D section balancing and 3D structural modelling: Presented at the Eastern Australasian Basins Symposium, A refocussed energy eprspective for the future, Petroluem Exploration Spciety of Australia, Special Publication, 373-390. (Refid: 13347).
- Rahmanian, V., P. Moore, W. Mudge, and D. Spring, 1990, Sequence stratigraphy and the habitat of hydrocarbons, Gippsland Basin, Australia: Geological Society, London, Special Publications, **50**, 525-544.
- Reine, C., M. van der Baan, and R. Clark, 2009, The robustness of seismic attenuation measurements using fixed- and variable-window time-frequency transforms: *Geophysics*, **74**, WA123-WA135.
- Root, R., C. M. Gibson-Poole, S. C. Lang, J. Streit, J. Underschultz, and J. Ennis-King, 2004, Opportunities for geological storage of carbon dioxide in the offshore Gippsland Basin, SE Australia: an example from the upper Latrobe Group: Presented at the Proceedings of the PESA Eastern Australasian Basins Symposium II, Petroleum Exploration Society of Australia.
- Shulakova, V., R. Pevzner, and M. Urosevic, 2012, A Otway Project 3D/4D seismic data processing Final report: CO2CRC.
- Zachariadis, R.G., Thomason, H.B. and Teague, H.E., 1983, Ocean Bottom Seismometers in Seismic Exploration Surveys: Planning and Operations: 53rd Annual Meeting SEG Expanded Abstracts, paper S15.6, p.468-470.

Every reasonable effort has been made to acknowledge the owners of copyright material. I would be pleased to hear from any copyright owner who has been committed or incorrectly acknowledge.

CHAPTER 5: QUANTIFYING TIME-LAPSE SEISMIC SIGNAL DETECTION FOR THE OTWAY PROJECT USING PRESTACK MIGRATION

5.1 Introduction

During Stage 2 of the Otway project it is planned to inject a small, up to 15,000 tonnes of gas, into a saline aquifer located at depth of 1500 m using the CRC-2 well, whose location is shown in Figure 5.1. In CO₂ sequestration, the ability to detect CO₂ plumes is one of the main purposes of using time-lapse seismic imaging. The detectability of CO₂ in seismic time-lapse surveys relies on two main factors: a sufficiently strong signal and sufficiently small noise. Therefore, to model time-lapse seismic records, we need to model not only the seismic response of the geology and the plume but also the time-lapse noise. Because plume detection is determined by the SNR, the ability to model realistic time-lapse noise is crucial in any feasibility study.

In time-lapse modelling, noise is sometimes added to the migrated data to match the observed SNR from field migrated data, for example (Urosevic et al., 2011; Pevzner et al., 2013; Alonaizi et al., 2014). In this chapter, I proposed a more realistic approach by adding band-limited random noise to the pre-stack data (shot gathers) to match the SNR of field data. Using these noisy gathers I then compared the detectability of CO₂ plume by using pre- and post-stack Kirchhoff migrations.

5.2 Study Area and Geology

One of the first on-shore CO₂ sequestration projects in the world is located in Victoria, Australia (Figure 5.1). In 2002, gas production began at the Naylor gas field, but by 2004 the supply was depleted. The CO₂CRC chose this depleted gas field for a CCS project. The CO₂CRC Otway Project is divided into two stages, as shown in Figure 5.2.

The first Stage involved the injection of a CO₂/CH₄ mixture (80% carbon dioxide; 20% methane) into a depleted gas reservoir (the Naylor gas field). The CO₂ plume in the Otway Project is structurally trapped beneath sealed rock in a storage reservoir with large bounding faults (Jenkins et al., 2009). The injection of a

CO₂/CH₄ mixture began in 2008 and finished in 2009. Several seismic time-lapse surveys were acquired for Stage 1: 3D VSP and repeated 2D and 3D surface seismic surveys. Approximately 66,000 tonnes of gas mixture were injected into the Waarre C formation at the depth of 2025 m.

In Stage 2 of the Otway project, the plan is to inject 15,000 tonnes of CO₂/CH₄ gas mixture into the saline aquifer (Paaratte formation) at a depth of about 1,400 m (Jenkins, Sharma and Morvell, 2009). The Paaratte formation is a heterogeneous reservoir formation with high porosity and very clean to shaly sandstone. The clean sandstone is interspersed with shaly interbedded layers and acts as a flow barrier for the gas plumes (Dance et al., 2012). The reservoir is capped by seals of carbonaceous mudstones (Dance, 2010).

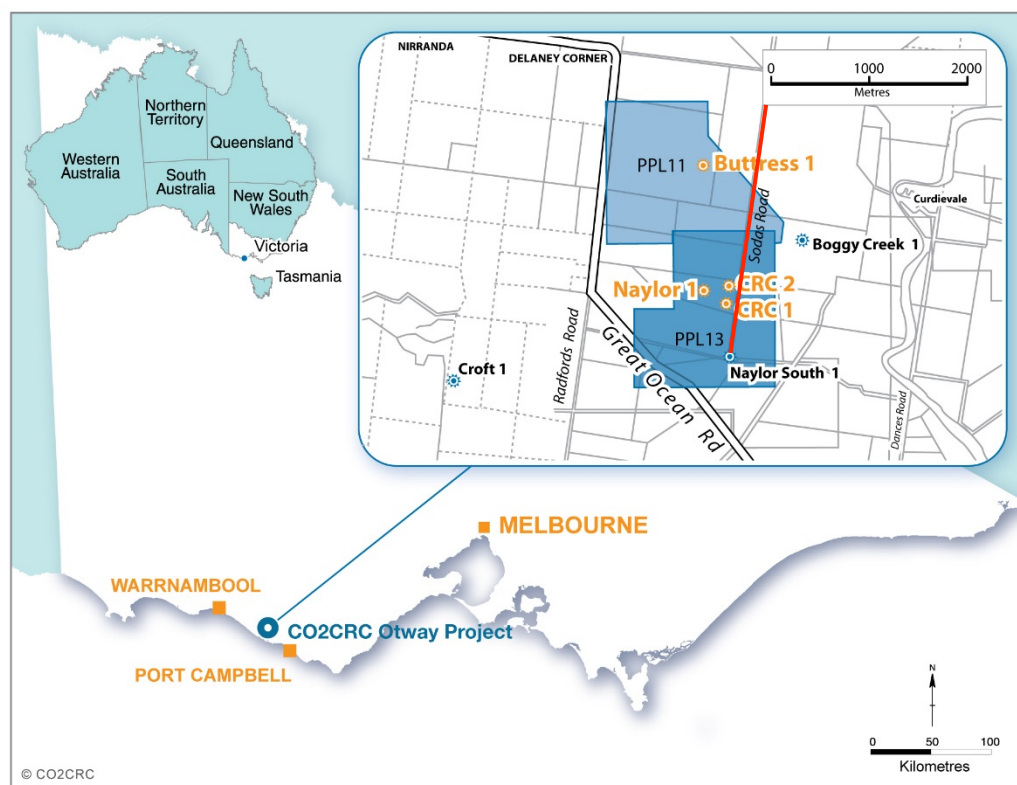


Figure 5.1: Otway project location map. The map shows the injection wells for Stage 1 (CRC1) and Stage 2 (CRC2) and the production well (Naylor-1) opposite the Sodas road (red line) (after CO2CRC, 2013).

Prior to commencing the field experiment, it is necessary to establish whether the seismic reflection method can be used to detect changes in the seismic response caused by the injection. Seismic imaging is highly recommended to detect CO₂ because the seismic reflection signal can be strengthened by diverse physical properties, temperatures, CO₂ saturated rock and the pressure of the injected CO₂ (Lumley, 2010).

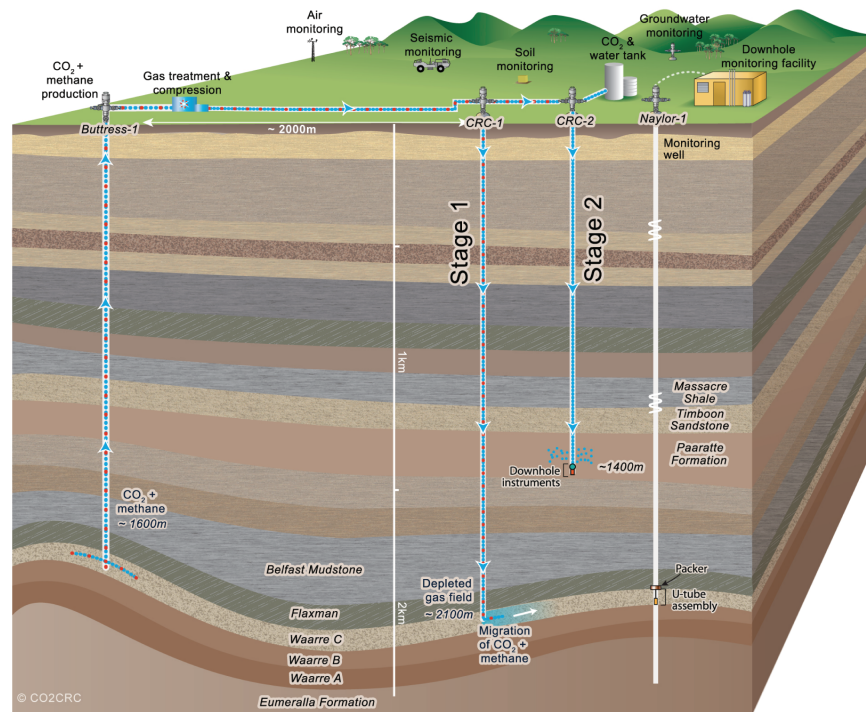


Figure 5.2: The Otway Project: Stages 1 and 2 of CO₂ sequestration. The injection zone of Stage 1, which is below that of Stage 2, provides the opportunity to model time-lapse seismic noise without a CO₂ plume cloud effect (CO₂CRC, 2013).

5.3 Data and Site Characterisation Approach

2D surface seismic data along Sodas Road was acquired in 2008 (Figure 5.1). The data were obtained using a vibrator source with a 10 m station interval, 10 m shot intervals and a nominal 159 channels per shot with a symmetrical split-spread geometry. The raw shot gathers of the data are shown in Figure 5.3. The seismic line has a CDP range of 2002–2314 with 80 full fold. The data is processed using ProMax[®] 2D processing software with common offset binned data and migrated using a pre-stack 2D Kirchhoff time migration algorithm with the parameters shown in Table 5.1. The migrated Sodas Road data is shown in Figure 5.4. By using this data, the main steps of the workflow for upcoming work are shown in Figure 5.5.

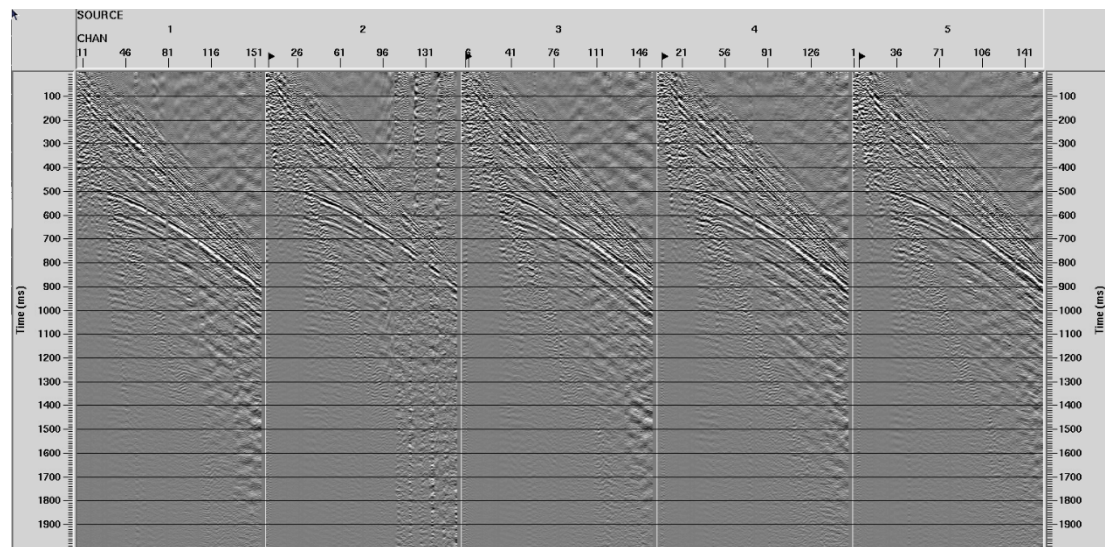


Figure 5.3: Seismic section of Sodas Road, the basis of a 2D synthetic dataset generating data to assess CO₂ detectability for the Otway Project.

Table 5.1: The parameters of the pre-stack 2D Kirchhoff time migration function used in the imaging of the seismic data.

Migration velocity	At 200 m intervals (10 CDPs)
Aperture	Stretch Mute 15
Dip limit	45 degrees
Bin size	10 m
Number of offsets	75
Output CDP interval	5 m

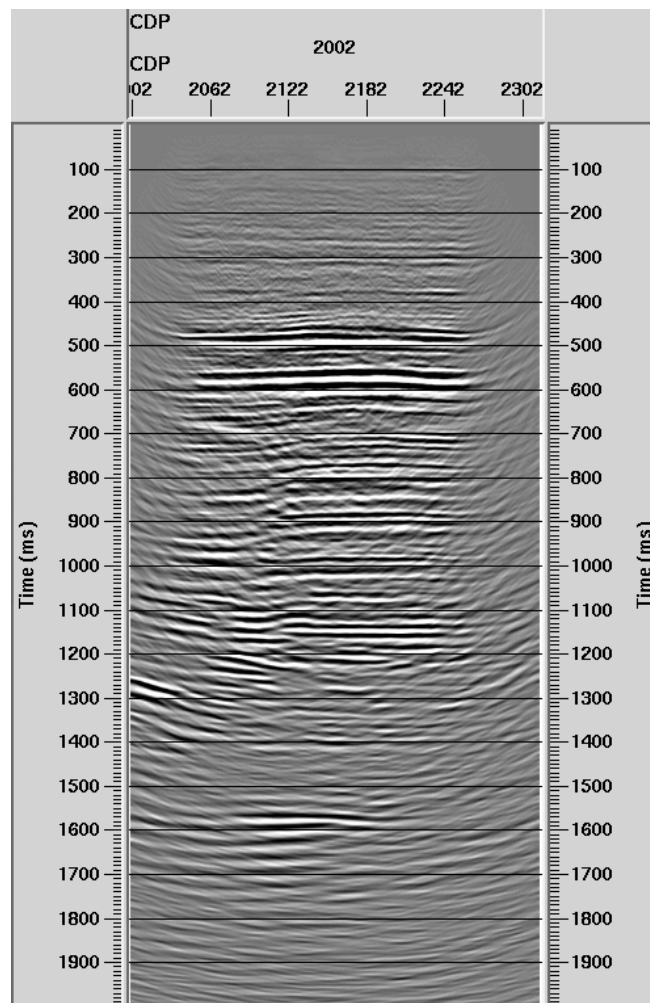


Figure 5.4: Pre-stack time migration of Sodas Road data from the Otway region with a CDP range of 2001–2314.

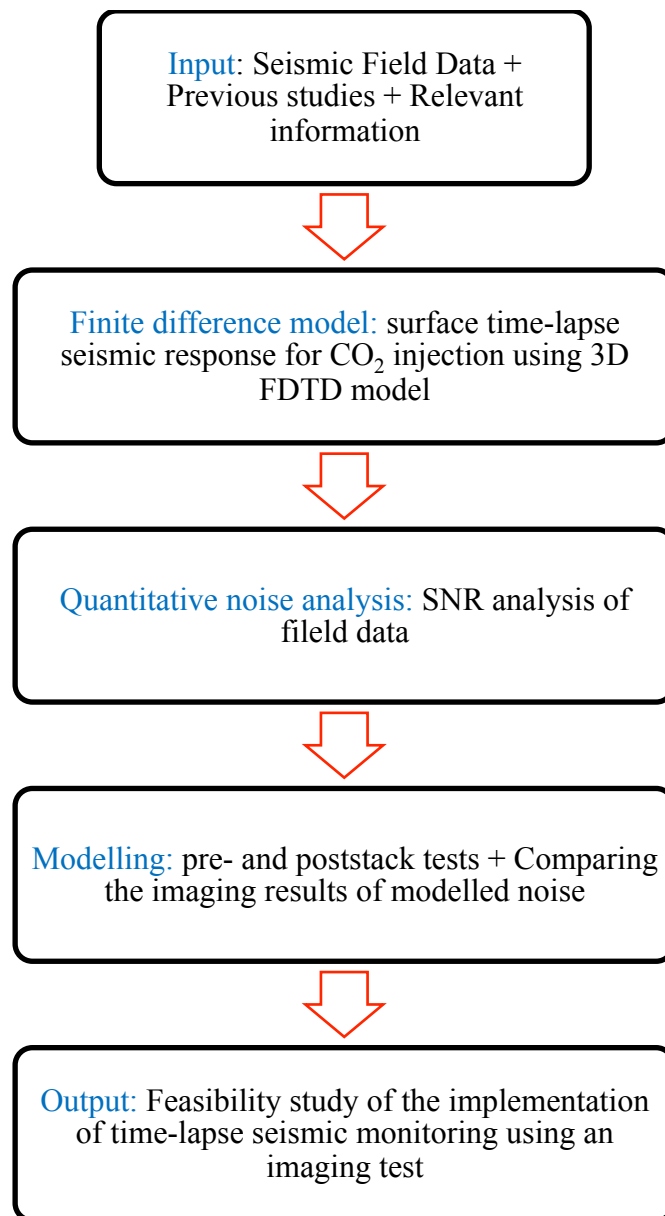


Figure 5.5: A flowchart of the main steps of feasibility analysis for CO₂ capture and storage for the Otway Project.

5.4 2D Synthetic Modelling Data

To investigate the seismic response of CO₂ injection and to image the difference in the seismic section for Otway Stage 2, a 3D finite-difference time-domain (FDTD) model was used to acquire 3D time-lapse synthetic data (baseline and monitor with plume). The 3D FDTD code SOFI3D (Karlsruhe Institute of Technology) program was used to generate the data with the regular Cartesian grid 2.5x2.5x2 m cell size covering approximately 2.5x2.5x2 km (Figure 5.6). The effects of the plume thickness on the detectability were studied by Urosevic et al. (2011) and Pevzner et al. (2012). They evaluated the gas plume for different amounts of injected gas for Otway Stage 2. The seismic modelling study of an injection of around 15,000 tonnes was considered the cases of plume between 10 000 tonnes to 30 000 tonnes at a depth of 1400–1500 m. The injection ceases after 10,000 tonnes; 57% of the injected gas is free while 18% is trapped and 12% is dissolved in brine. The thickness of the plume varies from 1–2 m for 10,000 tonnes and 2–4 m for 30,000 tonnes, with an average thickness of about 2–3 m for 15,000 tonnes. The average gas saturation in the plume is about 70%. Laterally, the 15,000 tonnes plume is about 400 m in diameter. The fluid properties are inferred from the flow simulations results for 15,000 tonnes, which provide predictions of gas distribution and saturation, brine density, overall molar compositions of CO₂ and CH₄ and pressure. They assume that only CO₂ dissolves and correct the gas composition of the free gas for dissolved CO₂. To simulate a realistic fluid flow and estimate realistic CO₂ injection, the plume geometry was estimated using a cut-off of 5% free gas in the pore space in the model (Gurevich et al., 2014). The geometry of the modelled data was based on the geometry of the 4D surface seismic acquired in 2008. The synthetic seismic record was acquired with 81 shots located along a straight line (parallel with Sodas road as shown in Figure 5.1) and recorded by 11 receiver lines. The modelling was 3D elastic model and a Ricker wavelet with a central frequency of 70 Hz was used as a source signature. The model parameters were designed to simulate the real field data and are summarised in Table 5.2.

In this test, I extracted a 2D seismic line, as shown in the yellow box in Figure 5.6 and from this, model 3D synthetic data to use in the work in this chapter. The shot gathers of the noise-free synthetic data for the baseline and monitor are shown in Figure 5.7. I used this synthetic data for the following two purposes:

firstly to model realistic 2D time-lapse noise and secondly to assess the detectability of CO2 in Otway Stage 2 by applying two different seismic migration imaging algorithms.

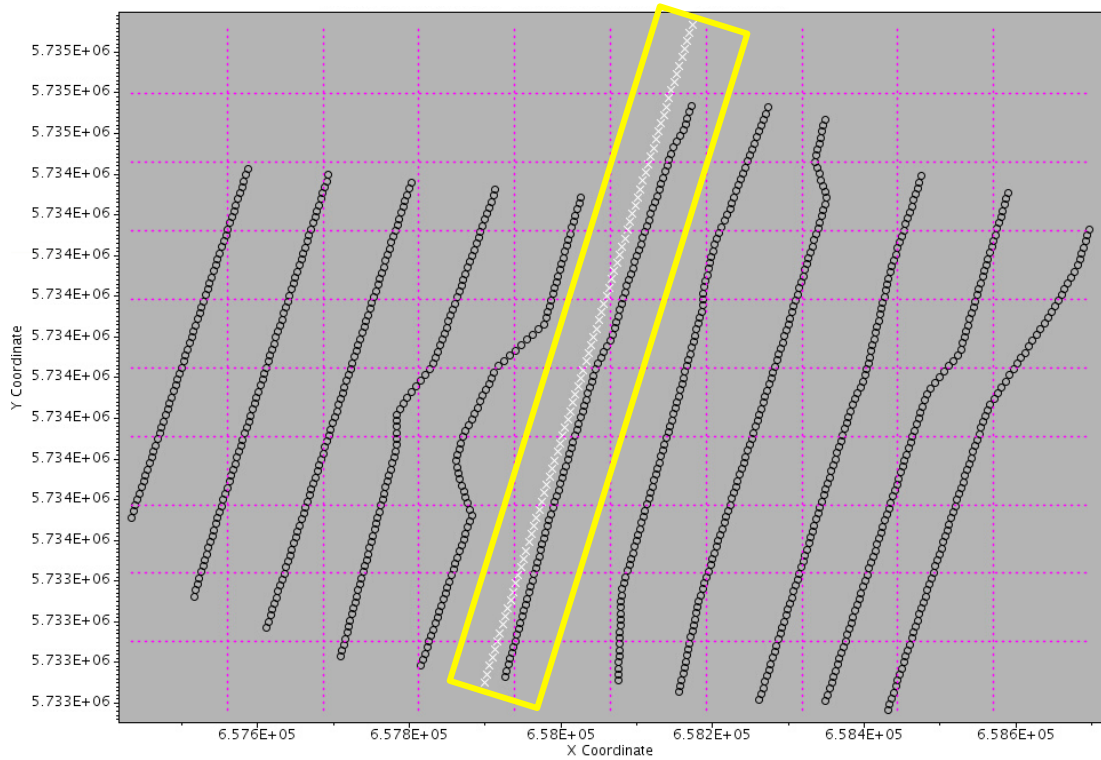


Figure 5.6: The 3D geometry layout of synthetic data with the sources line (white) and the receivers lines (black). The selected 2D line for the entire test is in the yellow box.

Table 5.2: The geometry parameters of the finite difference model for the Otway project Stage 2 synthetic data.

Simulation method	3D elastic finite-difference time-domain (FDTD)
Modelling method	3D-Elastic
Source type	Omnidirectional source
Source position	Surface
Seismic wavelet	Zero phase Ricker wavelet
Frequency	70 Hz
Number of sources	81
Source interval	10 m
Receivers lines	11

Depth	2 km
Receiver interval	10 m
Sample rate	1 ms

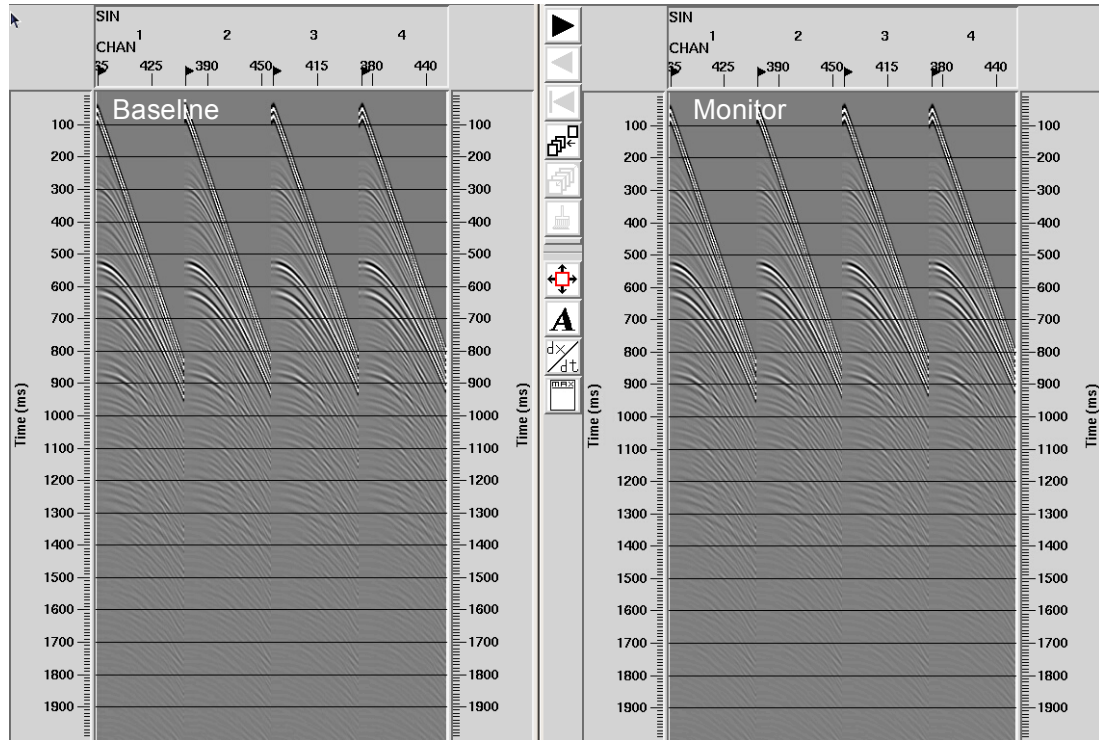


Figure 5.7: Noise-free shot gathers of synthetic baseline (left) and monitor (right) data acquired using MPI code SOFI 3D software.

5.5 Seismic Migration

Seismic migration is the method used to accurately image the subsurface by relocating and filtering recorded seismic waveforms to show the features from which the waves reflect/diffract. In other words, to present the seismic image with high accuracy, migration, reflection and diffraction algorithms are used to reposition the recorded waves to their correct locations, thus revealing actual underground events. However, the variation in velocities and layer dipping affect the imaging accuracy of the subsurface reflection and diffraction layers. This problem affects the two main methods, post-stack and pre-stack migrations, in different ways.

Post-stack migration is a widely used migration algorithm. That is because it is fast and cost-effective when compared to pre-stack migration. This migration algorithm is performed after applying the conventional seismic processing steps and stacking the data using normal moveout or dip-moveout corrections. It is used to relocate all primary reflection and diffraction events to their true subsurface locations based on the energy of relative position (Bancroft, 1997), as shown in Figure 5.8. The Post-stack algorithm is very useful in a small dipping and uncomplicated layer structure.

Pre-stack migration involves applying migration corrections to seismic data, without the stacking step of seismic processing, using information about the source and receiver locations. This type of migration requires a very accurate velocity model. It is very effective for very complex structures. To illustrate, imaging of salt diapirs is one of the most difficult tasks in seismic migration because they have complex geometry and attenuate the seismic signal. Pre-stack migration plays an important role in imaging their structure where hydrocarbons are commonly trapped (Malaguti et al., 2001). Pre-stack migration technique is very valuable in seismic imaging but it is costly in terms of time and money. Therefore, post-stack is usually the primary choice in seismic imaging of the subsurface. However, if the results are poor the pre-stack method is the preferred solution.

In 1882, Gustav Kirchhoff invented a new mathematical theory that would help in imaging the subsurface propagation of waves by combining two very important principles, Huygens' principle of wave propagation and Fresnel's principle for diffraction, reflection and refraction of waves (Miller, 1991). Kirchhoff migration algorithms assume that every reflected wave is a diffracted wave and comes from a diffraction point of unknown amplitude. This assumption is useful when imaging subsurface locations by capturing the smallest amount of energy from reflected or diffracted waves. More information about Kirchhoff's mathematical theory and formulas and their application can be found in (Schneider, 1978), (Miller, 1991), (Sheriff and Geldart, 1995), (Bancroft, 1997), (Yilmaz, 2001), (Biondi, 2001) and Malaguti et al. (2001).

In this chapter, I used Kirchhoff's theory in pre-stack and post-stack time migration because it is commonly used and more flexible when compared to other

algorithms. Moreover, it can be applied to 2D and 3D seismic data in time and depth domains. In addition, the Kirchhoff migration is a reference for many migration algorithms and can deal with shear waves and dip filters and can avoid imaging spatially aliased events by using increasing sampling (Biondi, 2001).

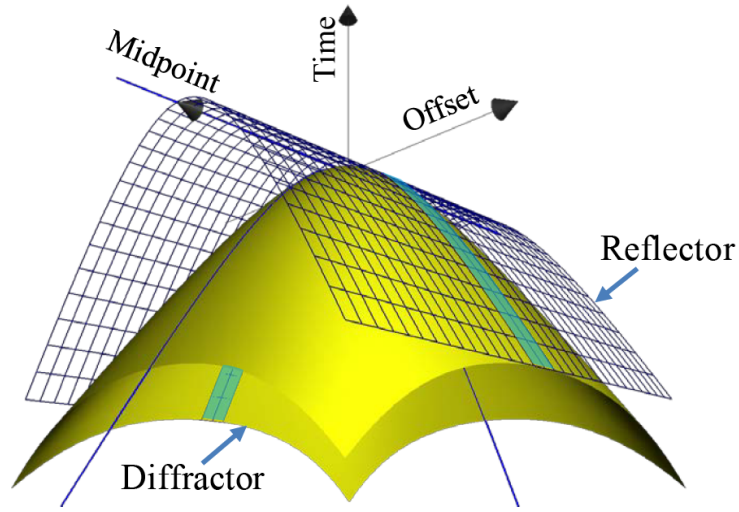


Figure 5.8: The depiction of seismic wave scattering on both reflection surfaces (blue) and diffraction hypersurfaces (yellow) (Tertyshnikov, 2014).

5.6 Modelling of 2D Time-Lapse Noise

5.6.1 Overview

CO₂ seismic monitoring is used to observe time changes in seismic signals and to help in understanding the causes that contribute to these changes. Modelling seismic time-lapse noise plays a significant role in assessing CO₂ seismic monitoring effectiveness. Herein, I estimated the real noise using the same SNR measurement technique used in Chapters 3 and 4 of this thesis. I then used the estimated noise to contaminate the synthetic shot gather data to the same level as that of real noise and then migrate them in two ways then compared the differences in their effect on CO₂ plume detectability.

5.6.2 Estimating the SNR of real data

Noise is one limiting factor in the seismic monitoring of CO₂ detectability. To model realistic noise in the time-lapse data, I first need to understand the level of noise in the real data. To this end, I evaluated the SNR attribute on the real data (the SNR attribute was discussed in section 3). As previously mentioned, I chose the Sodas Road data to apply this attribute.

The results of the SNR attribute with a time window length of 100 ms are shown for the Sodas road section in Figure 5.9. In this figure, the red ellipse highlights the amount of noise that I applied to the synthetic data. The reason for focusing on this depth is because it is the suggested location for the CO₂ injection in Stage 2 of the Otway project.

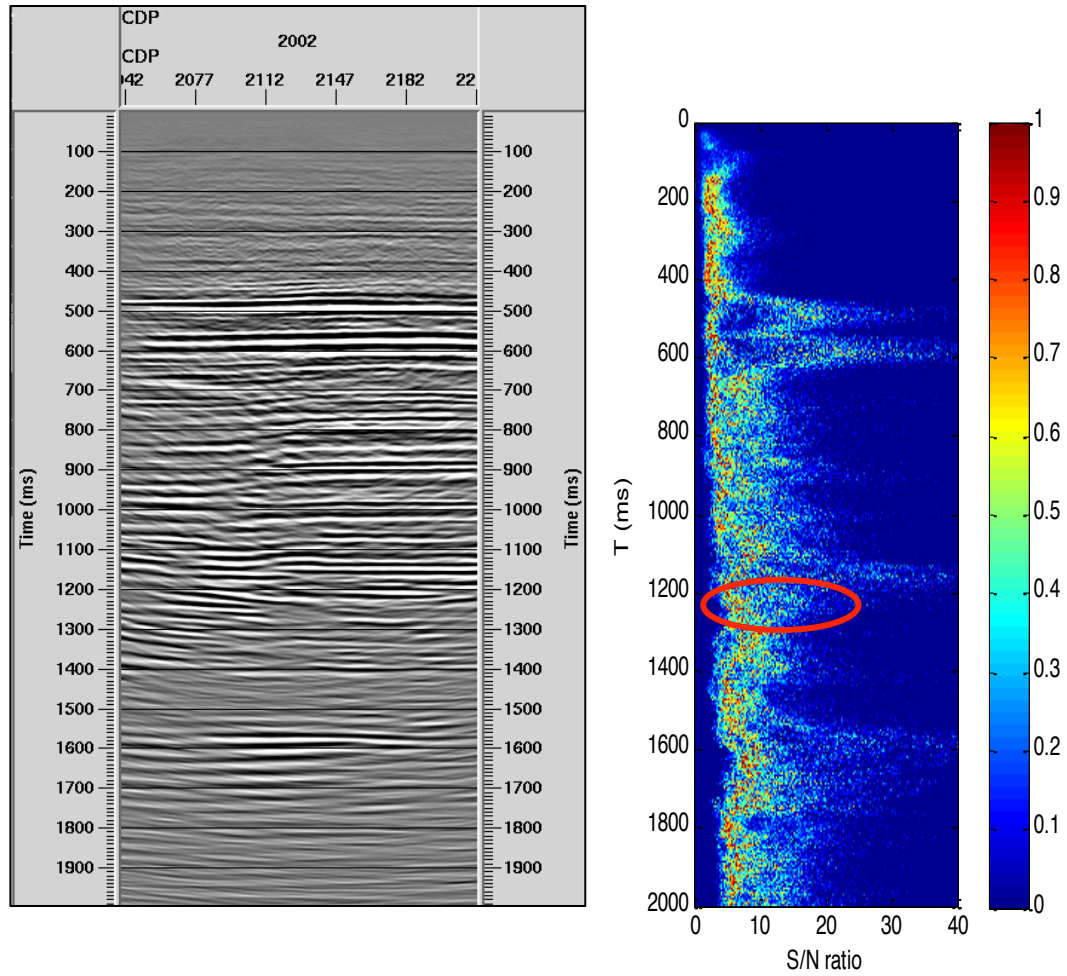


Figure 5.9: The migration section of Sodas Road data and its SNR results. The red ellipses show the level of noise around the suggested injection plume depth, which was added to the synthetic data to match the level noise.

The noise-free seismic response of the time-lapse synthetic baseline and monitor data and their differences are shown in Figure 5.10. This result shows high detectability of the CO₂ injection for the plumes. However, a noise-free result is not sufficient to evaluate CO₂ detectability and the response of the time-lapse seismic signal, which must be simulated using realistic noise in order to assess the actual detectability of the CO₂ plumes. To do that, I added band-limited noise to the data based on the observed SNR values of the real data, as shown Figure 5.11. In this figure, a comparison of the SNR histograms of real noise with modelled noise is shown; the

red ellipses indicate the amount of noise in real data (right) and modelled noise (left) corresponding to the amount of noise at the depth of the injection zone. This realistic modelled noise is added to the migration noise-free data using the same steps as in Chapters 3 and 4. The addition of realistic noise to the synthetic data for the baseline and the monitor is shown in Figure 5.12 together with their difference. The CO₂ plume is detectable in the monitor and difference sections.

The characteristics of the noise in the difference section around the plume does not have a realistic behaviour because it is not affected by the seismic migration algorithms, as shown in the zoomed view of Figure 5.12. To assess the detectability of CO₂ accurately, another way of involving modelled noise is required to make the modelled noise more realistic. Thus, I added the modelled noise to the synthetic shot gather data set before the migration operation in order to determine how much the modelled noise characterisation is impacted by the migration algorithms. To do that, I followed conventional seismic processing for synthetic base and monitor data with modelled noise.

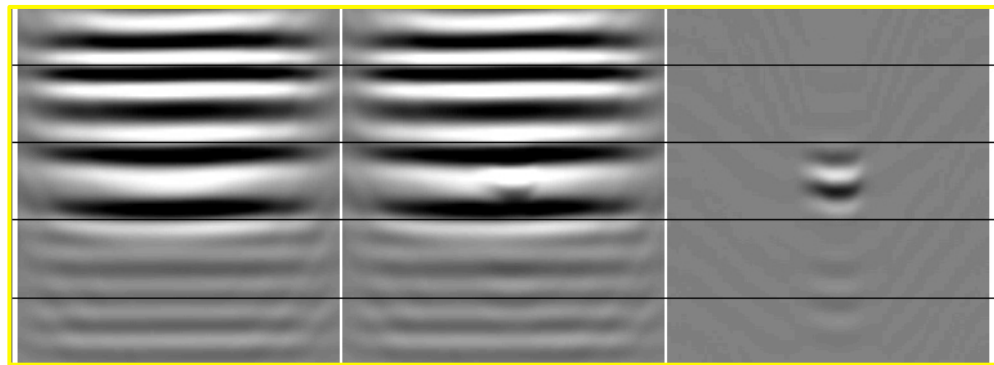
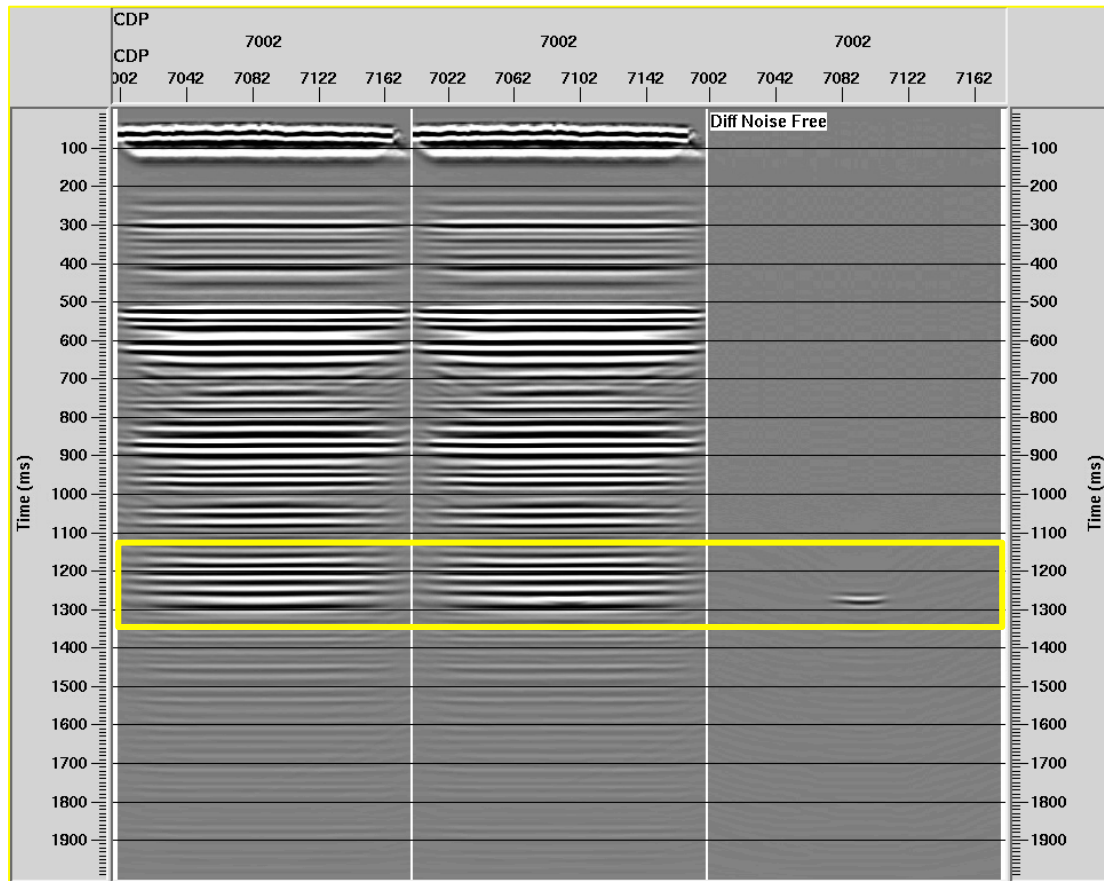


Figure 5.10: Noise-free seismic sections of the synthetic baseline, monitor, and difference data. The CO₂ plume is clearly detectable in the difference section and can be detected in the monitor section in the enlarged figure below. Realistic noise should be modelled and added to evaluate the actual detectability of CO₂.

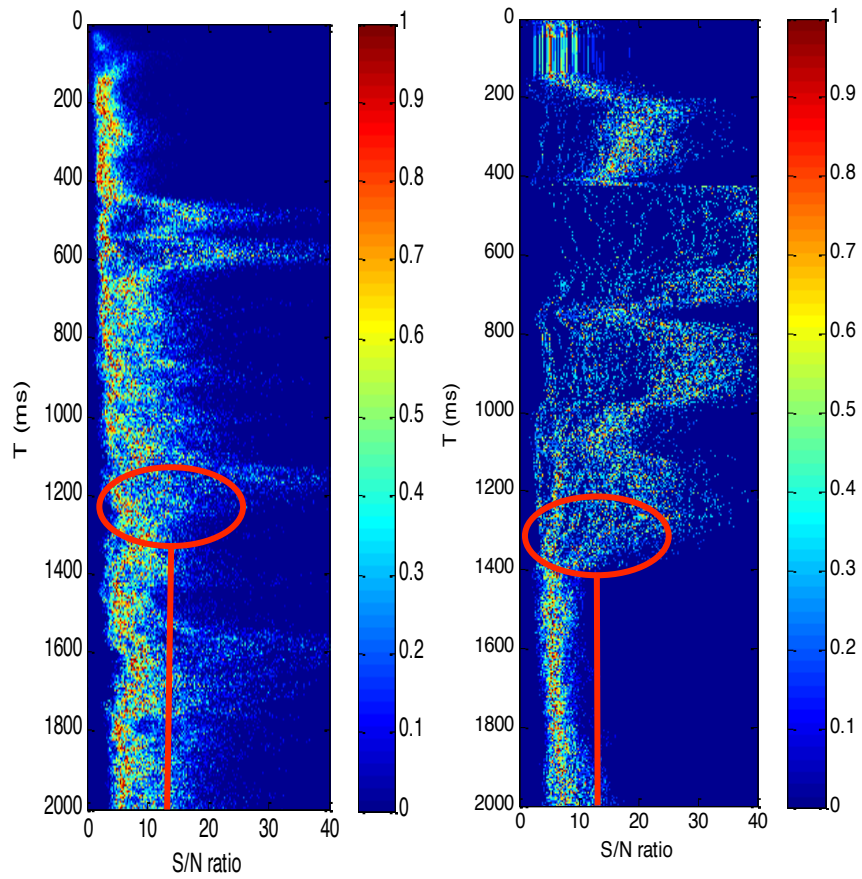


Figure 5.11: The comparison of the SNR computed with a 100 ms window in histograms for each time slice for real data (left) and matching realistic modelling noise (right). The red ellipses indicate the amount of noise that was added to the synthetic data to match the real level of noise in the injection zone. This amount of noise has a range of SNR between approximately 3 and 20 and the maxima of the distribution of SNR matches well for the deeper parts of the data.

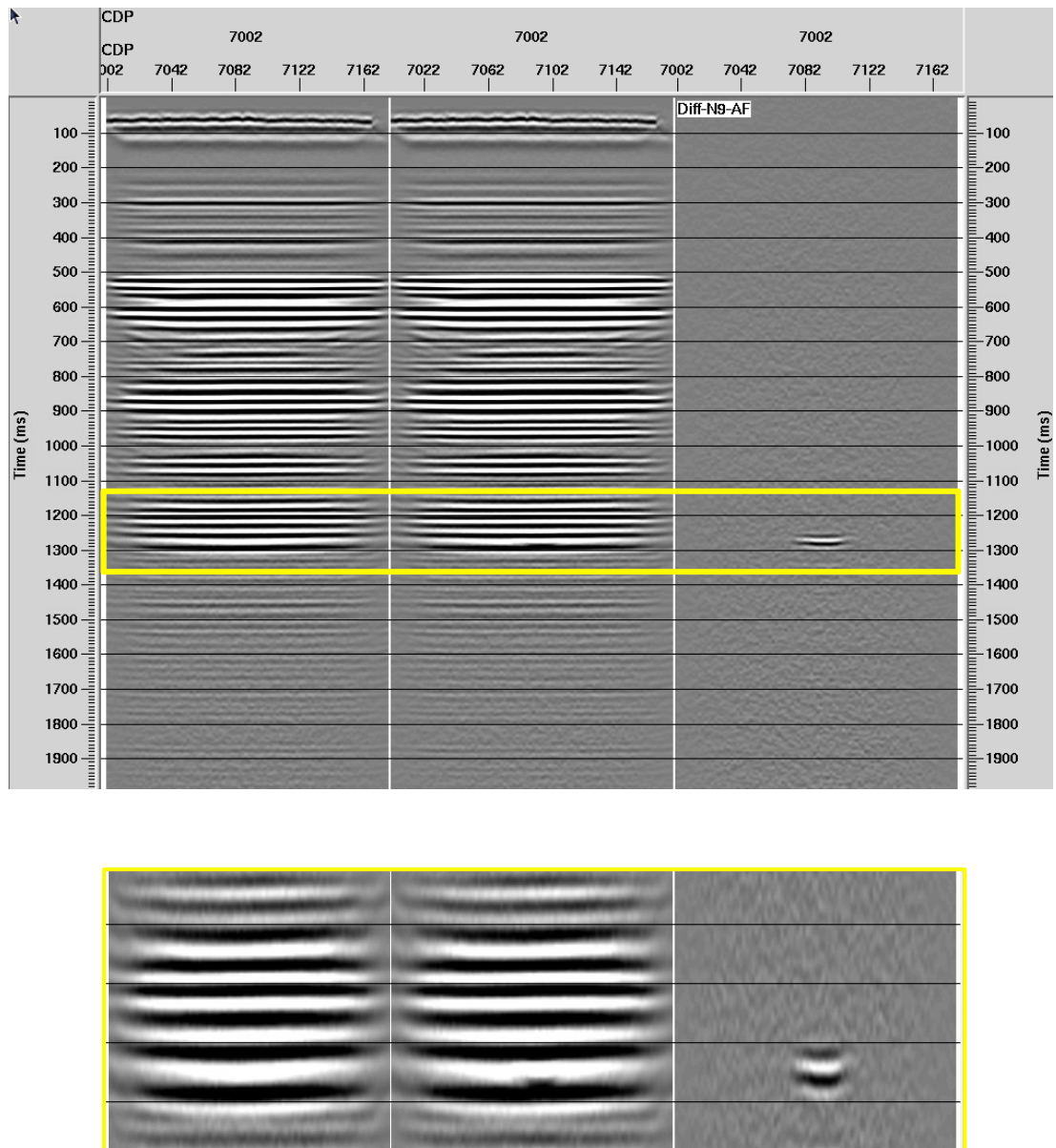


Figure 5.12: The results of the migrated synthetic baseline, monitor and difference section, with added filtered realistic noise from the SNR estimation. In the enlarged figure (below), the CO₂ plume is detectable, but the noise around the plume did not model realistically as it is affected by the migration algorithm and moveout correction.

5.6.3 Migration Comparison and CO₂ Detectability

In previous discussions in Chapters 3 and 4, I modelled realistic noise based on the estimation of the SNR of the real data and added the modelled noise to the synthetic migrated data to assess the detectability of CO₂. In fact, the modelled noise added to the baseline, monitor and difference section does not behave as real noise. To ensure the modelled noise correlates well with real noise in field data, I added the band-limited random noise to the synthetic shot gathers of baseline and monitor data before the seismic migration is carried out (Figure 5.13). The level-added noise was set to match the noise level after the migration with the real migrated data, as discussed in the previous section. I processed the data and pick the sample velocity to generate an accurate velocity model. To achieve the appropriate migration result, I smoothed the velocity for the pre-stack and post-stack time migration applications. Afterwards, I compared all the migration results to determine the appropriate realistic method I used in feasibility studies to evaluate CO₂ detectability in Stage 2 of the Otway project.

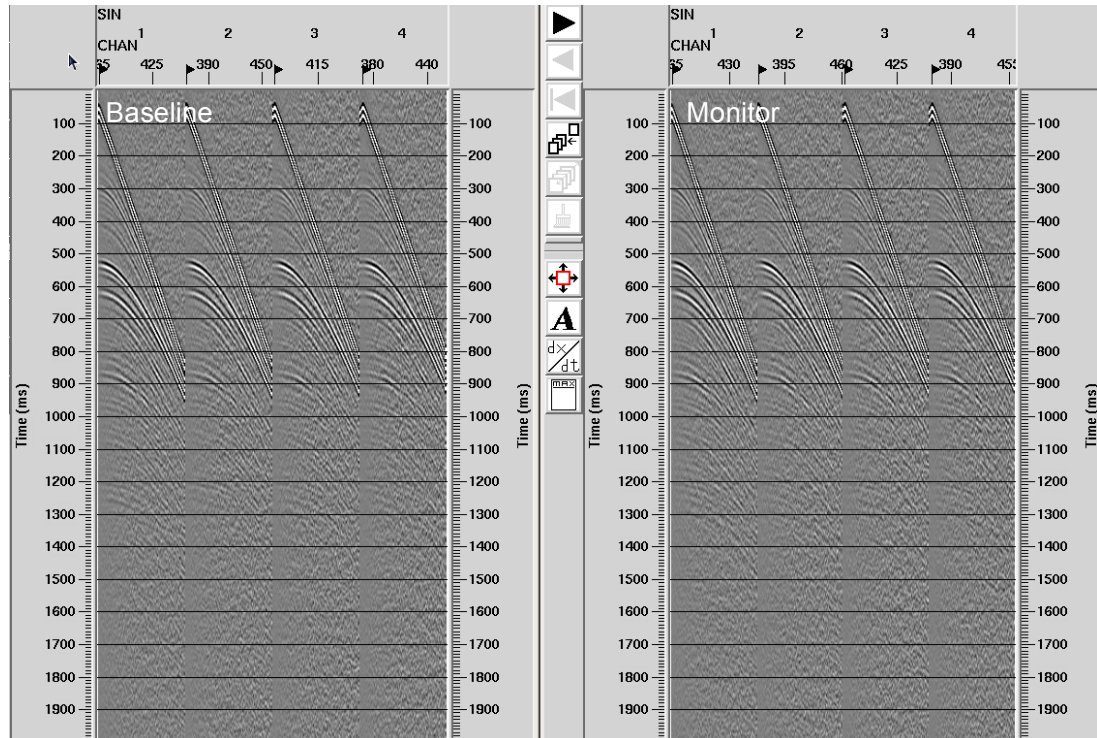


Figure 5.13: The synthetic shot gather baseline and monitor line with added filtered realistic noise from the SNR estimation.

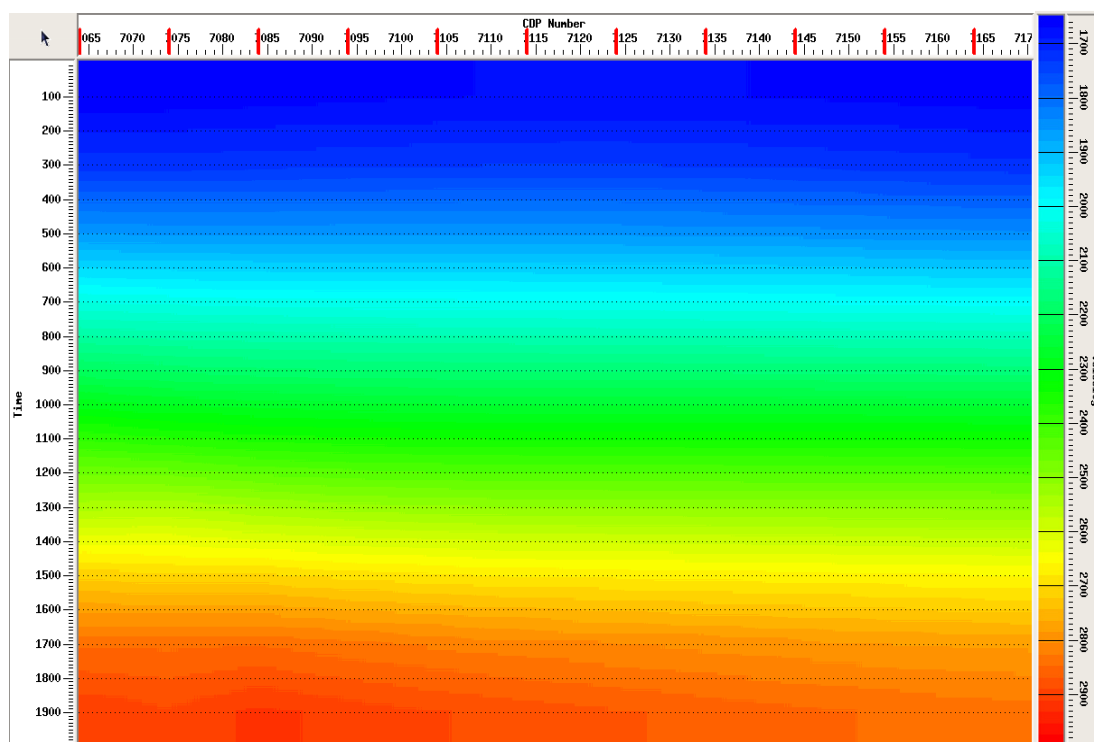


Figure 5.14: Smoothed root mean squared (RMS) velocity model of Sodas Road synthetic data.

I analysed and pick the velocity using super gather sample data to get the suitable stacking velocity for the normal moveout correction. I smoothed the velocity and generate the root mean squared (RMS) velocity to apply in both pre- and post-stack time migration (Figure 5.14). First, I stacked the data with this smoothed velocity and then migrated the stacking data using the Kirchhoff post-stack migration algorithm. The post-stack image with added realistic modelled baseline and monitor noise (Figure 5.15) shows a more realistic result; both the signal and noise are affected by the migration imaging. The CO₂ detectability is very low in the difference section and in the zoomed figure (below). The CO₂ plume in the white circle is significantly affected by the migrated band-limited noise, whether in the monitor or the difference section.

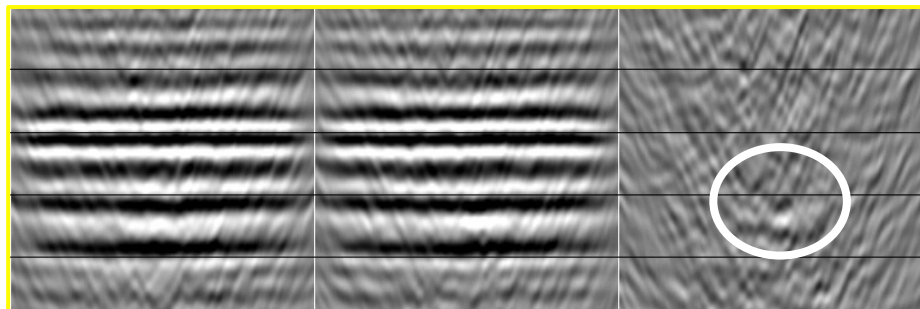
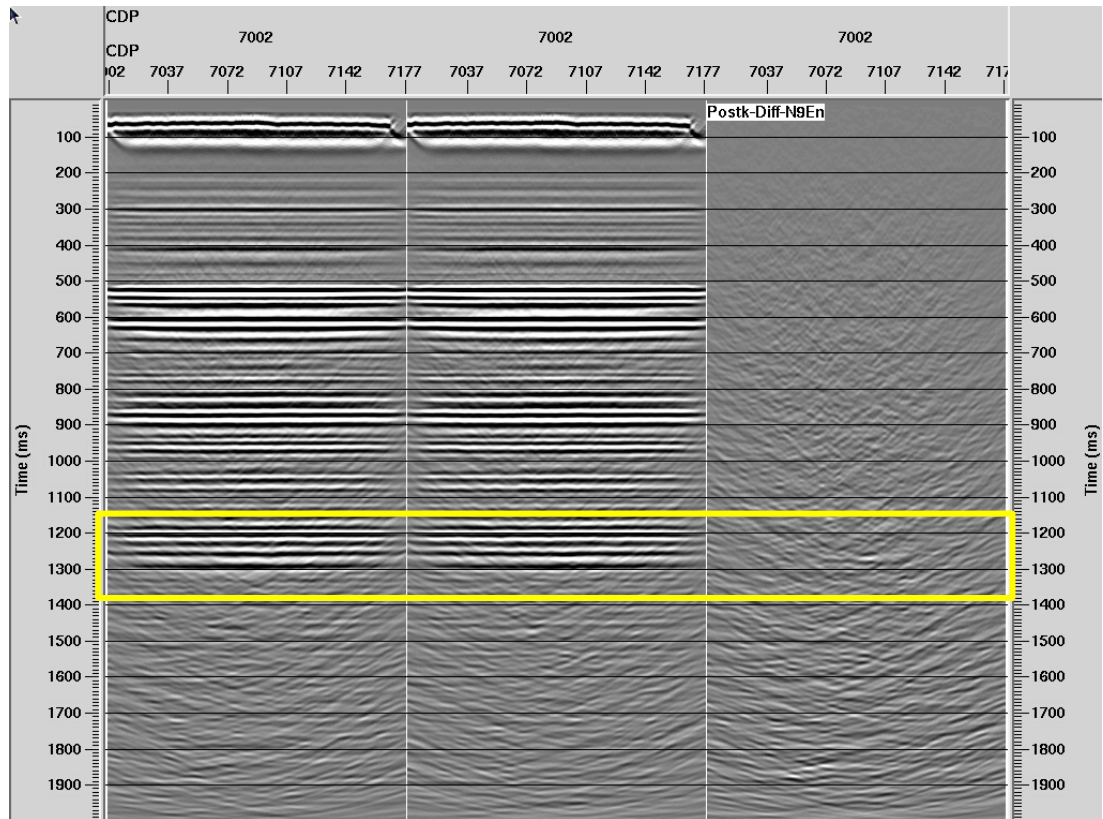


Figure 5.15: The imaging results of the post-stack migration baseline, monitor and difference synthetic section. It is clear that the modelled time-lapse noise is affected by the migration operation. In the zoomed figure (below), the low detectability of CO₂ in the monitor and difference sections is greatly affected by the post-stack migration technique, as shown in the white circle.

The result of post-stack migration is successful in showing the best form of realistic noise that can be observed in conventional migrated seismic signals (as we will see in the next chapter). However, the image of the CO₂ plume is not clear enough. Therefore, in the next test, I migrated the shot gathers directly using the Kirchhoff pre-stack migration algorithm with the same smoothed RMS velocity model and migration process parameters. The results of the migrated pre-stack baseline, monitor and difference sections are shown in Figure 5.16. The zoomed figure (below) shows good detection of the CO₂ plume, which is better than the post-stack result (Figure 5.15). In addition, to estimate the level of non-repeatable noise between the baseline and monitor using pre- and post-stack algorithms, I applied the NRMS measurement (see chapter 2 and 4 for more details about NRMS). The NRMS values show increasing non-repeatability (or difference in the two vintages) in the pre-stack image, in particular, at the injection zone (the white circle) (Figure 5.16). This indicates better plume detectability by using pre-stack time migration.

The analysis of the post-stack and pre-stack migration tests highlights two points. First, the added noise in these experiments is more realistic and correlates with the migrated signal compared to when the noise was added after the migration step. Second, the comparison of CO₂ detectability in the difference sections, as shown in Figure 5.17, emphasises that the pre-stack migration algorithm is more suitable for time-lapse signal detection of the CO₂ injection than the post-stack migration algorithm. Regardless of the CO₂ detectability, in comparing this result of adding noise before migration with the result of adding noise after migration, such as in the previous experiment, we find that adding the noise before migration shows a more realistic time-lapse signal and noise (Figure 5.19).

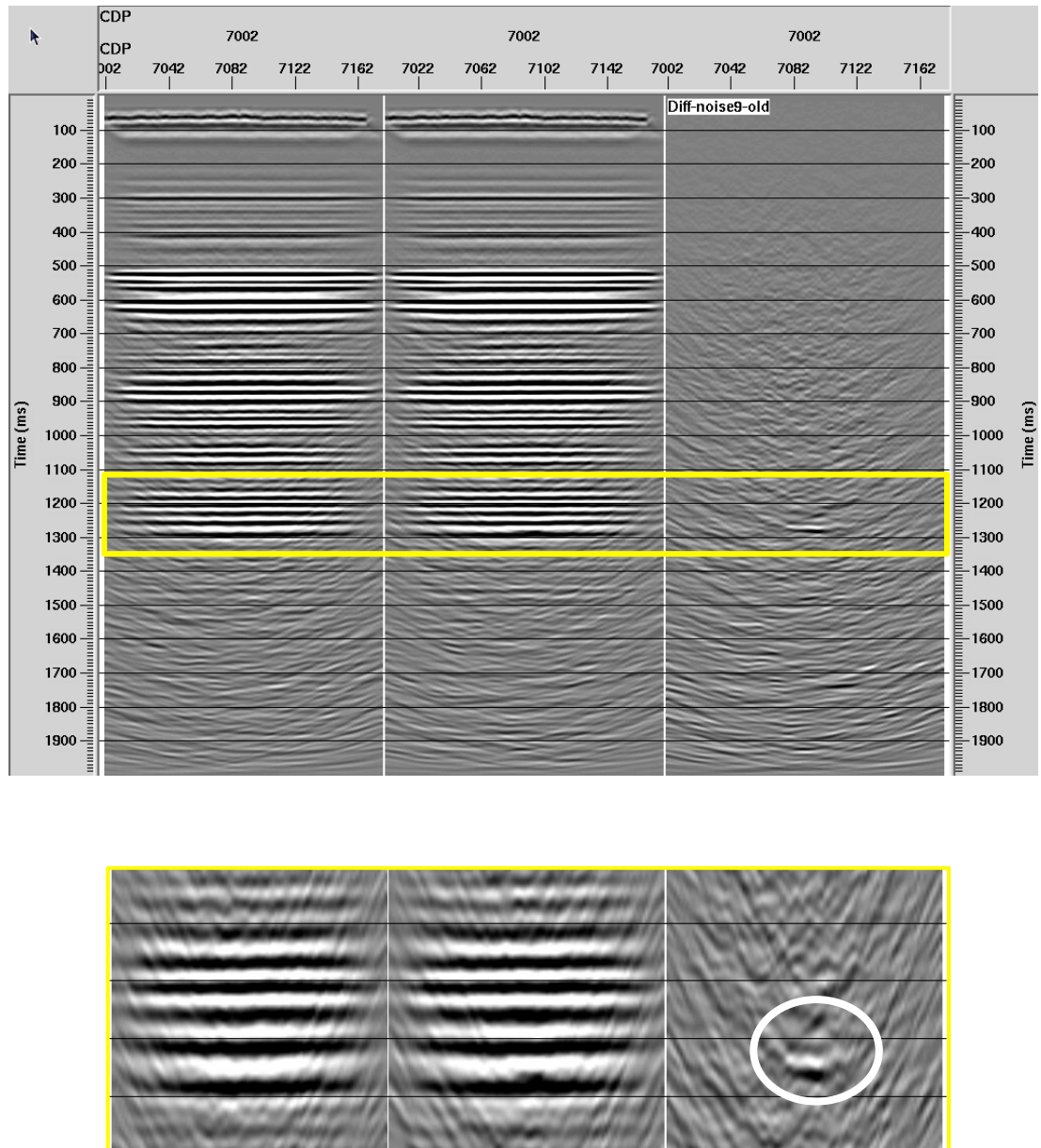


Figure 516: The imaging results of the pre-stack migration baseline, monitor and difference synthetic sections. In the zoomed figure below, the improvement in the detection of the CO₂ plume in the monitor and difference sections (in the white circle) can be seen, corresponding to the post-stack result. This makes this migration technique more powerful in time-lapse seismic evaluation of CO₂ detectability.

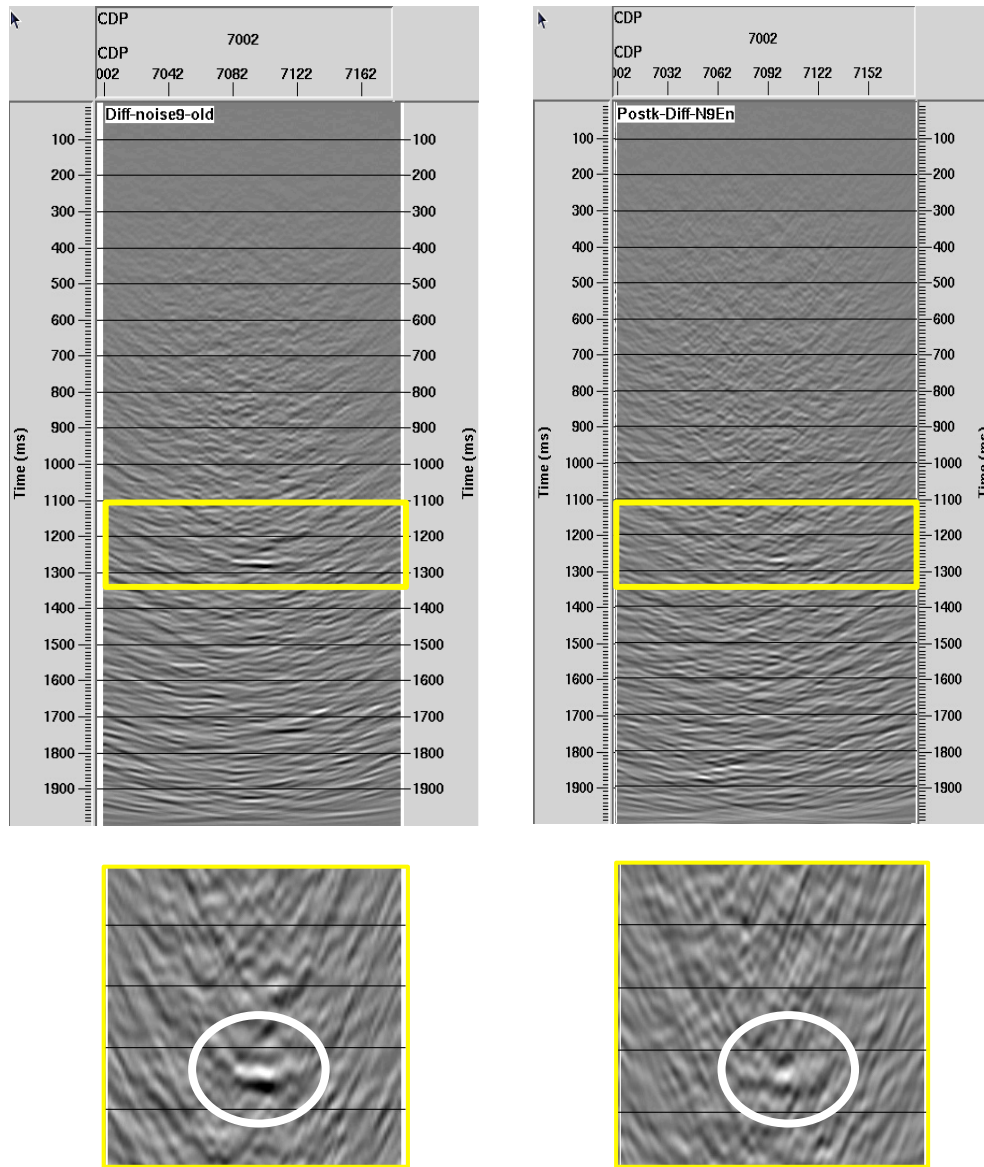


Figure 5.17: The comparison of the difference sections of pre-stack migration results (left) and post-stack (right) migration results. In the white circles in the zoomed figure below, it is clear that the pre-stack migration in the difference section can detect the time-lapse signal of the CO₂ plume using the same parameters and velocity that were used in the post-stack test. This proves the ability of the pre-stack migration algorithm in the time-lapse seismic evaluation of CO₂ detectability.

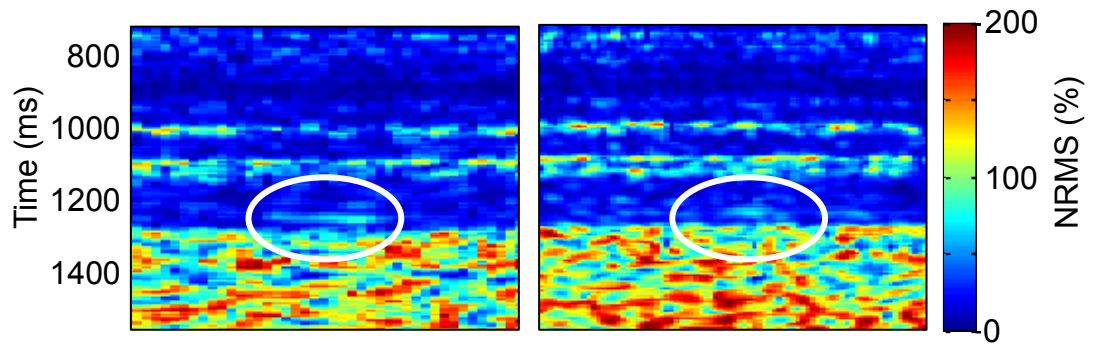


Figure 5.18: The NRMS result computing with a time window of 30 ms in log10 scale for pre-stack migration (left) and post-stack migration (right). The NRMS values show increasing non-repeatability in the pre-stack image comparing to post-stack image at the injection zone (the white circle).

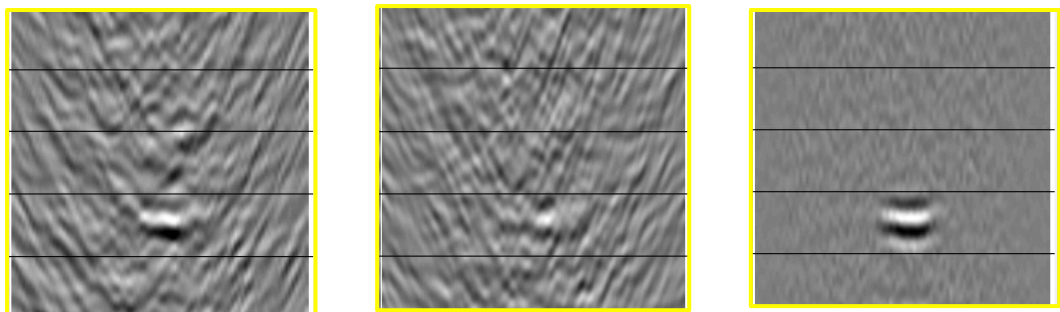


Figure 5.19: The comparison of the results of adding modelled noise before migration pre-stack (left) and post-stack (middle) and after migration (right). The evaluation of CO₂ seismic monitoring is more realistic when adding noise before migration compared to adding noise after migration.

5.7 Conclusion

In this chapter, I presented a feasibility study of time-lapse seismic methods in CO₂ monitoring and verification for Stage 2 of the Otway Project. 2D time-lapse seismic baseline and monitor synthetic data sets are extracted from 3D FDTD in order to investigate the detectability of CO₂ for Otway project Stage 2. In the case of noise-free time-lapse data, the difference of the migrated sections shows high detectability for the plumes. To study detectability of the plume, one needs to consider noise as well as the signal. One can try to add the noise after migrating the data to simulate realistic noise levels in time-lapse data. I did this by adding band-limited noise to the migrated sections to match observed SNR of real data. However, such noise modelling is not very realistic, as I will discuss in the next chapter. To make the time-lapse noise more realistic, I added band-limited random noise to the pre-stack data using the same SNR technique that was used in Chapters 3 and 4, based on the Sodas Road field data from the Otway region. The noise-polluted shot gathers were then migrated using two migration approaches.

In this chapter, I examined two applications of Kirchhoff migration algorithms for post-stack and pre-stack time migration. The difference section in the post-stack migration, including the modelled noise, shows relatively low detectability of CO₂. This indicates that the post-stack migration algorithm cannot fully image the response of the CO₂ plume signal in the difference section using this level of noise and that the migrated modelled noise hides the plume. This may be due to the fact that post-stack migration attenuates diffractions, which may contribute to the poor plume image of the studied size (15,000 tonnes). The next migration test to assess CO₂ time-lapse seismic monitoring is pre-stack migration. Using the same velocity model, migration tools and modelled noise, the results of the pre-stack monitor and difference sections show a detectable CO₂ plume, clearer than the post-stack results. Based on that, I can state that the CO₂ injection in Stage 2 of the Otway project is detectable and the time-lapse seismic surface is a feasible method to monitor the CO₂ injection.

To sum up, Kirchhoff pre-stack time migration is a highly effective time-lapse imaging method for CO₂ verification and monitoring and is therefore the recommended method. The limitation of this feasibility study is that all the tests are based only on baseline 2D field data. However, in the next chapter, we will use real

3D time-lapse data to assess the time-lapse method of CO₂ detectability for CCS in Stage 2 of the Otway project by applying a new approach of modelling the time-lapse noise.

In this chapter, I investigated the detectability of CO₂ in Otway Stage 2 by applying two different seismic migration imaging algorithms. I processed the field 2D seismic data and synthetic data with common offset binned data and migrated them using a pre-stack and post-stack 2D Kirchhoff time migration algorithm. I used modelled 2D synthetic shot gathers, data baseline and monitor with an injected plume of approximately 15,000 tonnes, which was injected at a depth of 1500 m. The finite-difference time-domain (FDTD) model was computed by Curtin University staff. I propose a more realistic approach by adding band-limited random noise to the pre-stack data (shot gathers) to match the SNR of field data. Using these noisy gathers, I then compared the detectability of the CO₂ plume by using pre- and post-stack Kirchhoff migrations. The downside of this assessment is that all the tests are based only on baseline 2D field data. However, in the next chapter, I will use real 3D time-lapse data to assess the time-lapse method of CO₂ detectability for CCS in Stage 2 of the Otway project by applying a new approach of modelling the time-lapse noise.

5.8 References

- Alonaizi, F., R. Pevzner, A. Bóna, M. Alshamry, E. Caspari, and B. Gurevich, 2014, Application of diffracted wave analysis to time-lapse seismic data for CO₂ leakage detection: *Geophysical Prospecting*, **62**, 197-209.
- Bancroft, J. C., 1997, A practical understanding of pre-and poststack migrations: Society of Exploration Geophysicists.
- Biondi, B., 2001, Kirchhoff imaging beyond aliasing: *Geophysics*, **66**, 654-666.
- CO₂CRC, 2013, The Cooperative Research Centre for Greenhouse Gas Technologies <http://www.co2crc.com.au/>.
- Dance, T., Year, A workflow for storage site characterisation: A case study from the CO₂CRC Otway Project, AAPG/SEG/SPE Hedberg Conference, 16–19 August, 2009 Vancouver, BC, Canada, AAPG Search and Discovery Article.
- Dance, T., M. Arnot, M. Bunch, R. Daniel, A. Hortle, M. Lawrence, and Ennis-King, 2012, Geocharacterisation and Static Modelling of the lower Paaratte Formation. CO₂CRC Otway Project–Phase II: Cooperative Research Centre for Greenhouse Gas Technologies.CO₂CRC Publication Number RPT12-3481.
- Gurevich , B., R. Pevzner, M. Urosevic, A. Kepic, V. Shulakova, and E. Caspari, 2014, 2D and 3D seismic investigations for Stage 1 and 2C, *in* P. J. Cook, ed., *Geologically storing carbon: Learning from the Otway Project Experience*: CSIRO Publishing, 155-196.
- Jenkins, C., S. Sharma, and G. Morvell, 2009, Proposal for an extension to the CO₂CRC Otway research and development project: CO₂CRC Report, RPT08–1147, .
- Lumley, D., 2010, 4D seismic monitoring of CO₂ sequestration: The Leading Edge, **29**, 150-155.
- Malaguti, R., M. Allen, A. Litvin, and C. Gregory, 2001, Sub-salt imaging using 3D pre-stack depth migration in the Uk Southern North Sea-a case history: first break, **19**.
- Miller, D. A., 1991, Huygens's wave propagation principle corrected: *Optics letters*, **16**, 1370-1372.
- Pevzner, R., R. Galvin, M. Madadi, M. Urosevic, E. Caspari, B. Gurevich, D. Lumley, V. Shulakova, Y. Cinar, and V. Tcheverda, 2012, Monitoring CO₂ injection into a saline aquifer: Otway Project feasibility study: Presented at the SEG Technical Program Expanded Abstracts 2012.

- Pevzner, R., M. Urosevic, E. Caspari, R. J. Galvin, M. Madadi, T. Dance, V. Shulakova, B. Gurevich, V. Tcheverda, and Y. Cinar, 2013, Feasibility of Time-lapse Seismic Methodology for Monitoring the Injection of Small Quantities of CO₂ into a Saline Formation, CO₂CRC Otway Project: Energy Procedia, **37**, 4336-4343.
- Schneider, W. A., 1978, INTEGRAL FORMULATION FOR MIGRATION IN TWO AND THREE DIMENSIONS: Geophysics, **43**, 49-76.
- Sheriff, R. E., and L. P. Geldart, 1995, Exploration seismology: Cambridge university press Cambridge.
- Tertyshnikov, K., 2014, Seismic imaging in hard rock environments: PhD, Curtin University
- Urosevic, M., R. Pevzner, V. Shulakova, A. Kepic, E. Caspari, and S. Sharma, 2011, Seismic monitoring of CO₂ injection into a depleted gas reservoir–Otway Basin Pilot Project, Australia: Energy Procedia, **4**, 3550-3557.
- Yilmaz, Ö., 2001, Seismic data analysis: Society of Exploration Geophysicists Tulsa.

Every reasonable effort has been made to acknowledge the owners of copyright material. I would be pleased to hear from any copyright owner who has been committed or incorrectly acknowledge.

CHAPTER 6: 3D TIME-LAPSE NOISE MODELLING USING DATA FROM THE CO2CRC OTWAY PROJECT

6.1 Introduction

In CO₂ sequestration, the ability to detect the CO₂ plume is one of the main purposes of using time-lapse seismic imaging. The detectability of CO₂ in seismic time-lapse surveys relies on two main factors: the signal and the noise. Thus to model such a seismic experiment, I needed to model not only the seismic response of the geology and the plume, but also the time-lapse 3D noise. Hence, since the detectability of a plume is given by the signal-to-noise ratio, the ability to model realistic time-lapse noise plays a crucial role in any feasibility study.

All seismic data sets, whether land, marine, or vertical seismic profiles, can be contaminated by a variety of unwanted signals, or noise. The designs of many seismic analysis algorithms used in the processing steps and seismic imaging techniques are based on the assumption of noise-free data. Thus, one of the main tasks of pre-processing data is to separate the signal and the noise, where the noise is partially defined by the imaging techniques (Linville and Meek, 1995); for example, multiples can be viewed as noise or a part of the signal, depending on the imaging algorithm. In general, seismic noise is divided into two main classes: coherent (linear and non-linear), and incoherent noise. Coherent noise consists of different waveforms generated by seismic sources such as surface waves (ground roll), multiples, tube waves and converted waves (Kearey et al., 2009). Incoherent noise (also called background noise or random ambient noise) is unwanted noisy waves produced, for example, by rain and wind and so on. Often the data is transferred to other domains to separate the signal from the noise; however, some of these operations may degrade the data, for instance, by suppressing some of the signal (Nemeth et al., 2000). In a 4D survey, the suppression of coherent noise will be influenced by the level of repeatability because the high repeatability of time-lapse data means that most coherent noise in the data will be subtracted in the difference section. This concept is different with random ambient noise because this noise will not repeat in every time-lapse survey or at the same levels even if the repeatability is high; this noise is called non-repeatable noise (Calvert, 2005).

Seismic monitoring is likely to be an important tool in CCS and quantifying its capability is of paramount importance. In particular, to quantify the detectability of CO₂ plume using time-lapse seismic methods, I needed to understand both the signal and the noise; herein I focused on the noise. To be able to perform statistical modelling of the likelihood of the detection, I needed to be able to generate many realisations of time-lapse noise, which have similar characteristics to the actual (or expected) noise. Potential sources of coherent time-lapse noise include changes in environmental conditions, the effect of source generation and acquisition geometry (Hughes, 1998; Landro, 2008). Among the many changes in environmental conditions, near-surface velocity changes play a dominant role (Pevzner et al., 2010). The variation in frequency content, time-shifting in time-lapse image processing and the changes in the phase and amplitude waveform of the 4D signal also have a significant effect on the repeatability of both the signal and noise (Lumley et al., 2003; Spetzler and Kvam, 2006).

Seismic modelling experiments play an important role in our understanding of the subsurface processes, in designing surveys and in interpreting recorded data. To account for uncertainties in our understanding of the subsurface, it is possible to use a statistical approach when creating the models, where one computes the seismic response of a distribution of the geological models. To create realistic models of such experiments, one needs to add noise to the models. Moreover, for the statistical approach one needs to efficiently generate many different realisations of the noise as well.

Generally speaking, there are two possible approaches in the modelling of noise. The first approach is based on a detailed understanding of all possible noise types in seismic data and their potential effects on processing. However, there are many sources of noise, as discussed above, and it is not easy to establish which noises contribute (and to what extent they contribute) to the total noise for each particular survey. Thus, modelling noise based on all these different sources would require a significant effort that would have to be repeated for each model and would not necessarily guarantee a realistic outcome.

The second approach is an empirical one, where the noise model is based on observed data. Often random signals (white or filtered to match the anticipated

frequency band of the seismic data) are added to the synthetic data, as I did in Chapters 3 and 4, which try to mimic the actual level of noise (Johnson, 2001; Pevzner et al., 2012). The downside of this approach is that such noise will not be spatially correlated, which is almost always the case in real conditions. Approach that I took in Chapter 5 alleviates this problem by adding the band-limited noise to the data before migration, which produces some of the observed spatially-correlated noise in the time-lapse section. Even though the time-lapse noise produced by such an approach shows the spatial correlation from the migration artefacts, other effects that normally contribute to the spatially correlated time-lapse noise are not taken into account.

In this work I proposed a simple enhancement to this noise modelling approach, which allows us to overcome this issue. The main aim of this method is to help with generating statistics on time-lapse data, such as detectability of the time-lapse signal, using Monte Carlo type statistical analyses. Such analyses require many realisations of noise. Herein, I proposed a method that generates such noise realisations by modifying the phase spectrum of the measured noise using a windowing approach. This approach aims to preserve the amplitude spectrum of the signal and thus the spatial and temporal correlation of the measured noise. One of the benefits of the proposed method is that it does not distinguish between the different origins of the coherent noise; I am not trying to analyse the different sources of the noise. I demonstrate the applicability of the approach on an example of measured time-lapse noise from the CO₂CRC Otway project. The background of the area, geology of Otway and information about the CCS of Otway Stage 2 project were discussed in detail in section 5.2.

6.2 Time-lapse Repeatability

6.2.1 Sources and Receivers Repeatability

Many surface seismic and VSP data were acquired to explore the Otway Basin field and the area of the Otway Project in particular. In 2000, a large 3D data set was acquired and a small gas field was discovered (Naylor field). In 2008, a Curtin University crew acquired 3D baseline surface seismic data (Figure 6.1). This survey provided the first baseline data before the first CO₂ injection. The survey size

was small, based on the available receiver's cable, at 1.6 x 1.9 km and was divided into two groups: odd source lines and even receiver lines. The first group consisted of 435 channels and were shot by odd lines from line 1 to line 27 together with the even line 28 and recorded by receiver lines (RL) 1–5. The second group consisted of 437 channels that were shot by even source lines (SL) from line 2 to line 24 together with the odd line 29 and acquired by RL 6-10 (Figure 6.2 (a)). The source type for this survey was a 1350 kg weight drop (WD) source (concrete breaker) free-falling from height of 1.2 m. All geophones were fixed during the survey. Due to the weakness of the single-to-noise ratio in the 2008 baseline, the source type was changed from the low energy WD source used in 2008 to a more powerful mini-buggy vibrator source (IVI 15,000 lbs). In all time-lapse data 2008, 2009 and 2010 vibrograms were correlated with sweep signal with following parameters: registration time 16 sec, sweep length 12 sec, start time of sweep 0.5 sec and sweep frequencies 10-150 Hz (Figure 6.3).

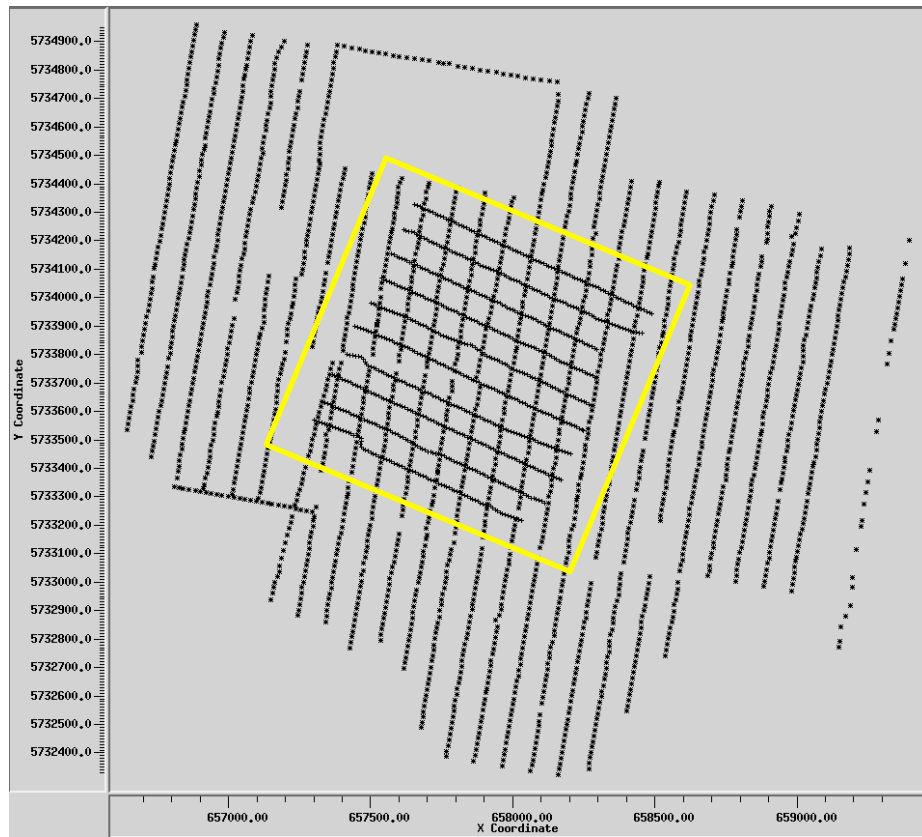
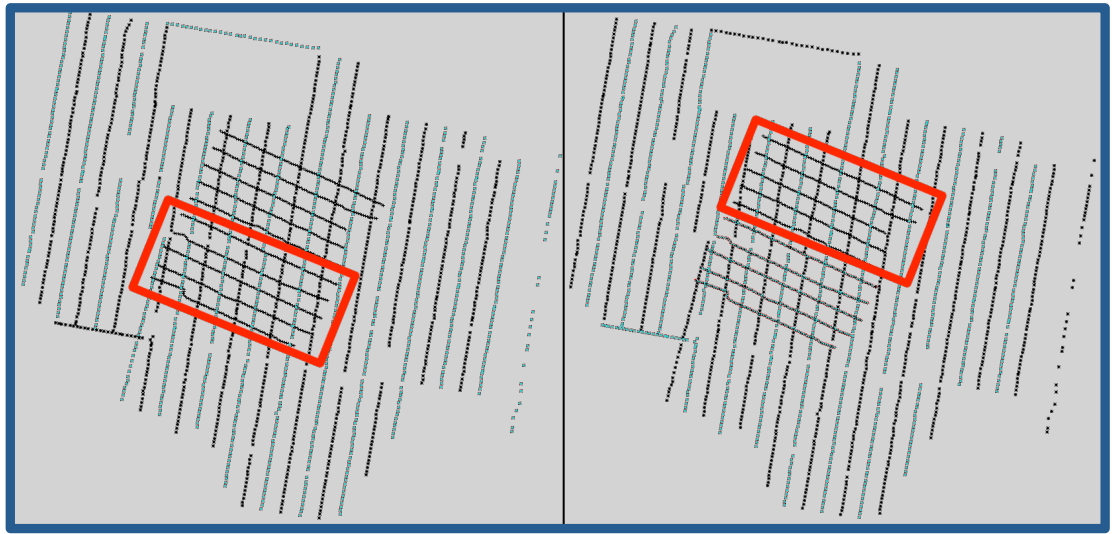


Figure 6.1: Basemap of the 3D Otway acquisition survey layout. The 10 lines in the yellow box are the receiver lines at 10 m intervals. The other lines are the source lines at 20 m intervals.

a)



b)

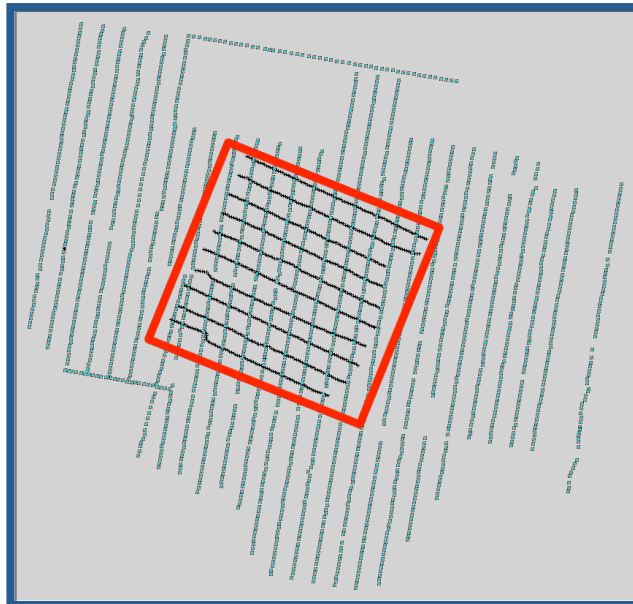


Figure 6.2: Basemap of the 3D Otway acquisition survey layout for (a) 2008 and (b) 2009 and 2010. (a) The right hand side figure shows the odd source lines 1–27 and 28 (marked as blue dots) recorded by receiver lines 1–5 (highlighted by the red rectangle). The left hand figure (a) shows even source lines 2–24 and 29 recorded by receiver lines 6–10. (b) For the 2009 and 2010 surveys all the source lines were recorded by all the receiver lines (highlighted by the red rectangle).

a)



b)



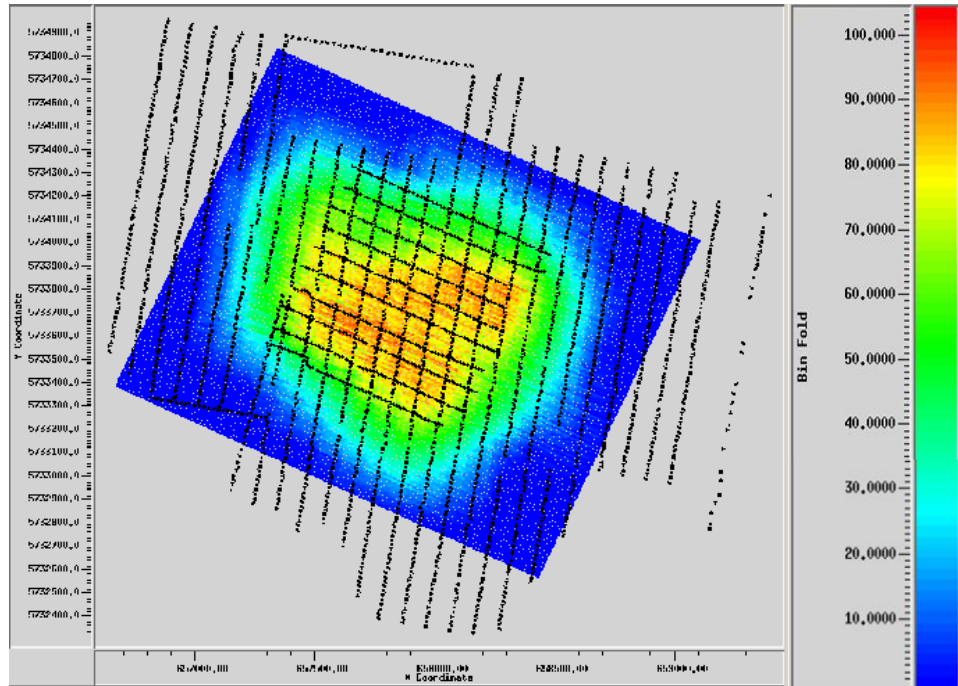
Figure 6.3: Seismic signal sources used in the Otway Project. (a) The weight drop source (a 1350 kg concrete breaker that free fell from 1.2 m) used in the 2008 baseline survey. (b) The mini-buggy source (IVI 15,000 lbs vibroseis) with a sweep frequency range of 10–140 Hz used in the 2009 and 2010 surveys.

Table 6.1: The 3D seismic acquisition parameters. These parameters were used for the time-lapse monitoring surveys in 2008, 2009 and 2010 at the Otway site.

Survey	I	II	III
Date	2008	2009	2010
CO₂ injection volume	Baseline	35 k tonnes	66 k tonnes
Bin size	10 x 10 m	10 x 10 m	10 x 10 m
Source type	Weight drop	IVI 15,000 lb, Mini-vibrator	IVI 15,000 lb, Mini-vibrator
Receiver type	10 Hz geophones	10 Hz geophones	10 Hz geophones
Area size	1.6 km x 1.9 km	1.6 km x 1.9 km	1.6 km x 1.9 km
Number of source points	2181	2223	2223
Source interval	20 m	20 m	20 m
Source line spacing	100 m	100 m	100 m
Number of source lines	10	10	10
Receiver interval	10 m	10 m	10 m
Receiver line spacing	100 m	100 m	100 m
Sample rate	1 ms	2 ms	2 ms

The survey was repeated in 2009 and 2010 in order to monitor the injected CO₂ volumes (which were about 35 k tonnes in 2009 and 66 k tonnes in 2010) that was a part of Stage 1 of the Otway project. The high nominal fold 3D survey was designed to optimise the SNR and improve the repeatability of the time-lapse signal (Urosevic et al., 2011). The nominal stacking fold was approximately 100 for the 2008 survey. This doubled in the 2009 and 2010 surveys to approximately 200, as shown in Figure 6.4, where the full spread (all receiver lines) was used for each shot point.

a)



b)

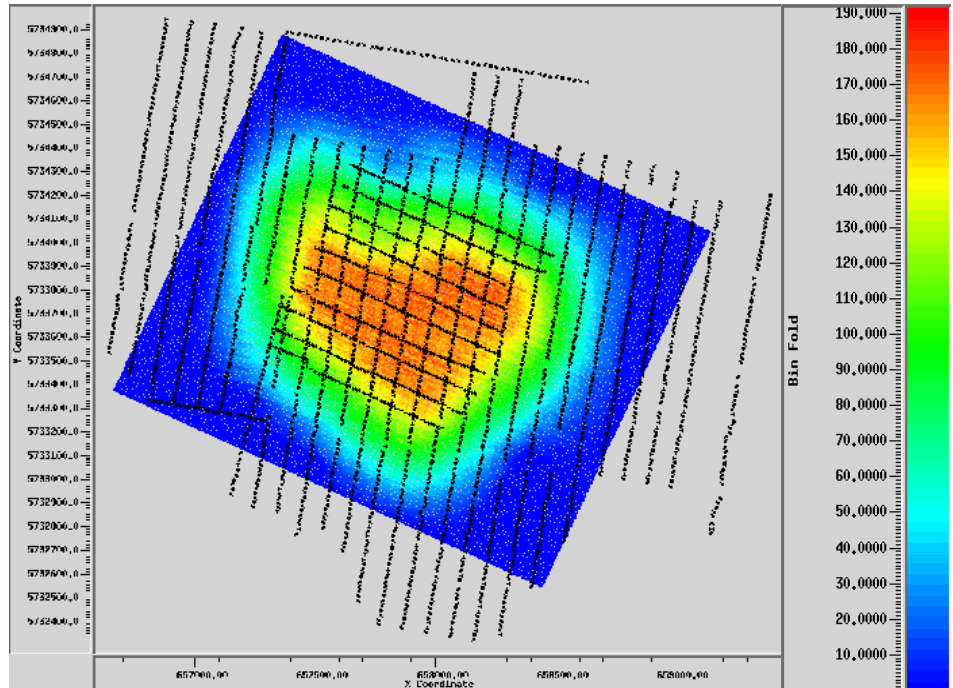


Figure 6.4: The CDP geometry fold map for (a) the 2008 survey and for (b) the 2009 and 2010 surveys. In 2008, the nominal fold was approximately 100, but with survey parameter changes, the nominal fold doubled in the 2009 and 2010 surveys to approximately 200.

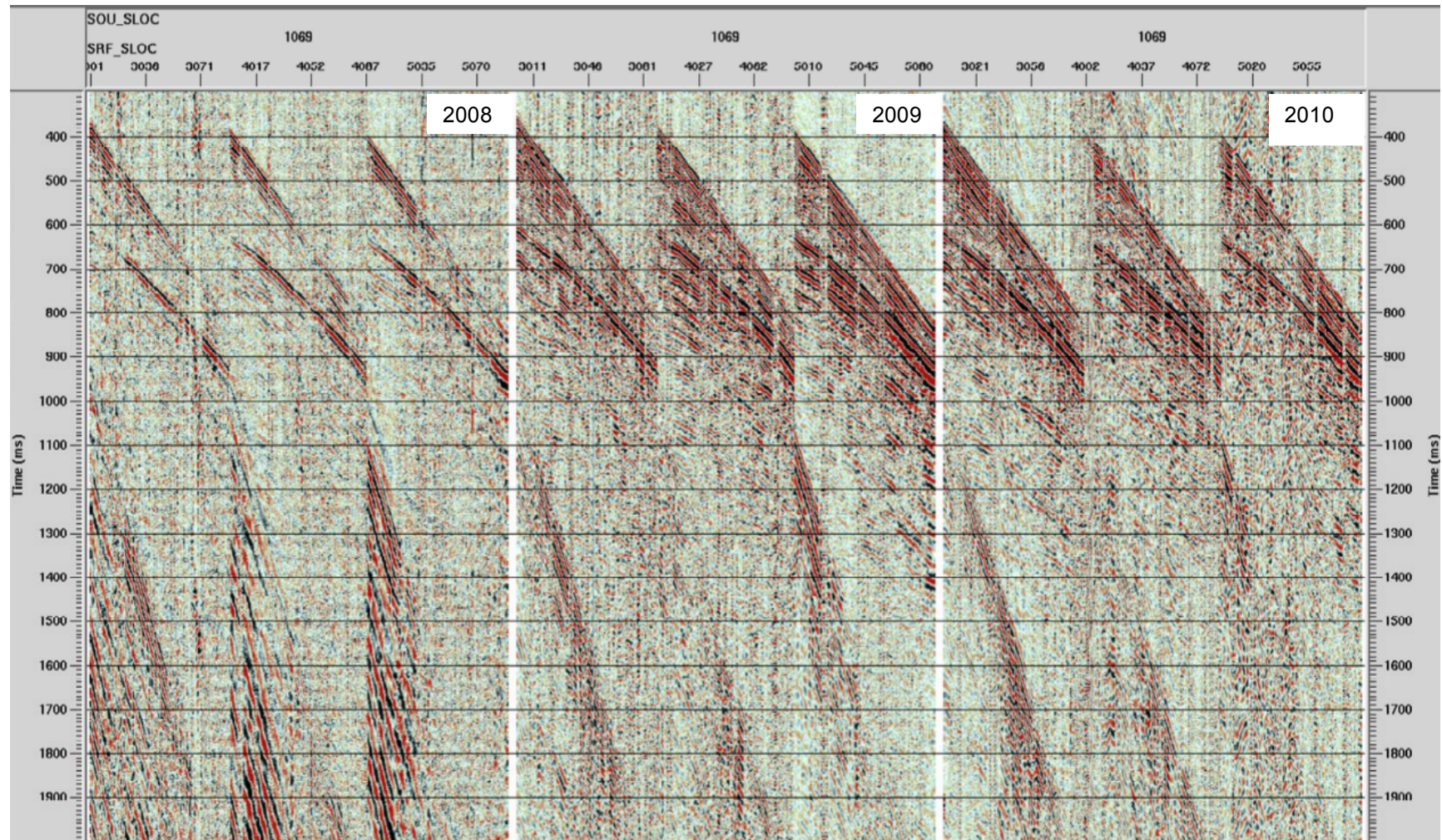


Figure 6.5: An example of the raw shot gather sections of the three volumes for 2008, 2009 and 2010. This example shows the differences in resolution between 2008, 2009 and 2010 that were mainly caused by the changes in the seismic energy, which was much weaker in 2008 using the weight drop source. That weakness in energy occurred because the spectral content varied significantly in the 2008 survey.

6.2.2 Cross-equalisation Processing

To create the time-lapse volumes, the three volumes in 2008, 2009 and 2010 were processed simultaneously, cross-equalised and subtracted from each other in order to detect possible changes in reflection amplitudes. In the 4D data, the variation in frequency content, time-shifting in time-lapse image processing and changes in the phase and amplitude waveform of the 4D signal have a significant effect on the repeatability of both the signal and noise (Lumley et al., 2003; Spetzler and Kvam, 2006). The acquisition differences between the 2008 survey and the 2009 and 2010 surveys in the source energy, surface conditions and the fold size affected the shape of the wavelet and the frequency content between surveys, as well as the coherent noise. This is clear in the shot gather examples of the three volumes (Figure 6.5). The purpose of the cross-equalisation technique is to remove these effects from the time-lapse data sets. Before equalising these three volumes, I decreased the number of channels per shot for the data sets for the 2009 and 2010 surveys to match the number of channels in the 2008 survey. The migrated time section of inline 87 in the three surveys with conventional seismic data processing is shown in Figure 6.6 (top). This step was done to prepare the data set in order to implement the cross-equalisation processing using the following three steps: static correction, shaping filter and time-variant static correction (time shifting). The static correction is required in cross-equalisation to correct the changes in the weathering layer (near-surface soil conditions) or the seismic datum in the repeated time-lapse data sets. A post-stack time shift was calculated and applied to match the reflector geometry in different surveys. Due to the high quality of the 2009 survey, it was chosen to be a reference survey for the time-shifting process. A crosscorrelation was then used between corresponding trace pairs of cubes (2008–2009, 2009–2010 and 2008–2010) and a calculated static shift was applied to the data for 2008 and 2010 to match the 2009 data. The crosscorrelation calculation was done using a 430–1400 ms time window. A correlation coefficient threshold of 0.1 was used, which means that all traces that display a lower correlation were excluded from the analysis. The average time shift was 2 ms for the 2008–2009 pair and was even less for the 2009–2010 pair.

After the time-shift equalisation step, a shaping matched filter was designed to remove the residual amplitude and phase between the three time-lapse data sets. The designed filter was applied to the 2009 and 2010 surveys to match them with the 2008 survey. The filter used was a Wiener filter with length of 100 samples.

Finally, a time-variant gain function (TVG) was applied to balance the amplitude of the different seismic volumes. The amplitude characteristic for the 2008 volume was different and weaker than that for the 2009 and 2010 volumes, which had similar high amplitudes. The 2008 weakness obviously stems from the source energy, which was the WD source. Therefore, a TVG function was only applied to the 2008 volume as an adjustment in order to match the amplitude spectrum of the 2009 and 2010 volumes (Figure 6.6, bottom).

Cross-equalisation processing was applied to these three 3D time-lapse surveys (2008, 2009 and 2010); the last two surveys (2009 and 2010) were conducted using a mini-vibrator seismic source with a higher fold and better quality than the WD source used in the 2008 survey. In this work, I proposed investigating the time-lapse signal detectability of CO₂ in stage 2 of the Otway Project by modelling 3D time-lapse noise. This requires high repeatability data sets as input data. Therefore, I used the cross-equalised 2009 and 2010 volumes, which have higher repeatability and more reliable results for 3D noise modelling than the 2008 volume.

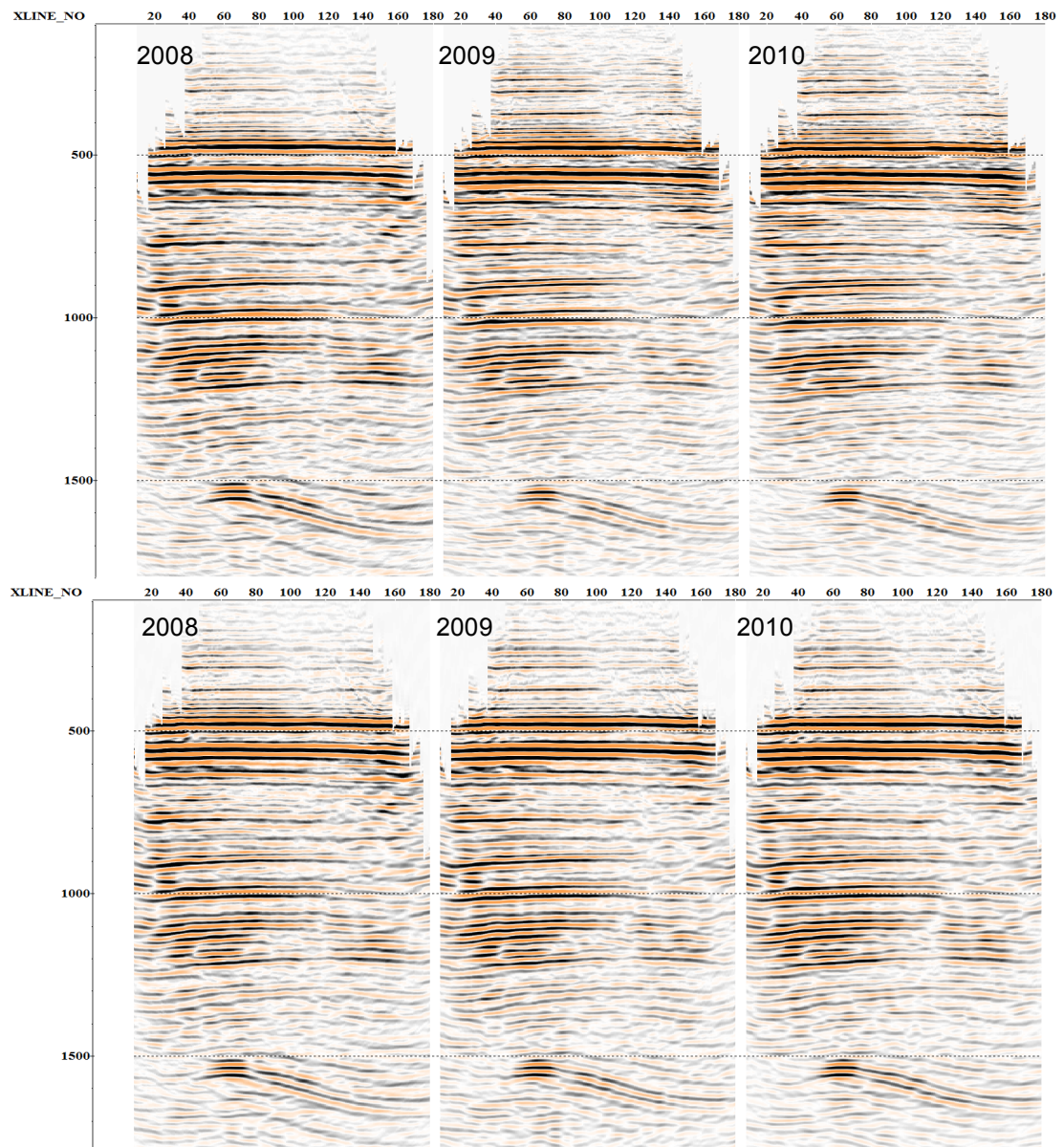


Figure 6.6: A comparison example of the inline 87 migrated section of the three surveys with conventional seismic data processing (top) and after applying the cross-equalisation processing steps (bottom). Note the weakness in the 2008 volume throughout the whole section, particularly in the near surface horizons. The 2009 and 2010 sections show high resolution and repeatability, making the 3D noise modelling results more reliable.

6.3 Modelling of 3D Time-Lapse Noise

6.3.1 Theory

The characteristics of noise can, and usually does, change with the coordinates of the data. For example, the time-lapse noise shown in Figure 6.7 from the CO2CRC Otway Project 4D seismic volume shows a clear change in its characteristics with changing time coordinates. There is also a noticeable change in the noise characteristics with a changing spatial location. To include such variability in the modelled noise, we can split the measured noise into windows, modify the phase spectrum of the windowed noise and then stitch the windows back together with the modified noise. Such spectral modification can be done in two ways: either by using a fixed window, or a systemically variable window (Reine et al., 2009). Here I chose to use the fixed window approach. The reason for using the fixed window approach is its simplicity; I tried to keep the number of the tuning parameters to minimum. However, if the frequency content of the data varies significantly with the time, one can consider using changing windows to account for this variability. To implement this technique, I modified the Short-Time Fourier Transform (STFT), first introduced by (Allen and Rabiner, 1977) and defined by

$$STFT(\tau, f) = \int_{-\infty}^{\infty} w(t - \tau)s(t)e^{-i2\pi ft} dt, \quad 6.1$$

where f is the frequency, t is the time, w is the time window, and τ the time at which I inspect the signal $s(t)$.

I aimed to modify the measured noise by replacing the phase spectrum in each analysis window with a random phase spectrum. Such a change will redistribute the signal from the window along the whole length of the sampled data. This is exemplified in Figure 6.8, where I considered a simple 1D signal shown in the upper panel in blue, while the window is shown in green. The resulting windowed signal is shown in blue in the second panel, while the windowed signal with the changed phase spectrum is shown in black. To combine the modified signals corresponding to different windows, I needed to use the weighted average of these signals using the windows as the weights. The STFT inverse is given by

$$s(t) = \frac{\sum_{i=1}^N w(t - \tau_i) \int_{-\infty}^{\infty} STFT(\tau_i, f) e^{i2\pi f t} df}{\sum_{i=1}^N w(t - \tau_i)}, \quad 6.2$$

where I assumed that the sum of the shifted time windows in the denominator is nonzero for all t ; in other words, the shifted time windows have to overlap.

This is exemplified in Figure 6.9 (middle). Due to the change in the phase spectra of the windowed signal, the amplitude of the modified signals can vary significantly. These variations in amplitude will be carried over to the weighted average and therefore the amplitude variation may be significantly different to that of the original signal. Depending on the application of the modified signal, this variation might be undesirable. To address this, I used a set of windows to scale the amplitude within these windows to the original amplitude of the signal within these windows, as exemplified in Figure 6.9 (bottom). I used the same windows for the rescaling, but in principle different windows could be used. The amplitudes are rescaled to maintain the same energy within the windows. I can summarise the whole workflow as a schematic, as shown in Figure 6.10.

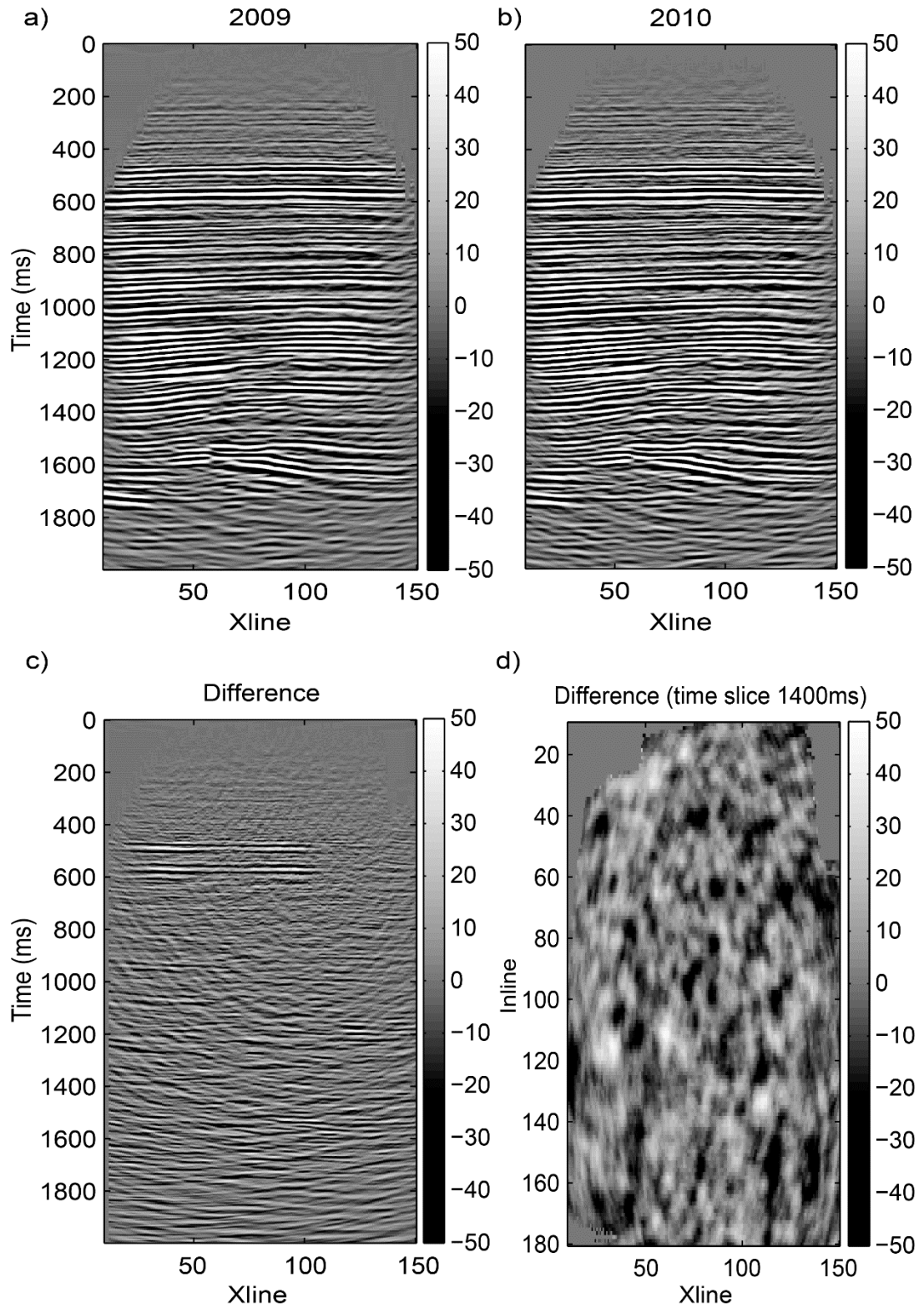


Figure 6.7: Examples of two cross-equalised, processed volumes (a) 2009 and (b) 2010 and (c), their difference in both temporal (Inline 112) and (d) spatial domains (Time slice 1400 ms). The difference section shows the real noise, which is used to model time-lapse noise for the Otway data. This result contains not only the

differences of the two acquisitions but also the result of imperfect cross-equalisation processing.

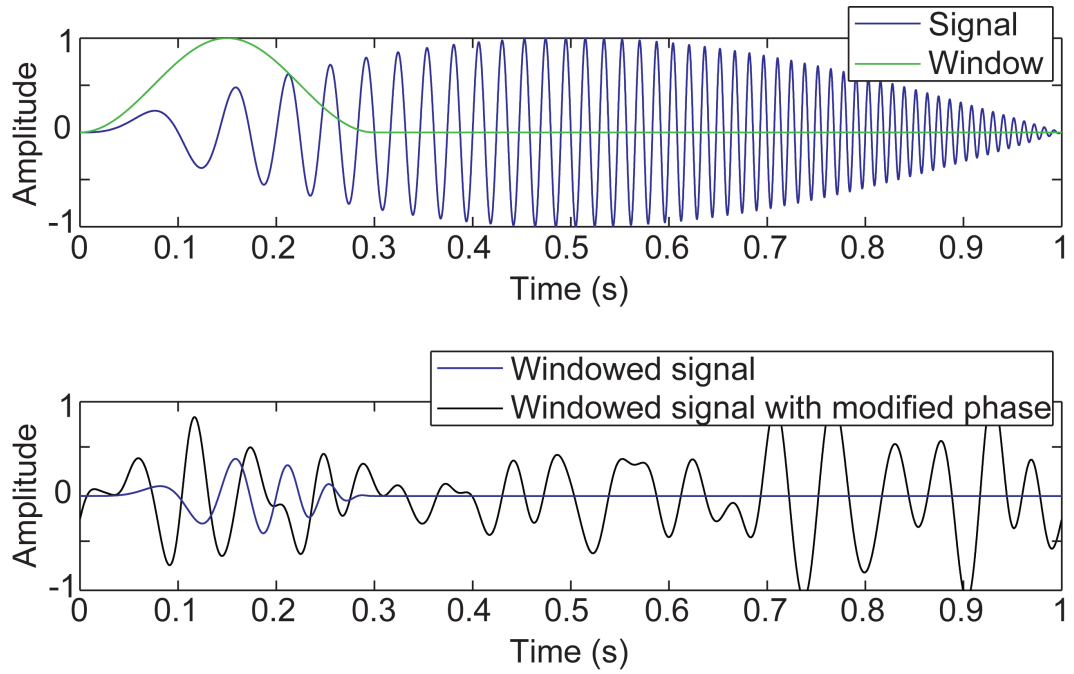


Figure 6.8: (top) Example of a signal with a window and (bottom) the windowed signal and the result of the changed phase spectrum.

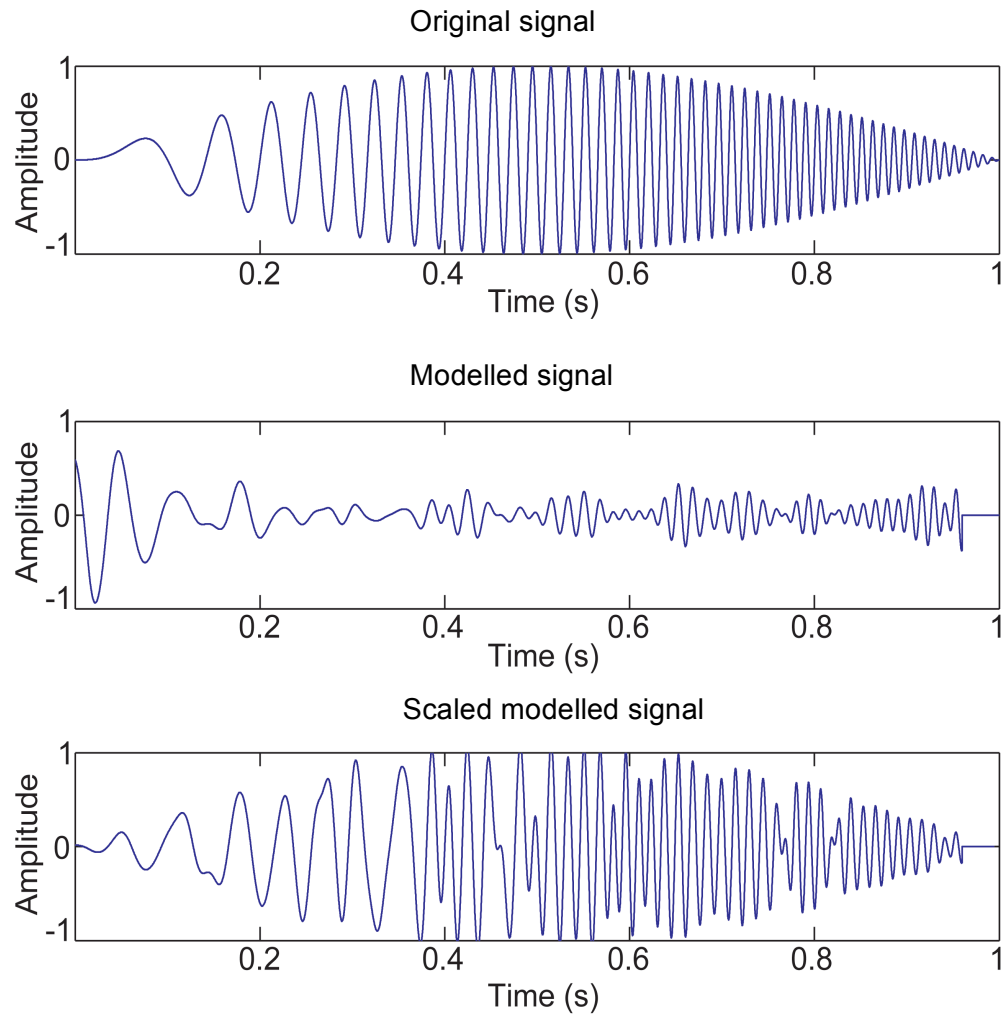


Figure 6.9: (top) Example of the original signal, (middle) the weighted average of the windowed signal with modified phase spectra and (bottom), the same average scaled using sliding windows to match the amplitudes or the original signal.

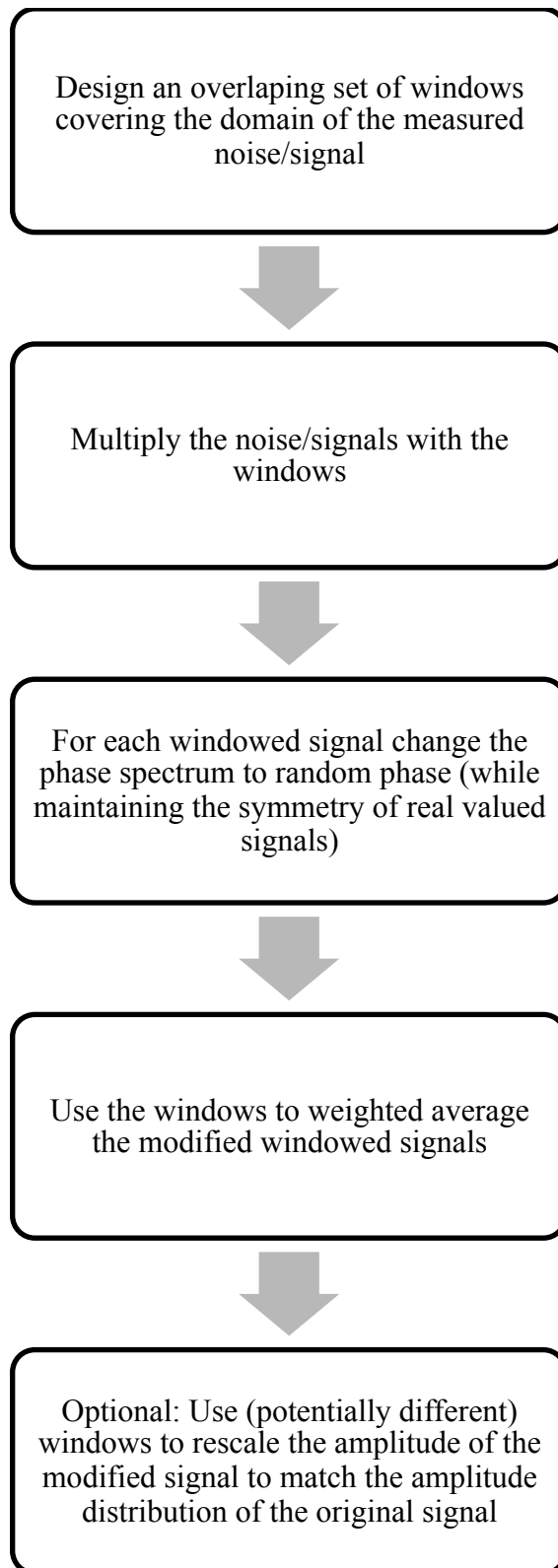


Figure 6.10: Workflow schematic for generation of the "randomised" signal.

I had to choose the windows such that their length/support is sufficient to sample the low frequencies and tapered enough so as not to introduce spurious high frequencies. The window type I used in this work is the Hann window (shown in Figure 6.11), which is defined as

$$w(\tau) = \sin^2 \left[\frac{\tau}{N} \pi \right], \quad 6.3$$

where N is the windowing time length. The properties and benefits of using the Hann window are summarised by Harris (1978). He stated that, typically, applying a sine window (Hann window) with a 50% or more overlap in time length in fast Fourier transform (FFT) decomposition decreases the leakage of spectral amplitude in the main lobe and shows a side lobe with a lower amplitude and far from the main lobe as shown in Figure 6.11. Hence, the window will chirp smoothly and preserve the amplitude distribution in the main lobe of windowed signal.

The size of the window has to be chosen carefully, since a limited window length would act as a low-cut filter, whereas a long window might cover the changes within the noise characteristics. There is a conceptual trade-off between the low-frequency retention and capturing the changes of the noise characteristics. Thus, if possible, the window type should be well tapered (such as Han window), the length of the window should be longer than the maximum wavelength/period in the measured noise and shorter than the variability in the noise, and the overlap (while it depends on the window type and how closely I wanted to mimic the spatial changes in the noise) should be usually more than 50% of the window size.

I chose to modify the phase spectrum of the windowed signal by using uniformly-distributed random numbers in the range from 0 to 2π while maintaining the symmetry of the spectrum of real-valued signals. This choice is based on the fact that the phase spectrum of a random signal is random (up to the symmetry due to the real values of the signal). There might be different possibilities of modifying the phase spectrum to generate signals that are more similar to the original; however, I am not investigating those in this paper.

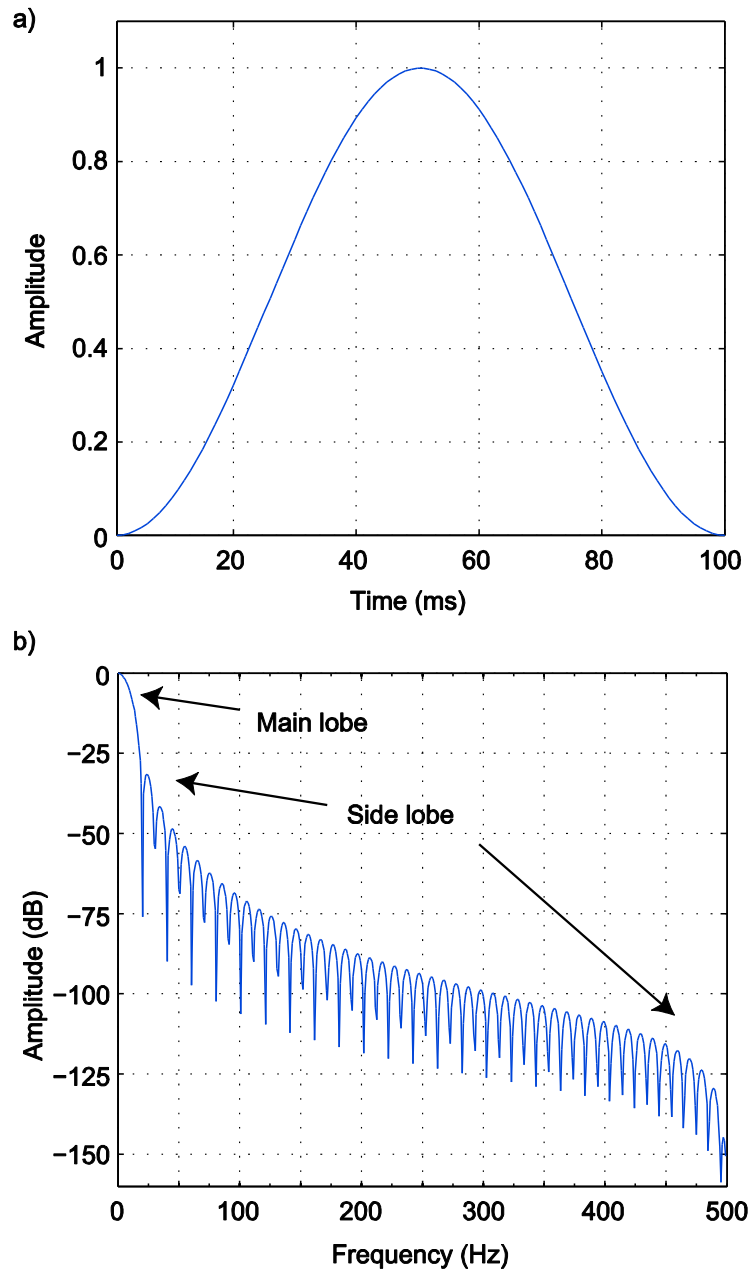


Figure 6.11: The Hann window in (a) time and (b) frequency domains. The smoothness shown in the Hann window is reflected on the transform frequency window by reducing the level of the side lobe and, in contrast, increasing the width of main lobe. This effect causes a decrease in the leakage of spectral amplitude in time-frequency transform decomposition.

6.3.2 Modelling of time-lapse noise for the Otway Project

The result of the subtraction of two data sets or image seismic surveys from each other is the residual energy of a time-lapse signal. This energy is called “time-lapse noise” or “non-repeatable noise.” Indeed, the result contains not only the differences of the two acquisition data sets, but also the result of imperfect cross-equalisation processing.

As mentioned in the introduction, there are two possible approaches to noise modelling. The first approach is based on a detailed understanding of all possible noise types in seismic data and their effects on processed signals. The second approach is an empirical one where the time-lapse noise model is based on observed time-lapse data. I focused on the second approach in the present work. This is possible since I had time-lapse data available from stage one of the Otway project. As previously discussed, there are three 3D time-lapse surveys (2008, 2009 and 2010); the last two surveys (2009 and 2010) were acquired using a mini-vibrator seismic source and at a higher fold and quality than the first survey, which used a weight-drop source (Urosevic et al., 2011).

The injection area for stage two will be above the injection area used during stage one as shown in Figure 5.2. Since the amount of the injected gas was small, I did not expect that the injection has caused changes above the injection interval. This means that I can use the acquired time-lapse data from 2009 and 2010 above the injection area to study the time-lapse noise.

The time-lapse noise is produced by subtracting the two migrated sections from each other after a cross-equalisation (Urosevic et al., 2011) (Figure 6.7). Some residual events between 400 ms and 600 ms, as shown in Figure 6.7 (c), are observed in the difference section, which are caused by time-shifting and cross-equalisation data processing. These residual events will not affect the assessment of CO₂ detectability using this time lapse noise model, because the suggested depth of the CO₂ injection for Otway Stage 2 is roughly 1400 m. However, if the injection interval was in this range, the detectability would be severely affected. This is one of the benefits of the presented method that preserves such strong artefacts and thus does not overestimate detectability in depths with poor signal-to-noise ratio.

To produce a realisation of a modelled time-lapse noise, I used the methodology described in section 6.3.1. The only tuning parameters for the method are: the type of the window, the size of the window and the overlap of the window. I used the three-dimensional Hann window (example shown in Figure 6.12) with size of 100 ms (time), 280 m (inline), 320 m (xline) that overlap by 83% in all the three directions—two spatial and one temporal. The window size was chosen to be as large as possible but not so large as to cover visually determined changes in the characteristics of the noise. Depending on the application, the matching characteristics of the modelled noise to the measured noise can change depending on the choice of the window and the overlap used. To achieve the desired result, one needs to experiment with the window parameters; I did not have a quantitative rule for their selection.

An example of the result of the modelled noise and their spectra are shown in Figure 6.13, 6.14 and 6.15. The presented examples demonstrate the advantages of the method: the coherent nature of the noise is preserved, including the shape of the migration artefacts. The preserved characteristics of the coherent noise can be also seen in the time slice shown in Figure 6.16.

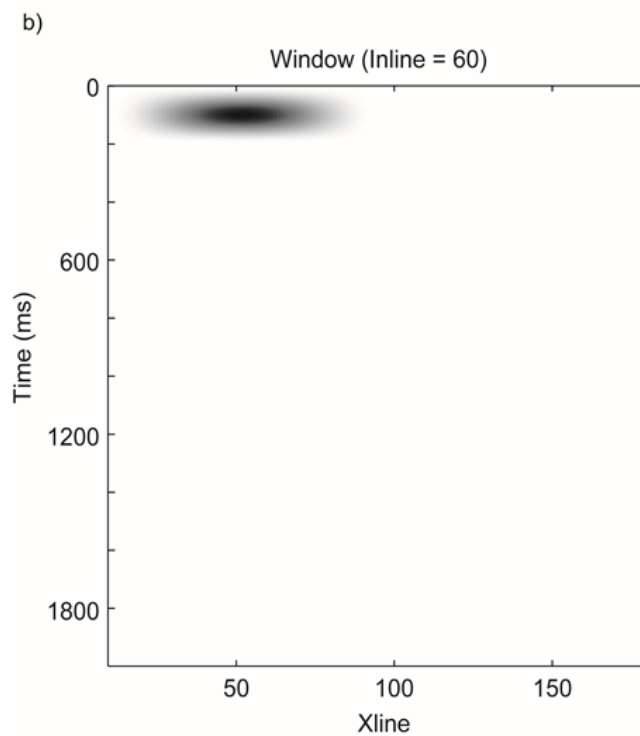
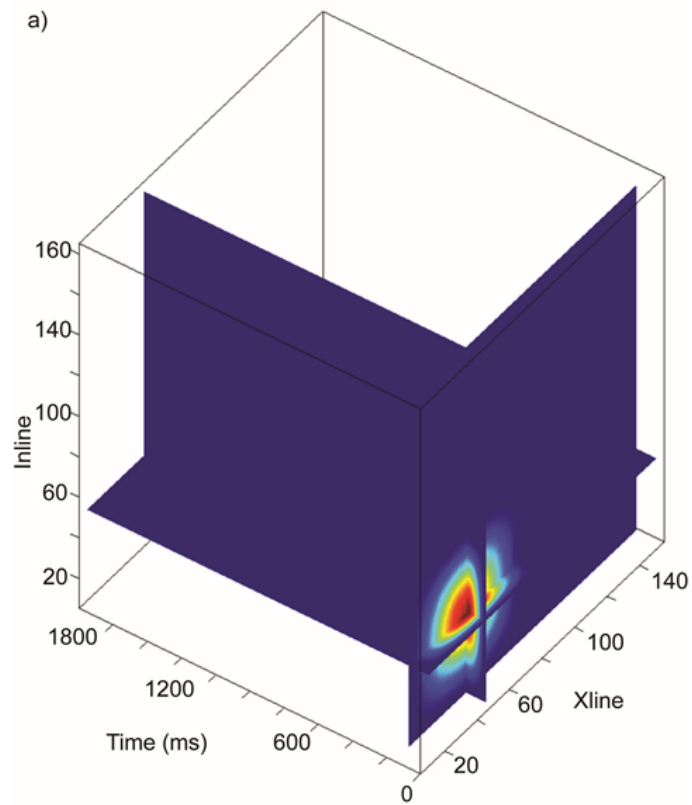


Figure 6.12: Window function used for the generation of the modified time-lapse noise in (a) 3d and (b) 2d displays. The sliding windows have an overlap of 83% in all the three directions—two spatial and one temporal.

6.4 Discussion

The presented method of generation of many realisations of time-lapse noise modifies the measured baseline noise. Thus the baseline noise will influence the modelled noise. While this might be a disadvantage in some situations when one would like to generate truly random noise realisations, I viewed it as a feature of the method, since the intended use is to apply it to real data sets whose characteristics are mirrored in the measured noise.

I had designed the method to be as simple as possible, while still being able to capture the spatial and temporal changes in the noise characteristics. One could include more variations in the modelled noise, for example, by changing the amplitude spectrum as well, or by using more complex windowing methods. Then the question is, at what stage one would stop in including extra tuning parameters that could allow for creation of a completely independent noise model from the baseline noise. Since statistical properties of the noise can be indeed influenced by the choice of the parameters and this dependence should be taken into account in the detectability analysis, I believe that it is beneficial to use a method with as few tuning parameters as possible.

This philosophy can be also applied to the question of why I do not try to model the time-lapse noise based on detailed analysis of the various possible sources of the noise. Even if I had sufficient understanding of all the time-lapse sources and were able to model them, the number of parameters that such noise would depend on would be simply too large.

The presented method is fast and easy to implement for the generation of many realisations of noise, which is crucial for statistical approaches when modelling the seismic response. The main feature and possible drawback of the presented method is the requirement of one measured field noise realisation. While this aspect of the method might be currently limiting its use to only few locations and projects, it is likely that there will be a gradual build-up of a library of time-lapse noise data. Such a library would allow an application of the method even to locations without actual time-lapse data by using an appropriate choice of the time-lapse noise (or combination of noises) from the library.

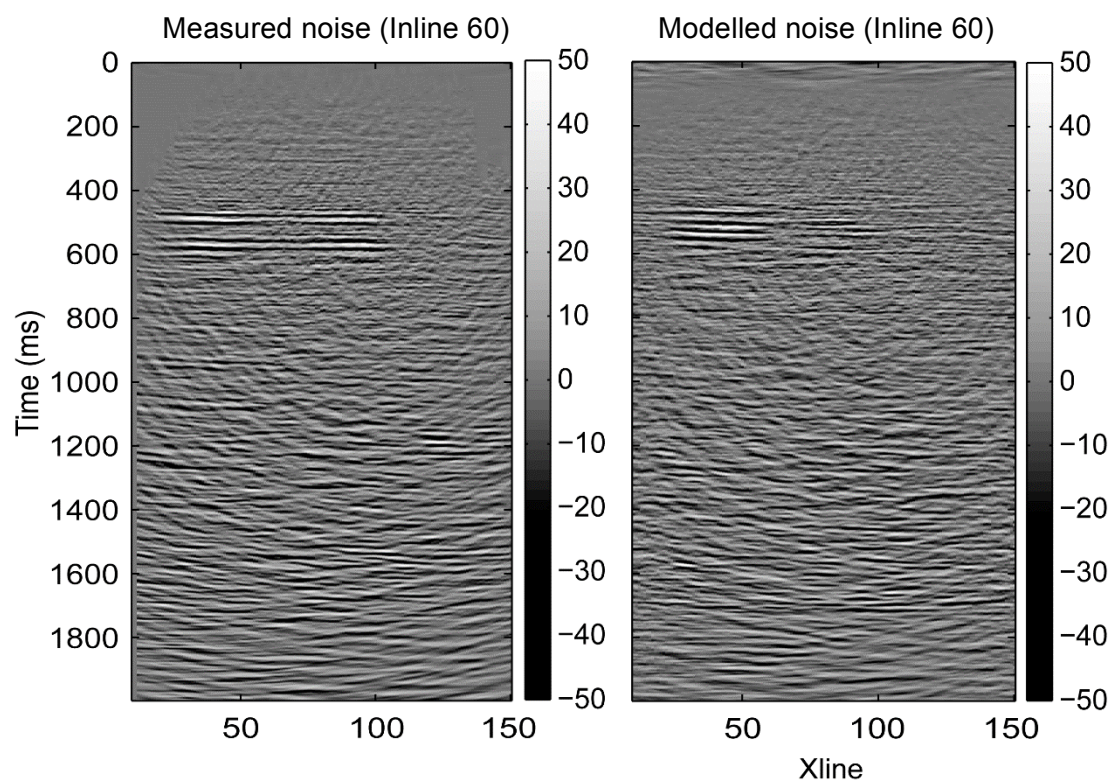


Figure 6.13: Inline section of the noise generated from (left) real time-lapse data and (right) our synthetic modelling noise. The simulation result of the modelled noise is seen to be similar to the actual noise of the difference section.

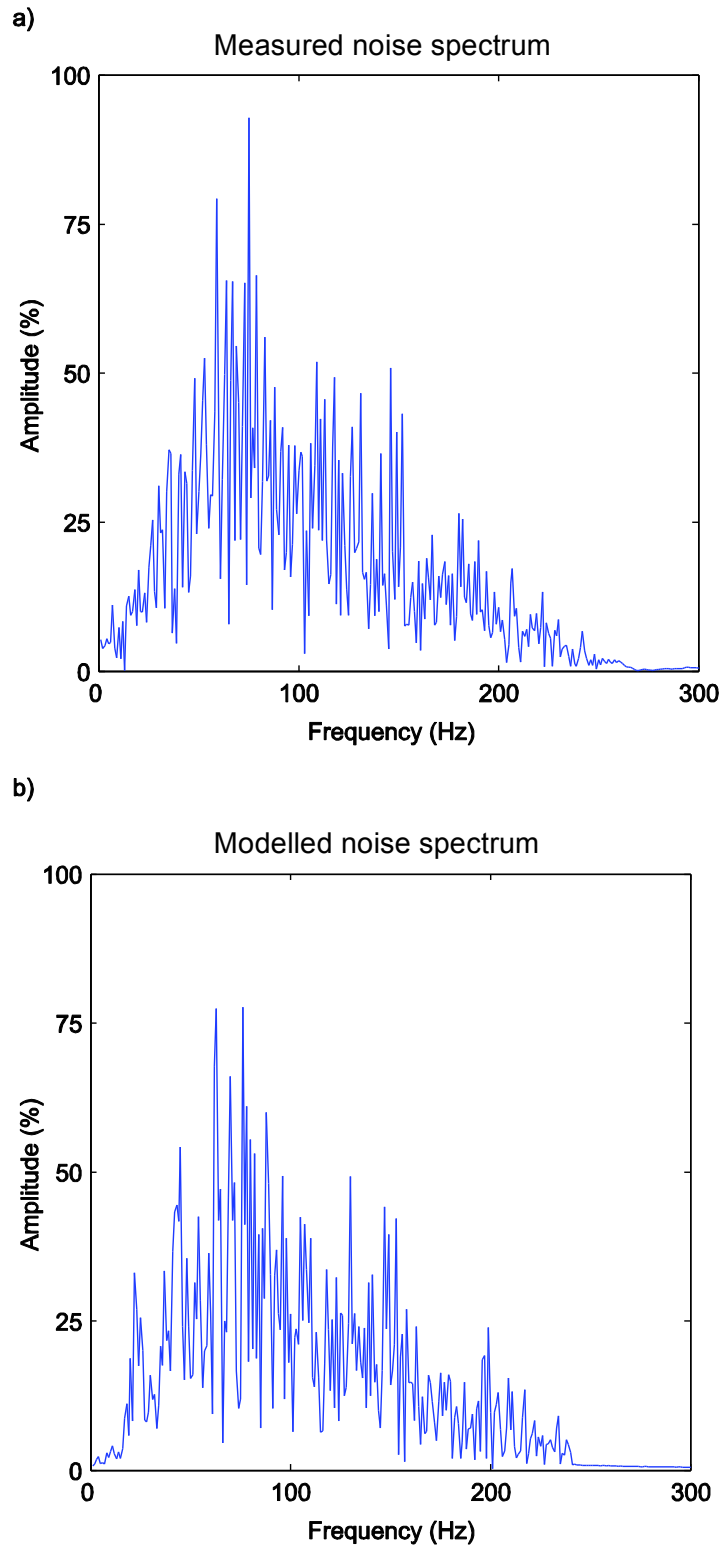


Figure 6.14: Amplitude spectrum comparison for a one trace of (a) the measured noise and (b) modelled noise. The spectrum shows high similarity between the modelled noise and the actual noise which denotes how the method preserves such frequencies of the real data.

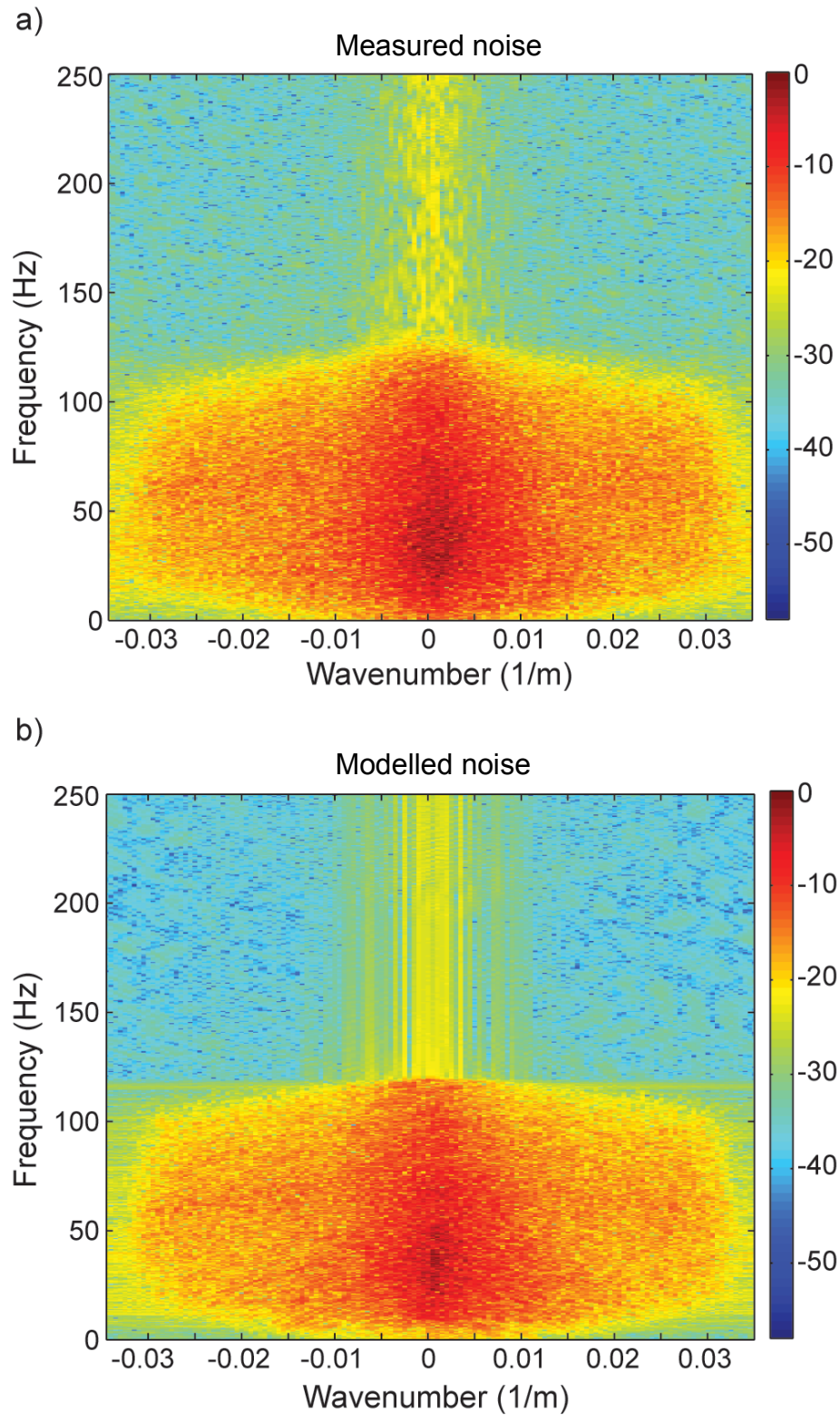


Figure 6.15: Amplitude spectrum comparison of (above) the measured noise and (below) modelled noise. The spectrum shows high similarity between the modelled noise and the actual noise, which denotes how the method preserves such frequencies of the real data.

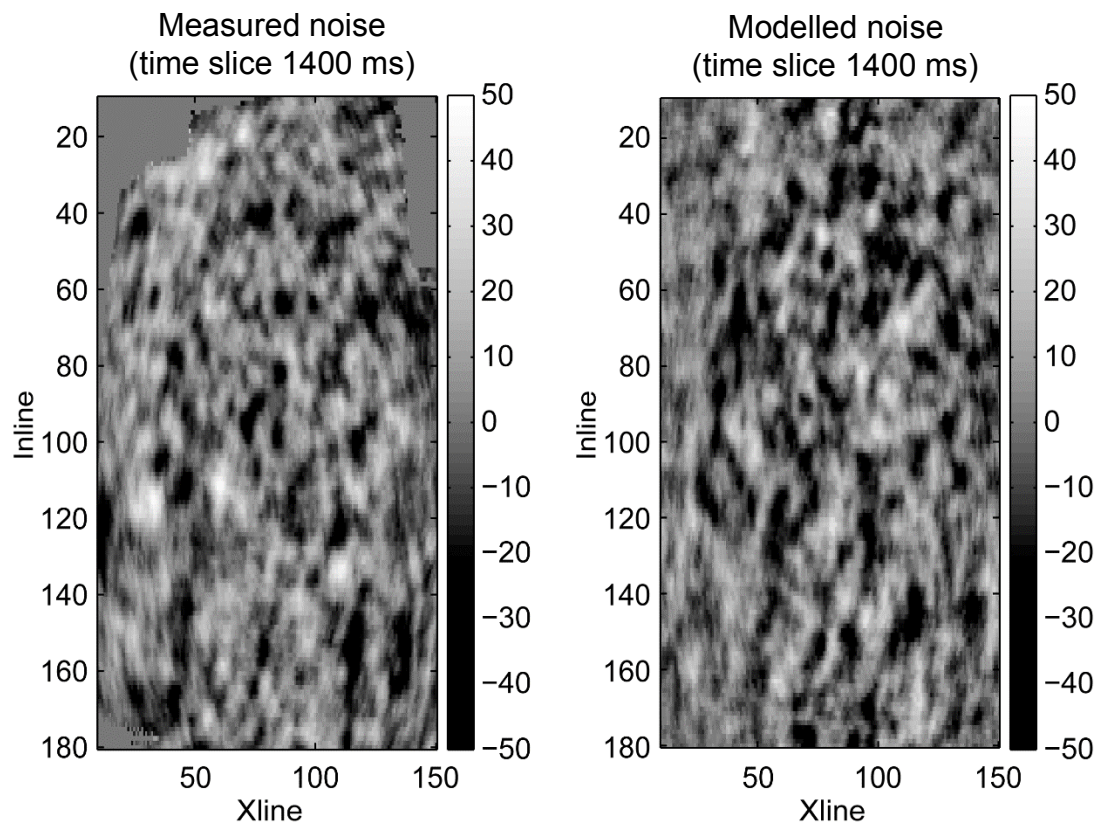


Figure 6.16: Time-slice comparison of (left) the real noise and (right) modelled noise at $t=1400$ ms.

6.5 Conclusion

The CO₂ detectability and monitoring by seismic time lapse can be assessed by studying the time-lapse signal and noise. In this chapter I presented a method to model 3D time-lapse noise. This method leads to evaluate the feasibility of CO₂ seismic monitoring for the Otway project Stage 2 for CCS. In the Otway project, I used real 3D time lapse data, which makes this evaluation more realistic and applicable than what I have done in the SW Hub and CarbonNet projects.

I used a modified STFT with a suitable weighting function in the time-lapse noise model to address the complications of measuring the time-to-frequency spectrum for 3D time-lapse random noise. By matching real data amplitude with the phase of the modelled noise, 3D time-lapse modelling noise is produced. I also showed and compare the results of real and modelled noise in time and space domains using time slices and inline sections. The resulting noise realisation matches the coherent characteristics of the measured noise, as desired.

Using the presented method to generate many realisations of time-lapse noise for a statistical determination of plume detectability is a part of the future work. Indeed, time-lapse seismic surveys play an important role in the Otway project Stage 1. This importance will be emphasised by using this model to investigate the CO₂ plumes detectability for Stage 2 using statistical methods, which is beyond the scope of this thesis. High-density 3D seismic surveys with high repeatability is required for future time-lapse data sets, which will help decrease time-lapse errors and noise and enhance the detection of the time-lapse signals.

In this chapter, I proposed a simple enhancement to this noise modelling approach, which allowed us to overcome the time-lapse noise using 3D time-lapse data from the CO₂CRC Otway project. I utilised two sets of real time-lapse 3D data from the Otway area acquired in 2009 and 2010. The time-lapse data were processed and migrated by Curtin University staff. I generated noise realisations by modifying the phase spectrum of the measured noise using a windowing approach. I preserved the amplitude spectrum of the signal and thus the spatial and temporal correlation of the measured noise. The method shows a good matching of the measured noise event and produces a very realistic model.

6.6 References

- Allen, J. B., and L. Rabiner, 1977, A unified approach to short-time Fourier analysis and synthesis: *Proceedings of the IEEE*, **65**, 1558-1564.
- Calvert, R., 2005, Insights and methods for 4D reservoir monitoring and characterization.
- Harris, F. J., 1978, On the use of windows for harmonic analysis with the discrete Fourier transform: *Proceedings of the IEEE*, **66**, 51-83.
- Hughes, J. K., 1998, Examination of Seismic Repeatability as a Key Element of Time-Lapse Seismic Monitoring: Presented at the European Petroleum Conference.
- Johnson, D. L., 2001, Theory of frequency dependent acoustics in patchy-saturated porous media: *Journal of the Acoustical Society of America*, **110**, 682-694.
- Kearey, P., M. Brooks, and I. Hill, 2009, An introduction to geophysical exploration: Wiley. com.
- Landro, M., 2008, The effect of noise generated by previous shots on seismic reflection data: *Geophysics*, **73**, Q9-17.
- Linville, A., and R. Meek, 1995, A procedure for optimally removing localized coherent noise: *Geophysics*, **60**, 191-203.
- Lumley, D., C. A. Donald, M. Mark, C. Steve, and W. Rich, 2003, 4D seismic data processing issues and examples: *SEG Technical Program Expanded Abstracts*, **22**, 1394-1397.
- Nemeth, T., H. Sun, and G. Schuster, 2000, Separation of signal and coherent noise by migration filtering: *Geophysics*, **65**, 574-583.
- Pevzner, R., R. Galvin, M. Madadi, M. Urosevic, E. Caspari, B. Gurevich, D. Lumley, V. Shulakova, Y. Cinar, and V. Tcheverda, 2012, Monitoring CO₂ injection into a saline aquifer: Otway Project feasibility study: Presented at the SEG Technical Program Expanded Abstracts 2012.
- Pevzner, R., V. Shulakova, A. Kepic, and M. Urosevic, 2010, Repeatability analysis of land time-lapse seismic data: CO₂CRC Otway pilot project case study: *Geophysical Prospecting*, **59**, 66-77.
- Reine, C., M. van der Baan, and R. Clark, 2009, The robustness of seismic attenuation measurements using fixed- and variable-window time-frequency transforms: *Geophysics*, **74**, WA123-WA135.

- Spetzler, J., and O. Kvam, 2006, Discrimination between phase and amplitude attributes in time-lapse seismic streamer data: *Geophysics*, **71**, O9-19.
- Urosevic, M., R. Pevzner, V. Shulakova, A. Kepic, E. Caspari, and S. Sharma, 2011, Seismic monitoring of CO₂ injection into a depleted gas reservoir—Otway Basin Pilot Project, Australia: *Energy Procedia*, **4**, 3550-3557.

Every reasonable effort has been made to acknowledge the owners of copyright material. I would be pleased to hear from any copyright owner who has been committed or incorrectly acknowledge.

CHAPTER7: SUMMARY, CONCLUSIONS AND FUTURE RESEARCH

7.1 Summary

Capturing CO₂ before it reaches the atmosphere and injecting it into geological subsurface formations is a relatively new approach that demands new technology in order to be fully successful. Therefore, to monitor and verify CO₂ sequestration correctly and to detect possible seepage from storage areas, I needed an effective method that will perform these roles. Many CCS projects have been established around the world. Australia has become one of the leading nations in this field as it has invested in several CCS onshore and offshore projects. Therefore, to monitor and verify CO₂ sequestration correctly and to detect possible leakage into the atmosphere from the desired storage area, an effective method is needed that will perform all of these functions. The possible estimation of the seepage size is required by detection the CO₂ plume with the proposed methods. This thesis aims to address this issue for seismic monitoring methods for three Australian CCS projects.

The key objective of the thesis is to study the feasibility of the use of time-lapse seismic methods in detecting the seismic response caused by CO₂ injections. Many features affect the time-lapse signal, for example, survey seismic repeatability, the contrast between the physical properties of CO₂, reservoir gas and fluid contents and reservoir lithology, structure and conditions (fluid pressure and temperature). Studying these features is very important in order to estimate CO₂ detectability. Thus, all these elements can be addressed by applying advanced seismic processing and cross-equalisation techniques. The analysis of the time-lapse signal and noise response also plays an important role. In this thesis, I presented a feasibility study of CO₂ detectability using time-lapse seismic methods including various techniques and tests for three Australian CCS projects: the South West Hub Project, the CarbonNet Project and Stage 2 of the Otway project.

For the SW Hub and CarbonNet projects (Chapters 3 and 4), I presented feasibility studies utilising the synthetic time-lapse seismic signal based on the real baseline seismic section. I constructed several numerical models based on geological and lithological reports. I also simulated different CO₂ plumes sizes and modelled them using Gassmann fluid substitution and other relations in order to calculate the velocities and densities of subsurface geological layers to make the model more

realistic. Many time-lapse seismic methods were employed to investigate the detectability of the CO₂ plumes. In the case of noise-free results in two projects, the different migration sections show high detectability for all investigated plume sizes. Realistic noise modelling was done by taking different SNR measurements and NRMS. In the SW Hub project, the matching SNR value at the interface of the injection zone is approximately 5. The CO₂ detectability in the difference section after adding the modelled realistic noise matching this value was low and detectable just for the large plumes of CO₂ (40 and 80 k tonnes). One of the reasons for this is the effective porosity of the injection zone, which is 11%. In the CarbonNet Project, I added noise to match a SNR of 10 and an NRMS of 50% for marine streamer data and an NRMS of 17% for OBC data. The CO₂ plumes in the difference section with added filtering noise were detectable for more than 3 kit plumes by streamer and for all plumes by OBC. In the CarbonNet Project, I achieved high detectability using the OBC method and satisfactory detectability using the marine streamer seismic method; with OBC I expected to detect 0.64 k tonnes, while with the streamer I expected to detect 3 k tonnes.

For the Otway project (Chapter 5), the detection of CO₂ plumes was assessed using two Kirchhoff time migration algorithms (post-stack and pre-stack). Realistic time-lapse noise was estimated based on the SNR for the Sodas Road field data to measure the level of real noise. To match this noise level, I added adequate band-limited random noise to the shot gathers. The time-lapse results of post-stack migration with added noise show low detectability of CO₂. The plume response was hidden by the level of modelled noise and was difficult to detect. In pre-stack migration tests, the CO₂ plume was more detectable. In this test, I proved the superiority of the Kirchhoff pre-stack time migration in time-lapse response imaging for CO₂ plumes.

Also in the Otway Project (Chapter 6), the availability of real 3D time-lapse datasets helps to investigating CO₂ detectability and monitoring and in modelling realistic 3D time-lapse noise. Modelling the time-lapse measured noise by preserving the real amplitude from the measured noise and filtering it with random phases is one of the more promising techniques used to generate realistic noise models. In this time-lapse noise model, the STFT was used instead of the conventional Fourier transform to address the variability of 3D time-lapse noise. The resulting noise

realisation matches the coherent characteristics of the measured noise. An advantage of this technique is that it can be used for the statistical determination of plume detectability, which is part of future work, by generating multiple noise realisations.

7.2 Conclusions and recommendations

To conclude, modelling the time-lapse signal and noise based on real or synthetic time-lapse data is crucial for any CO₂ plume detectability study. Modelling the time-lapse noise based on measured time-lapse data led to a better understanding of the noise and to more realistic evaluation of CO₂ detectability for Australian CCS projects.

Seismic methods are dependent on the elastic impedance change, which in the case of CO₂ injection, is highly dependent on the reservoir porosity. Time-lapse seismic signals suffer in low-porosity aquifers where very large quantities of CO₂ are required for an appreciable detection by the methods. Based on that, they will be more effective in high porosity regimes such as CarbonNet project, than in low porosity regimes such as SW Hub project.

I note that the time-lapse noise, which is result of a difference of the noisy baseline and monitor sections, combines in the difference section. Therefore, the noise level in the difference section, which hides most plumes, appears higher than the noise in monitor sections. However, the CO₂ plumes at the interfaces, such as in the VSP model for the SW Hub project, are hidden by the strength of the reflected waves. As a result, they are only detectable in the difference section. Hence, one should always investigate both the difference sections as well as the individual vintages.

Since we observed that the difference section in the post-stack migration, including the modelled noise, shows relatively low detectability of CO₂ when compared to the pre-stack migration, pre-stack time migration is a highly effective time-lapse imaging method for CO₂ verification and monitoring and is therefore the recommended method. One possible reason for this superiority is that post-stack migration attenuates diffractions, which might contribute to the plume image of the studied size. This also suggests that including diffraction imaging in a seismic monitoring program might enhance the detectability of small plumes.

Using a real 3D field data set, a new method was designed to model realistic 3D time-lapse coherent noise with as few tuning parameters as possible while still being able to capture the spatial and temporal changes in the noise. This method is fast and easy to implement in order to generate many realisations of noise. The results of these realisation models are crucial for statistical approaches when modelling seismic responses. The possible downside of this method is the requirement of one measured field noise realisation. While this aspect of the method might limit its use to only a few locations and projects, it is likely that there will be a gradual build-up of a library of time-lapse noise data. Such a library would allow the application of the method to locations without actual time-lapse data by using appropriate time-lapse noise (or a combination of noises) from the library.

High-density 3D seismic surveys with high repeatability are required for future time-lapse data in order to decrease time-lapse errors and noise and to enhance the detection of time-lapse signals for all projects. One possibility of increasing repeatability of surveys is to install a permanent seismic arrays that can dramatically reduce the effects of changing near-surface conditions and effects of ambient noise. Another potential benefit of permanently installed arrays might be long term cost saving, improved OHS, and reduced disturbance to the community during surveys.

7.3 Future Research

Modelling 2D and 3D realistic time-lapse noise models, such I did in these projects, helps in studying the CO₂ detectability whether we have a field time-lapse data or not. These models will help in generating statistics on time-lapse data, such as the detectability of the time-lapse signal using, for example, Monte Carlo-type statistical analyses. Such analyses require many realisations of noise, which can be exported from these models. This is part of future work and will be accomplished by generating many realisations of the subsurface and noise models. Thus, the availability of fast and relatively easy time-lapse noise models should have great potential in the future investigation of CO₂ plume detectability.

Even if there are no time-lapse data available, I still need to have a model of time-lapse noise to model seismic monitoring. While I have produced reasonably authentic time-lapse noise by migrating band-limited random noise, more work needs

to be done to include other contributors in the noise models, such as the effects of the changing surface conditions.

Every reasonable effort has been made to acknowledge the owners of copyright material. I would be pleased to hear from any copyright owner who has been committed or incorrectly acknowledge.

Appendix

Copyright Release Information

Permission 1

From: Linstrom, Peter [<mailto:peter.linstrom@nist.gov>]

Sent: Thursday, 8 May 2014 11:52 PM

To: 14430617@student.curtin.edu.au

Cc: data

Subject: RE: Reference Citation

Dear Mamdoh Alajmi,

This message is in response to your message which is reproduced below.

Please feel free to cite the web page in whatever format you would like. The fluid data pages have a link to a recommended citation page that yields the following:

E.W. Lemmon, M.O. McLinden and D.G. Friend, "Thermophysical Properties of Fluid Systems" in **NIST Chemistry WebBook, NIST Standard Reference Database Number 69**, Eds. P.J. Linstrom and W.G. Mallard, National Institute of Standards and Technology, Gaithersburg MD, 20899, <http://webbook.nist.gov>, (retrieved May 8, 2014).

Please note that this is only a suggestion and that you would probably want to adjust the date and format to your needs.

Thank you for your interest in NIST data.

Peter Linstrom

=====
Peter J. Linstrom

(301) 975-5422

NIST, Chemical Sciences Division
=====

From: Mamdoh Alajmi [[mailto:](#)]

Sent: Thursday, May 08, 2014 6:26 AM

To: data

Subject: Reference Citation

Dear NIST,

I am Mamdoh Alajmi , PhD student in Curtin University in Australia and I use the Thermophysical Properties of Fluid System (<http://webbook.nist.gov/chemistry/fluid/>) to calculate some data.

I want to reference the website with correct reference but I couldn't I found a lot but I don't know what is the correct one.

Could you please help me with that and send me Reference Citation.

My last access was on the 02/2012.

Regards,

Mamdoh

Permission 2

Hi Mamdoh,

In regards to the citation the author will just be Geoscience Australia and the website address with the viewed date. Can you please attribute the image in the following manner;



© Commonwealth of Australia (Geoscience Australia) 2014. This product is released under the Creative Commons Attribution 3.0 Australia Licence. <http://creativecommons.org/licenses/by/3.0/au/deed.en>

Regards

Elizabeth

Elizabeth Fredericks

IP and Copyright Manager

Client & Information Management

Corporate Services | **GEOSCIENCE AUSTRALIA**

Phone: +61 2 6249 9367 Fax: +61 2 6249 9989

Email: Elizabeth.Fredericks@ga.gov.au Web: www.ga.gov.au

Cnr Jerrabomberra Avenue and Hindmarsh Drive Symonston ACT

GPO Box 378 Canberra ACT 2601 Australia

Applying geoscience to Australia's most important challenges

From: Black Jane **On Behalf Of** Library Reference

Sent: Wednesday, 29 October 2014 10:09 AM

To: 14430617@student.curtin.edu.au

Cc: Copyright; Library Reference

Subject: FW: Reference and citation [SEC=UNCLASSIFIED]

Dear Mamdoh,

Thanks for your reply and additional information.

I have forwarded your email to our Copyright Advisor who will be able to assist you further with the specifics of that particular image.

Kind regards,

Jane Black

Information Services Librarian| Doc Fisher Geoscience Library| Information Management

Corporate Services | **GEOSCIENCE AUSTRALIA**

Phone: +61 2 6249 5895 Email: jane.black@ga.gov.au Web: www.ga.gov.au

Cnr Jerrabomberra Avenue and Hindmarsh Drive Symonston ACT

GPO Box 378 Canberra ACT 2601 Australia

Applying geoscience to Australia's most important challenges

Permission 3

From: Mamdoh Alajmi [<mailto:14430617@student.curtin.edu.au>]
Sent: Tuesday, 28 October 2014 5:34 PM
To: Library Reference
Subject: RE: Reference and citation [SEC=UNCLASSIFIED]

Dear Jane,

Thank you so much for your email.

The information what I got from the website below was a picture and there was not any reference or author I can put his/her names in citation.

<http://www.ga.gov.au/scientific-topics/energy/province-sedimentary-basin-geology/petroleum/offshore-southern-australia/gippsland>

So could please help me with to cite this picture.

Regards,

Mamdoh Alajmi

See Figure (4.2)

From: Jane.Black@ga.gov.au [<mailto:Jane.Black@ga.gov.au>] **On Behalf Of**
Reference.Library@ga.gov.au
Sent: Tuesday, 28 October 2014 8:32 AM
To: m.alajmi@student.curtin.edu.au
Cc: Reference.Library@ga.gov.au
Subject: RE: Reference and citation [SEC=UNCLASSIFIED]

Dear Mamdoh,

Thank you for your enquiry which has been referred to the Library for further assistance.

The Geoscience Australia website provides examples of how to cite our information, including information from our website. Here's the [link](#) to the page.

The exact citation style will depend on the preferred output style of your university faculty. I gather your [university Library](#) will be able to advise you which style to use.

All the best with your studies.

Kind regards,

Jane

Jane Black

Information Services Librarian| Doc Fisher Geoscience Library| Information Management

Corporate Services | **GEOSCIENCE AUSTRALIA**

Phone: +61 2 6249 5895 Email: jane.black@ga.gov.au Web: www.ga.gov.au

Cnr Jerrabomberra Avenue and Hindmarsh Drive Symonston ACT

GPO Box 378 Canberra ACT 2601 Australia

Applying geoscience to Australia's most important challenges

-----Original Message-----

From: contact-form@ga.gov.au [<mailto:contact-form@ga.gov.au>]

Sent: Monday, 27 October 2014 6:07 PM

To: Education

Subject: Reference and citation [SEC=UNCLASSIFIED]

Name : Mamdoh Alajmi

Email : m.alajmi@student.curtin.edu.au

Confirm email : m.alajmi@student.curtin.edu.au Type of enquiry : Education Topic of interest (optional) : Geographic Information Subject : Reference and citation Message : Dear, I am Mamdoh Alajmi , PhD student in Curtin University in Australia and I use some figures in my thesis from (<http://www.ga.gov.au/>) and I want to reference the website with correct reference.

Could you please help me with that and send me reference citation.

Regards,

Mamdoh Alajmi

Permission 4

Dear Mamdoh Alajmi:

Thank you for your inquiry to the United States Energy Information Administration (EIA).

Did you find that graphic on our website?

For our most recently published projection for the U.S., see Figure MT-9 at:

http://www.eia.gov/forecasts/aeo/MT_energydemand.cfm#renew_natgas

For the world, see Figure 16 at:

<http://www.eia.gov/forecasts/archive/ieo13/world.cfm>

There is no copyright restriction on the use of those graphs; see our reuse and copyright info at: http://www.eia.gov/about/copyrights_reuse.cfm

I hope this information helps. Please contact us again if you need additional assistance with energy data and statistics.

Paul Hesse | Information Dissemination Specialist

Z Inc., Contractor to the Office of Communications

U.S. Energy Information Administration

www.eia.gov

 [Like](#) EIA on Facebook

 [Follow](#) EIA on Twitter

 [Visit](#) EIA on Flickr

 [Follow](#) EIA on LinkedIn

[Sign up](#) for email notices of EIA data and report releases.

From: Mamdoh Alajmi [<mailto:14430617@student.curtin.edu.au>]

Sent: Wednesday, January 28, 2015 3:07 AM

To: InfoCtr (OC)

Subject: Copyright permission

Dear U.S. Energy Information Administration

It is my understanding that your organisation holds copyrights in the following figure. I would like to reproduce an extract of this work in a doctoral's thesis which I am currently undertaking at Curtin University of Technology in Perth, Western Australia.

I am carrying out this research in my own right and have no association with any commercial organisation or sponsor. The figure that I would like to use for the purposes of the thesis is (**Feasibility of Seismic Monitoring Methods for Australian CO₂ Storage Projects**). Once completed, the thesis will be made available in hard-copy form in the Curtin Library and in digital form on the Internet via the Australasian Digital Thesis Program.

The material will be provided strictly for educational purposes and on a non-commercial basis. Further information on the ADT program can be found at <http://adt.caul.edu.au>.

I would be most grateful for your consent to the copying and communication of the work as proposed. If you are not the copyright owner of the material in question, I would be grateful for any information you can provide as to who is likely to hold the copyright.

I look forward to hearing from you and thank you in advance for your consideration of my request.

Yours sincerely

Mamdoh Alajmi

See figure (1.1)

Permission 5

Dear Mamdoh,

Yes, you can use the images without restrictions as long as you do not alter the copyright watermark. You may want to add “image courtesy of CO2CRC” in the relevant captions.

Kind regards,

Matthias

From: info

Sent: Thursday, 29 January 2015 9:26 AM

To: Matthias Raab

Subject: FW: Copyright permission

Hi Matthias – For your consideration, please see below. Cheers, Fiona

From: Mamdoh Alajmi [<mailto:14430617@student.curtin.edu.au>]

Sent: Wednesday, 28 January 2015 7:20 PM

To: info

Subject: Copyright permission

Dear CO2CRC

I am Mamdoh Alajmi PhD student in the Department of Exploration Geophysics, Curtin and member of CO2CRC.

It is my understanding that CO2CRC holds copyrights in the below figures. I would like to reproduce an extract of this work in a doctoral's thesis which I am currently undertaking at Curtin University of Technology in Perth, Western Australia.

I am carrying out this research in my own right and have no association with any commercial organisation or sponsor. The figure that I would like to use for the purposes of the thesis is (**Feasibility of Seismic Monitoring Methods for Australian CO₂ Storage Projects**). Once completed, the thesis will be made available in hard-copy form in the Curtin Library and in digital form on the Internet via the Australasian Digital Thesis Program.

The material will be provided strictly for educational purposes and on a non-commercial basis. Further information on the ADT program can be found at <http://adt.caul.edu.au>.

I would be most grateful for your consent to the copying and communication of the work as proposed. If you are not the copyright owner of the material in question, I would be grateful for any information you can provide as to who is likely to hold the copyright.

I look forward to hearing from you and thank you in advance for your consideration of my request.

Yours sincerely

Mamdoh Alajmi

PhD Student | Department of Exploration Geophysics

Curtin University

Tel | +61 8 92663522

Fax | +61 8 9266 3407

Mobile | +61 0 43619503

Email | m.alajmi@postgrad.curtin.edu.au

Web | <http://curtin.edu.au>



Curtin University is a trademark of Curtin University of Technology.

CRICOS Provider Code 00301J (WA), 02637B (NSW)

See figures (1.2, 1.4, 1.6, 1.7, 1.8, 5.1 and 5.2)